Constraining landscape sensitivity to climate change using geomorphological and sedimentological approaches

Mitchall D'Arcy

Department of Earth Science and Engineering

Imperial College London

Submitted in fulfilment of the requirements for the award of the degree of Doctor of Philosophy

23rd September 2015

Declaration of Originality:

I declare that this thesis is original and solely the result of my own work during my Ph.D. studies, apart from where indicated in the text, for which full references are provided.

Mitch D'Arcy

23rd September 2015

Copyright Declaration:

Abstract

Climate exerts a profound control on the processes that shape landscapes and produce the sedimentary deposits with which we can interpret the Earth's history. However, we lack a complete understanding of how sensitive tectonically-active, eroding landscapes are to climate and climate change. How does a simple sediment routing system react to a change in rainfall rate? Can mountainous landscapes respond quickly enough to preserve a record of high-frequency climate changes, e.g., glacial-interglacial cycles? What effect does headwater glaciation have on downstream sediment characteristics? Can we quantify past climate changes using the sedimentological properties of terrestrial stratigraphy? Geologists lack complete answers to these questions, among many others. Theoretical work, using physical first principles and numerical models, has produced a range of hypotheses about landscape sensitivity to climate, but we now need empirical data to test and make sense of these ideas. This thesis therefore explores empirically how geomorphological and sedimentological records have responded to climatic gradients across time and space.

In the first part of this thesis, the extent to which spatial climate gradients are recorded by the longitudinal geometry of river channels is investigated. I use a simple stream power erosion law to predict an inverse relationship between channel steepness and average precipitation rate, and then test this theory using data from a variety of study areas and two complementary analytical approaches. Climate is found to be an important control on river longitudinal geometry across a range of climatic and tectonic conditions, in a way that conforms to existing theoretical knowledge and also allows the climatic signal to be discriminated from tectonics. This work therefore demonstrates that a widely-used geomorphological measurement—the channel steepness index—is quantifiably sensitive to climate in tectonically-active areas, and these findings offer a new explanation for geographic variations in channel steepness that cannot be explained by tectonics alone.

The second part of this thesis focuses on the sensitivity of simple mountain catchment-alluvial fan systems to climate changes associated with the last glacial-interglacial cycle, as expressed in the south-western United States. First, eight debris flow-dominated systems located in the south-eastern Sierra Nevada, California are examined. I establish a detailed chronostratigraphic model for these fan systems by building upon and integrating existing exposure age constraints reported by others, and additionally developing a new technique for estimating the ages of these fan deposits. This technique is based on calibrating the rate of enlargement of common weathering fractures observed in exposed surface boulders, which are shown to widen at a steady and predictable rate post-deposition, and can be used as reliable age indicators for > 100 ka at this location. Using the detailed temporal record of deposition established for these fan systems, a large (> 30,000 particle) grain size data set that spans

the last full glacial-interglacial cycle is examined. I demonstrate that debris flow grain size is a highly sensitive recorder of past climate changes, capturing the glacial-interglacial cycle as a sustained and high-amplitude time series with a rapid response timescale of < 10 ka. These debris flow deposits become significantly coarser-grained with warming and overall drying of the climate, and this thesis outlines quantitative reasons why this signal can be attributed to increasing storm intensity with warming.

Finally, these debris flow-dominated systems are contrasted with two carefully-selected stream flow-dominated fan systems in Death Valley, California. Using measures of down-system grain size fining and a self-similarity model of sediment calibre, sediment flux estimates during arid interglacial and wetter glacial climate conditions are derived and compared. This study shows that a decrease in average rainfall rate of ~ 30 % produced a corresponding decrease in sediment flux of ~ 20 %. However, I also demonstrate the circumstances in which signal buffering due to incision and sediment recycling destroys this climate signal.

Consequently, this thesis demonstrates both the causes and results of complexity in the relationship between climate change, geomorphology, and well-dated terrestrial sedimentary records. Ultimately, this is an expression of how sediment transport processes, tectonics, the magnitude-frequency distribution of rainfall, and other factors interact to generate different climate responses in different systems. Nevertheless, for both geomorphic and sedimentological records examined here, I demonstrate that the effects of climate can be quantified clearly: channel steepness can be quantified as a function of rainfall rate; debris flow sedimentology can be quantified as a function of storm intensity; and alluvial fan sedimentology in Death Valley can be quantified as a function of glacial-interglacial climate changes. Essentially, this thesis finds that terrestrial landscapes are sensitive to known climate changes in the recent geological past, and this result is profoundly important for improving our ability to decode geomorphic and stratigraphic archives effectively. The data and ideas within this Ph.D. research provide useful opportunities for (i) testing and updating our models of how sediment routing systems respond to climate, (ii) extracting quantitative information about past climates from the sedimentary record, and (iii) predicting the effects of future climate changes on the landscape.

Contents

Acknowledgements

My thanks to those who have supported me in writing this Ph.D. are many and large, but my foremost thanks go to my Ph.D. supervisor, Dr Alex Whittaker. It was on your undergraduate field course to the Italian Apennines in May 2010 that I decided I wanted to do a Ph.D., because it opened my eyes to the incredible and integrative power of field geology. Thank you for that excellent field trip, and thank you for taking me on as your Ph.D. student afterwards and placing your trust in my abilities and ideas. You have given me so much time and support, and I consider myself very lucky to have had such an attentive supervisor. Beyond supervising my work, you have taken care to mentor me as a scientist: teaching me how to structure my ideas, helping me write papers, encouraging me to apply for funding, supporting me at conferences, and giving me great advice throughout the whole process. You are an expert geologist as well as an excellent guide and mentor, and you made this Ph.D. an enjoyable as well as ambitious learning process. Thank you very much, Alex.

Special thanks also go to my field partner, colleague, and friend Duna Roda Boluda. I simply could not have asked for a better field partner, and working with you has made my Ph.D. brilliant fun. Thank you, Duna.

I thank the Department of Earth Science and Engineering at Imperial College for supporting me financially during the course of my Ph.D. with a Janet Watson scholarship. I would also like to thank the agencies that kindly sponsored my field research in California, and my trips to conferences to present my findings: the British Society for Geomorphology (BSG); the Geological Society of London; the International Association of Sedimentologists (IAS); the Jeremy Willson Charitable Trust; and the Royal Society (who sponsored my field research through funding awarded to my supervisor).

I am indebted to the many extraordinary people who have educated and inspired me over the years, and there are too many to thank personally. Heartfelt thanks go to all my family and friends who have supported me. Particular thanks go to my mother, Hazell. You have always inspired my curiosity and learning, guided my decisions, and supported me in every way you could. This Ph.D. thesis is your achievement as well.

It has been an absolute joy and privilege to spend these years studying amazing places, thank you to everyone who helped me along the way.

1. Introduction

1.1. Overview

The Earth's landscapes are varied, dynamic, and constantly evolving. To understand them, we must be able to explain how their features and processes are controlled by the various forces acting on the Earth's surface. Climate is one of these forces and it fundamentally governs erosional and depositional processes, meaning it is one of the primary controls of landscape morphology and the stratigraphic record (Langbein and Schumm, 1958; Leopold et al., 1964; Molnar and England, 1990; Miall, 1996; Burbank and Pinter, 1999; Blum and Törnqvist, 2000). As a result, climate changes should influence landscape form and leave records in stratigraphy that capture the erosional response of the Earth's surface to past environmental change (Wilson, 1973; Bull, 1991; Paola et al., 1992a; Blum and Törnqvist, 2000; Allen et al., 2013). However, deciphering these effects and 'reading' the geomorphic and sedimentary records in terms of past climate is non-trivial (Castelltort and Van Den Driessche, 2003; Jerolmack and Paola, 2010), and remains a first order challenge in the Earth sciences (Molnar et al., 1993; Montgomery et al., 2001; Dadson et al., 2003; Stolar et al., 2006; Bookhagen and Strecker, 2012). This thesis addresses this challenge by taking an empirical approach. I collect targeted geomorphological and sedimentological data, which allow the effects of climate on landscape form and processes to be examined over space and time. This includes a geomorphological analysis of how spatial gradients in climate affect river channel longitudinal geometry, and detailed sedimentological analyses that characterise how simple sediment routing systems have responded to the last glacial-interglacial cycle. I synthesis these findings in an integrative discussion and conclude that landscapes can, in some circumstances, be highly responsive to climate and climate change.

1.2. Background

1.2.1. Climate, tectonics, and erosion

Climate affects the Earth's surface over a wide range of spatial and temporal scales. The Earth's climate has been cooling for much of the past 50 Ma, as recorded by benthic oxygen isotope fractionation (Miller et al., 1987; Zachos et al., 2008), and the onset of glaciation and powerful orbital climate cycles in the Pliocene-Pleistocene coincided with a very large increase in the erosion rate of mountain ranges and the deposition rate of terrigenous sediment in the oceans (Hays et al., 1976; Hay et al., 1988; Kuhlemann et al., 2002; Molnar, 2004). This represents an amplification of erosional

processes on a global scale, which is likely to be coupled with tectonics in either one or both directions (Ruddiman et al., 1989; Molnar and England, 1990; Molnar et al., 1993). On a regional scale, the coupling between active tectonics and climate in shaping the surface has been documented in a variety of places. For example, in Taiwan the fastest erosion rates are found where active faults provide the fastest uplift rates but simultaneously where storms are most intense (Dadson et al., 2003). In the Andes, spatial gradients in climate (precipitation rate, temperature, glaciation) are expressed as differences in erosion rates, longitudinal channel slopes, and the overall morphology of the mountain range (Bookhagen and Strecker, 2012). Indeed, the high-elevation Altiplano of the Andes lies at a desert latitude where erosion rates are slow, and the elevation of the mountain range decreases at greater latitudes to the south where increasing glacial activity has accelerated erosion (Montgomery et al., 2001). In this sense, the latitudinal climate gradient has determined the expression of the convergent tectonics, but the regional climate and circulation pattern equally depends on tectonics in a two-directional feedback. Detailed numerical modelling of this kind of coupling between tectonics and erosion can simulate the asymmetry and form of other mountain ranges as well, notably for example in the New Zealand Southern Alps (Willett, 1999; Willett et al., 2001). These examples illustrate the extent to which the morphology of entire mountain ranges is intimately linked to the balance between tectonics (providing uplift) and climate (controlling erosion) (c.f., Kutzbach et al., 1989; Ruddiman and Kutzbach, 1989; Molnar and England, 1990; Raymo and Ruddiman, 1992; Molnar et al., 1993).

In recent years, a substantial body of literature has successfully shown that the longitudinal form of rivers is determined by the balance between uplift generating topography and erosional processes destroying it. For example, it is now widely established that the steepness of channels is sensitive to tectonic uplift rate across time and space (Whipple and Tucker, 2002; Whittaker et al., 2007a,b; 2008; Boulton and Whittaker, 2009; Cyr et al., 2010; Kirby and Whipple, 2012) and also gradients in erosion rate across time and space (Finnegan et al., 2005; Wobus et al., 2006; Whittaker et al., 2007a,b; Ouimet et al., 2009; DiBiase et al 2010). It is therefore not unreasonable to expect fundamental measures of climate (e.g., rainfall rate) to correlate with longitudinal channel form (e.g., the channel steepness index). For instance, in the Andes, Bookhagen and Strecker (2012) have already shown that channel slopes are steeper where precipitation rates are lower, and that through time erosion rates have also decreased as the climate became more arid after the last deglaciation.

Other geomorphological measurements have shown climatic dependency. For example, the density of drainage channels in formerly glaciated topography correlates with measured erosion rates (Salcher et al., 2014), and hillslope curvature in uplifting catchments increases with both erosion rate and sediment flux, and can predict erosion rate even where hillslope sediment transfer is dominated by non-fluvial processes like debris flows (Hurst et al., 2012). Detailed numerical modelling predicts that

drainage density and channel concavity should be related to storm intensity and duration (Sólyom and Tucker, 2004), and the χ metric for quantifying and non-dimensionalising the longitudinal geometry of river channels has been used to determine whether a stream network is in equilibrium with surface erosional processes and rates across space (Royden and Perron, 2013; Mudd et al., 2014; Willett et al., 2014). The rate of knick point retreat in channels crossing active normal faults in Turkey and Italy may also depend partly on precipitation rate and climate (Whittaker and Boulton, 2012). These mixed examples illustrate how simple quantifications of landscape morphology (drainage density, channel steepness, knick points, hillslope curvature, among others) contain useful information about climatic sensitivity. Now, new research is needed that identifies fundamental relationships between geomorphological metrics and climatic controls, which satisfy empirical observations from real landscapes and physical first principles.

1.2.2. Climate, sedimentation, and stratigraphy

The question of whether climate affects landscape processes and landforms has been asked for many decades, and in different ways. In 1958, Langbein and Schumm explored the question, does precipitation rate affect erosion rate, sediment yield, and therefore river behaviour in American landscapes? They used observed data to argue that sediment production reaches a maximum rate at ~ 300 mm yr^{-1} rainfall, and that it declines in drier and wetter conditions because of runoff inefficiency and increased vegetation cover, respectively. They also argued that river channels transporting this sediment would respond to climate changes through their gradients, widths, and aggradation rates. As such, they predicted a complex landscape response to climate changes through both geomorphology and sedimentology, and attempted to quantify this. A few years later, Beaty (1963) asked the question, what climatic and tectonic factors influence the formation of alluvial fans, and what information do these deposits contain? He understood the relevance of the interplay between tectonics and climate, and also recognised the volumetric importance of debris flows on dryland alluvial fans. His conclusions were limited, given the limited quantitative understanding of sediment transport at the time, however he proposed that the climatic signal recorded in debris flow-dominated fan deposits would capture high-magnitude storm events and not average conditions. He also measured the down-fan rates of grain size fining on three different fan surfaces in California, but lacked the models and tools to interpret these data fully.

Now, it is well established that climate affects surface processes via a range of drivers, including temperature, rainfall distribution and intensity, rates of erosion, plant assemblages and soil development, glacial activity, base level changes, and a range of other mechanisms (Langbein and Schumm, 1958; Schumm, 1968; Bull, 1991; Tucker and Slingerland, 1997; Blum and Törnqvist,

2000). What is less well understood is how climate and climate change are translated into the volumes and characteristics of sediment fluxes across the Earth's surface, and hence the sedimentary geology produced over the longer term, and how we can describe this quantitatively.

Ultimately, the effects of climate on erosion, geomorphology, sediment transport and deposition, all take place within sediment routing systems, which represent the source-to-sink trajectories of eroded sediment on the continents and can be thought of as sediment conveyor belts (Allen, 1997; Allen, 2008a,b; Covault et al., 2010; Michael et al., 2013). Within these systems, responses to climate (and climate change) might be expressed in the rates of erosion and volumes of sediment, sedimentology (the character of sediment flux), and stratigraphy (e.g., channel sizes, deposit architecture, and facies). As such, the response timescales and sensitivities to climate will vary spatially within a sediment routing system, and according to the type of response and the processes involved. Small systems with rapid erosion and sediment transport are likely to be more sensitive than large systems that are more buffered to external forcings (Castelltort and Van Den Driessche, 2003; McPhillips et al., 2013).

The depositional archive created by these sediment routing systems is the only record of past mass flux across the Earth's surface available to us (Burke et al., 1990; Allen, 2008; Whittaker, 2012). So, in principle, it should be a rich source of information about how climate affects landscape processes, and a major outstanding challenge is to extract this information effectively (Bull, 1991; Paola et al., 1992a; Blum & Törnqvist, 2000; Fedele and Paola, 2007; Balco et al., 2008; Duller et al., 2012). Promising clues exist about the sensitivity of sediment routing systems to climate change, for example the coarse-grained prograding conglomerates deposited in Wyoming, Colorado and the Pyrenees during the rapid (10^4 to 10^5 year) warming of the Palaeocene-Eocene Thermal Maximum (PETM) 56 Ma ago (Foreman et al., 2012; Allen et al., 2013; Foreman, 2014). To interpret sedimentary deposits fully, we need to be able to quantify them as time series that can be compared with detailed palaeoclimate records.

A range of numerical models, some based on physical first principles, have been developed to hypothesise what the effects of climate change might be on sediment production, characteristics, fluxes, and long-term basin fill (Paola et al., 1992a; Allen and Densmore, 2000; Moorehead et al., 2001; Densmore et al., 2007; Armitage et al., 2011; Rohais et al., 2012; Allen et al., 2013), and these provide one framework for how we might try to interpret actual deposits. Indeed, many landscape evolution models predict that simple sediment routing systems (e.g., small mountain catchments draining into subsiding basins) should clearly record changes in rainfall rate via changes in sediment fluxes and volumes delivered to basins, as well as the grain size and sedimentology of the material transported and deposited (e.g., Paola et al., 1992a; Allen and Densmore, 2000; Morehead et al., 2001; Densmore et al., 2007; Armitage et al., 2011, 2013; Simpson and Castelltort, 2012; Allen et al., 2013). Physical experiments also predict that sediment routing systems should be sensitive to climate

changes (e.g., Bonnet and Crave, 2003; Rohais et al., 2012), yet few empirical field studies are available with which to test these ideas, especially concerning the sedimentology of terrestrial basin deposits. Grain size data are known to contain sensitive information about sediment sources, tectonics, erosion rates and hydrological conditions, as well as climate potentially (Fedele and Paola, 2007; Whittaker et al., 2007; 2010; Duller et al., 2010; Waters et al., 2010; Foreman et al., 2012; Allen et al., 2013; Foreman, 2014; Michael et al., 2014), and such systems might therefore be a promising place to start.

Nevertheless, we need real data to make sense of these models and test them. In general, we do not understand whether and how even simple sediment routing systems have responded to well-constrained climate changes in the recent geological past. Questions remain about how sediment transport, deposition, fluxes and characteristics might all react to changes in precipitation rate, glaciation, temperature, vegetation changes, and a range of other expressions of climate, as well as how these signals might be transferred to stratigraphy. Additionally, we must improve our understanding of the erosional parts of sediment routing systems, including where sediment comes from and the information that landscape morphology left behind contains about climatic and tectonic forces.

I explore some of these ideas in this thesis, which I divide into 4 research chapters, below.

1.3. Wider thesis motivation

There are many reasons why we should seek to understand how climate change affects landscapes.

One reason is to obtain a full, process-based understanding of landscape dynamics, including how sediment is produced, transported, and deposited, and how this leaves a signature not only in stratigraphy but in the geomorphology of mountain catchments left behind. What roles do different sediment movements, e.g., debris flows, rivers, flash floods, play in creating the landscapes we observe today? How can we describe these processes quantitatively, reconstruct them from the geologic past, and realistically model landscapes as sediment routing systems? One challenge is to create a set of equations that describe the varied controls on sediment flux across the Earth's surface, and these equations should be based on observables from the geologic record. To achieve this, we need to understand the linkages within sediment routing systems and how they behave as integrated entities, from the localised evolution of a small catchment-alluvial fan system, to the large-scale debate about the interplay between climate and tectonics (e.g., Ruddiman et al., 1989; Molnar and England, 1990; Molnar et al., 1993; Beaumont et al., 2001; Burbank and Anderson, 2012).

Another reason is to improve our understanding of stratigraphy, and retrieve more information from the sedimentary record, whether this is about sedimentology or past environmental change and its consequences. We must therefore understand how terrestrial stratigraphy is created, not only in terms of physical process but also in terms of timescale. Does basin fill record smaller, common depositional events or the biggest, uncommon events? What is the relative importance of different forcings, such as a change in the uplift rate of a mountain range compared to a change in the rainfall rate, over different lengths of time from 10^3 to 10^7 years? How are sedimentological signals of these forcings preserved, and might they be transformed, damped, buffered, amplified or shredded by transport, or interference with self-organised criticality (Humphrey and Heller, 1995; Castelltort & Van Den Driessche, 2003; Paola et al., 2009; Clarke et al., 2010; Jerolmack and Paola, 2010; Simpson and Castelltort, 2012)? Complementary to the stratigraphic record, we must also obtain more environmental information from landscape morphology, for example from the longitudinal geometries of river channels and other quantifiable geomorphological metrics.

On a human timescale, we also live in a period of high-magnitude and extremely rapid climate change (IPCC, 2013), where global average temperatures might rise by several degrees Celsius by the end of the century (IPCC, 2014). This magnitude is comparable to that of entire glacial-interglacial climate cycles, which clearly bring profound reorganisations to the climate system and dramatic effects on surface processes. It is therefore very important that we are capable of using the record of past climate changes in Earth's history as a guide for what future warming might do to the landscapes on which we live and depend. The question of how climate change impacts surface processes is thus important, highly interdisciplinary, and offers many opportunities for new research.

1.4. Aims and objectives

The research comprising this thesis has two key aims. These will be returned to in the Discussion chapter.

1. **To integrate climate into a simple stream power erosion law that can be used to quantify the sensitivity of tectonically-active eroding landscapes to climate over large spatial (mountain ranges) and temporal (10^6 years) scales.**
2. **To examine small mountain catchment-alluvial fan systems as analogues for larger landscapes, and establish whether signals of past climate change over glacial-interglacial timescales (10^4 to 10^5 years) are recorded in the sedimentology of alluvial fan deposits.**

Aim (1) focuses on landscape geomorphology and the erosional part of sediment routing systems, and aim (2) focuses on sedimentology and the depositional part of sediment routing systems. Within each aim, there are several objectives. For aim (1), the objectives are to:

1.1) Select and characterise a range of mountain catchments using digital elevation models (DEMs) in terms of their topography, climate and precipitation rate, and longitudinal channel profiles.

1.2) Use stream profile analysis to evaluate the effects of climate gradients across space on a local to regional scale.

1.3) Compare a range of areas with different climates but similar tectonics in order to evaluate the effects of climate gradients across space and time in a generalised way.

For aim (2) both debris flow- and stream flow-dominated alluvial fan systems will be examined because they have fundamentally different processes. The objectives are:

2.1) Identify small catchment-fan systems where tectonic and lithological conditions are constant, but where climate has varied significantly over glacial-interglacial cycles.

2.2) Establish a chronostratigraphy for the alluvial fans at a high resolution in time and space.

2.3) Quantify the alluvial fan sedimentology, e.g., by measuring grain size distribution on each dated surface, and compare these data with suitable local or regional palaeclimate proxies in order to evaluate the sensitivity to past climate changes and explore the physical mechanisms that might explain observations.

2.4) Use observed data, e.g., sediment grain size, to estimate changes in sediment flux during periods of climate change, so that existing numerical models of catchment-fan systems can be tested.

I approach these aims and objectives in four research chapters, and the structure of this thesis is outlined below. In each chapter, I independently review the relevant background literature in detail to build upon the points raised in section 1.2, above, and I also describe the methodologies in each chapter as appropriate.

Aim 1 focuses on landscape sensitivity to climate from a geomorphological point of view, in particular using longitudinal channel geometry. Specifically, this aim is to test whether the channel

steepness index, k_{sn}, is sensitive to spatial climate gradients in a way that conforms to stream power erosion theory. This is one metric that is known to be sensitive to erosional processes (e.g., Wobus et al., 2006; Ouimet et al., 2009; DiBiase et al., 2010), so it is a sensible index to test.

Aim 2 is concerned with how sediment routing systems and their deposits respond to climate (and climate changes). A range of field studies have provided evidence that sediment routing systems are indeed sensitive to climate changes. These include 'PETM conglomerates' deposited in the United States and Europe during the rapid (10^4 to 10^5 year) warming during the Palaeocene-Eocene Thermal Maximum (Foreman et al., 2012; Allen et al., 2013; Foreman, 2014), and a range of dryland alluvial fan case studies that show higher aggradation rates, erosion rates, and sediment fluxes during periods of wetter and/or stormier climate (e.g., Bull et al., 1991; McDonald et al., 2003; Steffen et al., 2009; 2010; Miller et al., 2010; McPhillips et al., 2013). Many questions remain about the physical mechanisms that determine sediment routing system sensitivity to climate, e.g., the role of high intensity storms compared to average rainfall rates (Antinao and McDonald, 2013), or the role of vegetation change compared to precipitation (e.g., Pelletier, 2014), for instance. In this thesis I provide new sedimentological data from a number of sediment routing systems, focussing on deposited grain size distribution. I tackle some of these issues in chapters 4 and 5, but nonetheless, Aim 2 has been chosen because the range of case studies and examples cited above provide clear evidence that at least small sediment routing systems can be highly sensitive to climate.

1.5. Thesis outline and structure

This thesis is divided into four research chapters, a discussion and a conclusion, which together form an integrated thesis to address the Ph.D. aims and objectives described above. Each of the research chapters is also written and structured to serve as separate contribution to the literature, and therefore could be read as a stand-alone research study. As a whole, these four chapters combine to provide new insights as to when and in what circumstances the geomorphic and stratigraphic archives can be used as a record of climate and climate change on Earth.

Chapter 2 addresses aim (1) and is concerned with the gross geomorphology of small river catchments in uplifting mountain ranges. Here, I use the normalised channel steepness index, k_{sn}, to quantify river channel geometry as a function of precipitation rate in 6 different locations with contrasting climates.). This work outlines a simple approach to incorporating precipitation rate into the stream power erosion law, and demonstrates that channel steepness varies predictably with precipitation rate across a range of tectonically active landscapes. By examining > 800 channels, Chapter 2 takes a statistical approach to analysing large landscapes (entire mountain ranges), using longitudinal river

profiles that respond over a ~ 10^6 year timescale (Snyder et al., 2000; Whittaker et al., 2007a,b; Whittaker and Boulton, 2012). Thus, these geomorphological analyses are focussed on large spatial and temporal scales, and also on the erosional (catchment) zone of sediment routing systems.

The main finding in this chapter is that increasing precipitation rate acts to suppress the steepening of channels in response to tectonic uplift. In individual mountain ranges, there is an orographic coupling between uplifted topography and precipitation rate, so rainfall rates act as a proxy for the effects of uplift while also modulating the uplift signal by reducing the steepness of channels in the wettest catchments. When different mountain ranges are compared, the same uplift rate produces significantly steeper channels in areas that are dry (e.g., the Western Cordillera of the Andes) compared to those that are wetter (e.g., southern Italy). I show that the effects of precipitation rate on channel long profiles can be isolated and quantified in a way that matches expectations from simple stream power erosion theory, e.g., producing reasonable values for the discharge exponent '*m*'. These findings may help to explain some of the spatial variation in channel steepness, i.e., k_{sn}, documented by others, which cannot be explained by tectonics alone. A version of this chapter has been published in *Geomorphology* **201** (D'Arcy and Whittaker, 2014), pp. 366-381.

The remaining part of the thesis addresses aim (2) and is concerned with the depositional zone of sediment routing systems, and the way that signals of past climate changes are transferred into the sedimentary record of terrestrial basins over 10^4 to 10^5 year timescales. I have chosen to focus on small mountain catchment-alluvial fan systems, because they contain a range of sediment transfer processes and have volumetrically-closed deposits, often dated, that can be studied at a high temporal resolution. They are therefore simple analogues for larger landscapes. I have also chosen to examine their responses to climate changes over glacial-interglacial cycles, because these have brought high-magnitude and relatively high-frequency (10^4 to 10^5 years) climate changes that are very well constrained.

In Chapters 3 and 4, I analyse 8 different debris flow-dominated catchment-fan systems in Owens Valley, California, which offer a combined depositional record spanning the entire last glacial-interglacial cycle. Chapter 3 establishes the field maps, stratigraphy, and chronology of the Owens Valley fans, in part by re-interpreting published exposure ages from ^{10}Be cosmogenic nuclides, and in part by developing a new technique for correlating known ages in the field to un-dated surfaces. This technique is based on calibrating the rate at which age-sensitive weathering fractures in surface boulders are enlarged during exposure. I show that over a long period of time (> 100 ka), these fractures widen at a rate of ~ 1 mm ka^{1}. This is determined using high-resolution ^{10}Be age constraints provided by several previous works (Zehfuss et al., 2001; Dühnforth et al., 2007; Le et al., 2007), and gives an average boulder surface erosion rate of 0.5 mm ka^{-1} that precisely agrees with independent constraints at this location (e.g., Phillips et al., 2009; Rood et al., 2011). The implication is that

weathering fractures, in this setting and perhaps elsewhere, can be used as quantitative age indicators. In Chapter 3 I explore this concept in its own right, but I also apply it to the dating of several previously un-dated alluvial fan systems in Owens Valley, in order to establish a very detailed chronostratigraphy that is later used in Chapter 4. A version of this work has been published in *Earth Surface Processes and Landforms* **40** (D'Arcy et al., 2015), pp. 487-501.

In chapter 4, I exploit these new stratigraphic constraints to demonstrate that the grain size distributions of the studied debris flow deposits correlate closely with regional palaeoclimate proxies over the last ~ 125 ka, and contain a high-resolution record of past climate change. In particular, grain size coarsens exponentially with temperature in a way that strongly indicates a storm-intensity control on debris flow sedimentology. These analyses can be performed in great temporal detail because of the age model established in Chapter 3. Together, the Owens Valley chapters offer a new approach to examining debris flow fan sedimentology, and reveal a sensitive record of past climate change. A version of this chapter is in preparation for submission to *Basin Research*.

In Chapter 5, I move to Death Valley, also in eastern California, and analyse two alluvial fans dominated by stream flow and sheet floods. Here I again take a grain size approach to investigating how glacial-interglacial climate changes have affected alluvial fan sedimentation, but using a different methodology. Rather than using grain size as a time series, I measure the down-fan rate of grain size fining on glacial and interglacial surfaces, and use an adapted self-similarity model of sediment extraction, combined with sediment flux estimates from cosmogenic nuclide data reported by others, to reconstruct how sediment flux has changed as the climate warmed and dried from ~ 70 ka to present. Compared to the Owens Valley fans analysed in Chapter 4, this approach allows a more detailed quantitative analysis of grain size, and a reconstruction of sediment flux that is not yet possible for debris flow fans. I show that the down-fan rate of grain size fining is faster in the dry modern climate of Death Valley compared to the wetter climate of the mid-glacial period. My analyses indicate that this corresponds to a ~ 20 % decline in sediment flux exported to the alluvial fans, associated with a ~ 30 % decline in precipitation rate. This chapter serves as a direct test of some of the latest numerical models of how simple catchment-fan systems react to changes in rainfall rate (e.g., Armitage et al., 2011; Allen et al., 2013), and outlines a new approach to analysing landscape sensitivity to climate change based on an adaptation of models of self-similar grain size fining due to grain size-selective deposition. A version of this chapter is in review for *Sedimentology*.

In Chapter 6, I provide a discussion of the key research findings presented in this thesis, and illustrate where this body of work fits into the wider context of geomorphic and stratigraphic work with respect to climate. In particular, this thesis considers the effects of climate change on the erosional part of sediment routing systems over long (10^6 year) timescales and large spatial scales (Chapter 2), as well as the depositional part of sediment routing systems on much smaller, local spatial scales and over

shorter (10^4 and 10^5 year) timescales (Chapters 3-5). Finally, I outline the on-going and future research projects that have been directly motivated by the studies presented here, and highlight the key research questions that remain to be addressed. I finish by providing a clear statement of the key conclusions of this thesis (Chapter 7).

2. Geomorphic constraints on landscape sensitivity to climate in tectonically-active areas[†]

Chapter Abstract

The geomorphology of fluvial landscapes is known to record information about uplift rate, spatial patterns of faulting, and tectonic history. Data are far less available when addressing the sensitivity of common geomorphological metrics, such as channel steepness, to climatic boundary conditions. We test the relationship between channel steepness and precipitation rate by measuring a large number of channels in different mountainous areas. These regions exhibit a tenfold variation in precipitation rate between them (~ 100 – 1000 mm yr^{-1}) but have similar uplift rates, allowing the tectonic variable to be controlled. By accounting for the orographic coupling of rainfall with uplifted topography, we find that channel steepness is significantly suppressed by higher precipitation rates in a measurable way that conforms to simple stream power erosion laws and empirical constraints on their parameters. We demonstrate this using modern and estimated glacial precipitation rates; and climate emerges as an important, quantifiable control on channel geometry. These findings help to explain why highly variable measurements of channel steepness are reported from different locations, and provide empirical constraints on how climate shapes tectonically active landscapes.

[†]A version of this chapter has been published as the following paper:

D'Arcy, M. and Whittaker, A.C. (2014) Geomorphic constraints on landscape sensitivity to climate in tectonically active areas. *Geomorphology*, **204**, 366-381.

M.D. and A.C.W. conceived of the experiments. M.D. performed the data analyses, prepared the figures, and wrote the manuscript. A.C.W. commented on the manuscript.

2.1. Introduction

2.1.1. Background

The geomorphology of the landscape represents the balance between processes creating and destroying topographic relief. Over geologic time, topography is produced by tectonic forces through the time-integrated effects of surface and rock uplift, subsidence, and crustal deformation (e.g., Whipple, 2004; Wobus et al., 2006; Allen, 2008; Whittaker and Boulton., 2012). The resulting relief is significantly modified by erosion: a process that is strongly controlled by climate. The form and evolution of a landscape is therefore determined by several fundamental controls, including tectonics, erosion, climate, lithology, and preexisting geomorphology (Cowie et al., 2008; DiBiase and Whipple, 2011; Kirby and Whipple, 2012; Whittaker, 2012).

In principle, inverting the landscape for these boundary conditions in a quantitative way should be possible using theoretical, empirical, or modelling approaches (Kirby et al., 2003; Wobus et al., 2006; Tucker, 2009; Attal et al., 2008; Miller et al., 2012). This would enable us to convert geomorphological measurements into empirical information about uplift rates, spatial patterns of faulting, and landscape sensitivity to future climate change, among other useful insights (Whittaker, 2012). Deciphering the underlying equations that govern geomorphic form raises the prospect of using the landscape as a rich information archive about how tectonics, climate, and surface processes have evolved through time (Wobus et al., 2006; Allen, 2008; Whittaker et al., 2008; Kirby and Whipple, 2012). To achieve this goal, we need reliable measurements of landscape form that can be compared across time and space. A good example is the longitudinal geometry of river channels (e.g., Tucker and Whipple, 2002; Whipple and Tucker, 2002). Rivers are widespread, easily measured, and known to be patently sensitive to their tectonic and climatic boundary conditions (Whipple and Tucker, 1999; Snyder et al., 2000; Whittaker et al., 2008; DiBiase and Whipple, 2011; Whittaker, 2012). Stream power erosion laws describing channel geometry have been successfully applied to a range of tectonically active fluvial landscapes, and the way rivers transmit tectonic signals to the landscape has already been partially quantified (e.g., Tucker and Whipple, 2002; Whipple and Tucker, 2002; Crosby and Whipple, 2006; Whittaker et al., 2007a,b, 2008; DiBiase et al., 2010; Miller et al., 2012; amongst many). However, much less is known about how climate controls landscape form, and this remains a major challenge for geomorphologists (Wobus et al., 2010; Champagnac et al., 2012; Whittaker, 2012). The aim of this chapter is to introduce climate into a common stream power erosion law and to test how well this approach fits real landscapes.

2.1.2. Previous Work

As the longitudinal form of rivers responds to tectonic and erosional driving forces, it can capture the balance between processes creating and destroying topography (e.g., Whipple and Tucker, 1999; Kirby and Whipple, 2012). At a basic level, this balance can be described geometrically. A starting point is a steady-state equation where the rate of change of elevation, dz/dt, is zero if the local rock uplift rate, U, is equal to the local erosion rate, E (e.g., Whipple and Tucker, 2002):

$$\frac{dz}{dt} = U - E \qquad [2.1]$$

The erosion rate in turn depends on other factors; and for fluvial systems it is often expressed as a stream power erosion law (Howard, 1994; Whipple and Tucker, 1999):

$$E = KA^m S^n \qquad [2.2]$$

where K is a dimensionless erodibility coefficient that encapsulates lithology, climate, and transport processes; A is the drainage area raised to the power of an empirical constant m; and S is the local channel slope raised to the power of an empirical constant n (Hack, 1957; Seidl and Dietrich, 1992; Whipple and Tucker, 1999; Tucker and Whipple, 2002). Drainage area is typically taken as a proxy for discharge (Wobus et al., 2006). Given that discharge must also be a function of precipitation rate, P, averaged over a geomorphically relevant period of time, this can be incorporated into a stream power erosion law that has been used to describe varied landscapes (e.g., Whittaker et al., 2008; Whittaker and Boulton, 2012):

$$\frac{dz}{dt} = U - K(PA)^m S^n \qquad [2.3]$$

Assuming that uplift rate is counterbalanced by an equal erosion rate, i.e., the landscape is in 'topographic steady state', dz/dt in Eq. [2.3] is zero and the right-hand side can be rearranged to find the local slope S:

$$S = \left(\frac{U}{P^m K}\right)^{\frac{1}{n}} \cdot A^{-\frac{m}{n}} \qquad [2.4]$$

The exponent m/n is often represented as θ, the concavity index (Whipple and Tucker, 1999). The constant of proportionality between local slope and drainage area in Eq. [2.4] is termed the 'channel steepness index', k_s, i.e.,

$$k_s = \left(\frac{U}{P^m K}\right)^{\frac{1}{n}} \qquad [2.5]$$

Channel steepness is explicitly sensitive to rock uplift rate, U, and to precipitation rate, P (Wobus et al., 2006; Kirby and Whipple, 2012). Measuring k_s from a log-log plot of channel slope against upstream catchment area is simple, and it is usually normalised (k_{sn}) to a reference concavity index, θ_{ref} (Kirby and Whipple, 2012; Whittaker, 2012). Its units depend on the choice of this (dimensionless) concavity, e.g., $m^{0.9}$ for $\theta_{ref} = 0.45$. Normalisation facilitates k_{sn} comparisons between different rivers, locations, and studies (Kirby and Whipple, 2012), and if individual measurements of θ do not deviate widely from the local mean value, the effect of normalisation on k_s primarily reflects the scatter of the log-log plot (Snyder et al., 2000).

A significant quantity of research in the last 10 years has investigated the links between uplift and k_{sn} where climate (precipitation) gradients have either been neglected or assumed to be unimportant relative to the tectonic driver (c.f., Kirby et al., 2003; Boulton and Whittaker, 2009; Bookhagen and Strecker, 2012) These studies have successfully revealed a positive correlation between U and k_{sn}, albeit with some complexities in postulated functional form (e.g., Snyder et al., 2000; Kirby and Whipple, 2001; Ouimet et al., 2009; DiBiase et al., 2010). In some areas this correlation appears to be strongly linear (e.g., Lague and Davy, 2003), in others it appears sublinear (e.g., DiBiase et al., 2010), while in some places it has apparent linearity until a threshold uplift rate above which significant nonlinearity is observed. For example, in northern and southern Italy, Cyr et al. (2010) observed a threshold of nonlinearity at ~ 1 mm yr^{-1} mean catchment uplift rate. More data is needed to shed further light on this relationship; we provide some in this study. Nevertheless, stream profile analysis is often compatible with independent erosion rate measurements (Ouimet et al., 2009; DiBiase et al., 2010) and has been used both to identify transient responses to tectonic change and to deduce rock uplift rates across a landscape (Kirby et al., 2003; Harkins et al., 2007; Whittaker et al., 2007b, 2008). Other work has shown that indices such as k_{sn} can capture fine spatial details in uplift rate. For example, in eastern Idaho, USA, Densmore et al. (2007) observed that channels near active normal fault tips are characterised by gentler slopes, while those nearer to the faults' along-strike centres are steeper and less concave.

Other workers have found that channel geometry is also sensitive to erosion rate, the other half of Eq. 2.1 (e.g., Finnegan et al., 2005; Whittaker et al., 2007a; Ouimet et al., 2009; DiBiase et al., 2010). Of particular relevance is a review of six different regional studies by Kirby and Whipple (2012) and references therein, which demonstrates a logarithmic (sublinear) scaling between normalised channel steepness and measured erosion rates for catchments in tectonically active ranges. In addition, channel steepness depends on a set of 'erodibility' variables including bedrock lithology and climate. This is likely why a wide range of k_s values have been reported from different locations when tectonics alone is considered to be the primary variable (Whittaker, 2012). One example that highlights this problem is a comparison of Boulton and Whittaker (2009) and Snyder et al. (2000). Boulton and Whittaker

(2009) studied channels in southern Turkey where uplift rate has been well-constrained at 0.45 mm yr^{-1}, and using $\theta_{ref} = 0.5$ they measure k_{sn} averaging 230 m and up to a maximum of 485 m. In contrast, Snyder et al. (2000) measured channels in northern California with uplift rates of 0.5 mm yr^{-1} and k_{sn} values < 60 $m^{0.86}$ (the authors use a slightly lower reference concavity, $\theta_{ref} = 0.43$). This large difference in k_{sn}, despite equivalent uplift rates, cannot be explained by small differences in θ_{ref}. Both areas drain mixed sedimentary bedrock, so it is also unlikely to reflect lithological differences alone. The discrepancy may be partially climatic in origin: while the Turkish catchments receive ~ 800-900 mm yr^{-1} rainfall, the Californian catchments receive significantly more at ~ 1500-1800 mm yr^{-1} (Hijmans et al., 2005).

That a higher precipitation rate would correlate with reduced k_s values (uplift rate being constant) is clear within equations 2.4 and 2.5. However, little empirical work has directly tested the relationship between channel steepness and precipitation rate. A global investigation by Champagnac et al. (2012) used digital elevation models (DEMs) to examine 69 mountain ranges and compared their gross geomorphology with tectonic and climatic variables. From a broad perspective, they found that the size and shape of mountainous landscapes is partly controlled by latitudinal variations in climate. This invites more detailed work examining the direct effects of climate on longitudinal channel form. Recently, Bookhagen and Strecker (2012) found that channels in the Argentinian Andes tend to have higher slopes where the precipitation rate is lower. They also found cosmogenic nuclide erosion rates decreasing by an order of magnitude in response to local aridification, following a wetter period 25-40 ka ago. Their data suggest that even in a tectonically active area, rainfall rate is an important control on river long profiles and that this control can be quantified. However to date, no precipitation signal has been explicitly extracted from k_{sn} data gathered in disparate study areas, suggesting that there is some way to go before we have a complete understanding of how channel steepness records climatic and tectonic boundary conditions together.

However, theoretical studies have already emphasized the influence of precipitation rate on channel form (Sólyom and Tucker, 2004; Wobus et al., 2006, 2010; DiBiase and Whipple, 2011). For instance, DiBiase and Whipple (2011) used a numerical model calibrated with erosion rate constraints from the San Gabriel Mountains in California to demonstrate that the relationship between erosion rate and channel steepness is controlled by river discharge and, furthermore, can be strongly nonlinearized by the variability of discharge through time. This raises questions about the importance of low frequency but high magnitude storm events on landscape evolution because parameters like storminess are notoriously difficult to reconstruct as a geological time series (DiBiase and Whipple, 2011; Whittaker, 2012).

A major issue with all of the studies highlighted above is that climatic variables (especially precipitation rate) and tectonic variables (such as rock uplift rate) are normally coupled in one or both

directions (Champagnac et al., 2012). In many locations, precipitation rate increases with altitude, while high elevation and relief are often correlated with high uplift rates (Roe et al., 2002). Consequently, k_{sn} will embody the combined effects of uplift and precipitation together (Bookhagen and Strecker, 2012). Breaking this coupled circle is a major challenge. A second challenge lies in addressing the variability of climate through time. This is important because modern climate averages are constrained with a high spatial and temporal fidelity, while palaeoclimate data and reconstructions are far more limited, particularly further back into the geologic past. So while many studies addressing the interactions between tectonics and climate have exploited modern records for necessary reasons (Champagnac et al., 2012), these records cannot truly represent an integration of climate across many glacial–interglacial cycles. This raises uncomfortable questions regarding the use of modern climate averages to explain landscapes with a response timescale that may be on the order of 10^5 or 10^6 years (Snyder et al., 2000; Whittaker et al., 2007a,b; Whittaker and Boulton, 2012), and we consider the implications of this for our data.

Here, we begin to address the important question of how climate controls landscape morphology. We provide new constraints about how precipitation rate controls channel steepness index in six carefully selected landscapes where the uplift variable can be controlled. We attempt to generalize our observations in order to assess the extent to which modern day landscapes record climatic differences within well-known geomorphic indices like k_{sn}. We note that 'climate' embodies a range of characteristic variables, so we concentrate on precipitation rate as a logical starting point because these data are widely available as modern records and can be (partially) reconstructed for the geologic past (section 3.2). Other variables that may count, such as storminess or rainfall intensity (c.f., DiBiase and Whipple, 2011), remain extremely difficult to reconstruct into the geologic past.

2.2. Sensitivity of k_{sn} to uplift and precipitation rates

If the simple assumptions laid out in equations 2.1-2.5 are valid, then channel steepness, Eq. 2.5, should be positively correlated with uplift rate, U, and linearly proportional to it for the case of any specific stream power model in which $n = 1$ and $m = 0.5$ (Fig. 2.1a). In contrast, k_{sn} should be inversely proportional to precipitation rate, P, raised to the power m (Eq. 2.5), which would imply that $k_{sn} \sim P^{-0.5}$ for an identical specific stream power model (Fig. 2.1b). So, if we select a value of K that gives 'realistic' estimates of channel steepness index for reasonable uplift and precipitation rate inputs (i.e., $k_{sn} = 200$ m$^{0.9}$ for $U = 1$ mm yr^{-1} and $P = 500$ mm yr^{-1}), we can generate simple relationships for k_{sn} against a range of uplift rates for varying P (black curves, Fig. 2.2a), and for k_{sn} against a precipitation rate for varying U (black curves, Fig. 2b). In principle, these relationships are easily

identified in areas with uniform lithology where U and P are independent variables, and this is indeed the standard approach for deducing rock uplift rates from variations in channel steepness index (e.g., Wobus et al., 2006; Whittaker, 2012). However, as we point out above, climate and tectonics are rarely decoupled. Even for a simple orographic precipitation case, in which rainfall rate is linearly proportional to uplift rate (driven for instance by the generation of relief: see insets, Figs. 2.2a and b), the functional form of the relationship between channel steepness and uplift rate would effectively scale as $k_{sn} \sim U^{0.5}$ because of the implicit dependence of P on U (red lines, Fig. 2.2a). Consequently, enhanced precipitation 'acts to limit' the steepening of channel gradients as topography is uplifted. Moreover, the precise shape of the $k_{sn} - U$ curves would be controlled by the magnitude and rate of change of P with respect to U (red lines, Fig. 2.2a).

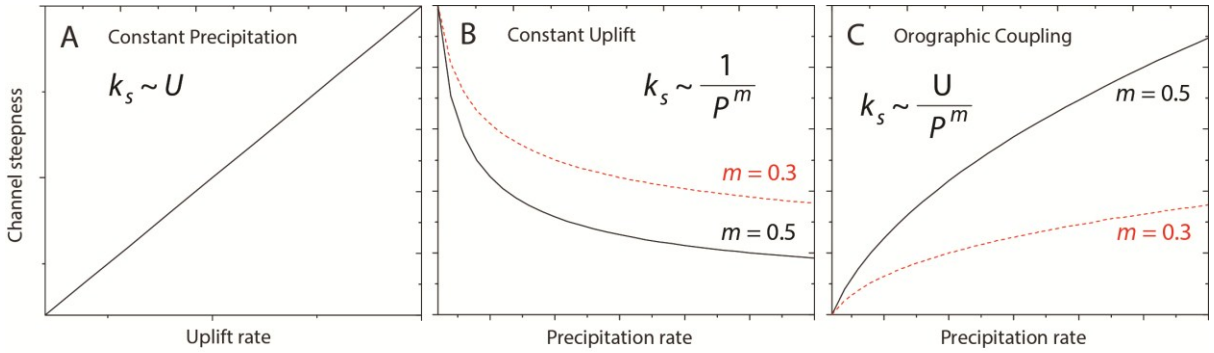

Figure 2.1. Expected relationships between channel steepness, uplift, and precipitation rate. (A) Channel steepness increases linearly with uplift rate (assuming constant precipitation rate). (B) Channel steepness decreases with precipitation rate, following a power law relationship where *P* is raised to the exponent *m* (assuming constant uplift). (C) The effect of orographically coupling precipitation rate with uplift rate: channel steepness sublinearly increases with precipitation rate (behaving as an uplift rate proxy), following a power law with exponent *m*.

In a similar way, a linear relationship between U and P is theoretically capable of producing a complex relationship between channel steepness index and local precipitation rates (red lines, Fig. 2.2b). For a K value again selected to produce a realistic $k_{sn} = 200$ m$^{0.9}$ for $U = 1$ mm yr^{-1} and $P = 500$ mm yr^{-1}, if uplift rates are low (i.e., 0.2 mm yr^{-1}) and precipitation rates are low (i.e., < 200 mm yr^{-1}), a linear increase in U with P (here with a gradient of 2 x 10^{-3}) produces a slow rise of channel steepness index with precipitation rate, which necessarily approximates $k_{sn} \sim P^{0.5}$ (c.f., Eq. 2.5). In contrast, if baseline uplift rates are relatively high (i.e., > 1.5 mm yr^{-1}) for low precipitation rates, the same rate of increase of U with P produces a decline in k_{sn} with increasing precipitation. In this case, we would observe the steepness index of high uplift rate landscapes becoming relatively insensitive to these measures of 'tectonics' or 'climate' at realistic precipitation rates above ~ 400 mm yr^{-1}.

Intermediate uplift rates (~ 1 mm yr^{-1}) produce a situation in which k_{sn} falls with an initial increase in precipitation rate (as wetter landscapes require lower slopes to balance the imposed uplift field), but then increases for higher precipitation rates. This is simply because the implicit increase in uplift rate for wetter conditions starts to dominate over the precipitation signal. Therefore, for any initial uplift rate (Fig. 2.2c), whether k_{sn} decreases (scenarios 1-2), increases (scenarios 5-9), or stays the same (scenarios 3-4) with respect to precipitation rate depends on the magnitude and rate of increase of P relative to U (Fig. 2.2c) (c.f., Eq. 2.5). Although K and initial conditions make a significant difference, in general terms for a specific stream power model where $m = 0.5$ and $n = 1$ and $U \sim P^a$, if $a > 0.5$, then k_{sn} will (eventually) increase with precipitation rate; if $a < 0.5$ then k_{sn} will decrease with precipitation rate; and if $a \sim 0.5$, k_{sn} is relatively insensitive to tectonics and climate. If m varies in the stream power erosion law, then the principles involved are the same (i.e., if $a > m$, k_{sn} will increase with precipitation rate), although the details will differ.

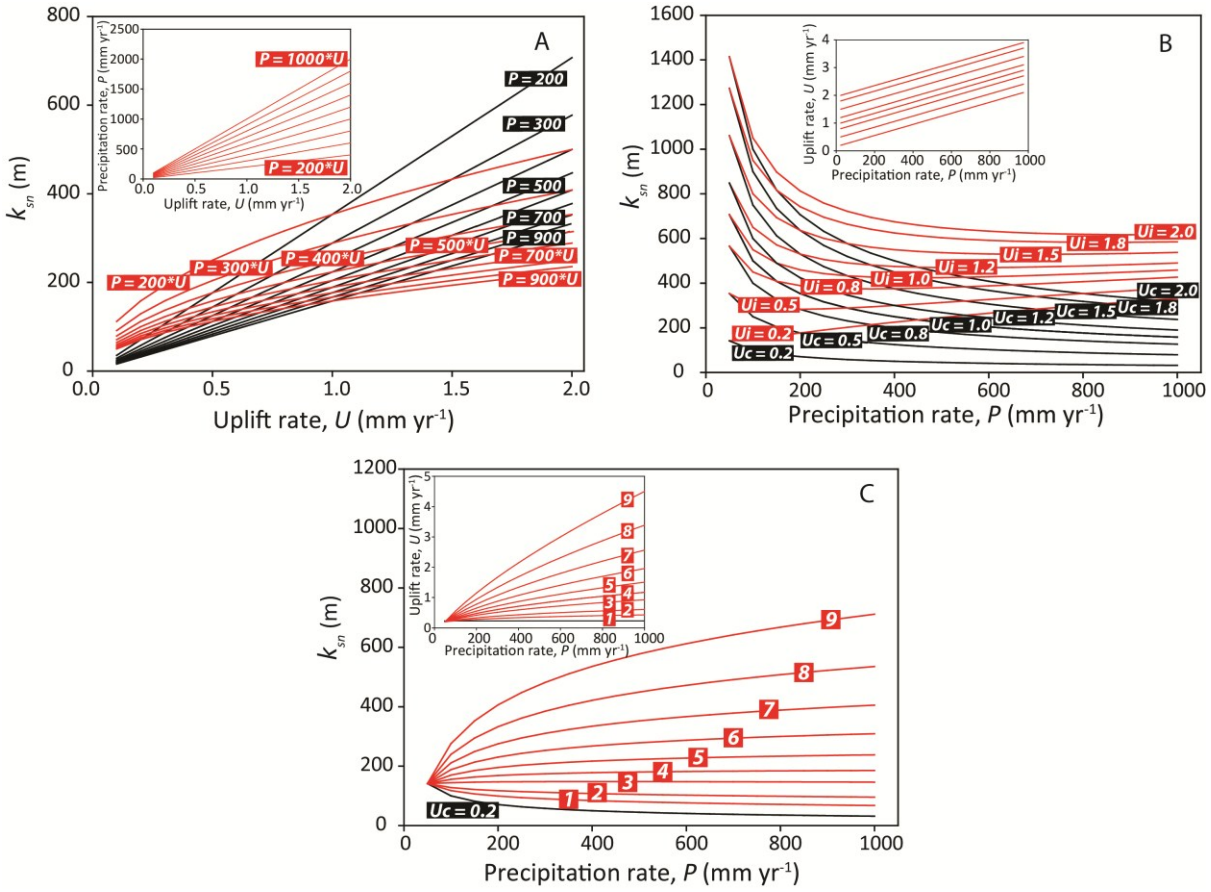

Figure 2.2. (A) Sensitivity of k_{sn} on uplift rate, U, for constant precipitation rate, P, (black lines) and varying P that also depends on U (red lines), assuming that $k_{sn} \sim U$. Inset shows dependence of U and P used to reconstruct red lines. (B) The k_{sn} against P for constant U in the case that $k_{sn} \sim U/P^m$, with $m = 0.5$ (black lines). Red lines show k_{sn} against P for varying precipitation rates that are correlated with varying U (inset). (C) The k_{sn} against P for a set uplift rate (0.2 mm yr^{-1}) (black line). Red lines show functional form of k_{sn} against P for varying intensities of the relationship between U and P.

This analysis suggests that to quantify the sensitivity of landscapes to a climate parameter such as precipitation rate, one approach is to plot the variation of k_{sn} with P and extract the 'true' dependence of channel steepness on precipitation rate by accounting for the component of the trend that is explained by a variation in tectonic rates. We take this approach by combining theory with empirical data. It is important to remember that channel steepness index is a necessary simplification (c.f., Wobus et al., 2006), and the landscape response to climate or tectonics will not be fully captured by a single metric. In the following analyses, we assume that uplift, climate, and erodibility are constant across the many catchments we evaluate; and we do not consider alternative climate variables such as temperature change or storm size. Therefore, k_{sn} only approximates how landscape form is related to its primary controls. At this stage, such a generalisation is needed to gain first order insights that can be extended by future work.

2.3. Study areas

To test for a precipitation control on channel steepness, we compare the six mountainous areas summarised in Table 2.1 and located in the central maps in Fig. 2.3. These areas occupy a range of climatic zones and have a large number of mountain front catchments, making them ideal locations for this type of analysis. Four of the regions have time-averaged catchment uplift rates of ~ 1 mm yr^{-1} (this is a maximum rate, as it decays to zero approaching individual fault tips). These are the Western Cordillera of the Peruvian Andes; the southern Sierra Nevada and adjacent ranges in eastern California, USA; the Sierra de San Pedro Mártir of northern Baja California, Mexico; and the Aspromonte massif in southern Calabria, Italy. Two additional areas are selected that have much lower catchment uplift rates (< 0.3 mm yr^{-1} to negligible): the Beaverhead, Lemhi, and Lost River ranges of central Idaho, USA; and the Sinai High Mountains on the southern Sinai Peninsula, Egypt. With these locations, we can compare the effects of precipitation rate on longitudinal channel geometry in tectonically active areas where uplift rate is reasonably controlled.

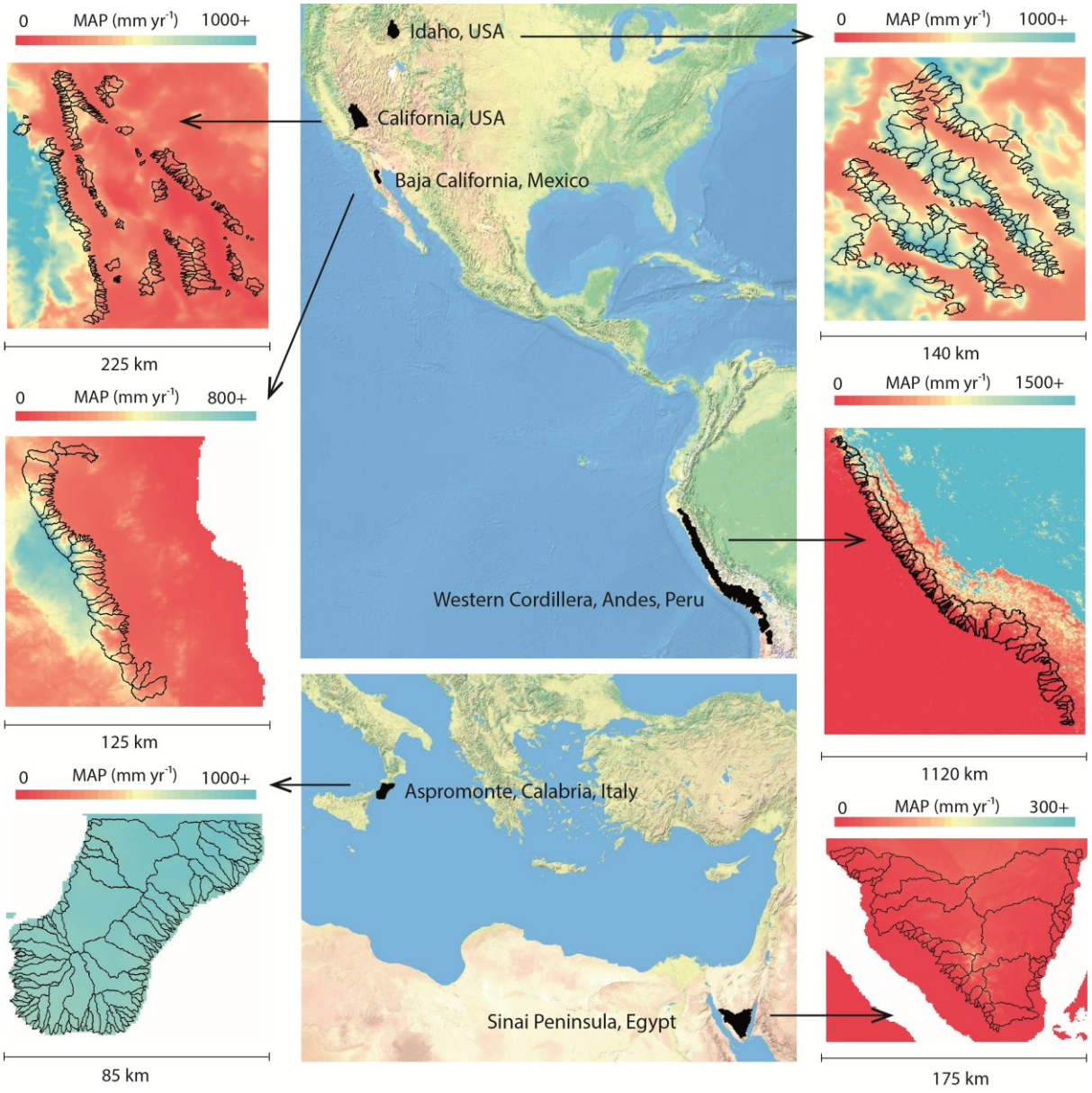

Figure 2.3. Maps locating the six study areas (centre). Those with catchments uplifting at about 1 mm yr^{-1} relative to base level are (i) eastern California, USA (southern Sierra Nevada and nearby ranges); (ii) the Sierra de San Pedro Mártir, northern Baja California, Mexico; (iii) the western Cordillera of the Peruvian Andes; and (iv) the Aspromonte, Calabria, Italy. Two additional study areas are selected with minimal rates of catchment uplift: (v) the Beaverhead, Lemhi, and Lost River ranges of Idaho, USA; and (vi) the southern ranges of the Sinai Peninsula, Egypt. See Table 2.1 for location summaries. Inset maps around the edge display the detailed mean annual precipitation (MAP) rate gradients (averaged over recent decades, in mm yr^{-1}) within each study area. Catchments are outlined in black. MAP has been scaled differently to display rainfall gradients most clearly in each area. See the text for details about the data sources.

Study area	Number of channels studied	Recent normal component of slip rate (mm yr^{-1})	Mean annual precipitation rate (mm yr^{-1})	Estimated LGM rainfall	Major bedrock lithology
Faster uplift rates (up to ~ 1 mm yr^{-1})					
Southern Sierra Nevada, White-Inyo, Panamint, Silver Peak and Funeral Mountains, California/Nevada, USA	295	0.5-1.0 mm yr^{-1} at the centres of most range-bounding normal faults (USGS, 2006; Jayko, 2009). Fish Lake Valley fault and Panamint Valley fault are slightly slower at ~ 0.35 mm yr^{-1} (Reheis and Sawyer, 1997; Vogel et al., 2002).	Above 1000 mm yr^{-1} in the high Sierra Nevada, causing a rain shadow on the other ranges < 500 mm yr^{-1}. As low as 100 mm yr^{-1} in low-lying catchments (Danskin, 1988; Daly et al., 2008).	Wetter: estimates range from 1.5-4.0 times modern annual rainfall rates (Thompson et al., 1999; McDonald et al., 2003; Kessler et al., 2006). The penultimate glaciation may have been even more severe (Quade et al., 2003).	Mostly granodiorites, smaller outcrops of mafic igneous, metamorphic, and carbonate units (USGS, 2006).
Sierra de San Pedro Mártir, Baja California, Mexico	62	Slip rate on the San Pedro Mártir fault is not explicitly reported, but there has been 5 km displacement in ≤ 11 Ma, so the long-term normal slip rate must be at least 0.45 mm yr^{-1} (Lee et al., 1996). Dixon et al. (2002) estimate a horizontal extension rate of 2.8 ± 1.4 mm yr^{-1}, which if multiplied by tan(60°) = ~ 0.9 ± 0.4 mm yr^{-1} for an Andersonian normal fault.	200-600 mm yr^{-1} (TRMM – see Kummerow et al., 1998; Hijmans et al., 2005).	Dated pollen and stratigraphic records suggest a wetter glacial climate (Holmgren et al., 2011), and a vegetation record from packrat middens indicates that around the end of the glacial period rainfall rates were at least 2.0 times modern rates (Rhode, 2002).	Predominantly tonalites and granodiorites (O'Connor and Chase, 1989).
Coastal catchments of western Cordillera, Peruvian Andes	120	Dated marine terraces indicate catchment uplift rates of 0.2-0.5 mm yr^{-1} in the north of the study area (Pedoja et al., 2006) increasing to 0.4-0.9 mm yr^{-1} in the south (Saillard et al., 2011).	≤400 mm yr^{-1} for most catchments (TRMM – see Kummerow et al., 1998).	Wetter as pluvial lakes existed similar to California; however, the magnitude of change has not been quantified (Hillyer et al., 2009; Kanner et al., 2012).	Dominant volcaniclastic sediments and Pliocene sediments. Some Paleogene–Neogene volcanics. (Gonzalez and Pfiffner, 2012).
Aspromonte Mountains, Calabria, Italy	94	0.8-1.0 mm yr^{-1} (Olivetti et al., 2012). Detailed constraints are provided by Ferranti et al. (2006) and Antonioli et al. (2006, 2009).	Averaging ~850 mm yr^{-1} (Hijmans et al., 2005).	Vegetation and sediment supply data suggest a wetter glacial period (Le Pera and Sorriso-Valvo, 2000; Massari et al., 2007). However, pollen records in Sicily indicate a more arid LGM (e.g., Incarbona et al., 2010). PMIP II 21 ka synthesis suggests that the LGM was drier by a modest < 100 mm y-1 (Braconnot et al., 2007).	Gneisses, quartzites, and other metamorphics, turbidites, and recent sediments (Atzori et al., 1983).

Study area	Number of channels studied	Recent normal component of slip rate (mm yr^{-1})	Mean annual precipitation rate (mm yr^{-1})	Estimated LGM rainfall	Major bedrock lithology
Slower uplift rates (< 0.3 mm yr^{-1})					
Beaverhead, Lost River and Lemhi Mountains, Idaho, USA	203	0.1-0.3 mm yr^{-1} at the centres of range-bounding faults (Foster et al., 2008).	400-800 mm yr^{-1} (Daly et al., 2008).	Similar to modern rainfall rates, however, the ranges were glaciated (Johnson et al., 2007).	Carbonates, metasediments, and quartzites (Foster et al., 2008).
Sinai High Mountains, Sinai Peninsula, Egypt	72	Fault blocks formed during the Oligocene–Miocene opening of the Suez Rift and have since been abandoned (Sharp et al., 2000). During formation, slip rates were low at 0.1-0.2 mm yr^{-1} (Kohn and Eyal, 1981).	Very dry, ≤ 50 mm y^{-1} (TRMM – see Kummerow et al., 1998; Hijmans et al., 2005).	Wetter, probably ~ 200 mm yr^{-1} (Issar and Bruins, 1983; Issar et al., 2012).	Mostly granitoids, but some small outcrops of various metamorphics and sediments (Eyal et al., 1980).

Table 2.1. The main tectonic, climatic, and lithological properties of the six study areas.

2.3.1. Geologic and climatic settings

Each study area has at least 60 mountain catchments that drain substantial relief, exiting to either an alluvial plain with an axial river or to the sea (in the cases of Italy and Peru). See the supplementary information for detailed maps. The study areas occupy different tectonic settings, but in each case constraints are available on the catchment uplift rates relative to base level. Mostly, this is equivalent to the vertical displacement rates on range–bounding normal faults, documented for the Pleistocene–Holocene period. The exception is Peru, where we examine coastal catchments from an active continental margin. Here, uplift rate is relative to average sea level and determined by the thrust belt generating relief. In our study area, uplift rates of 0.5-1.0 mm yr^{-1} (representative of the last 400 ka) have been well constrained using marine terraces dated with cosmogenic radionuclides (Pedoja et al., 2006; Saillard et al., 2011).

In Fig. 2.3, we have inset detailed maps of each study area, displaying the spatial distribution of mean annual precipitation rate, averaged over recent decades. These illustrate the climatic gradients in and between the six regions. The Peruvian catchments are dry, on average receiving < 400 mm rainfall yr^{-1} owing to their location along the Western Cordillera (Kummerow et al., 1998). We only select westward-draining channels, as these are driest. These bedrock-channelled rivers drain Cretaceous volcaniclastics and some volcanic lithologies around the headwaters (Gonzalez and Pfiffner, 2012). The significant relief of the catchments—in some cases approaching 6000 m from headwaters to mouth—has been built by the subduction of the Nazca plate, with at least half the uplift of the Western Cordillera having occurred in the last 25 Ma (Gregory-Wodzicki, 2000). We restrict our study to the Peruvian segment of the Andes not only because catchment uplift has been well–constrained but also because volcanoes are generally absent (Gonzalez and Pfiffner, 2012) and do not complicate landscape evolution.

The Californian catchments lie in the east California shear zone and drain into four main valleys at the western edge of the basin and range: Owens Valley, Panamint Valley, Fish Lake Valley, and Death Valley. These probably formed by several phases of extensional breakup of a Miocene plateau, and the rate of extension has changed through time (Phillips, 2008). For this reason we adopt only recent (Pleistocene–Holocene) constraints on the relative catchment uplift rates. Like Peru, these reach an upper rate of ~ 1 mm yr^{-1} (see a review by Jayko, 2009, and references therein). This study area includes the eastward-draining part of the southern Sierra Nevada, along with smaller neighbouring ranges bordering the valleys (see supplementary information). Their frontal catchments receive a tenfold range of precipitation rates between them, from ~ 100 mm yr^{-1} bordering Death Valley to ~ 1000 mm yr^{-1} in the high Sierra Nevada (Danskin, 1988; Daly et al., 2008).

The Sierra de San Pedro Mártir in northern Baja California, Mexico, also experiences an intermediate range of precipitation rates from ~ 200 to 600 mm yr^{-1} (Kummerow et al., 1998; Hijmans et al., 2005). All of the catchments we measure are eastward-draining and bound by the (normal) San Pedro Mártir fault. The dip-slip rate on this fault is not explicitly reported, but 5 km of displacement has occurred in < 11 Ma, so the long–term slip rate must be a minimum of 0.45 mm yr^{-1} (Lee et al., 1996). Dixon et al. (2002) estimated a modern horizontal extension rate of 2.8 ± 1.4 mm yr^{-1}, which is supported by a regional tectonic model. Assuming Andersonian geometry, we multiply this by tan 60^{o} to obtain a throw rate estimate of 0.9 ± 0.4 mm yr^{-1}. In both the Californian and Mexican study areas the dominant bedrock lithology is granodiorite, but a variety of metamorphic, igneous, and sedimentary lithologies do crop out also (O'Connor and Chase, 1989; U.S. Geological Survey, 2006).

The catchments of the Aspromonte in Calabria, Italy, receive the most rainfall of the four U_{max} ~ 1 mm yr^{-1} areas. Mean precipitation rate is 800-900 mm yr^{-1} owing to the mid–latitude location in the Mediterranean, and the catchments drain mixed metamorphics and sediments (Atzori et al., 1983). The Pleistocene–Holocene uplift rate of the Calabrian arc is 0.8 to 1.0 mm yr^{-1} (Olivetti et al., 2012), and spatially detailed constraints are provided by Ferranti et al. (2006) and Antonioli et al. (2006, 2009).

Two additional areas are studied that have undergone comparatively less tectonic activity in the Pleistocene–Holocene. The Sinai High Mountains on the Egyptian Sinai Peninsula are extremely arid, with precipitation averaging just 50 mm yr^{-1} (Kummerow et al., 1998; Hijmans et al., 2005). The rivers predominantly drain granitoid basement, but a mixture of metamorphic and sedimentary rocks are also present (Eyal et al., 1980). Today, tectonic activity on the range-bounding faults is small, with most deformation having taken place in the Oligocene and Miocene (Sharp et al., 2000). Much 'wetter' are the catchments in the Idaho, USA, study area with precipitation averaging 400-800 mm yr^{-1} (Daly et al., 2008). These catchments have also undergone little Pleistocene–Holocene tectonic uplift with range–bounding faults slipping at a maximum of only 0.1 to 0.3 mm yr^{-1} in the centres, decaying to zero at fault tips (Densmore et al., 2007; Foster et al., 2008). The Idaho catchments lie along the Beaverhead, Lemhi, and Lost River ranges and include those investigated by Densmore et al. (2007).

2.3.2. Palaeoclimate constraints

Given the likelihood that the geomorphological response time to a tectonic–climatic perturbation may exceed 10^4 or even 10^5 years (Snyder et al., 2000; Armitage et al., 2011; Whittaker and Boulton, 2012), one should consider the effects of glacial–interglacial climate changes on time-averaged

precipitation rates. Modern climate norms are well-constrained, but they represent the interglacial end-member of a cyclic climate. We therefore consider precipitation rate differences at the Last Glacial Maximum (LGM) and explore the implications of this for our analysis.

With respect to glacial palaeoclimate, the California study area is the most researched. It was measurably wetter during recent glacial periods, and lake-highstand data suggest that LGM precipitation rates could have been up to four times modern rates (Anderson and Wells, 2003). However most estimations agree on ~ 1.5-2.0 times modern rates (Thompson et al., 1999; McDonald et al., 2003; Kessler et al., 2006). With a modern mean rate of ~ 450 mm yr^{-1} in the study area, this equates to LGM rates of between ~ 700 and 900 mm yr^{-1}. Slightly more modest are the findings of the PMIP II project (Paleoclimate Modeling Intercomparison Project), a synthesis of climate simulations. These estimate a California climate at 21 ka with ~ 150 to 300 mm yr^{-1} more rainfall than present (see Braconnot et al., 2007, for project details), equating to 600 to 750 mm yr^{-1}. For our purposes, we adopt a mid-range estimate of LGM precipitation rate of 750 mm yr^{-1} for California, satisfying empirical data and climate simulations.

Multiple lines of evidence suggest that the western Cordillera in Peru became arid 10 to 15 Ma ago and that the current dry climate has been established for a long period of time (Gregory-Wodzicki, 2000). The climate was wetter during glacial maxima as indicated by the existence of pluvial lakes, but the magnitude of the rainfall rate change is not yet known empirically (Hillyer et al., 2009; Kanner et al., 2012). However these pluvial lakes were similar to those in California at the LGM, which were themselves sustained by an estimated increase in precipitation rate of ~ 300 mm yr^{-1} (see above). Syntheses of LGM climate models suggest an increase of 100-200 mm yr^{-1} for the Peruvian study area compared to present (PMIP II project, see Braconnot et al., 2007). We therefore adopt an estimate of + 200 mm yr^{-1} precipitation at the LGM. The modern mean rate for this study area is ~ 150 mm yr^{-1} (Hijmans et al., 2005) so this corresponds to ~ 350 mm yr^{-1}.

In northern Baja California, a vegetation record from packrat middens indicates that around the end of the glacial period rainfall rates were at least 2 times modern rates (Rhode, 2002). However Holmgren et al. (2011) examined part of the northern Sierra de San Pedro Mártir and found that, while precipitation rates might have been slightly higher, the difference was minimal enough not to cause a significant vegetation response. These findings are in disagreement with a study by Spelz et al. (2008) who found no sedimentological evidence that the glacial climate was any wetter than at present. Syntheses of coupled atmospheric–oceanic general climate models like the PMIP II project indicate that at the LGM northern Baja California was receiving 100 to 200 mm yr^{-1} more rainfall than at present. The modern average rate is ~ 410 mm yr^{-1} (Hijmans et al., 2005), so we adopt an LGM rate of 550 mm yr^{-1} as a balanced estimate. This is a fair compromise between the vegetation records of Rhode (2002) and Holmgren et al. (2011) and the PMIP II findings.

Limited evidence from vegetation and sediment supply data indicates that the LGM climate was wetter in the Aspromonte of southern Italy (e.g., Le Pera and Sorriso-Valvo, 2000; Massari et al., 2007). However pollen records from neighbouring Sicily indicate a more arid LGM (e.g., Incarbona et al., 2010, and references therein), which agrees not only with data from elsewhere in Italy (e.g., Giraudi, 1989) but also with the PMIP II synthesis, which predicts the LGM was ~ 100 mm yr^{-1} drier (Braconnot et al., 2007). We therefore assume that LGM precipitation rates were lower on average by ~ 100 mm yr^{-1}, taking the modern mean of ~ 850 mm yr^{-1} (Hijmans et al., 2005) down to ~ 750 mm yr^{-1}. The LGM precipitation rates in the Idaho area were probably slightly lower than today (Meyer et al., 2004; Johnson et al., 2007) and the Sinai Peninsula in Egypt was probably wetter by around 200 mm yr^{-1} (Issar and Bruins, 1983; Issar et al., 2012).

For our study areas, these are all helpful constraints. However, unavoidable uncertainties in reconstructing past climates mean that these are first-order estimations. Together, they show that the difference in precipitation rates from the LGM to the present day is on the order of 100-300 mm yr^{-1}. While not negligible, it is less than the annual rates themselves and the variation between study areas.

2.4. Materials and methods

We analyse ASTER digital elevation models (DEMs) to extract a detailed stream network of channels draining catchments in each study area. The ASTER DEMs have a spatial resolution of ~ 30 m, and we only consider catchments with a drainage area > 10 km^2. Aerial imagery, the DEMs, geological maps, and slope maps are used together to identify the points where mountain catchment channels cross the mountain fronts and exit onto an alluvial plain (or the ocean in the cases of Peru and Italy). Upstream of these points, we extract and mask the watersheds using the DEMs. In total, 846 channels are measured in this study.

To extract longitudinal channel profiles, we use the 'Stream Profiler' methodology of Whipple et al. (2007). Profiles are measured from the highest tributary in each catchment following a central path down to the mouth. Where the main channel forks, each channel is extracted separately. Channel concavity, θ, is taken as the gradient of a plot of log-slope against log-drainage area, and the normalised channel steepness index, k_{sn}, is calculated as the intercept using Eq. 2.5 and a reference concavity of 0.45. Normalising the channel steepness is a useful way of comparing different catchments and areas, but it also means that our data does not capture the effects of varying concavity, e.g., along fault strikes (Densmore et al., 2007). As the purpose of this study is to investigate the precipitation control on channel steepness by comparing many different channels and locations, we choose to normalise k_s and overlook concavity variance arising from small-scale effects.

We display characteristic longitudinal profiles for each study area in Fig. 2.4, to illustrate our data. This shows two sets of channels: (i) the median channels (sorted by k_{sn}) for each study area (in black), which are therefore representative of each location. We also show (ii) typical channels with k_{sn} = 130 $m^{0.9}$ (in red). Examples of this steepness occur in all six regions, so these plots allow the study areas to be compared with each other. The longitudinal profiles and the log-log plots of slope against upstream drainage area are shown. We note that on the few occasions where glacially eroded, flat reaches were observed at the headwaters in the upper channel profiles, we did not include those sections in our measurements. This is to minimise the effects of glacial erosion in our data.

For each watershed extracted, the mean elevation, mean annual precipitation, and total relief (defined as the difference in elevation from the headwaters to the mouth of the catchment) were calculated using zonal statistics tools in ArcGIS. Mean annual precipitation was calculated from the best data set available for each location. In the United States, this is the PRISM model (Daly et al., 2008), and in Baja California and Italy we use the global WorldClim model (Hijmans et al., 2005). These are both based on multi decadal precipitation averages (from 1971 to 2000 for PRISM, and from 1950 to 2000 for WorldClim) collected from a large number of terrestrial climate stations. These measurements are treated as point data, and a precipitation rate model is interpolated between them, in both cases with a spatial resolution of 30 arcsec (~ 1 km). For the Sinai High Mountains and the Peruvian Andes, annual precipitation rate averages (for the period 1997 onward) are available from the Tropical Rainfall Measuring Mission (TRMM) (see Kummerow et al., 1998, for a description of methods), and we select this as the best data source for these study areas. We have used TRMM product 2B31, which has a spatial resolution of around 5 km^2 and climate norms averaged from 1997 to present. Given that the mean catchment sizes in the Peru and Sinai study areas are 1490 and 190 km^2, respectively, this spatial resolution is more than sufficient for characterising precipitation rate. We have selected the TRMM data over the WorldClim model in these areas because the latter is based on surface weather station data, which is not very extensive in these regions. The TRMM satellite data is therefore much more reliable for these locations. One drawback of the satellite data is that it could underestimate the annual contribution of snowfall to the precipitation budget. We make the assumption that this is not a significant issue in Egypt and the most arid part of western Peru.

The PRISM, WorldClim, and TRMM precipitation averages were compared in areas where they overlap geographically, and they are all in close agreement. The uncertainty arising from the differences between the models is much smaller than the differences in precipitation rate within and between the six study areas. We compare our channel steepness data with precipitation rates using the statistical package Origin 8.6. We fit our data with linear regressions or allometric power laws of the form $y = ax^b$ consistently throughout the study.

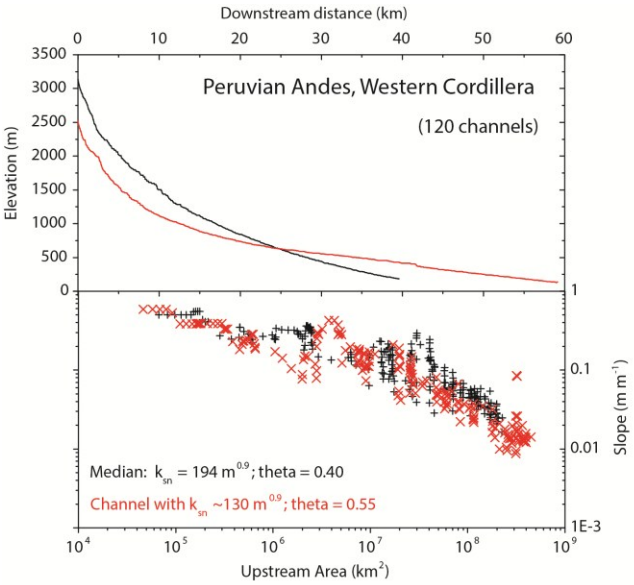
Downstream distance (km)
Peruvian Andes, Western Cordillera
(120 channels)
Elevation (m)
Slope (m m^{-1})
Median: k_{sn} = 194 m$^{0.9}$; theta = 0.40
Channel with k_{sn} ~130 m$^{0.9}$; theta = 0.55
Upstream Area (km^2)

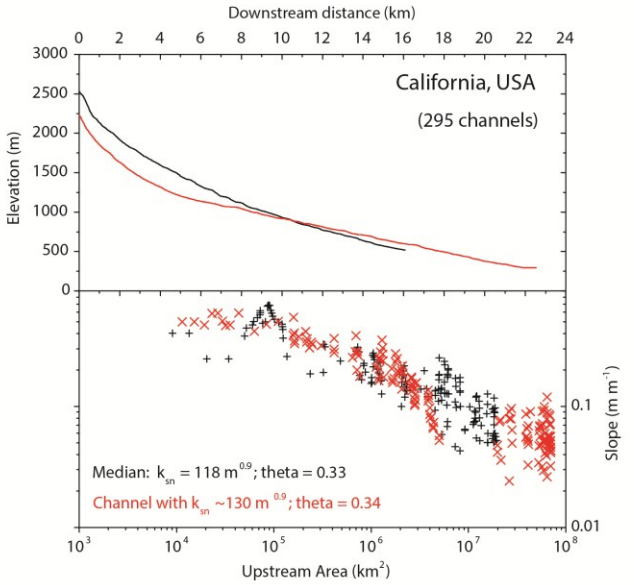
Downstream distance (km)
California, USA
(295 channels)
Elevation (m)
Slope (m m^{-1})
Median: k_{sn} = 118 m$^{0.9}$; theta = 0.33
Channel with k_{sn} ~130 m$^{0.9}$; theta = 0.34
Upstream Area (km^2)

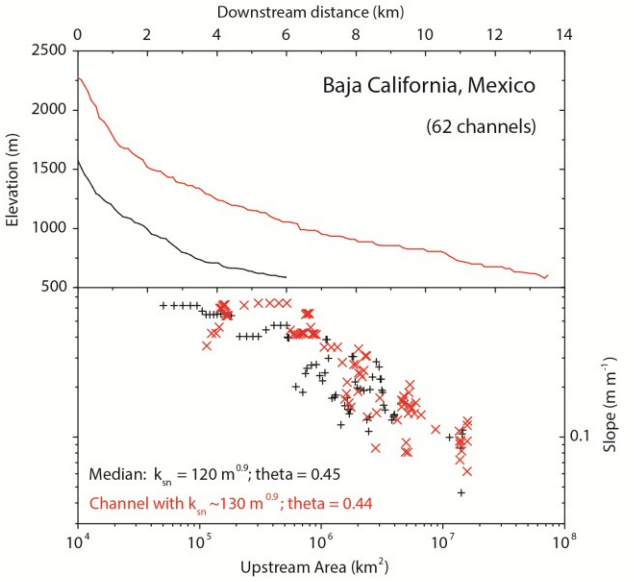
Downstream distance (km)
Baja California, Mexico
(62 channels)
Elevation (m)
Slope (m m^{-1})
Median: k_{sn} = 120 m$^{0.9}$; theta = 0.45
Channel with k_{sn} ~130 m$^{0.9}$; theta = 0.44
Upstream Area (km^2)

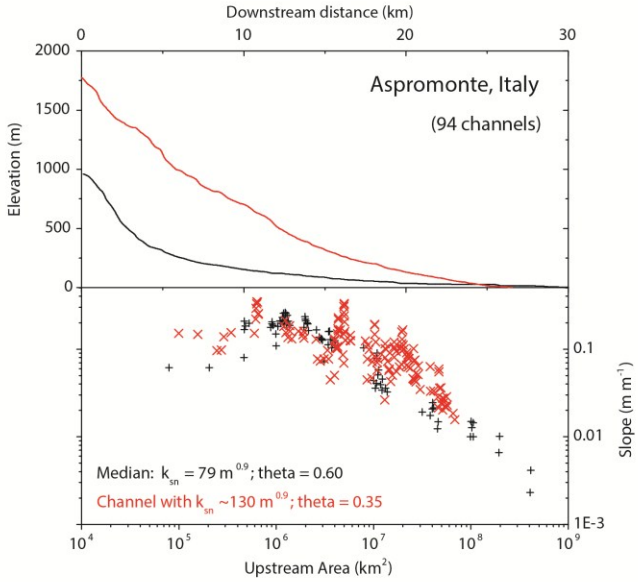
Downstream distance (km)
Aspromonte, Italy
(94 channels)
Elevation (m)
Slope (m m^{-1})
Median: k_{sn} = 79 m$^{0.9}$; theta = 0.60
Channel with k_{sn} ~130 m$^{0.9}$; theta = 0.35
Upstream Area (km^2)

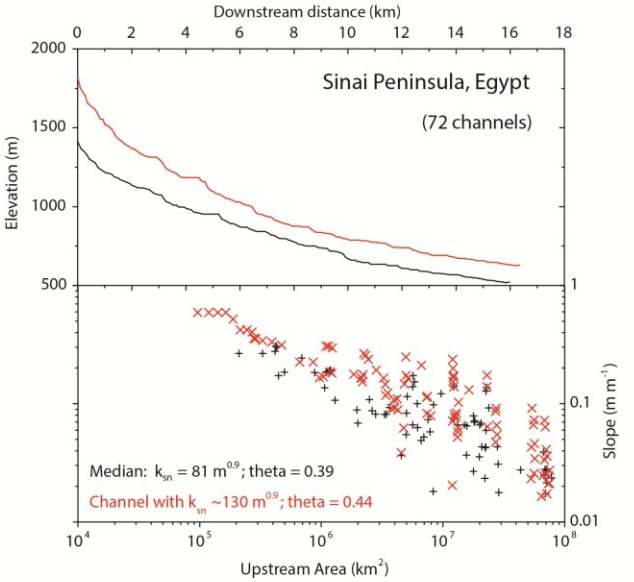
Downstream distance (km)
Sinai Peninsula, Egypt
(72 channels)
Elevation (m)
Slope (m m^{-1})
Median: k_{sn} = 81 m$^{0.9}$; theta = 0.39
Channel with k_{sn} ~130 m$^{0.9}$; theta = 0.44
Upstream Area (km^2)

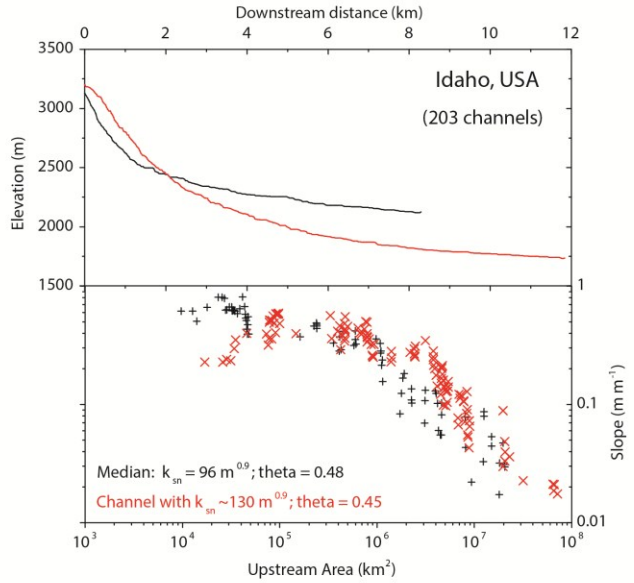
Downstream distance (km)
Idaho, USA
(203 channels)
Elevation (m)
Slope (m m^{-1})
Median: k_{sn} = 96 m$^{0.9}$; theta = 0.48
Channel with k_{sn} ~130 m$^{0.9}$; theta = 0.45
Upstream Area (km^2)

Figure 2.4 (previous page). Representative longitudinal profiles (top graphs) and log-log plots of channel slope against upstream drainage area (bottom graphs) for the six study areas. Two sets of data are shown. In black are the channels with median k_{sn} values for each region, which are therefore average channels representative for each study area. In red are channels with k_{sn} = 130 $m^{0.9}$; examples of this steepness occur in all six data sets. These are not necessarily average channel profiles, but allow the study areas to be compared with each other for the same channel steepness.

2.5. Results

2.5.1. Channel steepness variation with precipitation rate

Figure 2.5 shows k_{sn} varying with mean annual precipitation rate for the six study areas. Each data point represents one catchment, and the graphs share the same axis ranges to ease comparison. Best-fit allometric power laws of the form

$$k_{sn} = aP^b \qquad [2.6]$$

have been fitted to the data (solid red lines), where P is the mean annual precipitation rate. The standard errors on the coefficient a and exponent b have also been calculated. On each graph, this statistical fit has then been duplicated with the same value of constant a, but with b varying at 0.1 intervals, producing the dotted grey lines. These curves help to visualise the upper and lower bounds of the exponent b between which the data sets lie.

In general terms, channel steepness increases sub-linearly with precipitation rate rather than decreasing as one might simplistically expect (Figs. 2.1b, 2.2b). Of the study areas with catchments uplifting at ~ 1 mm yr^{-1} (Fig. 2.5a), the channels in Peru exhibit the highest k_{sn} values reaching well above 300 $m^{0.9}$ in the upper quartile. This study area is also the driest, with most catchments receiving < 250 mm yr^{-1} precipitation. The best statistical fit is a strongly sublinear power law, with most catchments falling within the limits of b = 0.2 to 0.3, with a heavy weighting of the data toward the dry extreme.

The channels in California and Mexico have lower k_{sn} values than those in Peru, rarely exceeding 300 and 200 $m^{0.9}$ respectively. They are also wetter, mostly occupying the range of P ~ 200 to 600 mm yr^{-1}. The California data spans the widest range of precipitation rates of all the areas, and the best statistical fit is a power law with an exponent b ~ 0.6. In the case of Baja California, most of the channels fall between the bounds of b = 0.6 and 0.9. The Italian channels have lower k_{sn} values still, averaging only ~ 100 $m^{0.9}$, and these catchments also receive the highest precipitation rates of 800-900 mm yr^{-1}. They display very little variation in rainfall, and we exploit this later.

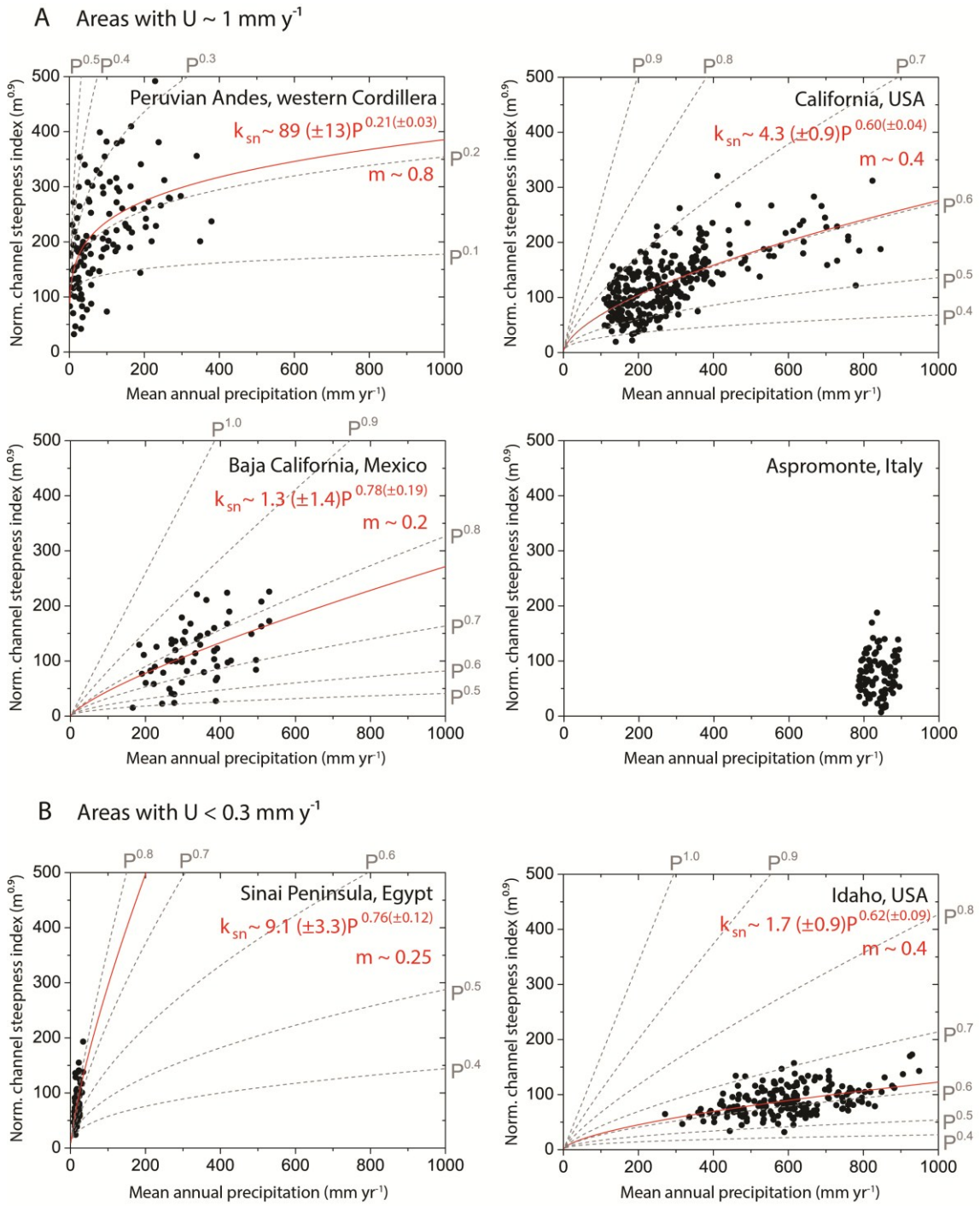

Figure 2.5. Variation in normalised channel steepness index (θ_{ref} = 0.45) with MAP rate for (A) the four study areas with U_{max} ~ 1 mm yr^{-1} and (B) the two study areas with lower uplift rates < 0.3 mm yr^{-1}. The solid lines are allometric power laws fitted to each plot, with the form $y = ax^b$. The dotted lines show similar curves with the same value of a, but with P raised to 0.1 intervals of b. Channel steepness increases with precipitation rate, sublinearly, for all areas apart from Aspromonte, Italy, where the catchments occupy a narrow range of P. Values of m are estimated, assuming that the exponent of the best-fit power law is equal to ($1 - m$). The two study areas with the broadest ranges of P (California and Idaho) give estimates of m around 0.4. The slower uplifting study areas have lower k_{sn} values. Of the graphs in (A), the highest k_{sn} values are found in the driest area (Peru) and decline through California and Mexico to the lowest values in the wettest area (Italy).

Despite the four areas sharing similar maximum uplift rates of ~ 1 mm yr^{-1}, between them exists at least a threefold variation in k_{sn} across precipitation rates from < 200 to ~ 900 mm yr^{-1}. Upper–quartile k_{sn} values clearly decline from Peru, through the two California areas, to Italy, which follows the trend of increasing precipitation rate.

In the two study areas with low uplift rates (Fig. 2.5b), channel steepness also increases as the mean annual precipitation rate rises. The very arid catchments in Egypt occupy an extremely narrow precipitation range, yet they still show evidence of a slightly sublinear increase in k_{sn} with precipitation rate, where $b = 0.76 \pm 0.12$. The wetter Idaho catchments span a much wider precipitation range, with the best statistical fit being a power law with $b = 0.62 \pm 0.09$. These data cover the broadest range of precipitation rates of all areas besides California (~ 250 to 950 mm yr^{-1}); and also suggest that k_{sn} scales with P sub-linearly. Nevertheless, in contrast to the faster-uplift study areas, the total range of k_{sn} (~ 20-200 $m^{0.9}$) is similar for the Egyptian and Idaho catchments in spite of their different climates.

The graphs in Fig. 2.5 exhibit scatter about the power law trends fitted, although this is significantly smaller than the differences between the study areas. We attribute this scatter to a combination of effects arising from lithological variations, fault distribution and interactions, and other uncontrolled variables like differences in hydraulic geometry and perhaps vegetation dynamics affecting erosion. In section 2.5.3, we will introduce an averaging approach that aims to accommodate this scatter.

2.5.2. Coupling of orographic precipitation, relief, and tectonics

The data in Fig. 2.5 shows a general sub-linear increase in normalised steepness index with mean annual precipitation rather than a decrease (c.f., Fig. 2.1b). An obvious way to explain this trend is that channels with greater precipitation are also those with higher local elevations or relief. The sub-linear increase of k_{sn} with P could therefore be masking a tectonic uplift trend (e.g., Fig. 2.2b,c) because we know that in general, higher rates of recent tectonic uplift are correlated with higher elevation, Z, and relief (c.f., Ahnert, 1970; Pinet and Souriau, 1988; Tippett and Kamp, 1995; Burbank and Anderson, 2001). In fact, plots of precipitation rate against catchment elevation above local base level (Fig. 2.6) demonstrate unambiguously that greater rainfall directly correlates with greater elevations in all study areas, although the precise gradient varies because of location, latitude, and topographic constraints. In each case, the best statistical fit is a linear increase in P with mean catchment elevation; allometric power laws of the form $P = aZ^d$ also give d values around 1 but have similar or lower R^2 values.

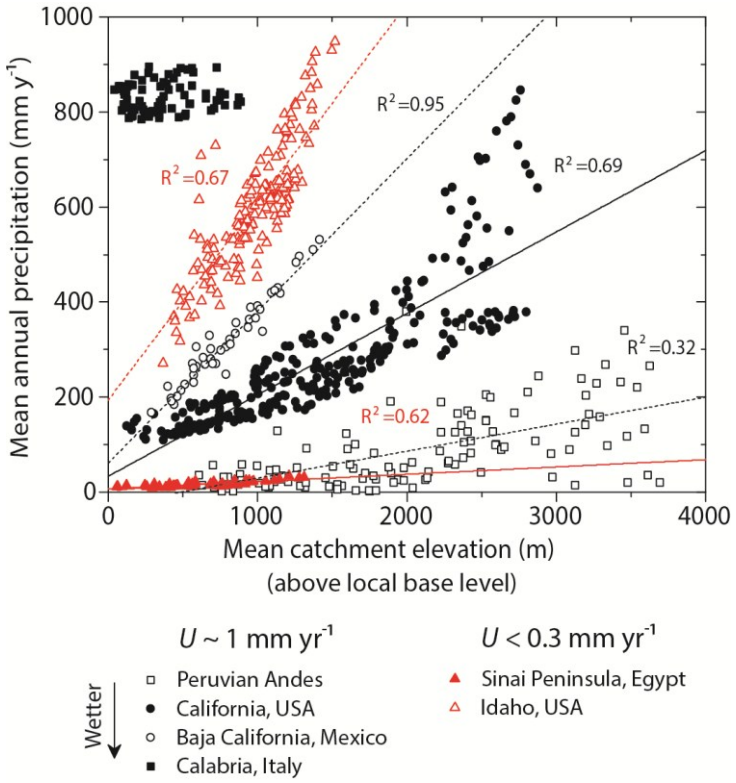

Figure 2.6. The relationship between precipitation rate and mean catchment elevation. Elevation is adjusted to be above base level in each location. Calabria has uniformly low-lying and wet catchments. In the other five areas, precipitation rate increases orographically with elevation, and the best statistical fit is a linear trend in each location. These trends are annotated with their R^2 values.

This orographic coupling of elevation with both uplift rate and precipitation rate complicates any attempt to extract either signal geomorphologically as outlined in section 2.2. However, we can use the Italian (south Calabria) study area to break this coupling circle because these coastal catchments lack the apparent orographic signal that is inherent to the other areas. This difference can be observed clearly in Fig. 2.6. The Italian catchments have mean elevations of < 1000 m, with precipitation rate narrowly clustered around 850 mm yr^{-1}. Not only does it lack a pronounced orographic signal, southern Calabria also has Pleistocene–Holocene uplift rate estimates that are constrained with a high spatial resolution (Antonioli et al., 2006, 2009; Ferranti et al., 2006). Alongside uniform rainfall, this allows us to explore how k_{sn} varies with uplift rate alone, i.e., test the schematic graph in Fig. 2.1a. We have taken local uplift rate constraints reported by Antonioli et al. (2006, 2009) and Ferranti et al. (2006), and calculated the average k_{sn} values of the catchments in the immediate vicinity of each (Fig. 2.7). Seventy-seven channels and sixteen uplift constraints were used to estimate how mean k_{sn} values vary with U, and the error bars reflect ± 1 standard deviation, σ, of the data. The best statistical fit is a linear trend that intersects the origin. The trend is not sufficient to disprove a sub-linear k_{sn}-uplift (or erosion) relationship in other areas, as has been suggested in some studies (Tucker, 2004; DiBiase and

Whipple, 2011; Kirby and Whipple, 2012), although we note these studies do not tend to account for orographic rainfall effects.

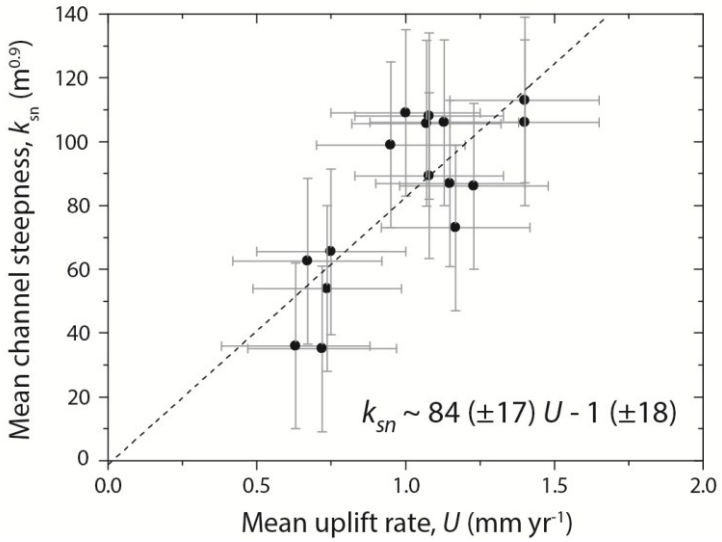

Figure 2.7. Mean values of normalised channel steepness index (θ_{ref} = 0.45) plotted against mean catchment uplift rate in Aspromonte, Italy. Uplift rate estimates were taken from Antonioli et al. (2006, 2009) and Ferranti et al. (2006), and the error bars show the ± 1 σ uncertainty in the data set. The Italian study area is an ideal location to explore this relationship as it occupies a very narrow range of P (~ 800-900 mm yr^{-1}) with no orographic trend (see Figs. 4 and 5). A linear trend offers a good fit to the data and intersects the origin.

2.5.3. Extracting a precipitation signal?

The data above demonstrate that to successfully evaluate the true dependence of landscape on climate we need to tease apart the competing roles of tectonics and precipitation. To do this, we adopt two complementary methods. The first uses data within each study area to estimate the true scaling of k_{sn} and precipitation if the coupling between uplift and k_{sn} is known (above). The second uses comparisons between areas to pull out statistical differences between regions with similar uplift rates but different precipitation rates, for the modern day and for the geologic past.

2.5.3.1. Comparison within field sites

The linear $k_{sn} \sim U$ scaling suggested by the southern Calabrian data (Fig. 2.7), in the known absence of orographic precipitation, implies that the exponent n in Eq. 2.5 for k_{sn} is approximately equal to 1. Many data sets also demonstrate the linear scaling between topographic elevation and the uplift rate generating it (Ahnert, 1970; Pinet and Souriau, 1988; Tippett and Kamp, 1995; Burbank and Anderson, 2001). Consequently, to first order the effective precipitation rate exponent b, Eq. 2.6 must

be related to the true precipitation exponent m (Eq. 2.5), as $b = 1/d - m$. For each graph in Fig. 2.5, corresponding values of m have been estimated where $d \sim 1$ as argued above (see Fig. 2.6). The California data provides the most accurate estimate of m, as these data points span the broadest range of precipitation rates with the wetter catchments needed to clearly show sub-linearity. Almost all the data fall between the limits of $b = 0.5$ and 0.7, thereby constraining estimates of m to between 0.3 and 0.5. This indicates that, all other things being equal, channel steepness is inversely proportional to approximately the square root of precipitation. Similar findings are obtained for Idaho in the USA at lower maximum uplift rates. This is compatible with the empirical findings of other workers (e.g., Sklar and Dietrich, 1998; Stock and Montgomery, 1999; Wobus et al., 2006) and new work by Ferrier et al. (2013) who recovered $b = 0.5$ to 0.6 using a bedrock river analysis on the Hawaiian island of Kaua'i. In contrast, data for the more arid Sinai, Baja California, and Peru are most consistent with lower values where $m \sim 0.2$, which would suggest these more arid catchments may be relatively insensitive to precipitation gradients in time or space, at least for the range of mean annual precipitation rates considered here. We take this opportunity to comment on the Peruvian data: the scatter and weighting of the data to the arid extreme mean that this particular estimate of m and the constant a are quite uncertain. This dataset becomes much more useful in comparison with the other three $U_{max} \sim 1$ mm yr^{-1} locations as we now discuss.

2.5.3.2. Comparison between field sites

Our field sites have mean annual rainfall rates from < 100 to almost 1000 mm yr^{-1}. To compare the landscapes as a whole, we calculated arithmetic mean values of k_{sn} and P for each of the study areas to enable us to compare the relatively large data sets statistically (Fig. 2.8a). However, we chose to restrict our averaging to the upper quartile of channel steepness in each study area for several reasons. First, the precipitation signal is most pronounced where the uplift rates are highest, precisely because of the orographic coupling deduced above, so it is in this domain that (i) our data is most sensitive and (ii) our signal is less likely to be affected by other factors that may affect the signal-to-noise ratio such as lithology changes (c.f., section 2.6, below). Secondly, this allows us to more effectively compare channels with similar $U_{max} \sim 1$ mm yr^{-1}, e.g., by excluding less steep channels sitting at fault tips or between fault strands. Thirdly, Fig. 2.5 shows us that steeper channels are more likely to capture any precipitation effect; in Fig 2.5a, the differences between the four $U_{max} \sim 1$ mm yr^{-1} areas is most apparent when comparing the steepest channels. This is because each area has points where U decays to zero, so k_{sn} similarly decays to low values in places. We need to isolate the steeper, most sensitive channels.

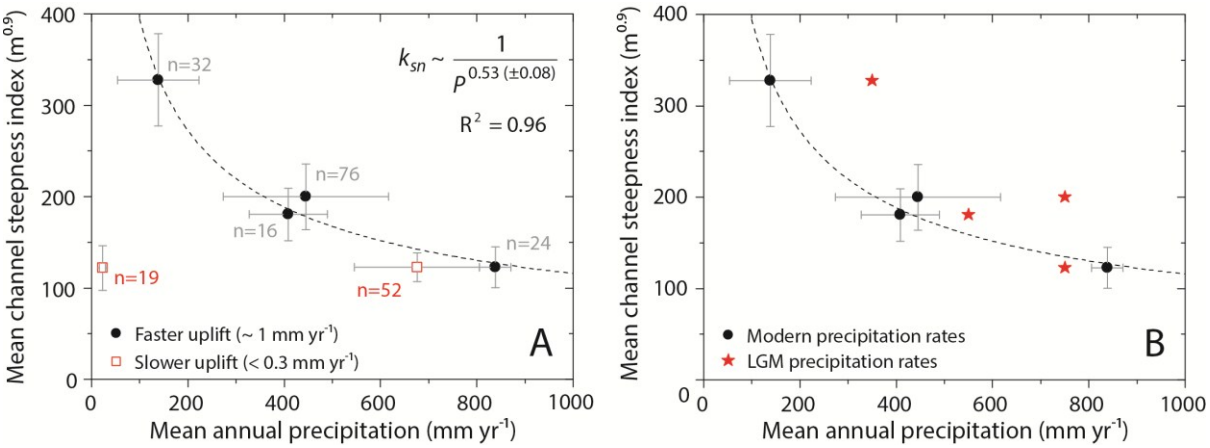

Figure 2.8. (A) Mean normalised channel steepness index (θ_{ref} = 0.45) plotted against mean annual precipitation rate, for the upper quartile of channels (selected by k_{sn}) in each area. The annotation gives the number of channels that are included in each average, and the error bars show ±1 σ uncertainty. For the two areas with slower catchment uplift (open squares), k_{sn} averages ~ 125 m$^{0.9}$ regardless of P. For the areas with faster U_{max} ~ 1 mm yr^{-1}, k_{sn} averages more than double this in Peru (P < 200 mm yr^{-1}), declining as precipitation rate increases. This relationship can be approximated with a power law of $k_{sn} \sim 1/P^m$ where m is an expected value of ~ 0.5. The average k_{sn} reaches a comparable value to the low uplift areas when P ~ 800 mm yr^{-1}. (B) The ~ 1 mm yr^{-1} uplift data only, comparing modern precipitation rates (black circles) with estimates of LGM precipitation rates (red stars).

The number of measurements included in each data point is annotated on Fig 2.8a. Error bars reflect ±1 σ standard deviation within each set of channels, hence the greater error on the Peru point. For the U_{max} ~ 1 mm yr^{-1} areas (black circles), mean k_{sn} decreases from Peru, through the California and Baja California examples, to Italy as the mean precipitation rate increases. The best fit to the data is an inverse power law where $k_{sn} \sim P^{-0.53 \pm 0.08}$. This result compares well with the analysis for individual catchments in Fig. 2.5; with the 'expected' value of m derived from theory (Sklar and Dietrich, 1998; Wobus et al., 2006) and is in very good agreement with the empirical findings of others (Stock and Montgomery, 1999; Snyder et al., 2000; Ferrier et al., 2013). We emphasize that the two- to threefold decrease in mean k_{sn} (from ~ 320 m$^{0.9}$ in arid Peru to ~ 110 m$^{0.9}$ in wetter Italy) over a precipitation range from ~ 100 to > 800 mm yr^{-1} cannot be explained by uplift rate differences. However, for the two areas with catchment uplift rates below 0.3 mm yr^{-1} (open red squares), mean upper quartile k_{sn} averages ~ 120 m$^{0.9}$ in both areas despite the difference in rainfall rates. In these two cases, the absolute range and magnitude of k_{sn} values is small.

In Fig. 2.8b we plot k_{sn} as a function of P reconstructed for the LGM using the data discussed in section 2.3.2 to evaluate the likely climate ranges these catchments have been exposed to. We only focus on the four U ~ 1 mm yr^{-1} areas as these clearly capture the precipitation signal. The red stars represent the precipitation rate of each area, shifted to the predicted LGM position (c.f., section 2.3.2). This is only a first–order insight because the uncertainties on LGM climate are large (and also difficult to meaningfully quantify, so we have omitted error bars). Nonetheless, a general decline in

k_{sn} with precipitation rate is observed, suggesting that channel steepness declines with precipitation rate whether or not LGM or modern data are used. In reality, these precipitation rates form the two end–members of glacial–interglacial conditions. Geomorphic response timescales are currently a topic of intense debate (Armitage et al., 2011; Castelltort et al., 2012; Whittaker and Boulton, 2012) but catchment response times are likely to cover at least one glacial–interglacial cycle. Averaged over this period, effective precipitation rates probably lie somewhere between the data sets in Fig. 2.8b. Accounting for palaeoclimate variability may alter the estimate of *m* slightly, but it is secondary to the finding that precipitation rate measurably suppresses the steepening of channels in response to uplift.

2.5.4. The importance of relief

Relief is the integrated product of uplift and erosion, both of which are moderated by tectonic and climatic boundary conditions. Consequently, any geomorphic index that captures the fundamental controls on landscape morphology should potentially scale with relief. For our study areas, we test the scaling of normalised channel steepness index with mean catchment relief using the whole data set, comprising six study areas and 846 channel measurements in total (Fig. 2.9). We measure catchment relief as the vertical difference in elevation between the highest and lowest points in a catchment. The result is striking because (i) this suggests that k_{sn} is linearly proportional to catchment relief with a gradient of ~ 7 %; and (ii) the graph shows that the data all collapse together on a similar trend. In other words, for an order of magnitude range in precipitation rate (~ 100 to 1000 mm yr^{-1}) and uplift rate (~ 0.1 to ~ 1 mm yr^{-1}) and despite possible differences in bedrock erodibility, the relationship between channel steepness and relief is almost identical in these six areas. Channel steepness indices are therefore extremely efficient predictors of catchment relief and vice versa. Importantly, this indicates that for these regions, topographic relief and channel geometry are responding in similar ways to boundary conditions and probably with a similar response time.

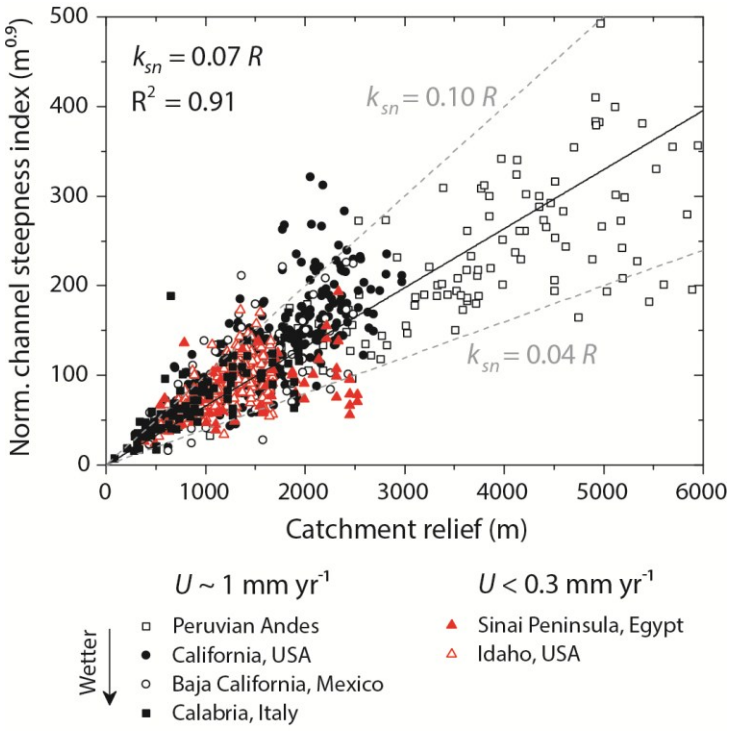

Figure 2.9. Normalised channel steepness index (θ_{ref} = 0.45) plotted against total catchment relief (*R*, the elevation difference between the highest and lowest points). Channel steepness increases linearly with relief, in a similar way for all six study areas, across gradients in climate and in tectonics.

2.6. Discussion

2.6.1. Decoupling tectonics and relief?

Our data highlight the fact that tectonic and climatic variables play important roles in determining channel steepness, but they also emphasize how difficult they are to deconvolve. In simple plots such as Fig. 2.5, k_{sn} increases with precipitation when theory suggests it should decline. We attribute this to an orographic coupling of precipitation rate and tectonic uplift; so in order to constrain the precipitation–k_{sn} signal we need to remove the uplift signal. This is a complicated task primarily because many areas of the world do not have robust constraints on the rate of rock or surface uplift. Moreover, we still do not know the 'typical' response timescale over which tectonic–climatic boundary conditions ought to be averaged (e.g., Whittaker and Boulton, 2012). Fortunately, in our four 'faster uplift' study areas, existing work has constrained U_{max} at ~ 1 mm yr^{-1}, determined using a range of methods and representative of the recent ~ 1 Ma (see Table 2.1 for references). We have chosen uplift rate estimates averaged over the Pleistocene–Holocene period because this corresponds with current best estimates of the geomorphic response times of fluvial landscapes: between 10^5 to 10^6 years (Snyder et al., 2000; Whittaker et al., 2007; Armitage et al., 2011; Whittaker and Boulton,

2012). These areas also have different climates and are, therefore, some of the best landscapes for testing climatic ideas using stream profile analysis. We investigated the dependency of k_{sn} on average precipitation rate in two complementary ways. Initially, we deduced the orographic covariance of uplift and precipitation (Fig. 2.6); we showed that the k_{sn}–U relationship can also be treated as linear for our purposes (Fig. 2.7). Consequently, the significant sublinearity of the k_{sn}–precipitation relationships in the various study areas (Fig. 2.5) suggests that precipitation does have a reducing effect on k_{sn}. However, the effect of the orographic coupling with uplift rate is such that precipitation 'acts to limit' the increase in k_{sn} with uplift. In other words, precipitation rate is acting as a proxy for the uplift signal but transforming it simultaneously, producing a composite signal. For the two areas that receive a substantial range of precipitation rates (California and Idaho), we extract values of m around 0.4 ± 0.1 (Eq. 2.5), in agreement with published constraints (Sklar and Dietrich, 1998; Stock and Montgomery, 1999; Snyder et al., 2000; Wobus et al., 2006; Ferrier et al., 2013). All of the study areas provide evidence for sub-linearity in Fig. 2.5, other than the Aspromonte which is used to decouple uplift and precipitation. The second approach we take to characterising the precipitation dependence of k_{sn} is to draw a comparison between the four areas uplifting at ~ 1 mm yr^{-1} so that the tectonic variable is largely controlled. Averaging the steepest quartile of channels in each area, to represent the landscape as a whole, produces a power law decline in k_{sn} with modern mean annual precipitation rate (Fig. 2.8), which also reveals an expected value of m around 0.5. A comparison with LGM precipitation rates indicates that k_{sn} also declines as palaeoprecipitation rate increases.

We also find that k_{sn} scales linearly with catchment relief in a near-identical fashion for our study areas despite differences in uplift rate, precipitation rate, and erodibility. Figure 2.9 is encouraging because it suggests that k_{sn} does intrinsically quantify the time-integrated equilibrium between uplift and erosion.

A key concern in any study of this type is whether mean annual precipitation rate is the best way of quantifying a 'climate', which evidently can be (and is) characterised by a range of variables (e.g., Champagnac et al., 2012; Whittaker, 2012). Mean annual precipitation is a variable explored in the majority of advanced landscape evolution models (e.g., Carretier and Lucazeau, 2005; Armitage et al., 2011; Allen et al., 2013), but others clearly matter too, such as the magnitude-frequency distribution of storm size and maximum rainfall rates, the seasonal distribution of precipitation, and the effects of temperature on landscape evolution transmitted by vegetation dynamics, glaciation, and the spatial distribution of rainfall (Sólyom and Tucker, 2004; Istanbulluoglu and Bras, 2005; Anders et al., 2008; Wobus et al., 2010; Wulf et al., 2010; DiBiase and Whipple, 2011; Egholm et al., 2012). Such effects may be complicated further by erosion thresholds (Molnar, 2001). The two big questions we must answer are (i) which climatic data closely scale with the geomorphically effective channel discharge? and (ii) which climatic or landscape variables can we realistically measure in space and also back in

time (c.f., Whittaker, 2012)? In principle, mean annual precipitation is directly related to effective discharge and hence landscape form, so a good way to address this debate is arguably to test the first-order relationship between geomorphological data and mean precipitation rate, as we have done here, before moving on to other variables. We also exploit one of the main advantages of using such data: it is possible (to an extent) to reconstruct these rates for the past. Other parameters like maximum storm magnitudes, rainfall intensity, or vegetation density remain very challenging to reconstruct over 10^5 to 10^6 year periods in reliable detail. This is clearly an issue that needs to be addressed by future work.

2.6.2. Lithological effects and other study limitations

It is worth commenting on the effects of bedrock lithology in our findings. We have not controlled the lithology variable between or within our study areas (see Table 2.1); and there are necessarily a range of sedimentary, metamorphic, and igneous bedrocks exposed in the catchments for any global-scale investigation such as ours. Nonetheless, we can make a very important observation. The steepest channels were found in the Peruvian data, and these catchments predominantly drain volcaniclastic sediments and other recent Pliocene sediments, with more resistant Paleogene–Neogene volcanic rocks only cropping out near the catchment headwaters (Gonzalez and Pfiffner, 2012). In contrast, the Italian catchments with the lowest k_{sn} measurements for the same uplift rate largely drain highly resistant gneisses, quartzites, and other metamorphics of the Aspromonte massif (Atzori et al., 1983). The Peruvian catchments may indeed have the most erodible lithologies of all the areas, yet have the steepest channels with the greatest relief and the highest headwaters. Therefore, while rock erodibility obviously adds scatter to the data, we do not consider that lithology explains away the relationships between uplift rate, precipitation rate, relief, and channel steepness deduced here. Similarly, we suggest that lithological differences do not explain why the Sinai and Idaho data sets have similar ranges and magnitudes of k_{sn}: both have a range of sedimentary, metamorphic, and igneous lithologies. Channel steepness is more likely to be low in these areas simply because the uplift rate is very low.

We have also not directly addressed glaciation effects in our data. As previously mentioned, we have excluded from our measurements any obvious glacially eroded plateaus in the upper reaches of channels to minimise the effects of glacial erosion. However, glaciers did occupy the headwaters of some of the 846 catchments we measured here, and effects arising from this perhaps contribute to some of the unexplained scatter on our plots. Future studies may benefit from isolating the glaciation variable alone to elucidate its controls on channel geometry in locations where other climatic and tectonic variables are controlled.

This is a broad–scale study encompassing six study areas around the globe. If each of these were examined in close spatial detail, the precise fluvial erosion process, the positions of individual faults, and/or lithological boundaries probably play a role in determining k_{sn} in individual catchments. We emphasize that the focus of this study was to derive first–order regional trends using a statistically large data set, rather than attempting to quantify everything knowable about individual catchments. This applies through time as well as across space: we have used uplift rate averages over the most likely geomorphologically relevant timescale according to recent research, and we have assumed that modern topography captures the integrated uplift history averaged over this timescale. However, future studies could explore variations in boundary conditions averaged over different time periods.

2.8. Conclusions

In this chapter we demonstrate that longitudinal channel profiles are sensitive to mean annual precipitation rate in tectonically active landscapes. We find that channel steepness increases with precipitation rate sub-linearly but in a way that can be explained by the orographic coupling of precipitation and recent topographic uplift. While greater rainfall has a reducing effect on channel steepness, this coupling means it acts as a proxy for the uplift signal whilst also modulating it. Put another way: precipitation rate limits the amount that channels can steepen in response to tectonic uplift. This effect can be detected in the sub-linearity of the relationship between normalised channel steepness and precipitation rate from individual study areas and also by comparing the steepest, most sensitive channels from different regions that share equivalent uplift rates.

Our twin approaches to characterising the k_{sn}–P relationship are complementary and give similar results to each other, to existing theoretical work (Sklar and Dietrich, 1998; Wobus et al., 2006) and to localised empirical studies (Stock and Montgomery, 1999; Snyder et al., 2000; Ferrier et al., 2013). We therefore argue that channel steepness in arid locations like western Peru is measurably higher by combination of significant uplift rates and a dry climate and that channel steepness declines when either uplift rate slows or precipitation rate rises. When comparing multiple locations, channel steepness cannot be explained by either tectonics or climate alone; both must be considered together. We also demonstrate that k_{sn} scales with catchment relief in a linear, similar way for all our study areas, despite their differences in climatic, tectonic, and lithological boundary conditions. This is an encouraging testament to how intrinsically linked channel steepness is to the balance between uplift and erosion.

To our knowledge, this is the first time a clear precipitation rate signal has been empirically extracted from k_{sn} data representing different landscapes where the effects of tectonic uplift have been largely

controlled, in keeping with theoretical considerations. The results are significant because they demonstrate that climate and palaeoclimatic rainfall averages play an important but often neglected role in determining the geomorphic form of the landscape. A key challenge for future studies is to quantify climatic controls on upland catchments more widely, including the magnitude–frequency distribution of storminess, associated vegetation dynamics, and channel erosion thresholds. Of course, these effects need to be characterised across a range of landscape metrics including hillslope angles and curvatures, not just k_{sn} (c.f., Abbühl et al., 2011; Bookhagen and Strecker, 2012; DiBiase et al., 2012; Hurst et al., 2012). To answer these questions fully, workers therefore need to tackle the outstanding 'big-ticket' question in quantitative geomorphology—what is the characteristic response time of landscapes to climatic or tectonic perturbations (c.f., Jerolmack and Paola, 2010; Aguilar et al., 2011; Armitage et al., 2011; 2013)?

3. Dating alluvial fan surfaces in Owens Valley, California, using weathering fractures in boulders[†]

Chapter Abstract

A wide range of sedimentological and geomorphological field research depends on the availability of accurate and detailed depositional age models. Although exposure dating techniques such as cosmogenic nuclide and luminescence dating are now widely available, they remain expensive and time-consuming, and this frequently limits the density of age constraints and the resolutions of age models for many study areas. We present a simple and effective, field-based approach for extending and correlating existing age models to un-dated surfaces. In Owens Valley, California, we make use of detailed ^{10}Be chronologies reported for 4 different alluvial fan systems, to precisely calibrate the rate at which weathering fractures are enlarged in granitic surface boulders. We show that these fractures have widened at a time-integrated rate of 1.05 ± 0.03 mm ka^{-1} for at least 140 ka at this location, and this relationship can be represented by a linear regression that makes them ideal chronometers for surface dating. Our analysis offers a new approach to refining the uncertainties of both surface erosion rate and cosmogenic age estimates at this location. Ultimately, we integrate our observations to devise a robust age calibration for clast fracture widths in Owens Valley, and we demonstrate its application by estimating the ages of 27 additional local fan surfaces. We present an updated and extended stratigraphy for 8 Sierra Nevada fan systems in total, with exceptional age control. This novel approach to dating sedimentary surfaces is inexpensive and easily applied in the field, and has the potential to significantly increase the temporal and spatial density of age constraints available for a particular study area.

[†]A version of this chapter has been published as the following paper:

D'Arcy, M., Roda Boluda, D.C., Whittaker, A.C. and Carpineti, A. (2015) Dating alluvial fan surfaces in Owens Valley, California, using weathering fractures in boulders. *Earth Surface Processes and Landforms*, **40**, 487-501.

M.D. conceived of the idea of the investigation. M.D. and D.C.R.B. collected data in the field. M.D. performed the analyses, prepared the figures, and wrote the manuscript. All authors commented on the manuscript, and A.C. checked the statistics and uncertainty calculations.

3.1. Introduction

Precise age models for terrestrial sediments and geomorphic surfaces are in extremely high demand. Spatially- and temporally-detailed chronostratigraphies are crucial for interpreting deposits in landscapes sensitive to time-dependent controls, such as fault evolution and linkage (e.g., Frankel et al., 2007a,b; 2011). The influence of climate change on erosional landscapes is also a subject of considerable debate (e.g., Coelho-Netto, 1999; Castelltort and Van Den Driessche, 2003; D'Arcy and Whittaker, 2014), and a number of recent numerical models have predicted that climate change may be fully or partially captured in the sedimentary record of river and alluvial fan systems (e.g., Simpson and Castelltort, 2012; Allen et al., 2013; Armitage et al., 2013). However, such hypotheses, like others in the geosciences, cannot be tested in the field without detailed depositional age models that offer good stratigraphic resolution in time and space. Although a number of laboratory techniques are now effective tools for estimating bedrock and sediment exposure ages alike, such as optically-stimulated luminescence and cosmogenic radionuclide dating (Burbank and Anderson, 2011; Ivy-Ochs et al., 2013), these remain expensive and time-consuming to use widely, which often limits the density of age constraints reported for a particular study area. Therefore, novel strategies for dating sedimentary surfaces and correlating existing age models would be very useful.

A number of post-depositional processes affect sediments that, in principle, could be used to estimate exposure age if their rates could be measured. Many of these processes are already used to qualitatively distinguish alluvial fan surfaces in the field, for example the formation of dissected 'ridge and ravine' topography, superficial desert varnish on clasts, and the precipitation of soil carbonate content (e.g., Bull, 1991; Kirby et al., 2006; Machette et al., 2008). These methods are commonly used to establish relative chronologies in Plio-Pleistocene sedimentary deposits. Clasts and boulders in desert landscapes are often also dissected by vertical weathering fractures (McFadden et al., 2005; Eppes et al., 2010; Goudie, 2013) (Fig. 1). These meridional fractures are thought to be gradually expanded by erosional processes, including freeze-thaw action and salt shattering (Eppes et al., 2010; Griffiths et al., 2012; Goudie, 2013), and are therefore good candidates for an age calibration.

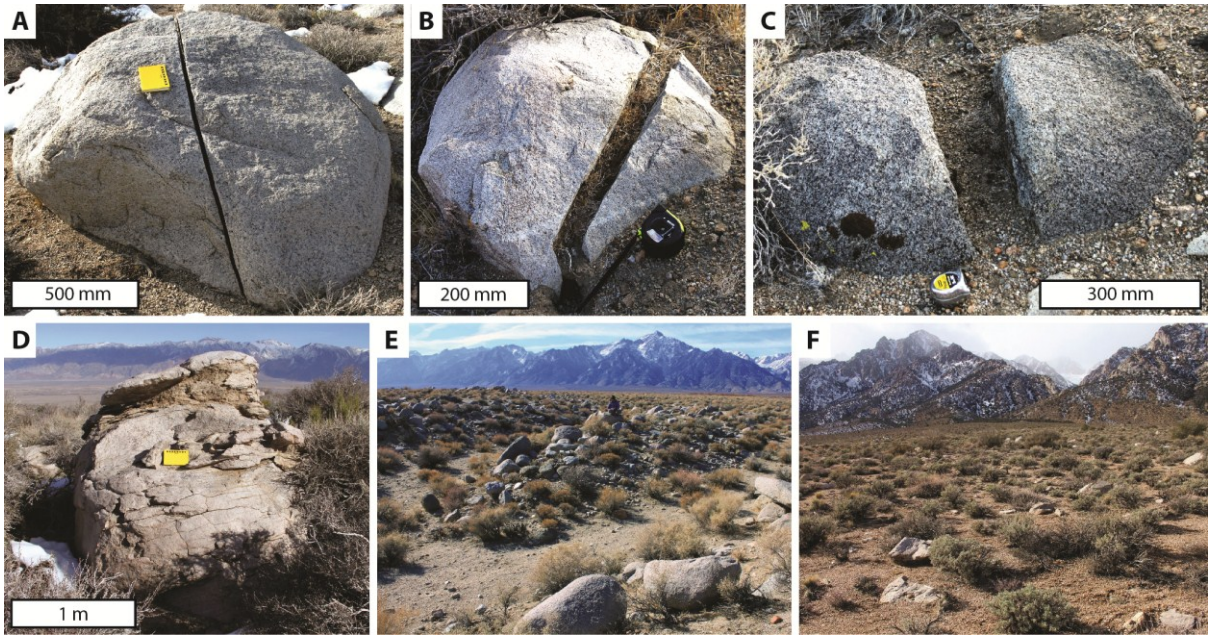

Figure 3.1. Representative examples of granitic boulder fractures and alluvial fan surfaces in Owens Valley. (A) Q3 boulder; younger clasts are less weathered and have narrower fractures. (B) Q2b boulder; weathering of the fracture surfaces causes the fracture to widen. Note the kink in the fracture trace, which prevents the boulder halves being geometrically restored and requires the removal of material within the fracture. (C) Q1 boulder; fractures are wider in older clasts, with smoothed and weathered outer surfaces. (D) Heavily weathered boulder on Q1 surface; superficial exfoliation, cracking and elephant-skin textures allow older units to be easily discriminated in the field. (E) Outcrop photo on Q4; younger surfaces have well-preserved bar-and-swale topography with defined debris flow levees and gravel channels. (F) Outcrop photo on Q1; relief has diffused away and is replaced by flat surfaces and ridge-and-ravine topography. Note the redder surface colouration compared to (E), due to oxidation and desert varnish.

This opportunity for dating is qualitatively illustrated in Fig. 3.1. Here, a relatively young clast (Fig. 3.1a, ~ 20 ka) is compared with an older clast (b, ~ 60 ka) and an even older clast still (c, ~ 140 ka), which between them show striking, macroscopic increases in the widths of weathering fractures that correlate with the ages of the boulders and the degree of surface erosion each has experienced. Such boulder fractures are common and easily identified, and are therefore potentially very useful age indicators. The alluvial fan surfaces on which they are observed can be placed in a relative chronological sequence using traditional approaches to stratigraphic correlation, e.g., older clasts display evidence of exfoliation weathering, 'elephant-skin' textures and cracking (Fig. 3.1d). Younger surfaces have well-defined depositional topography and fresh clast surfaces (Fig. 3.1e), whereas older units lose their relief by diffusion, are abandoned by incisional events, and are discoloured by oxidation and varnishing (Fig. 3.1f). However, the ability to use fully-calibrated, age-sensitive features—such as the widths of clast fractures—offers of the advantage of providing a high density of quantitative age constraints, with which an absolute chronology can be reconstructed.

In this study, we demonstrate that it is possible to use cosmogenic nuclide age constraints to carefully calibrate the rate at which weathering fractures, such as those in Fig. 3.1, are enlarged in boulders exposed on alluvial fan surfaces in Owens Valley, California (Fig. 3.2). We use 9 dated surfaces on 4 fans to produce a detailed age calibration, and we develop a model for the rate of fracture opening in the study area that can be used for dating equivalent local surfaces. We show that the widths of these fractures, which can be easily and inexpensively measured in the field, widen at a measurable rate that is likely governed by time-integrated surface erosion. We demonstrate that the fracture plane erosion rate can be reconciled with the erosion rate on the boulder surface to reduce the uncertainties on the ^{10}Be calibration dates. Furthermore, we show how this approach to dating can be used to estimate the ages of 27 extra fan surfaces neighbouring our calibration sites in Owens Valley, and we are therefore able to present a new, extended age model for 8 fully-dated Sierra Nevada alluvial fans, with strong age control throughout the entire last glacial-interglacial cycle.

3.2. Study area

Owens Valley is one of several grabens in the south-western USA that formed during the extensional break-up of a Miocene-Pliocene plateau (Phillips, 2008). Subsidence in Owens Valley probably accelerated after a westward shift in the main locus of extension 3.0 to 4.0 Ma ago, after which the Sierra Nevada has been uplifted relative to the subsiding valley floor at a rate of up to ~ 1 mm yr^{-1} (Jones et al., 2004; Phillips, 2008; Jayko, 2009; Lee et al., 2009). Geodetic constraints from modern GPS and InSAR data reveal that this tectonic regime is still active today (Hammond et al., 2012), and the uplift rate throughout the recent geological past has been relatively consistent (Zehfuss et al., 2001; Le et al., 2007). Basin sedimentation in response to these long-term tectonic boundary conditions has been largely dominated by Pleistocene to recent alluvial fans, sourced from catchments draining the Sierra Nevada.

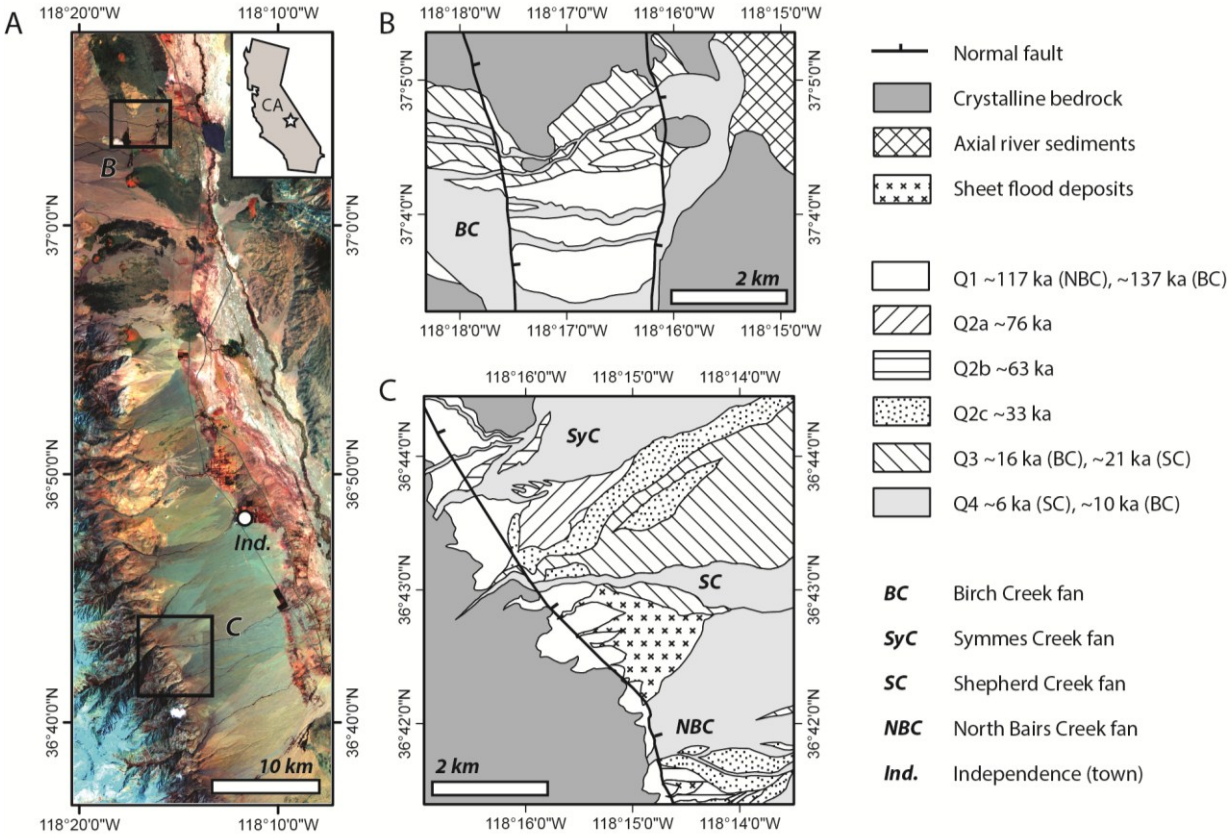

Figure 3.2. (A) Regional Landsat 8 false colour composite image (642 RGB) locating the target alluvial fan surfaces in southern Owens Valley, California. The coalesced debris flow fan complex mantles the eastern front of the Sierra Nevada, with younger sediments appearing bluer in colour. Inset chronostratigraphic maps show details for (B) the Birch creek fan, and (C) the Symmes, Shepherd, and North Bairs creek fans, which have been dated in detail using ^{10}Be cosmogenic nuclides by previous studies (Zehfuss et al., 2001; Dühnforth et al., 2007; Le et al., 2007). Our maps and stratigraphic model reconcile these studies. Coordinates are in the WGS-84 system.

We have targeted 4 different debris flow-dominated alluvial fan systems in Owens Valley, California, which mantle the eastern range front of the southern Sierra Nevada. These sites—the Birch, Symmes, Shepherd, and North Bairs creek fans, Fig. 3.2—have been dated in detail by others using ^{10}Be cosmogenic nuclides, and have a range of depositional fan surfaces dating throughout the last glacial-interglacial cycle (Zehfuss et al., 2001; Dühnforth et al., 2007; Le et al., 2007). The fans form part of a ~ 10 km wide bajada primarily comprising aggrading Pleistocene to recent debris flow deposits with boulders 0.5 to ~ 3 m in diameter. Debris flow sediments account for almost all of the alluvial fans by volume, with a characteristic network of abandoned channels lined with coarse boulder levees, and average surface inclinations of 4 to 6 ° (Whipple and Dunne, 1992). These sediments are exclusively granitic, owing to the uniform bedrock lithology supplying the parent catchments, and form a major part of the valley fill alongside axial river and lacustrine sediments. The alluvial fans have unconfined toes, and some fans are back-filled while others exhibit fan-head trenching (Dühnforth et al., 2008). All show evidence for frequent avulsion events and surface incision that can exceed 60 m. Our maps

focus on the proximal halves of the alluvial fans, where these incision-aggradation relationships are clearest. Minor resurfacing by sheet-floods exported from small frontal catchments has been mapped but not sampled (Fig. 3.2). We focus on 9 extensive debris flow surfaces, which are well dated by cosmogenic studies to the late Pleistocene and the Holocene, and which are covered with large granitic boulders with obvious meridional weathering fractures that dissect the clasts completely (Fig. 3.1).

Today, Owens Valley is a semi-arid basin within the rain shadow of the Sierra Nevada, with annual rainfall rates of 50 to 200 mm yr^{-1} and temperature averaging 14 to 18 °C (2004-2013 records from Independence; NOAA National Climatic Data Center, 2014). During past glacial periods the valley was substantially cooler and wetter, dominated by *Pinyon-Juniper* woodland and pluvial lakes, where today exist sparse desert scrub and dry playas (Phillips, 2008). Climate estimates for the LGM are 5 to 10 °C cooler and 2 to 4 times wetter than at present (Anderson and Wells, 2003; McDonald et al., 2003). The local climate history has been constrained in great detail by a combination of dated lacustrine cores (Benson et al., 1996; Lowenstein et al., 1999) and shorelines (Orme and Orme, 2008), pollen assemblages (Thompson et al., 1999; Woolfenden, 2003), dated glacial moraines (Phillips et al., 2009; Rood et al., 2011), and a range of high resolution geochemical proxies both terrestrial (e.g., oxygen isotope curves; Winograd et al., 1997; 2006; Quade et al., 2003) and marine (e.g., sea surface temperature reconstructions; Yamamoto et al., 2007; Lyle et al., 2010).

Given that this study area has well-dated fan sediments, a very well-constrained tectonic and climatic history and uniform lithological boundary conditions, it is a well-suited location for quantifying post-depositional weathering processes, such as clast fracturing, that operate in typical dryland areas.

3.3. Methods

3.3.1. Stratigraphic model

We mapped the 6 regionally characteristic alluvial fan units (Q1 to Q4) shown in Fig. 3.2 in the field, defining boundaries according to: (i) existing ^{10}Be age constraints (Zehfuss et al., 2001; Dühnforth et al., 2007; Le et al., 2007); (ii) incision-aggradation and cross-cutting relationships; (iii) diagnostic topographic and grain size characteristics (Bull et al., 1991); (iv) superficial clast weathering and varnishing; and (v) high-resolution aerial photographs, elevation data, and Landsat 8 multispectral imagery. Our detailed mapping builds and improves on the work of others (Zehfuss et al., 2001; Dühnforth et al., 2007; Le et al., 2007) and reconciles the differences between the maps of Dühnforth et al. (2007) and Le et al. (2007), who both provide ^{10}Be age constraints for many of the same

surfaces. Therefore, we combined the cosmogenic nuclide data sets reported by these studies and Zehfuss et al. (2001), to achieve the greatest possible density of age constraints in time and space. As these three studies made slightly different assumptions in deriving age estimates from their cosmogenic samples, including best-estimate surface lowering rates, ^{10}Be production rates and scaling schemes, we have re-calculated their age estimates using the CRONUS-Earth cosmogenic age calculator (version 2.2; Balco et al., 2008) with up-to-date age models and consistent parameters. The original studies excluded a small number of anomalous samples from their average surface ages, i.e., due to inheritance, and we have also excluded these outliers in our analysis, leaving a total of 66 individual age estimates across 9 carefully mapped surfaces.

We have assumed a surface lowering rate, e, of 0.5 (+ 0.5, - 0.3) mm ka^{-1}, which is slightly lower than the rates used by Zehfuss et al. (2001), Dühnforth et al. (2007), and Le et al. (2007), but is likely to be more appropriate for surface lowering in this area, in light of new constraints from Owens Valley that have recently been published (Phillips et al., 2009; Rood et al., 2011); we discuss this in section 3.4.2. We have used discrete mean ages to represent the alluvial fan surfaces because they display clear records of abandonment in the field, but we plot error bars on our depositional age estimates that include (i) analytical uncertainties from the original ^{10}Be data; (ii) ± 1 standard deviation, σ, of the age constraints per surface; and (iii) uncertainty arising from the surface lowering rate of 0.2 to 1.0 mm ka^{-1}. We applied the time-constant production rate and scaling scheme of Lal (1991) and Stone (2000), taking density as 2700 kg m^{-3}. Although time-varying production rates have been reported, they vary systematically from that of Lal (1991) and Stone (2000), and have maximum uncertainties smaller than those arising from the factors listed above, so their effects are already represented in our error bars. All of our data are provided as supporting information.

Our maps (Fig. 3.2) update the stratigraphic models reported by previous workers, and we have developed a new surface numbering scheme. This respects regional conventions, can be easily correlated with previous studies (see Table 3.1 for equivalent unit names), and increases in number after a fan incision event, i.e., Q3 incised into Q2, which incised into Q1, etc. We have further divided Q2 into three sub-units a, b, and c, because it spans a comparatively long part of the last glacial period in which there were no incision events, but where older and younger fan surfaces can still be discriminated, consistent with previous workers (Dühnforth et al., 2007; Le et al., 2007). We also mapped a further 27 fan surfaces lacking age constraints from neighbouring fans, which we correlated to the existing stratigraphy (Table 3.1), using the same diagnostic field properties listed above. We discuss these surfaces in section 3.5.3.

Surface	Alluvial fan	Surface age estimates			Fracture width measurements			Equivalent fan units		
		Number of ^{10}Be samples (excluding outliers)	Mean age (ka)	Uncertainty (± ka)	Number of fracture measurements (excluding outliers)	Mean fracture width (mm)	Standard deviation of fracture widths (mm)	*Le et al.* (2007)	*Duhnforth et al.* (2007)	*Zehfuss et al.* (2001)
Q4	Shepherd Creek	8	6.2	3.0	27	4.3	2.2	Qf4	F	-
Q4	Birch Creek	4	9.5	2.1	17	8.7	4.8	-	-	nB
Q3	Birch Creek	13	15.7	1.7	21	18.4	5.7	-	-	nA / nC
Q3	Shepherd Creek	9	20.9	3.7	51	24.1	10.7	Qf3c	E	-
Q2c	Shepherd Creek	10	33.1	4.5	53	28.5	13.6	Qf3a	C / D	-
Q2b	Symmes Creek	3	63.2	6.9	13	48.9	14.4	Qf2b	-	-
Q2a	Shepherd Creek	7	76.3	7.5	23	85.5	39.6	Qf3b	A / B	-
Q1	North Bairs Creek	4	117.3	11.9	7	122.9	27.6	Qf1 / Qf2a	-	-
Q1	Birch Creek	8	137.0	14.5	7	149.1	30.6	-	-	W

Table 3.1. Summary of mean alluvial fan surface ages estimated using ^{10}Be cosmogenic nuclide data reported by Zehfuss et al. (2001), Dühnforth et al. (2007), and Le et al. (2007), and mean fracture width data, W, ± 1 σ. Equivalent fan units from earlier studies are listed.

3.3.2. Sampling

We collected boulder fracture measurements from each dated surface mapped in the field. We sampled only granitic boulders 0.5 to 3.0 m in diameter, dissected completely by vertical (or sub-vertical within 25 °) meridional fractures with planar, parallel faces. These boulder fractures are very common, being observed within the vicinity of almost every field locality we studied. In total we measured 219 fracture widths, averaging 24 per fan surface (Table 3.1). We also collected 274 additional fracture width measurements from 27 un-dated fan surfaces on neighbouring fans, using identical criteria, which we return to later.

We used a tape measure to measure each fracture width to the nearest millimetre in the field, and we recorded any along-strike width variability, from which we calculated the mean width, w, ± 1 standard deviation, σ (complete data set provided as supporting information). Fractures with noticeably variable widths were ignored in the field, i.e., due to disturbances such as boulder movement or plant root growth. However, the typical variability along a single fracture (~ 2 mm) is an order of magnitude smaller than ± 1 σ variation in mean widths on a given surface and is therefore negligible in our analyses. We measured the strike orientation of every fracture to the nearest degree using a compass, because previous studies of desert clast fractures have identified preferential alignments (McFadden et al., 2005) that provide information about the fracture initiation process (Eppes et al., 2010). We did not control for boulder size within our 0.5 – 3.0 m sampling window, nor did we consider small variations in composition or crystal size between the granite boulders, although they typically have crystal sizes between 2 and 8 mm. Representative photos of fractures and surfaces sampled are shown in Fig. 3.1. Some boulders, e.g., Fig. 3.1b, show kinks in the fracture traces that mean the boulder halves cannot be restored back together by simple migration. This requires removal of material from the fracture plane post-deposition. We also observed spalling textures on the fracture planes, and smoothed geometric profiles due to surface erosion within older, heavily weathered clasts (e.g., Fig. 3.1c). These observations suggest that, after fracture initiation, the fracture planes retreat by surface erosion; this has been documented in detail in several nearby deserts in California, Arizona, and New Mexico (McFadden et al., 2005; Eppes et al., 2010; Goudie, 2013).

3.3.3. Data Analysis

For each dated surface, we calculated mean fracture widths, W, ± 1 σ. The standard deviations capture the variation of sampled widths above and below the mean values, which may be attributed to subtle differences in boulder susceptibility to erosion, the precise range of ages of sampled debris flow deposits on a single surface, or transient factors like partial sediment infilling of fractures during their

opening. We occasionally observed anomalously wide or narrow fractures compared to the typical range recorded on a particular fan surface. These outliers may have a number of explanations, such as unidentified disturbance or exposed patches of weathered, older deposits due to incomplete fan re-surfacing. These outliers were obvious, but we eliminated them using Chauvenet's criterion, a standard approach, to ensure statistical significance (Taylor, 1997): Using the mean and standard deviation of all data on a given surface, we predicted the probabilities of measuring each individual width in the data population. This assumes that the data are normally-distributed, which we provide evidence for in our results. Per sample, we then multiplied these probabilities by the total number of measurements on that surface to predict the number of expected occurrences of that width, in that data population. We excluded measurements with expected occurrences below the standard threshold of 0.5 (Taylor, 1997). This approach identified just 14 outliers from the entire calibration data set (6 % of the total data set, 1 to 3 measurements per surface), which had predicted occurrences averaging 0.23, well below the 0.5 sample criterion. Excluding outliers, we calculated new mean widths, W, ± 1 σ. We analysed our data using OriginPro v.8.6, ArcGIS v.10.0, OpenStereo (Grohmann et al., 2011), and DensityPlotter (Vermeesch, 2012).

3.4. Results

3.4.1. Fracture properties

Figure 3.3 displays probability density estimates for all the fracture width measurements (excluding outliers) recorded on fan surfaces with cosmogenic age constraints, where *n* represents the number of fractures measured. These have been generated using *DensityPlotter* (Vermeesch, 2012), a program that estimates probability densities using a kernel density estimation function. This is a useful tool for visualising our fracture data, as it sums Gaussian curves representing each sample, with standard deviations reflecting the local probability density (Vermeesch, 2012). The fracture widths have approximately normal distributions on each surface, and can be represented effectively using mean widths, W, ± 1 standard deviation, σ.

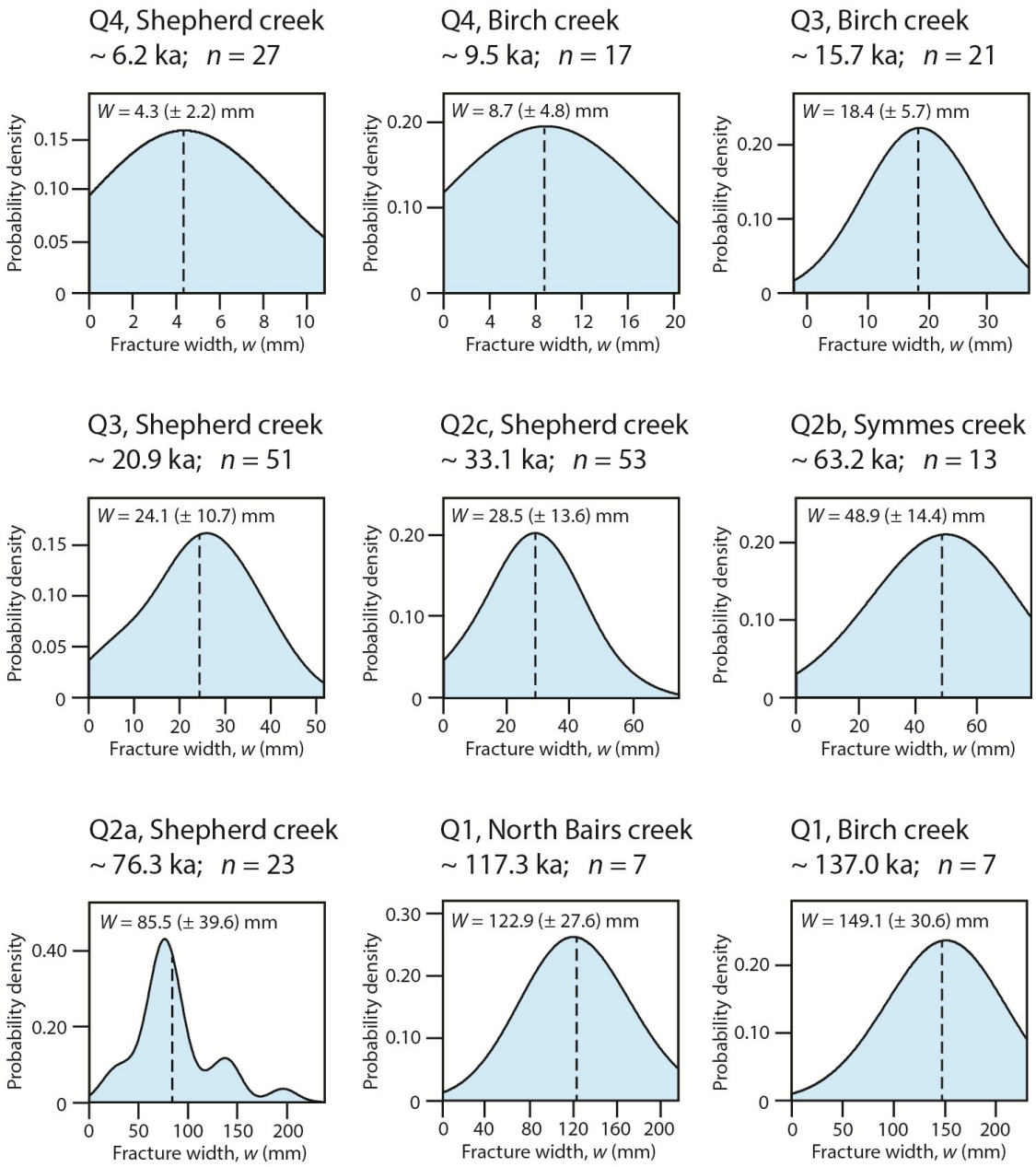

Figure 3.3. Fracture width variations about the mean value, *W* (dashed line), measured on each alluvial fan surface. See Table 3.1 for the stratigraphy. These curves were produced using *DensityPlotter* (Vermeesch, 2012), and *n* gives the number of recorded fractures per surface. In general, the widths are normally-distributed about the means and can be represented effectively using averages.

The azimuths of these fractures are shown as Rose diagrams in Fig. 3.4. We have combined the fracture azimuths measured on surfaces in the Shepherd creek area (Fig. 3.1c, for which we have the greatest spatial density of measurements) according to whether they were deposited under interglacial (Fig. 3.4a, surfaces Q1 and Q4) or glacial (Fig. 3.4b, surfaces Q2 and Q3) climatic conditions. We used a bin increment of 15 °, and have listed the number of azimuthal measurements, *n*, as well as the

circular variance of each data set, V_C, calculated according to Borradaile (2003). Circular variance ranges from 0 (perfect alignment) to 1 (no alignment). Fig. 3.4a shows that while boulder fractures of interglacial ages have initiated with a complete range of orientations, they have a partial alignment along the north-south axis and a V_C of ~ 0.8. Fractures initiated under glacial climates (Fig. 3.4b) show a more random distribution of orientations, which is also supported by a slightly greater circular variance (~ 0.9). This comparison can also be made using a Fisher uniformity plot (Fig. 3.4c), where each fracture azimuth, x_i, is plotted as $x_i/180$ (as the data are axes) against i / (n + 1), where i is the ranking of azimuths from 1 to the total number of data, n. Circular data with uniform distributions should follow the linear regression (in black) with a slope of 1 and intersecting the origin, while systematic deviations from this model indicate non-random preferential alignments (Borradaile, 2003; Eppes et al., 2010). While the glacial data (blue) follows the linear model closely, indicating random orientations, the interglacial data (red) shows a systematic deviation that also supports a partial degree of alignment in accordance with the lower V_C and the north-south bias visible in Fig. 3.4a. We discuss these data in section 3.5.1.

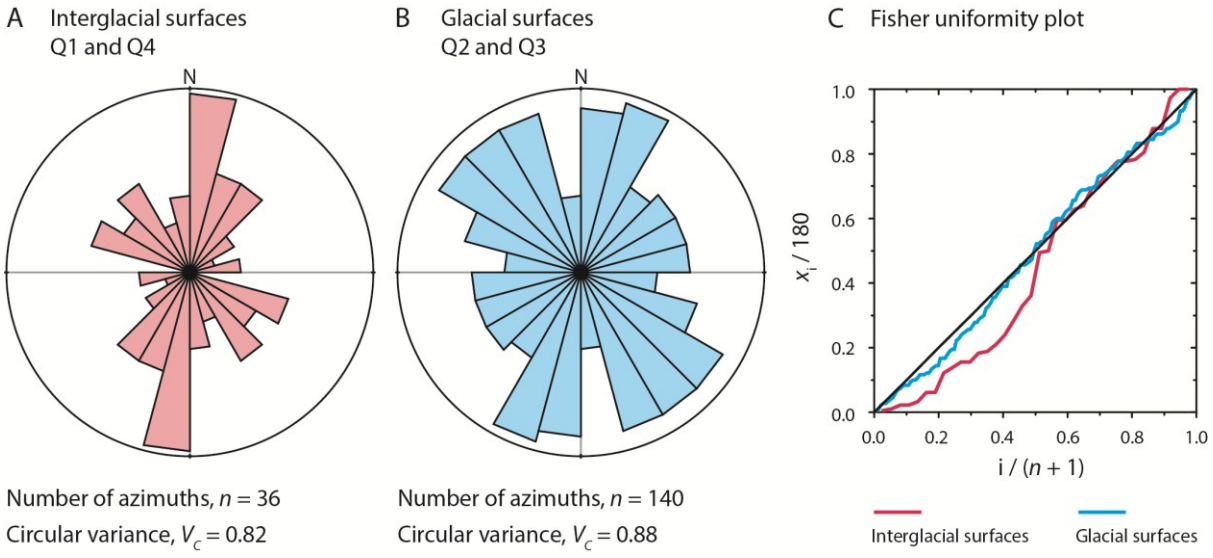

Figure 3.4. Rose diagrams showing the orientations of boulder fractures on (A) surfaces deposited under interglacial climate conditions (Q1 and Q4), and (B) under glacial conditions (Q2 and Q3). The number of fracture azimuths, *n*, and the circular variance of the data sets, V_C, are given below each Rose diagram; see the text for details. The bin increment is 15 ° and the sector length 10 %. Fractures that initiated under interglacial conditions show less variance in their orientations and a stronger north-south alignment than those initiated under glacial conditions. (C) A Fisher uniformity plot for the same data. Uniformly distributed data should plot along the linear black line with a slope of 1.0, which the glacial data set (blue) approximately follows. The interglacial data set (red) systematically deviates from the linear model, indicating a non-uniform azimuthal distribution and a degree of preferential alignment.

3.4.2. Fracture width-age relationship

Fig. 3.5a displays how the mean fracture width, W, (± 1 σ) increases with the mean surface age estimated using ^{10}Be cosmogenic nuclides (Table 3.1; Zehfuss et al., 2001; Dühnforth et al., 2007; Le et al., 2007). We fitted a linear regression that intersects the origin, because it naturally does so within uncertainty, and this simple function describes the relationship between age and fracture width well. In Owens Valley, the average boulder fracture is gradually widened for at least the duration of our records (approximately 140 ka) at a time-averaged rate of 1.05 ± 0.03 mm ka^{-1}. As the fractures have two parallel planes, half of the enlargement rate, 0.52 ± 0.02 mm ka^{-1}, must represent the time-integrated rate at which each boulder surface is retreating, and we denote this as e_f. Although this relationship cannot capture any temporal variability in the rate of fracture enlargement over time, it demonstrates the close correlation between fracture width and surface age.

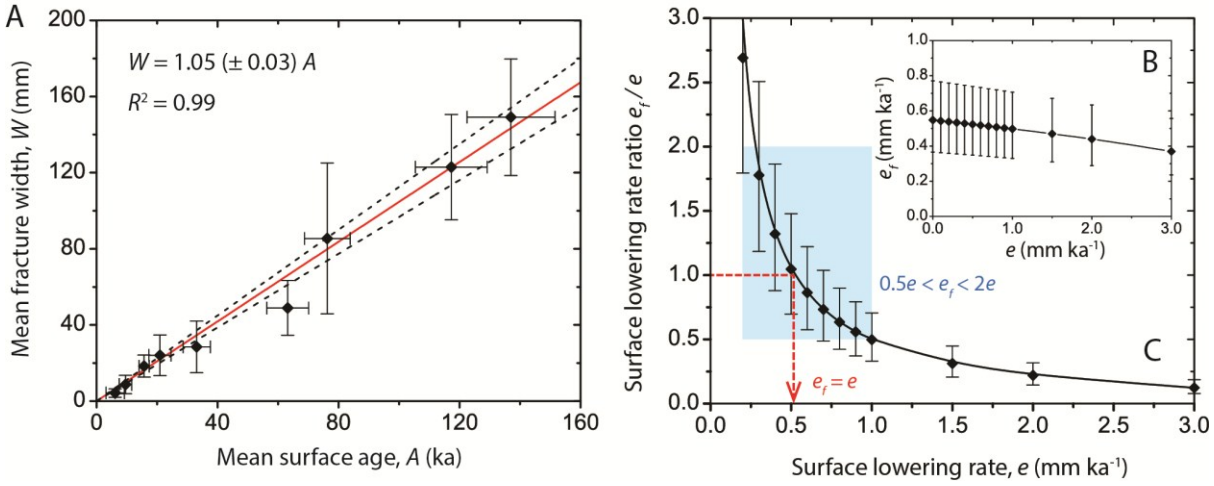

Figure 3.5. (A) The positive, linear correlation between mean fracture width, W (± 1 σ) and alluvial fan surface age in Owens Valley. Age error bars incorporate uncertainty due to the surface lowering rate, ^{10}Be measurement errors, and ± 1 σ. A strong linear regression can be fitted (R^2 = 0.99) that intersects the origin and has a gradient equal to the time-averaged rate of fracture widening. (B) Half of this gradient is equal to the surface lowering rate on one fracture plane, e_f. This is calculated with the surface lowering rate used in the ^{10}Be age calculations, e, allowed to vary between 0 and 3 mm ka^{-1}. Estimates of e_f lie around 0.5 mm ka^{-1} and are relatively insensitive to the assumed surface lowering rate. (C) The ratio e_f / e can therefore be plotted against e. Values of e < 0.2 and > 1 mm ka^{-1} require a large discrepancy between e_f and e. The blue box highlights the range of surface lowering rates that satisfy the assumption $0.5 \cdot e < e_f < 2.0 \cdot e$. The surface lowering rates converge on a best-fit solution of 0.5 mm ka^{-1}, which we therefore apply (+0.5, -0.3) to the age estimates plotted in graph (A).

It is important to note that the ^{10}Be model ages derived from boulder samples taken by previous workers (e.g., Dühnforth et al., 2007; Le et al., 2007), and therefore the derived fracture opening rate, both depend on the assumed surface lowering rate, e, applied in the age calculations above (c.f., Balco

et al., 2008). However, as these fractures are themselves enlarged by surface erosion, for which we have documented field evidence including, (i) spalling textures with minor granular disaggregation; (ii) gradual smoothing of fracture edges (Fig. 3.1c); (iii) kinked fracture paths that cannot be restored in the absence of surface retreat of the fracture plane (Fig. 3.2b); and (iv) no evidence of pivoting or migration of the clast halves about a rotation point, it seems likely that the rate of fracture opening should be correlated with the surface lowering rate. Although shielding effects may cause the erosion rate on the fracture plane, e_f, to deviate slightly from other parts of the boulder surface, e, we argue that these rates must be similar within some physical limits.

Previous workers using cosmogenic age estimates (derived for the same localities at which we have measured clast fractures) have permitted the boulder surface lowering rate to be up to ~ 3 mm ka^{-1} (Small et al., 1997; Zehfuss et al., 2001; Dühnforth et al., 2007). We have calculated the model exposure ages using a range of boulder surface lowering rates between 0 and 3 mm ka^{-1}, and derived e_f from half the slope of a linear regression fitted in each case, i.e., iterations of Fig. 3.5a. The results are shown in Fig. 3.5b. The half fracture opening rate, e_f slowly declines with increasing surface lowering rate, e, varying between 0.6 and 0.4 mm ka^{-1}. This small decline is due to the estimated surface ages increasing slightly with increasing e, with the half-rate e_f declining as a result. The variation in e_f is an order of magnitude smaller than the variation in the assumed surface lowering rate, e.

The trade-off between these two variables is clearly demonstrated in Fig. 3.5c. Here, we plot how the ratio e_f / e changes with e. If the boulder surface lowering rate is slow, the fracture surface must be retreating at a relatively faster rate; i.e., for e = 0.2 mm ka^{-1}, e_f must be a factor of ~ 2.7 times faster, and if e = 0.1 mm ka^{-1} the ratio e_f / e rises to 5.4 (not shown on the graph); in other words, the boulder surface would need to be retreating > 5 times faster on the fracture plane compared to elsewhere on the surface where the ^{10}Be samples were collected. The opposite situation is observed for rapid boulder surface lowering rates. If e = 2.0 to 3.0 mm ka^{-1}, e_f must be a factor of 4.5 to 8.1 times slower than e, respectively. These are time-averaged rates that apply for the entire ~ 140 ka period represented by our data set, including such macroscopic fractures as Fig. 3.1c. As we have no a-priori reason to argue that the boulder fracture surface erosion rate is drastically different from the assumed surface lowering rate for the boulder itself, these extreme values seem physically implausible. The blue box shows the range of surface lowering rates for which $0.5 \cdot e_f < e < 2.0 \cdot e_f$; satisfying the assumption that the lowering rate on the fracture surface ought to be similar to the lowering rate elsewhere on the boulder, taken here to be within a factor of 2. We explore the implications of Figs. 3.5b and 3.5c further in the discussion. However, it can be observed that the two lowering rates converge to value of ~ 0.5 mm ka^{-1}, which is satisfying because it produces a consistent relationship between the surface ages and fracture widths for the same erosion rate. Consequently we have

adopted this rate in our age calculations for Fig. 3.5a, with error bars of +0.5/-0.3 mm ka^{-1}, i.e., satisfying $0.5 \cdot e_f < e < 2.0 \cdot e_f$.

A simple linear regression fits the data in Fig. 3.5a well and can be used as a reliable age calibration. However, any small deviations from this trend may represent small physical changes in the erosion rate e_f. For instance, the data for surfaces Q2c (~ 33 ka) and Q2b (~ 63 ka) show fracture widths that are somewhat smaller than the one might predict from the linear regression. We therefore investigate the hypothesis that the fracture opening rate is not, in detail, constant, and may vary to some extent through time. We have estimated time-varying fracture surface lowering rates using three- and four-point moving gradients, which constrain how the best-fit slope in Fig. 3.5a varies throughout the data population. We have calculated ± 1 standard deviation error bars on these rates, and plotted them against age in Fig. 3.6a. Again, half the gradient is shown as this represents the lowering rate on a single fracture surface, e_f. We have not included two-point moving rates (i.e., simply differencing surface average widths between fan surfaces of successive ages), even though they show very similar results, because (i) it is impossible to assess the accuracy of a line fitted between two adjacent points; (ii) these averages would be derived from widths that are too similar (e.g., the two Q4 points), including some rates within the same stratigraphic unit; and (iii) the averaging 'window' would be highly variable in a 2-point moving average, whereas 3- and 4-point moving averages suffer less from this effect.

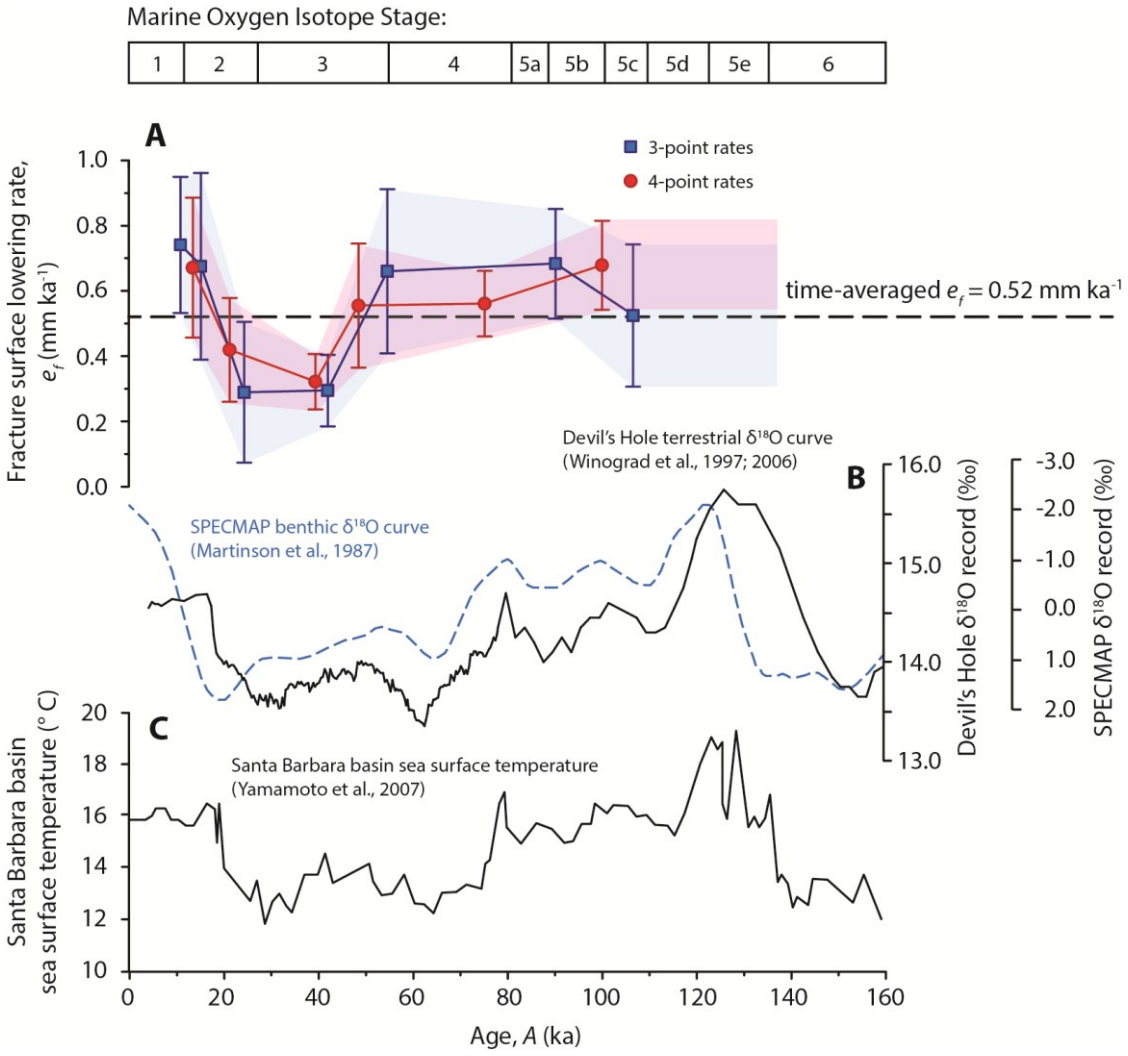

Figure 3.6. (A) Time-varying estimates of the lowering rate on the average fracture surface, e_f, produced using three-point (blue squares) and four-point (red circles) moving gradients fitted to the data in Fig. 3.5a. Error bars show ± 1 σ calculated for these rates (shaded). There is a pronounced decline in e_f to approximately 0.3 mm ka^{-1} between ~ 20 to 50 ka, which later rises to ~ 0.7 mm ka^{-1} in the post-glacial period. No significant fluctuations are observed prior to ~ 50 ka, although the data has a lower temporal density in this period. (B) Palaeoclimate reconstructions from benthic marine (SPECMAP, Martinson et al., 1987) and terrestrial (Devil's Hole, Winograd et al., 1997; 2006) oxygen isotope records, and also (C) a sea surface temperature reconstruction for the Santa Barbara basin (Yamamoto et al., 2007). The fracture surface lowering rates in (A) correlate with these palaeoclimate proxies, with e_f suppressed during the cooler and wetter late glacial period, and increasing in concert with warming and drying of the climate in the post-glacial period.

Three- and four-point rate deconstructions produce very similar patterns through time. There is a statistically significant decline in e_f to 0.2 – 0.4 mm ka^{-1} between ~ 20 and 45 ka, after which e_f increases by a factor of ~ 2.5 to approximately 0.7 mm ka^{-1} in the post-glacial period. Prior to ~ 45 ka, e_f approaches the time-averaged rate and no significant variations are detected within the uncertainty of this approach. Of course, these points are averages, even though we have placed them at the central

age in each case. Therefore, as with any moving average data, this gives a first-order impression of how fracture surface retreat rates have changed through time. These estimates are compared with local palaeoclimate proxies (Figs. 3.6b and c) including the SPECMAP (benthic marine) and Devil's Hole (terrestrial) oxygen isotope records (Martinson et al., 1987; Winograd et al., 1997; 2006) and a sea surface temperature reconstruction from the Santa Barbara basin (Yamamoto et al., 2007). See section 3.2 for a palaeoclimate summary.

3.5. Discussion

3.5.1. Fracture initiation and enlargement

As shown in Fig. 3.4, the azimuths of Q1 and Q4 fractures tend to have partially non-random distributions. Previous studies of clast fractures have documented very similar observations of partial north-south alignment in comparatively arid landscapes (McFadden et al., 2005; Adelsberger and Smith, 2009; Eppes et al., 2010). Although the mechanical process responsible for this alignment remains the subject of debate (Griffiths et al., 2012; Goudie, 2013), one suggestion is that some fractures are initiated by east-west tensile stresses produced by diurnal thermal gradients within the clasts, arising from directional insolation and solar heating (McFadden et al., 2005). This may induce microscopic cracks that propagate and are subsequently weathered, and numerical simulations have shown that this mechanism could produce fracture orientations consistent with field data such as ours (Moores et al., 2008; Molaro and Byrne, 2012).

The Q1 and Q4 surfaces date to the previous and present interglacial periods, with arid conditions and strong daily temperature gradients in Owens Valley (c.f., Woolfenden, 2003; Phillips, 2008). During these periods, this mechanism of thermal stress cracking may have initiated some (but not all) of the fractures we document, offering an explanation for the partial alignment. In contrast, Q2 and Q3 surfaces date to the last glacial period, which was significantly wetter and cooler, with regional pluvial lakes and juniper woodland instead of desert scrub (Phillips, 2008). Fractures that initiated during the glacial period display more random orientations with greater circular variance V_C, and this may reflect the diminished effects of thermal stresses on fracture initiation under a cooler climate. Instead, we expect that multi-directional processes like freeze-thaw cracking contributed more to the formation of fractures during glacial periods. The goal of our study is not to constrain the precise mechanism by which these fractures initiated, but we include this large azimuthal data set because it provides new information about how the alignments of through-going meridional clast fractures vary to some degree with past climate. More research is clearly needed to further our understanding of this phenomenon (c.f., Eppes et al., 2010; Goudie, 2013).

The approximately normal distributions of fracture widths about the surface mean values (Fig. 3.3), and the intersection of the width-age relationship with the origin (Fig. 3.5), together indicate that most fractures initiate early on after deposition, with few continuing to initiate during continued exposure. If the fractures continued to initiate throughout the subsequent exposure period, we would not expect a normal distribution about a peak width that increases with exposure age. Instead, we would expect a wider range, biased towards narrower (younger) widths on each surface similarly, with a much shorter old tail. We propose that after initiation, the fractures are gradually enlarged by surface erosion of the granitic boulders, as opposed to physical movement of the detached boulder halves. Migration does not explain the sensitive relationship between exposure age and fracture width (Fig. 3.5a), because (i) we did not observe fractures with vertical components of rotation or evidence of pivoting; (ii) it is very unlikely that migration would preserve parallel fracture planes, or occur at the same rate for hundreds of different boulders of variable size; (iii) some fracture traces have marked kinks (e.g. Fig. 3.1c), which show geometrically that the two boulder halves cannot be restored without the removal of material; and (iv) surface weathering is evident from the shapes and textures of older boulders (Fig. 3.1c, d) and is therefore expected to enlarge existing fractures, giving the slight smoothing of the edges shown clearly in Fig. 3.1c. In the field, we observed that most material is eroded from the boulders by spalling, with some granular disaggregation. None of the surfaces we sampled have been buried in the past, because they were abandoned by fan incision and avulsion, and are therefore preserved as terraces that have been continuously exposed. A small number of fractures had a partial gravel infill at the base, transported from the adjacent surface, and if this has an effect on the widening rate then it may contribute to the $\pm$ 1 σ error bars on the mean fracture width measurements.

3.5.2. Surface lowering rates

As we explain above, exposure age estimates using cosmogenic nuclides are sensitive to the assumed boulder surface lowering rate, *e,* used in the calculation (Balco et al., 2008). Previous workers have calculated ages using erosion rates up to ~ 3 mm ka^{-1} (e.g., Zehfuss et al., 2001; Dühnforth et al., 2007; Le et al., 2007), in light of a study by Small et al. (1997), who reported ^{10}Be and ^{26}Al erosion rate estimates from bedrock exposures at the Sierra Nevada summits. However, the alluvial fan surfaces in Owens Valley occupy a significant rain shadow, lying at lower elevations in considerably drier conditions. Therefore, constraints from the range summits are likely to overestimate the actual surface erosion rate at the floor of Owens Valley. Also, constraints from bedrock exposures are normally faster than the erosion rates on boulder surfaces, because they are usually more weathered and susceptible to accelerated erosion (Phillips et al., 2009): Granitic inselbergs exposed in Owens Valley are eroding up to ~ 5 mm ka^{-1} (Nichols et al., 2006), compared to boulder surfaces eroding less

than 1 mm ka^{-1} very nearby (Bierman and Gillespie, 1991). In light of these effects, Phillips et al. (2009) suggest that surface erosion rates of granitic boulders in the Owens Valley area are most likely up to 1.1 mm ka^{-1}, and probably less than 0.7 mm ka^{-1} since the last glaciation. Similarly, Rood et al. (2011) report a preferred surface erosion rate of 0.6 mm ka^{-1} for granitic boulders exposed in Owens Valley moraines.

It is essential to understand and address these discrepancies, because if the surface erosion rate applied in ^{10}Be age calculations is too high, it yields model ages that are too old and have misleadingly large error bars. The recent constraints provided by Phillips et al. (2009) and Rood et al. (2011) indicate that the $\leq$ 3 mm ka^{-1} erosion rates derived from bedrock summits by Small et al. (1997) are in fact too high, and should not be used in ^{10}Be age calculations for alluvial fan surfaces in Owens Valley as previous workers have done (e.g., Dühnforth et al., 2007; Le et al., 2007). Our data offers a unique opportunity to improve the constraints on boulder erosion rates on the Owens Valley fan surfaces. If it is accepted that the observed fractures are enlarged by surface weathering, then it is reasonable to expect e_f and e to have similar values. As shown by Fig. 3.5b, the fracture opening half rate, e_f averages ~ 0.5 mm ka^{-1} and is relatively insensitive to the surface lowering rate, e, assumed in the age calculations. While some shielding effects could plausibly mean the weathering rate within a fracture is different to the rate on the rest of the boulder surface (e.g., increased ice or salt retention, reduced exposure), the strong linear correlation observed in Fig. 3.5a suggests that these effects quickly become negligible as the fractures widen. The measured rate of e_f ~ 0.5 mm ka^{-1} is time-averaged, and so applies to fully-exposed fracture surfaces even at macroscopic widths of > 10 cm (e.g. Fig. 3.1c). As shown by Fig. 3.5c, adopting surface lowering rates of 2 and 3 mm ka^{-1} requires the fracture surfaces to be weathering substantially more slowly, by factors of ~ 4.5 and ~ 8.1 times respectively. This discrepancy is unreasonably large, and incompatible with our field observations, the macroscopic dimensions of the fractures, and their open exposures to weathering processes (Fig. 3.1c).

The rates e and e_f can thus be reconciled, and converge at a value of 0.5 mm ka^{-1} (Fig. 3.5c). Within error, this is equal to best estimates of erosion rates on granitic boulders in Owens Valley reported by recent studies (Phillips et al., 2009; Rood et al., 2011). We propose the conservative assumption that $0.5 \cdot e_f < e < 2.0 \cdot e_f$, and thereby estimate a preferred surface lowering rate of 0.5 mm ka^{-1} with uncertainty from 0.2 to 1.0 mm ka^{-1}. This still allows e_f to vary between half and double the rate e, encompassing various uncertainties, but also accommodating shielding effects that may influence e_f early on when the fractures are narrow.

We also observe that while ~ 0.5 mm ka^{-1} is a suitable time-averaged erosion rate for the past ~ 140 ka, in detail our data do indicate slight fluctuations during the last glacial-interglacial cycle (Fig. 3.6). The observed decline in e_f from ~ 0.7 mm ka^{-1} at approximately 10 ka, to ~ 0.3 mm ka^{-1} at the last

glacial maximum, indicates that the fracture surface erosion rate was suppressed during the cooler, wetter glacial climate (Phillips, 2008). This may reflect changes in the mechanical processes eroding the boulder surfaces, e.g., slowed chemical weathering due to cooler temperatures (Dixon et al., 2009), diminished salt shattering due to pluvial lakes acting as salt reservoirs (Benson et al., 1996), increased snow cover shielding the boulder surfaces seasonally (Benedict, 1993), or even reduced wildfire frequency (Bierman and Gillespie, 1991). These hypotheses are currently speculative, but the e_f fluctuations are consistent with regional palaeoclimate proxies, both marine and terrestrial (Fig. 3.6b and c). We note that these rate variations are short-lived and small in magnitude, and as the linear age calibration models the data extremely well (Fig. 3.5a), we have not incorporated this temporal variability into our age calibration.

3.5.3. Application to dating sedimentary surfaces

The very strong correlation between the mean widths of boulder weathering fractures and surface age (Fig. 3.5a) offers a unique opportunity for dating sedimentary and geomorphic surfaces. Our age calibration introduces a robust relationship between fracture width and age, representing 219 individual samples, and giving a time-integrated rate of fracture widening of 1.05 ± 0.03 mm ka^{-1}, half of which represents the surface lowering rate on a single fracture surface, e_f. A time-constant age model (Fig. 3.5a) can therefore be expressed as:

$$A = \frac{W}{2 \cdot e_f} \qquad [3.1]$$

where A is the estimated surface age (ka); W is the mean fracture width (mm), and e_f is well-constrained to 0.52 ± 0.02 mm ka^{-1}. We recommend using ± 1 σ on W to calculate uncertainty on the age estimate.

Our age calibration is accurate for at least 140 ka in the Owens Valley study area. It is likely that weathering fractures continue to widen until the clasts are destroyed, or the fracture form becomes unrecognisable. In this scenario, the upper age limit of our dating approach would be set by the balance between erosion rate and the ratio of fracture width to clast diameter. It is also important to note that we have measured a minimum number of fractures per surface in order to converge on accurate mean values. As guidance, our calibration surfaces are defined by no fewer than 7, and on average 24, samples. We recommend that fracture widths are only used to estimate surface age if ≥ 4 repeat measurements with similar values are recorded, or a Gaussian distribution can be approximated as shown in Fig. 3.3, particularly because standard deviation is required to estimate uncertainty.

There are clear advantages of using mean fracture widths for estimating surface ages, as the age relationship is, (i) highly sensitive; (ii) applicable for at least 140 ka, (iii) easily, quickly and inexpensively applied; and (iv) can be used during a field campaign. As our calibration data are distributed across 9 surfaces on 4 different fans up to 40 km apart (Fig. 3.2), this trend is spatially-consistent and can be applied in Owens Valley (below), and potentially in other semi-arid settings with equivalent conditions.

We apply equation 3.1 to a total of 274 fracture width measurements from 18 additional Q1 to Q4 fan surfaces in Owen's Valley. These surfaces lie on the Independence, Pinyon, north and south Bairs, and George creek alluvial fans (Fig. 7), which sit directly north and south of the calibration sites, and also have exclusively granitic boulders exposed on debris flow surfaces. Using the same methodology as outlined above, we measured the mean widths, $W \pm 1\ \sigma$, of all boulder fractures observed on these surfaces. These data are included in Table 3.2 (full data set available in the supporting information).

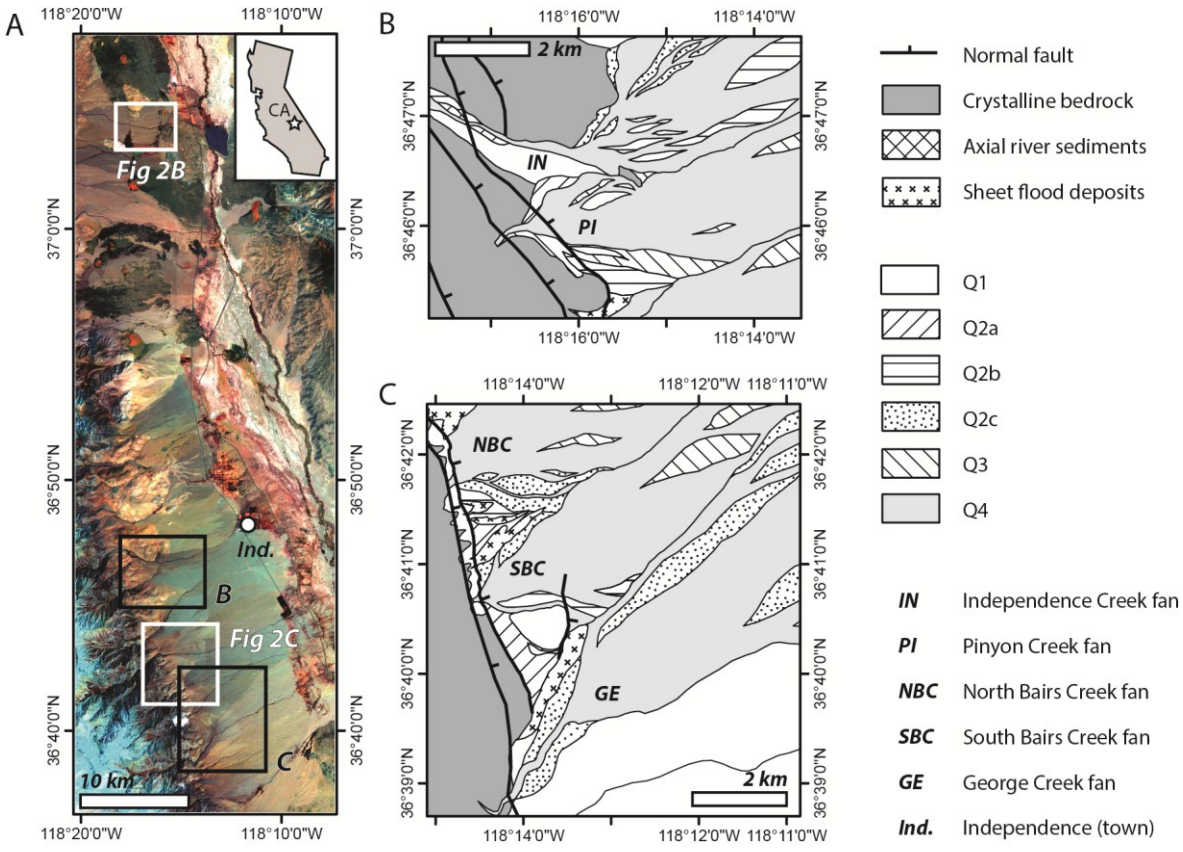

Figure 3.7. (A) Regional Landsat 8 false colour composite (642 RGB) locating alluvial fan surfaces directly north and south of our calibration sites (Fig. 3.2, shown in white boxes). Inset maps show fan surfaces mapped in the field on the Independence, Pinyon (B), north Bairs, south Bairs, and George creek (C) alluvial fans. These were correlated with the stratigraphy shown in Table 3.1 and Fig. 3.2 using the diagnostic criteria outlined in section 3.3. We have collected fracture width measurements on these surfaces with which their ages can be estimated.

Alluvial fan	Surface	Dating method	No. samples	Mean fracture width (mm)	Width uncertainty (± mm)	Estimated age (ka)	Age uncertainty (± ka)
Birch Creek	Q4	^{10}Be nuclides	4	-	-	9.5	2.1
	Q3	^{10}Be nuclides	13	-	-	15.7	1.7
	Q1	^{10}Be nuclides	8	-	-	137.0	14.5
Independence Creek	Q4	Fractures	16	16	4	14.6	4.6
	Q2c	Fractures	21	35	9	45.0	10.4
	Q2b	Fractures	23	61	17	65.6	13.9
	Q2a	Fractures	18	89	10	88.3	7.4
	Q1	Fractures	13	105	24	101.6	18.1
Pinyon Creek	Q4	Fractures	12	9	3	8.4	3.4
	Q3	Fractures	8	23	4	23.7	4.3
	Q2b	Fractures	21	47	12	54.4	12.0
	Q2a	Fractures	15	77	11	78.6	8.1
	Q1	Fractures	4	124	23	117.1	17.3
Symmes Creek	Q4	^{10}Be nuclides	9	-	-	4.4	1.6
	Q2b	^{10}Be nuclides	3	-	-	63.2	6.9
	Q2a	Correlation	-	-	-	81.1	14.6
	Q1	Correlation	-	-	-	116.4	35.1
Shepherd Creek	Q4	^{10}Be nuclides	8	-	-	6.2	3.0
	Q3	^{10}Be nuclides	9	-	-	20.9	3.7
	Q2c	^{10}Be nuclides	10	-	-	33.1	4.5
	Q2a	^{10}Be nuclides	7	-	-	76.3	7.5
	Q1	Correlation	-	-	-	116.4	35.1
North Bairs Creek	Q4	Fractures	45	8	5	7.5	5.7
	Q3	Correlation	-	-	-	20.1	7.9
	Q2c	Fractures	11	32	8	40.7	9.4
	Q2b	Correlation	-	-	-	63.1	20.8
	Q1	^{10}Be nuclides	4	-	-	117.3	11.9
South Bairs Creek	Q4	Fractures	10	7	2	6.2	2.4
	Q3	Correlation	-	-	-	20.1	7.9
	Q2c	Fractures	10	33	12	41.8	13.5
	Q2b	Fractures	12	65	14	69.5	11.2
	Q2a	Correlation	-	-	-	81.1	14.6
	Q1	Correlation	-	-	-	116.4	35.1
George Creek	Q4	Fractures	7	14	5	13.3	5.1
	Q2c	Fractures	17	32	12	39.3	13.2
	Q1	Fractures	11	114	20	108.9	14.9

Table 3.2. Complete stratigraphic summary for all 8 alluvial fans studied in Owens Valley, California, including mean fracture width data, W, ± 1 σ, on the additional fan surfaces mapped in Fig. 3.7. See text for data sources.

Note: These surface ages have been estimated using the linear age calibration from Fig. 3.5a. Correlated surfaces were assigned units in the field according to their diagnostic sedimentary properties and stratigraphic relationships. They have been given mean ages for each unit as dated on all other fans, with error bars between the youngest and oldest possible occurrences on any other fan.

Because these fracture width measurements are from un-dated alluvial fan surfaces neighbouring our calibration sites (Table 3.2), they can be used to extend our chronostratigraphic models to these alluvial fans. None of the mean widths exceed the calibration range, so our age model is appropriate. We carefully mapped exposed fan surfaces on the Independence, Pinyon, North Bairs, South Bairs, and George creek fans (Fig. 3.7). In the field, we correlated the fan surfaces in Fig. 3.7, prior to estimating their ages, with the dated units from Fig. 3.2 by comparing stratigraphic and cross-cutting relationships, superficial clast weathering, grain size and desert varnishing properties, the gradual loss of depositional morphology (Fig. 3.1e and f), fault scarp heights, and clear incision-aggradation cycles observed on the fans. This qualitative approach to mapping has been traditionally used by other workers (e.g., Le et al., 2007), and fracture-derived age estimates from these surfaces should support these field correlations. Therefore, as well as improving the coverage of the existing stratigraphic models, this serves as in important test of our dating technique.

In Fig. 3.8a-e, we estimate the ages of the undated fan surfaces mapped in Fig. 3.7, using mean fracture widths. The alternating white and grey boxes show the periods of activity for each of the units Q1 to Q4 as defined by the ^{10}Be calibration data discussed earlier. We have estimated the surface ages by fitting the mean fracture widths, W, to the calibration regression from Fig. 3.5a, with error bars showing $\pm$ 1 σ on W. Each point is labelled with the fan unit we qualitatively correlated to in the field. In every case, the age estimates derived from $W \pm 1\ \sigma$ agree well, within error, with both our field observations and the ^{10}Be ages of correlated surfaces from Fig. 3.2. This is very encouraging, and demonstrates that our age calibration of weathering fractures can be used to quantify a relative stratigraphic model devised in the field, providing absolute age estimates that conform to the stratigraphic framework in place. In this respect, our mapping strategy has been the same as previous workers (e.g., Le et al., 2007), but the application of the fracture width-surface age calibration has supplemented this approach with quantitative age control. By adding another 18 dated surfaces to the existing 9 with cosmogenic nuclide data, this also highlights the potential for substantially increasing our understanding of the timing and locus of deposition on fans in the Owens Valley area. These additional data are compiled in Fig. 3.8f. The boundaries of units Q1 to Q4 satisfy both the calibration data and the new age estimates from neighbouring correlated surfaces. Figure 3.8f illustrates that, together, these coalesced fans have experienced continual deposition through time.

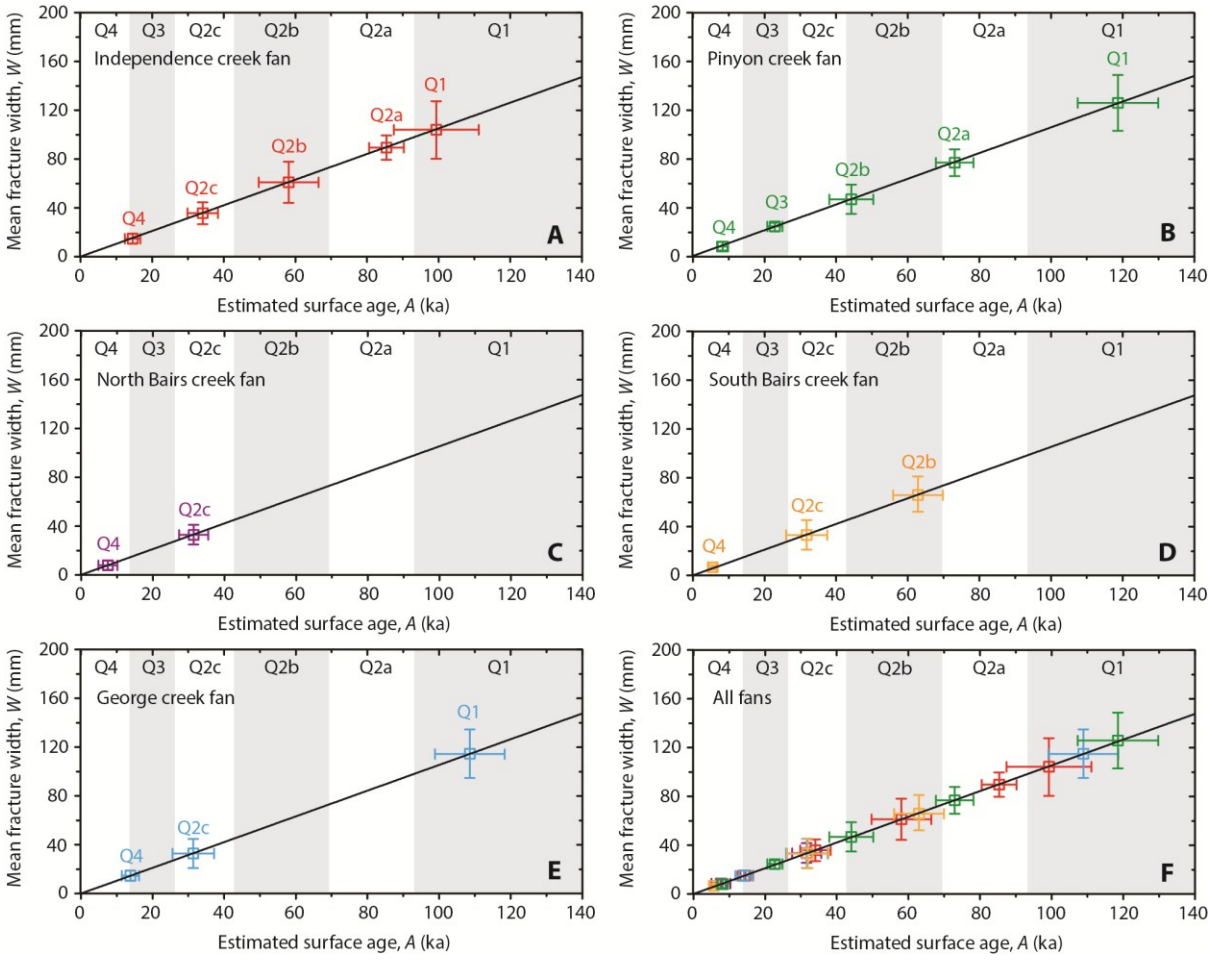

Figure 3.8. Mean fracture width measurements (± 1 σ) recorded on the fan surfaces shown in Fig. 3.7, fitted to the age calibration derived in Fig. 3.5a. (A) Independence creek fan; (B) Pinyon creek fan; (C) north Bairs creek fan; (D) south Bairs creek fan; and (E) George creek fan. Alternating white and grey boxes show the periods of activity on the Q1 to Q4 fan units, as defined by the calibration surfaces from Fig. 3.2. Each mean width is labelled with the correlated unit assigned in the field, on the basis of diagnostic criteria listed in section 3.5.3. Within error, all of the age estimates derived from mean fracture widths agree with the correlated surfaces, indicating that this is a successful approach to estimating quantitative surface ages in an otherwise qualitative stratigraphy. (F) Composite plot of all the data, showing the temporal density of age constraints that can be achieved using this approach.

In total, we can present revised/new stratigraphies for a total of 36 mapped surfaces on 8 large alluvial fan systems in Owens Valley, which we summarise in Fig. 3.9. This includes correlated surfaces (in orange), for which we did not observe a sufficient number of fractures to estimate the age numerically. For example, we observed 1 fracture 63 mm wide on the Q2b surface of north Bairs creek, and 2 fractures 103 and 122 mm wide on the Q1 surface of south Bairs creek. We decided against using single or double measurements to estimate surface ages, but had we done so we note that these observations would still support our field correlations. Instead, we have assigned each correlated surface mean ages for that unit as dated on all the other fans, with maximum error bars

between the youngest and oldest occurrences on any fan. On all surfaces, the error bars encompass the actual time-spans of physical activity as well as uncertainty. Importantly, we have also extended all Q4 surfaces to 0 ka. These are the youngest surfaces, on which we also observed evidence for modern debris flow activity. As young deposits could exhibit no weathering fractures at all, it is unreasonable to derive minimum ages for Q4 fan surfaces.

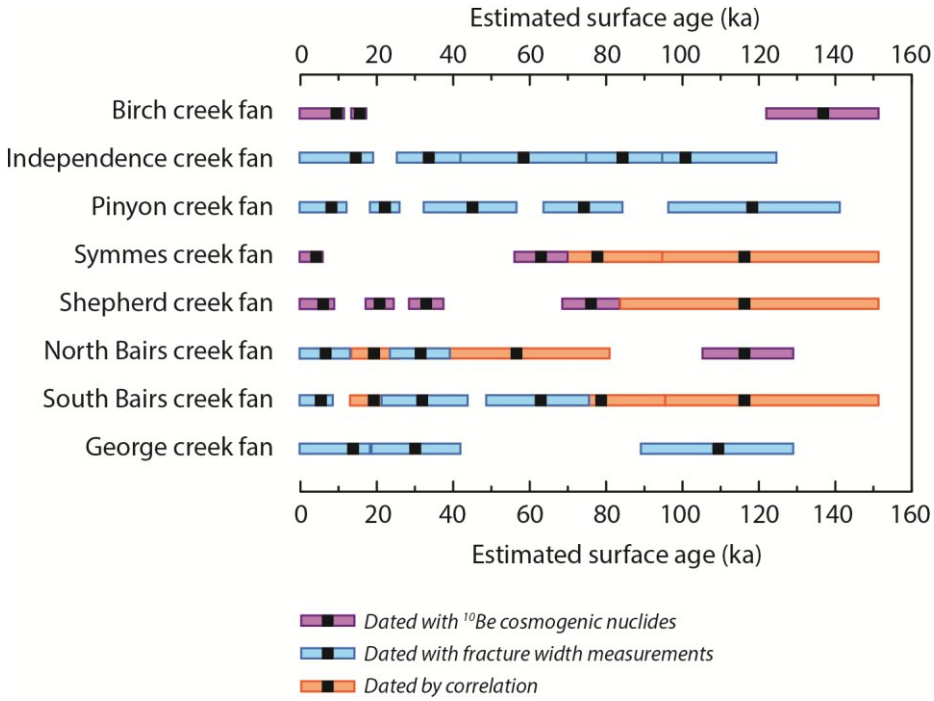

Figure 3.9. Summary stratigraphy of the 8 Owens Valley alluvial fans analysed in this study. Black squares show the best age estimates for mapped fan surfaces (Figs. 3.1 and 3.7), with error bars shown as coloured boxes. Incorporating uncertainties, these error bars additionally capture the time periods of activity on these fan surfaces. Coloured purple are the calibration surfaces dated using the ^{10}Be cosmogenic data reported by previous studies (Zehfuss et al., 2001; Dühnforth et al., 2007; Le et al., 2007). Blue shows the new surface ages estimated in this study using fracture width measurements (Fig. 3.8), and orange shows age estimates for the remaining surfaces correlated in the field. Correlations have error bars between the youngest and maximum uncertainties for each unit, observed across all of the dated occurrences on the other fans. Taken together, these fans preserve a detailed depositional record throughout the last glacial-interglacial cycle.

This chronostratigraphy establishes the Owens Valley fans as exceptionally well-dated sites for alluvial fan research. The field sites studied here are now fully mapped, have unprecedented age control, and as shown by Fig. 3.9, they preserve a combined record of practically continuous deposition spanning the entire last glacial-interglacial cycle.

3.5.4. Future research opportunities

These data clearly raise the prospect of this work being applied elsewhere. Our age calibration of fracture widths should only be applied to granitic boulder clasts with equivalent properties to those we document, in the Owens Valley area (Fig. 3.2). Future research could explore how the rates of fracture enlargement vary in clasts with different lithological properties. Our analysis also indicates that the fractures widen by surface erosion, and so the rate constant e_f required in age calculations may also reconcile with independent constraints on boulder surface erosion rates elsewhere. This would be extremely advantageous for dating applications, and should be tested further. Our analysis also indicates that the surface lowering rate may subtly record past climatic changes (Fig. 3.6), and future research should attempt to reconcile e_f and e in different climates, and measure the sensitivities of these rates to spatial and temporal climatic gradients. Weathering fractures similar to those in Owens Valley have been documented in various deserts across North America, Asia, Australia, and Africa (McFadden et al., 2005; Adelsberger and Smith, 2009; Eppes et al., 2010; Goudie, 2013). Weathering is a universal process affecting clasts exposed in many different landscapes. Although the erosion rates, and therefore the age calibrations, will surely vary geographically, we argue that the fundamental principle of our approach to sediment dating could be applied in a diversity of settings. Further research is encouraged to test this and derive appropriate age models.

3.6. Conclusions

Our analysis makes use of detailed ^{10}Be cosmogenic nuclide age models established on four alluvial fan systems in Owens Valley, California, to measure the rate at which weathering fractures are enlarged in granitic surface boulders. We demonstrate that these fractures widen at a time-integrated rate of 1.05 ± 0.03 mm ka^{-1} for the last 140 ka, making them ideal chronometers for estimating surface ages.

These fractures are weathering products, with a time-averaged surface lowering rate of ~ 0.5 mm ka^{-1} that is largely insensitive to the assumed surface lowering rate applied in cosmogenic age calculations. This insensitivity allows us to reconcile cosmogenic estimates of age and surface erosion rate, to place tighter constraints on both at this location. Matching our measured fracture surface lowering rate, e_f, with the assumed surface lowering rate, e, gives a best-estimate solution of ~ 0.5 mm ka^{-1}. This precisely agrees with independent estimates of granitic boulder erosion rate in Owens Valley (Phillips et al., 2009; Rood et al, 2011), and by placing physical limits on the ratio e_f / e, we are able to reduce the uncertainty on this rate.

The strong relationship between fracture widths and alluvial fan surface ages make these fractures ideal chronometers for dating surfaces up to ~ 140 ka in this area. Using a linear calibration, we report new age estimates for alluvial fan surfaces neighbouring our original study sites, substantially extending the mapped stratigraphy to include 36 surfaces on 8 alluvial fan systems in total, fully-dated in temporal and spatial detail throughout the entire last glacial-interglacial cycle.

4. Glacial-interglacial climate changes recorded by debris flow fan deposits, Eastern Sierra Nevada, California†

Chapter Abstract

It is hotly debated whether climate changes are recorded in terrestrial stratigraphy. Theoretical considerations suggest that small, volumetrically-closed, simple sediment routing systems, like mountain catchments and alluvial fans, might preserve a record of past climate fluctuations in their sedimentology. However, to-date few high-resolution field data sets have been produced to test current hypotheses. In particular, uncertainties remain about the sensitivity and response time of the landscape, the amplitude of climate signals recorded in stratigraphy, and the physical mechanisms by which changes in rainfall, temperature, glaciation and other expressions of climate actually translate into a physical signal in basin sediments. Here, we take a grain size approach to characterising 35 different debris flow fan surfaces in Owens Valley, California, which have been deposited from eroding granite catchments in the eastern Sierra Nevada during the last 125 ka. We find that when tectonic and lithological boundary conditions are constant, glacial-interglacial climate changes are captured as a high-resolution record in the grain size distribution of ancient debris flows. In the glacial climate, smaller debris flows exported finer-grained sediment, and these flows have become measurably coarser-grained as the climate warmed and dried overall into the Holocene. We explore the mechanisms that might explain this signal, and we demonstrate that changing sediment sources in the parent catchments, including the effects of glaciation, moraine erosion and paraglacial sediment supply, cannot explain the majority of the grain size variability through time. Instead, the strong exponential correlation between warming sea surface temperatures and coarsening grain size leads us to conclude that these debris flow fan deposits contain a high-resolution record of past storm rainfall intensity and surface runoff rates.

---

†A version of this chapter is in preparation for submission to *Basin Research*, to be authored by **D'Arcy, M.**, Roda Boluda, D.C., and Whittaker, A.C. M.D. planned the data collection, conducted the analyses, prepared the figures and wrote the manuscript. All authors collected data in the field. A.C.W. and D.C.R.B. commented on the manuscript.

4.1. Introduction

Constraining the sensitivity of eroding landscapes and their resultant sediment routing systems to climatic forcing is a key challenge for geoscientists (Molnar & England, 1990; Blum & Törnqvist, 2000; Castelltort & Van Den Driessche, 2003; Allen, 2008; Champagnac et al., 2012, 2014; D'Arcy and Whittaker, 2014; Herman et al., 2014). In particular, a major question is whether and in what circumstances sedimentary signals of past climate changes are preserved in terrestrial stratigraphic records with high fidelity (Blum & Törnqvist, 2000; Allen, 2008; Whittaker, 2012; Armitage et al., 2013; Foreman 2014). Over long (10^6 to 10^7 year) timescales, climate change has had a profound impact on erosion and sedimentation on the Earth's surface; the onset of Plio-Pleistocene glacial-interglacial cycles is synchronous with a dramatic global increase in the erosion rates of mountainous landscapes and the accumulation of terriginous sediments (Hay et al., 1988; Molnar & England, 1990; Kuhlemann et al., 2002). Climate changes during individual glacial-interglacial cycles (over 10^4 to 10^5 year timescales) bring high-amplitude changes in ocean and atmospheric temperatures, precipitation rates and distributions, glacial activity and ecosystems, among other effects; and these changes significantly impact landscape processes. This includes the erosion, transport, and deposition of sediment, meaning climate is one of the primary architects of the stratigraphic record and climate changes may generate characteristic signals in sedimentary deposits (e.g., Burke et al., 1990; Molnar & England, 1990; Bull, 1991; Miall, 1991; Paola et al., 1992; Blum & Törnqvist, 2000); it is for this reason that the sedimentary record is typically presented as an archive of past environmental change on Earth.

This assumption has recently been challenged, particularly by theoretical studies proposing that sediment routing systems could be buffered against high-frequency climate changes (Castelltort & Van Den Driessche, 2003; Allen, 2008b; Armitage et al., 2013), and that sediment transport processes might 'shred' signals of external controls (Hallet, 1990; Humphrey & Heller, 1995; Jerolmack & Paola, 2010). Even if landscapes do react to climate changes, major questions remain about how climate signals are transferred into the stratigraphic record, over which timescales, and with what sensitivity. To answer these questions, we need to test the outputs and predictions of landscape evolution models with observations from well-constrained study locations. In particular, quantitative measures of well-dated stratigraphy are essential for understanding the effects of climate change on sedimentation. Here, we present a detailed study of mountain catchment-alluvial fan systems in the eastern Sierra Nevada, California, and we examine their sensitivities to known glacial-interglacial climate changes in the past. We characterise the properties of the climatic signal preserved in these alluvial fan deposits, and explore its physical origins.

4.2. Background

4.2.1. Theory

Understanding sedimentary basin fill is a significant research challenge, because basin deposits constitute a temporal and spatial record of sediment transfer from eroding catchments to depocentres, and therefore contain information about how erosion, transport, and deposition have adjusted to tectonic and climatic boundary conditions (Heller & Paola, 1992; Paola, 2000; Duller et al., 2010; Allen, 2008; Whittaker, 2012). A key boundary condition is climate because the efficiency of weathering, erosion and sediment transfer is largely determined by climate variables such as moisture availability and rainfall (e.g., Dixon et al., 2009a,b; Steffen et al., 2009; DiBiase & Whipple, 2011; McPhillips et al., 2013).

Many questions about the environmental controls on basin fill have been explored using numerical models. These allow us to investigate what effects climate changes might have on sediment routing systems (e.g., Paola et al., 1992; Allen & Densmore, 2000; Morehead et al., 2001). Coupled mountain catchments and alluvial fans are good analogues to work with, because they contain a range of sediment transfer functions, but are self-contained and relatively simple to conceptualise and compare with real examples. Recent catchment-fan models have represented 'climate change' as step-changes or cyclicity in average precipitation rates, and they predict characteristic responses in sediment volumes and grain size distribution delivered to alluvial fans, and also fan architecture governed by aggradation and incision (e.g., Densmore et al., 2007; Armitage et al., 2011; Simpson & Castelltort, 2012; Allen et al., 2013). Generally, models predict that an abrupt increase in precipitation rate would increase sediment flux and cause the transient progradation of coarse-grained sediment on an alluvial fan, with a reduced down-system rate of grain size fining that is preserved in stratigraphy (Densmore et al., 2007; Armitage et al., 2011; Allen et al., 2013). In these models, an increase in precipitation of 50 to 100 % (realistic for glacial-interglacial cycles), approximately doubles sediment flux, causing several kilometres of fan progradation and generating a coarse spike in grain size on the order of ≥ 10 mm (or ~ 50 % change in grain size) through a virtual fan cross-section. Conversely, a decrease in precipitation rate is predicted to cause fan retrogradation and a transient decrease in grain size deposited (e.g., Densmore et al., 2007; Armitage et al., 2011; Allen et al., 2013). These grain size predictions are for the gravel fraction meaning they would be easily detected in real deposits. Physical experiments also indicate that eroding landscapes should be sensitive to specific climate changes, e.g., in precipitation rate (Bonnet & Crave, 2003). Scaled-down laboratory models of alluvial fans demonstrate that doubling rainfall rate and sediment flux to the fan causes transient coarsening of grain size in stratigraphy (Rohais et al., 2012), an outcome consistent with numerical models. These

studies clearly suggest that climate changes could be recorded by some landscapes as diagnostic sediment flux and grain size signals delivered to basin stratigraphy.

During the past ~ 1 Ma years, the greatest amplitude climate fluctuations have been associated with glacial-interglacial cycles with a dominant periodicity of ~ 100 ka. However, some diffusion-based models suggest that sedimentological responses of catchment-fan systems may take several 100s of ka to adjust to a perturbation (e.g., Densmore et al., 2007). For instance, Armitage et al. (2013) argued that catchment-fan systems will be buffered against climate cycles with periodicities shorter than the response timescale of the landscape, which in their model was of the order of 10^6 years. This estimate of landscape response time concurs with recent field studies, which indicate that rivers adjust their longitudinal profiles in response to tectonic perturbation over 10^6 year timescales (Whittaker & Boulton, 2012; D'Arcy & Whittaker, 2014). In contrast, other numerical models (e.g., Simpson & Castelltort, 2012) make different assumptions about landscape behaviour and predict strong sensitivity to high-frequency climate changes. Moreover, a range of important sediment transport processes, e.g., landslides, debris flows, and large floods, potentially erode and deposit sediment much more rapidly than time-averaged bedrock river processes (Ritter et al., 2000), and these timescales are not fully understood. Other models indicate that hillslope sediment flux may react to climate changes over 10s of ka or much longer periods depending on assumptions and parameterisation (Fernandes & Dietrich, 1997). In reality, response time is likely to vary between processes and types of landscape (Castelltort & Van Den Driessche, 2003; Allen, 2008b), so empirical studies are necessary to evaluate the integrated sensitivity to climate changes. Models are also limited by necessary process simplifications, and may not fully account for important factors like the magnitude-frequency distribution of precipitation, runoff modulators like vegetation cover, or sediment transport by threshold-controlled hillslope processes (e.g., Fernandes & Dietrich, 1997; Tucker & Slingerland, 1997; Trauth et al., 2003; Istanbulluoglu & Bras, 2006).

It has also been argued that climatic signals might be obscured by autogenic processes or by 'signal shredding' within some sediment routing systems (e.g., Humphrey & Heller, 1995; Clarke et al., 2010; Jerolmack & Paola, 2010). Here, a climate signal may be damped by a long landscape response timescale (Armitage et al., 2013), filtered by thresholds within the sediment transfer pathway (Jerolmack and Paola, 2010), and/or suffer interference with sediment transport fluctuations arising from self-organised behaviour (Paola and Foufoula-Georgiou, 2001). Additionally, a number of studies predict similar responses in sediment flux and grain size from a tectonic driver, such as varying basin subsidence rate, compared to a climate change (Paola et al., 1992; Densmore et al., 2007; Armitage et al., 2011; Allen et al., 2013), making it potentially difficult to discriminate primary controls even if they are captured by the sedimentary record. Consequently, it remains unclear from

theoretical work whether we should expect to find records of high-frequency, high magnitude climate change in basin stratigraphy or not.

4.2.3. Observations

The best way to evaluate these hypotheses is to examine real depositional systems and establish whether and how their sedimentary deposits preserve records of known climate changes in the past. Some studies have already identified evidence for sensitivity. For example, thick and transient prograding deposits of coarse conglomerates have been identified in western Colorado, Wyoming, and the Spanish Pyrenees, associated with the Palaeocene-Eocene Thermal Maximum (PETM), a dramatic warming event that occurred over a relatively rapid (10^4 to 10^5 year) timespan ~ 56 Ma ago (Foreman et al., 2012; Allen et al., 2013; Foreman 2014). Supported by a carbon isotope excursion as well sedimentology (Foreman et al., 2012; Foreman, 2014), these deposits are good evidence for climate-driven sedimentation being recorded rapidly in the stratigraphic record (e.g., Simpson & Castelltort, 2012; Allen et al., 2013).

Glacial-interglacial climate cycles offer another opportunity to study landscape responses to environmental change, generating well-constrained, high-amplitude, high-frequency, climate fluctuations over short (10^4 to 10^5 year) timescales, during which tectonic conditions are typically constant. Small mountain catchment and alluvial fan systems are good landscapes to study the sedimentological results of these cycles, because they preserve volumetrically closed records of past erosion and sedimentation that can be reconstructed easily. As a result, late Pleistocene-Holocene climate changes have been invoked to explain alluvial fan deposits from a range of locations, often correlated with the timings and magnitudes of fan aggradation and incision events (e.g., Bull, 1991; McDonald et al., 2003; Steffen et al., 2009, 2010; Miller et al., 2010). Where precise chronologies are available, depositional events have been linked to periods of enhanced precipitation and storm intensity, e.g., in the south-western United States (McDonald et al., 2003; Miller et al., 2010; Antinao & McDonald, 2013a,b), Israel (Enzel et al., 2012), and Peru (Steffen et al., 2009, 2010; Bekaddour et al., 2014).

Along the western escarpment of the Peruvian Andes, Bookhagen and Strecker (2012) and McPhillips et al. (2013) used ^{10}Be cosmogenic nuclides to show that catchment erosion rates were significantly higher in the late Pleistocene compared to the Holocene, potentially due to a wetter, stormier climate increasing sediment supply by surpassing erosion thresholds. In the same area, Steffen et al., (2009, 2010) and Bekaddour et al. (2014) were able to link fan aggradation sequences for the last ~ 100 ka with wetter periods in the late Pleistocene, followed by incision events when hillslope sediment

supplies were exhausted. In the Mojave Desert of California, another dry landscape, Miller et al. (2010) demonstrated that alluvial fans aggraded at 3 – 6 ka and 9 – 14 ka, driven by heavy rainfall associated with enhanced monsoonal activity and warmer sea surface temperatures. Nearby in Baja California, Mexico, Spelz et al. (2008) inferred that fan deposition was promoted by wetter climates, and that fan terraces can be correlated with Milankovitch cycles during the last ~ 200 ka. All these examples imply that catchment-fan systems can be sensitive to glacial-interglacial climate changes in terms of their depositional architecture, sediment characteristics, and deposition rates. However, some uncertainties remain about whether fan aggradation is promoted by wetter climates (Bartov et al., 2002; Steffen et al., 2009, 2010; Waters et al., 2010; Bekaddour et al., 2014; Owen et al., 2014), stormier climates (Keefer et al., 2003; McDonald et al., 2003; Miller et al., 2010; Enzel et al., 2012; Antinao & McDonald, 2013a,b), arid climates and a decrease in vegetation cover (Langbein and Schumm, 1958; Bull, 1991; Pelletier, 2014) or may simply be due to autogenic processes unrelated to climate (Humphrey & Heller, 1995; Paola et al., 2009; Clarke et al., 2010).

Other studies have addressed the sedimentological characteristics of the deposits themselves. Grain size distribution in particular can be quantified easily, is readily preserved, and is known to record key information about sediment supply, sediment transport, and the sensitivity of catchments to tectonic and climatic boundary conditions (e.g., Whittaker et al., 2007, 2010; Duller et al., 2010; Waters et al., 2010; Foreman et al., 2012; Allen et al., 2013; Foreman, 2014; Attal et al., 2015). For example, Waters et al. (2010) examined late Pleistocene stream-flow alluvial fan deposits in southern Cyprus, and concluded that significantly coarser grain sizes were deposited during periods of wetter climate, largely due to enhanced seasonal storms and monsoonal rainfall increasing transport capacity. Yet, sedimentological responses to climate change (e.g., grain size) are much less well-studied in alluvial fan systems compared to morphological responses (e.g., incision and aggradation), despite models predicting a clear climate change signal in grain size (Densmore et al., 2007; Armitage et al., 2011; Rohais et al., 2011; Allen et al., 2013).

Now, detailed data sets are needed from catchment-fan systems to test these ideas. Suitable study areas need to meet five key criteria: (1) Sedimentary deposits need to be mapped and dated at a high resolution in time and space; (2) Catchment-fan systems need to have experienced high-amplitude climate changes in the past that are well documented; (3) Other boundary conditions need to be constant, including tectonics and bedrock lithology; (4) Good sediment preservation is important, including the rapid generation of accommodation, frequent abandonment of fan terraces, and minimal post-depositional reworking of volumetrically-closed deposits; (5) Multiple discrete systems can be compared to evaluate the reproducibility of any climate signal observed. We have targeted Owens Valley, California, as an ideal study area meeting these criteria.

4.3. Study area

4.3.1. Geomorphological and geological setting

We examined 8 different mountain catchment-alluvial fan systems along the eastern front of the Sierra Nevada mountain range in California, located near the towns of Independence and Big Pine (Fig. 4.1). From north to south, these are the Birch, Independence, Pinyon, Symmes, Shepherd, north Bairs, south Bairs, and George creek systems. They drain eastwards into Owens Valley, a subsiding basin, constructing a coalesced bajada of large alluvial fans ~ 10 km long and with surface gradients of 4 to 6 ° (Whipple & Dunne, 1992). These basin deposits have a total thickness of ~ 2.4 km in Owens Valley (Pakiser et al., 1964; Jayko, 2009), and are not toe-cut by the axial Owens river or ancient lake shorelines at this location.

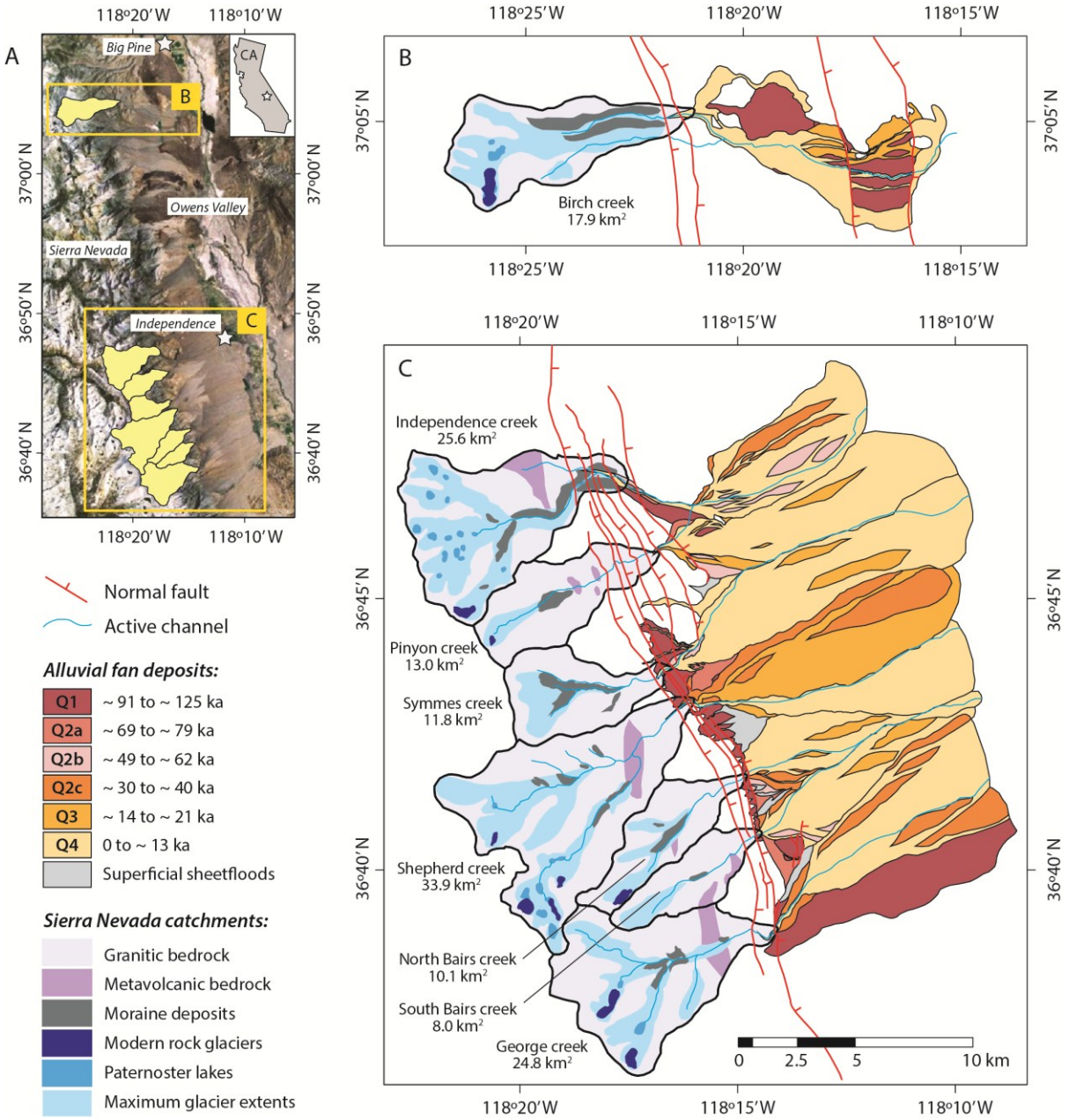

Fig. 4.1. (A) Locations of the catchment-fan systems studied in the eastern Sierra Nevada, draining into Owens Valley, California. Details are provided for the Birch creek system near Big Pine (B), and the remaining systems near Independence (C). Alluvial fan deposits are mapped according to the stratigraphy of D'Arcy et al. (2015), and the age ranges of the deposits are given in the key; see text for details. Range-bounding normal fault strands dip towards the ENE. All 8 catchments are eroding granitic bedrock apart from minor outcrops of metavolcanics (Moore, 1981; Moore & Sisson, 1987). Modern glacial features are shown, including glacial moraine sediment sources. The maximum advances of LGM glaciers are mapped in blue, after Moore & Mack (2008), and today the catchments are unglaciated apart from small rock glaciers in north-facing cirques.

The fans occupy an elevation of 1500 to 2000 m above sea level, with the catchments rising to the Sierra Nevada crest line at approximately 4000 m, eroding ~ 2 km of total relief (Fig. 4.2). Catchment areas range from 8.0 km^2 (south Bairs creek) to 33.9 km^2 (Shepherd creek). All 8 catchments erode almost exclusively granitic bedrock—comprising Mesozoic granodiorites and quartz monzonites of a number of plutons, particularly the Bullfrog, Dragon, and Paradise granites—with very minor outcrops of metavolcanic rocks (Moore, 1981; Moore & Sisson, 1987). The alluvial fan sediments are therefore granitic in composition, and have been mapped and dated in detail by a number of previous studies (Zehfuss et al., 2001; Dühnforth et al., 2007; Le et al., 2007; D'Arcy et al., 2015). Constant bedrock lithology across the study area is important, because differences in erodibility may modulate alluvial fan responses to climate changes (Arzani, 2012; Goudie, 2013). Catchment hillslopes are steep (we characterise this later) and vegetation cover is sparse, with low-density pine and juniper woodland at middle elevations transitioning to desert scrub on the alluvial fans. Sediment supply is from widespread landsliding and steep scree cones (even at low elevations), weathering of exposed bedrock faces, and incision into glacial moraine deposits. The catchments are dominated by hillslope processes, and as a result their alluvial fans have been almost entirely constructed by debris flows (Dühnforth et al., 2007; Le et al., 2007; D'Arcy et al., 2015). Representative field photographs are shown in Fig. 4.3.

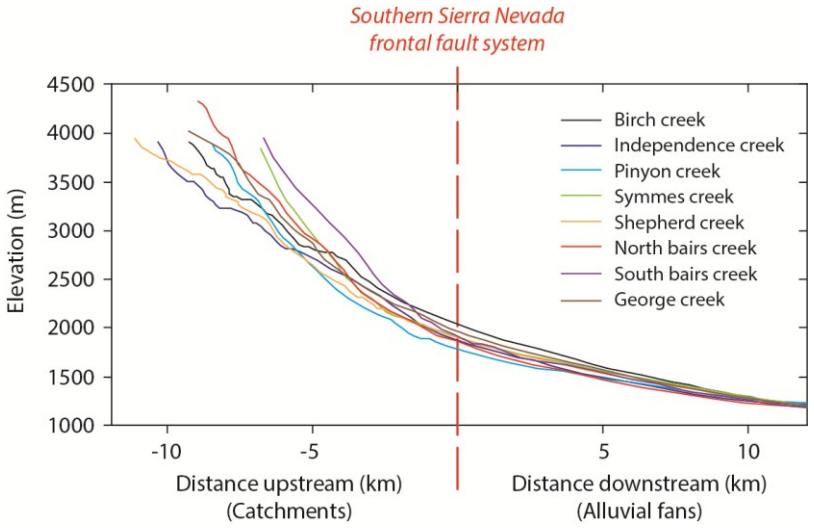

Fig. 4.2. Longitudinal profiles for the 8 catchment-fan systems studied. The catchments are steep and eroding ~ 2000 m of relief independent of channel length. Those that experienced the most glaciation have stepped profiles, e.g., Birch and Independence creeks, punctuated by hanging valleys. The alluvial fans are ~ 10 km long and form a coalesced bajada with surface slopes of 4 to 6 °.

The catchments are separated from the fans by the southern section of the Sierra Nevada Frontal Fault Zone (SNFFZ), an active normal fault system generating a steep, range-bounding escarpment striking north-north-west (Fig. 4.1). The SNFFZ was likely active from the late Miocene onwards, and involved in the break-up of a pre-existing plateau (Phillips, 2008; Jayko, 2009). The slip rate on the SNFFZ accelerated during the Plio-Pleistocene, attributed to lithospheric delamination (Wakabayashi & Sawyer, 2001; Jones et al., 2004; Stock et al., 2004, 2005; Clark et al., 2005; Jayko, 2009), but the current tectonic regime has been stable for > 1 Ma. With a total SNFFZ displacement of > 5 km (Jayko, 2009), these-catchment fan systems are mature and have been active for several million years.

Fig. 4.3. Representative field photographs. (A) Hillslopes at the top of the Independence creek catchment. Vegetation is sparse, leaving exposed granitic bedrock that supplies sediment by landsliding and debris flows. (B) Main valley at the bottom of the Independence creek catchment, looking upstream. The U-shaped trough is evidence of former glaciation, and the road is cut into moraine deposits with embedded boulders visible in the right-foreground. (C) View of the apex of the Shepherd creek fan, looking towards the catchment. Distinct raised debris flow terraces are easily distinguished in the field, having been abandoned and incised by younger deposits. The modern active channel is incising into Holocene deposits, and can be traced from the tops of trees. (D) A Q4 debris flow nose on the Shepherd creek fan. The distinction between boulder-rich lateral levees and gravel-rich channel deposits is clear. Note the person sitting on the levee for scale. (E) A clear debris flow levee on the Independence creek fan (Q4) viewing up-fan. (F) Cross-sectional view of a Q4 debris flow levee on the Shepherd creek fan, with clear inverse-grading and rafting of coarse boulders to the top of the levee. The finer gravel channel is visible at the bottom of the photo.

In detail, the frontal fault zone is composed of multiple east-dipping en-echelon normal fault strands that create visible scarps in alluvial fan terraces, glacial moraines, and bedrock. Estimates of slip rate vary in detail along the SNFFZ from north to south (Jayko, 2009; Rood et al., 2011), but vertical scarp offsets from dated alluvial fan terraces produce vertical displacement rates of 0.2 to 0.3 mm yr^{-1} (Zehfuss et al., 2001; Le et al., 2007). Later, we provide additional slip rate constraints from exposed scarps on newly-dated fan terraces, which agree well with these earlier estimates. Importantly, slip rate constraints for the frontal fault system are constant through time for at least the last 300 ka, and show no changes in tectonic boundary conditions during the last glacial-interglacial cycle (Gillespie, 1982; Martel et al., 1987; Zehfuss et al., 2001; Le et al., 2007). This is also supported by data from elsewhere along the SNFFZ (Rood et al., 2011). These catchments have therefore experienced constant lithological and tectonic conditions during the pronounced climate changes of the last ~ 125 ka, allowing the climatic control on sedimentation to be isolated.

4.3.2. Modern and past climate

The catchments along the eastern escarpment of the Sierra Nevada occupy a significant rain shadow, as the majority of precipitation originates from Pacific sources to the west. The average annual precipitation rate is only ~ 600 mm yr^{-1} at the top of the study catchments (compared to up to ~ 1200 mm yr^{-1} on the western side of the range), and decreases abruptly with relief towards the east (Kessler et al., 2006). Annual temperatures average 2 to 5 °C at the Sierra Nevada crest (PRISM Climate Group, 2004). At the alluvial fan toes, the average annual precipitation rate is 50 to 200 mm yr^{-1} depending on the year, and average annual temperature is 14 to 18 °C (2004–2013 records from Independence station; NOAA National Climatic Data Center, 2014). Much of the annual precipitation budget is delivered by storms, from several Pacific moisture sources including extra-tropical cyclones, ‘pineapple-express’ storms carried by atmospheric rivers, convective thunderstorms during the North

American Monsoon, and the remains of tropical cyclones from the east Pacific (Antinao & McDonald, 2013a). These storms often bring precipitation intensities of 5 to 10 mm hr^{-1}, and debris-flow triggering storms in recent years have generated peak rainfall rates as high as ≥ 25 mm hr^{-1} over short (10-15 minute) periods (DeGraff et al., 2011; Antinao & McDonald, 2013a). Known thresholds for modern debris flow initiation are surpassed at rainfall intensities of 5 to 10 mm hr^{-1} for a duration of 1 - 2 hr, and with greater rainfall intensities only short downbursts are required to trigger a debris flow (Cannon et al., 2008; Coe et al., 2008). In summary, the study catchments experience a relatively dry climate today, with sharp orographic gradients in average precipitation rate and temperature with elevation, and a substantial rainfall contribution from storms.

In the south-west USA, the climate during the last glacial period was significantly cooler and wetter than at present. Evidence for this includes dated pluvial lake shorelines (Orme & Orme, 2008) and cores (Benson et al., 1996; 1997), vegetation records (Woolfenden, 2003), glacial moraines and landforms (Phillips et al., 2009; Rood et al., 2011), and terrestrial oxygen isotope records (Winograd et al., 1997, 2006), among other data (Phillips, 2008, provides an extensive review). Parts of our study catchments were occupied by valley glaciers during the coolest parts of the last glacial-interglacial cycle, which have since retreated (Dühnforth et al., 2008; Moore & Mack, 2008). Glaciation has produced stepped longitudinal profiles (Fig. 4.2), U-shaped troughs in some parts of the catchments, and modern landforms including cirques, arêtes, hanging valleys, moraines, and numerous paternoster lakes. Detailed time series of glacial rock flour deposition in Owens Lake cores have also been described (e.g., Bischoff et al., 1997; Menking, 1997). The maximum extent of glaciation varies significantly between our study catchments (Fig. 4.1). Some, for example Birch creek and Independence creek, show clear glacial troughs and moraine deposits extending down to the fan apices, and were fully occupied at the peak of glaciation. However others, for example Shepherd creek, Pinyon creek, and the Bairs creek catchments, were only ever partly glaciated and have clear V-shaped valleys unaffected by glaciation in their lower reaches.

Several different methods have been used to estimate how much cooler and wetter the Last Glacial Maximum (LGM) was compared to today. Pollen data from packrat middens in western Nevada, at the same latitude as our study catchments, indicate the LGM was 5 to 8 °C cooler and 2.2 to 2.4 times wetter than today (Thompson et al., 1999). Similarly, oxygen isotope data from ostracode fossils in southern Nevada suggests the LGM was at least 5.6 °C cooler (Quade et al., 2003), and hydrological restorations of pluvial lakes generally model the LGM as ~ 5 °C cooler and 1.5 to 2.0 times wetter than present (e.g., Menking et al., 2004). Sensitive numerical models of mountain glaciers in the southern Sierra Nevada require a temperature depression of 5.6 °C and a factor of 1.9 increase in total precipitation in order to simulate the correct spatial extents known from mapped LGM glacial landforms and moraines (Hostetler and Clark, 1997; Kessler et al., 2006). This analysis was made for

our precise study area between the Birch creek and George creek catchments (Fig. 4.1; Kessler et al., 2006), and is in close agreement with the other pollen, geochemical, and hydrological data mentioned above. Therefore, the LGM climate is tightly constrained at 5 to 6 °C cooler and ~ 2 times wetter (on average) than modern conditions. This represents the amplitude of glacial-interglacial climate changes in this area, although the penultimate glaciation was probably even more severe, with larger glacial advances (Phillips et al., 2009), and temperatures > 10 °C colder than today (Quade et al., 2003).

To characterise the entire last glacial-interglacial cycle in full, several continuous regional palaeoclimate records are available. The Devil's Hole $\delta^{18}O$ record is a high-resolution terrestrial oxygen isotope curve recovered from calcite veins in southern Nevada, very close to our study area (Winograd et al., 1997, 2006). It has a precise chronology based on $^{230}Th/^{234}U$ series dating, captures 10^3 to 10^5 year climate fluctuations in detail, and is highly correlated with past sea surface temperatures (Winograd et al., 2006). The Devil's Hole $\delta^{18}O$ record has minima below 14 ‰ (representing low temperatures and high continental ice volume) during the coolest periods of the glacial climate, and rises to ~ 14.6 ‰ in the current interglacial and > 15 ‰ during the last interglacial (Fig. 4.4). A number of alkenone-derived sea surface temperature reconstructions have been reported along the Californian coast (e.g., Herbert et al., 1995; Lyle et al., 2010), of which the ODP site 1016 record in the Santa Barbara basin (Yamamoto et al., 2007) is the closest to our study area. This record shows modern temperatures of ~ 16 °C decreasing to ~ 12 °C at the LGM, having gradually cooled from a peak of ~ 18 °C during the last interglacial (Fig. 4.4). The ODP-1016 sea surface temperature curve of Yamamoto et al. (2007) is highly correlated with equivalent reconstructions from nearby locations (Lyle et al., 2010), albeit the absolute temperature range varies with latitude.

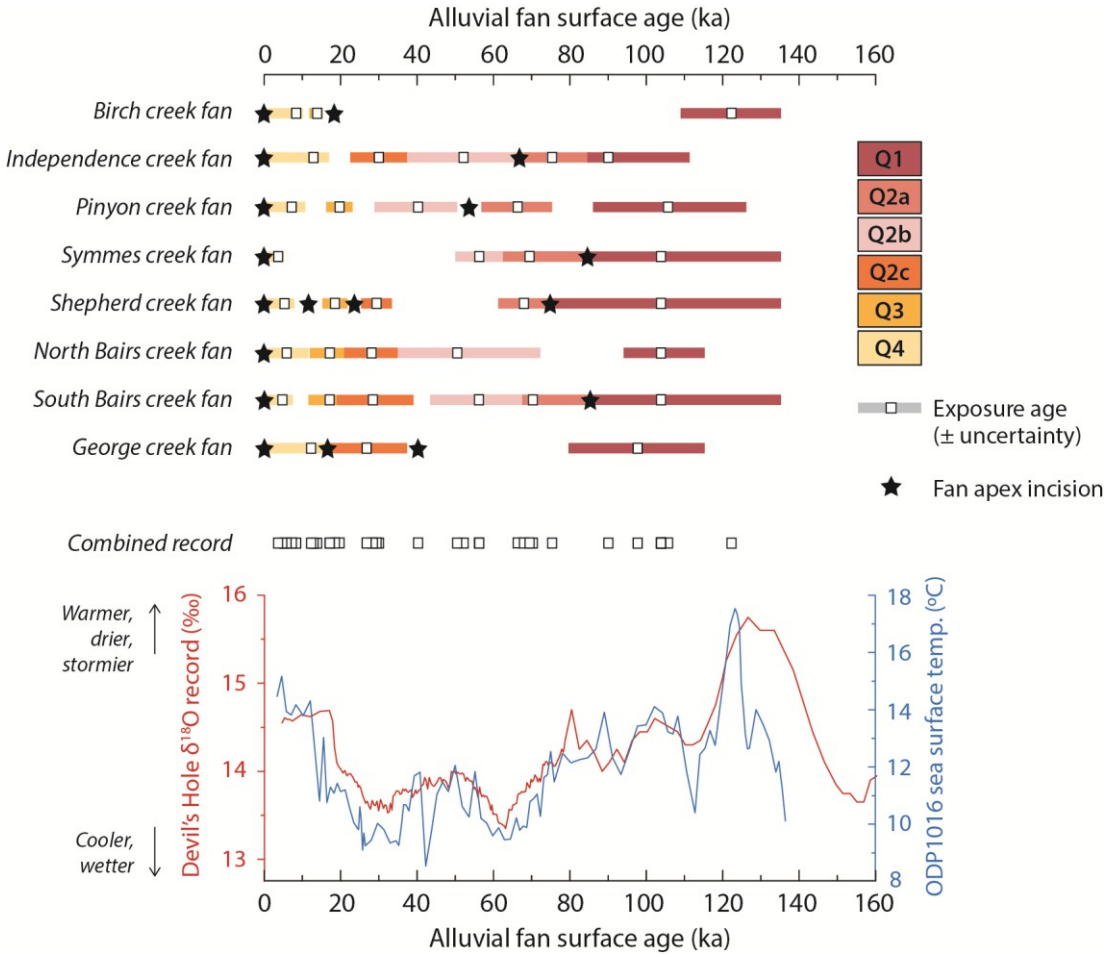

Fig. 4.4. Complete stratigraphy for the 8 alluvial fans studied, after D'Arcy et al. (2015) and based on exposure ages reported by Zehfuss et al. (2001), Dühnforth et al. (2007), and Le et al. (2007). Surfaces correspond to the maps in Fig. 4.1 and stars show the timings of incision at the fan apices. Coloured bars show the full age uncertainty. The 'combined record' shows the estimated ages for all mapped surfaces; these fans offer a semi-continual record with a high density of age constraints throughout the last glacial-interglacial cycle. Past climate changes are shown for comparison, represented by the Devil's Hole $\delta^{18}O$ curve (Winograd et al., 1997, 2006) and the ODP site 1016 sea surface temperature from the Santa Barbara basin (Yamamoto et al., 2007).

The timings of climate changes within the last glacial cycle are equally important for our analyses as their amplitudes. Detailed exposure dating of LGM (Tioga) moraines shows that mountain glaciers advanced to their peak extents at ~ 26 ka, and retreated rapidly at 21 to 17 ka along the entire eastern margin of the Sierra Nevada (Phillips et al., 2009; Rood et al., 2011). In Owens Lake cores, *Juniperus* and other tree pollen dominate from 26 to 18 ka, before declining from 18 to 10 ka as the drying climate allowed desert scrub to dominate (Woolfenden, 2003). *Juniperus* pollen in particular is highly correlated with orbital climate shifts captured by $\delta^{18}O$ records (Woolfenden, 2003). Organic and inorganic carbon input into Owens Lake also decreased abruptly between 26 and 20 ka (Benson et al., 1996), and dessication events in the lake have been identified from 18.3 ka onwards (Benson et al.,

1997). The LGM in the Sierra Nevada also correlates with a 25 to 18 ka high-stand of the former pluvial Lake Manly in neighbouring Death Valley (Ku et al., 1998; Lowenstein et al., 1999). The penultimate (Tahoe) glaciation was longer in duration and more extreme, with moraines extending further down the catchments and their ^{36}Cl exposure ages indicating retreat around 135 ka ago (Phillips et al., 2009), which is in agreement with global timings (e.g., Martinson et al., 1987). This was followed by a rapid decrease in *Juniperus* pollen in Owens Lake cores between 126 – 130 ka (Woolfenden, 2003), and a rise in temperatures indicated by the Devil's Hole $\delta^{18}O$ curve, placing the last interglacial at 120 to 130 ka (Winograd et al., 2006; Masson-Delmotte et al., 2013).

4.3.3. Debris flow-dominated alluvial fan deposits

The 8 alluvial fans studied here (Fig. 4.1) are dominated by debris flow deposits (Dühnforth et al., 2007; Le et al., 2007; D'Arcy et al., 2015), with only very minor and localised reworking by streams and small superficial sheet-floods. Debris flows are typically triggered by threshold-surpassing, high intensity rainfall events (David-Novak et al., 2004; Griffiths et al., 2004; Goudie, 2013), evolving from either saturated landslides or during critical surface runoff, the latter being particularly important in alpine watersheds with sediment traps such as the glacial troughs visible in the longitudinal profiles of our study catchments (Fig. 4.2) (Cannon et al., 2008; Coe et al., 2008; Kean et al., 2013). As such, debris flows are highly sensitive to triggering storms, surface runoff and discharge rates when sediment supply is abundant and non-limiting (Cannon et al., 2008; Kean et al., 2011, 2013). They are major sediment transport processes in a range of landscapes, playing a particularly key role in building alluvial fans in arid and semi-arid areas (Goudie, 2013), and furthermore present a significant landscape hazard in populated areas (Fernandes et al., 2004; Sepulveda et al., 2006).

The sediment transport mechanics of debris flows are not fully understood, and realistic sediment transport laws are likely to be considerably more complex than for streams (e.g., Iverson et al., 2010). Nonetheless, the sedimentology of debris flow deposits contains useful information about properties such as event size and discharge, especially for flows initiated by surface runoff and which entrain significant amounts of sediment (McCoy et al., 2013). For example, the grain size carried by some debris flows in the USA has been shown to be coarser in larger debris flows (Coe et al., 2008; McCoy et al., 2012, 2013), indicating empirically that grain size may scale with flow power, even if the underlying equations remain unknown. One key characteristic of debris flows is the segregation of larger particles to the tops, sides, and fronts of flows, resulting from internal fluid pressure gradients (Anderson & Anderson, 2010; Johnson et al., 2012). Debris flow deposits therefore have distinct gravel channels bound by coarse boulder-rich lateral levees exhibiting upward-coarsening in section view. These properties are very clear on the alluvial fan surfaces in Owens Valley, which display a

network of abandoned and cross-cutting debris flow channels and levees carrying boulders typically 0.5 to 3.0 m in diameter, but sometimes 10 m across or larger, especially on Holocene surfaces. Individual flow deposits are 10s of metres wide, measured from levee to levee, and sometimes inherit pre-existing flow channels (Fig. 4.3). Due to the clear channel and levee segregation, depositional relief and inverse grading in these deposits, we interpret them to represent high viscosity debris flows (Whipple & Dunne, 1992).

Debris flows can move several metres per second (Anderson & Anderson, 2010; DeGraff et al., 2011), rapidly transferring sediment from catchment sources to the fans, and potentially minimising the effects of transient sediment storage on signal propagation. They have a high preservation potential, forming thick aggradational terraces on the Owens Valley fans (Fig. 4.3c). These terraces are clearly exposed on the upper fans near their apices, dissected by younger surfaces that incise into older deposits as a result of the continuing subsidence of the basin (D'Arcy et al., 2015). All of the fans exhibit incisional events (Fig. 4.4), but the timings of incision vary from fan to fan, resulting in morphological differences. For example, the Symmes creek fan is largely back-filled at the apex by Q4 (Holocene) deposits, which have aggraded onto older sediments. In contrast, the Shepherd creek fan displays significant fan-head trenching, with Q4 (Holocene) debris flows incising by ~ 60 m into older units (Fig. 4.3c) (Dühnforth et al., 2008). Modern active channels on all 8 fans are now incising into older fan deposits, including Holocene sediments. Other than the timing of ancient incision events, few differences exist between the fans. Their debris flow deposits are comparable in terms of both sedimentological properties and sizes, and the fans share the same depositional lengths, granitic source catchments, and tectonic conditions. As a result of incision and avulsion, older surfaces quickly become inactive and are abandoned (within 10 to 20 ka). A total of 35 debris flow fan surfaces, distributed across the 8 fans, have been mapped and dated by previous workers using ^{10}Be cosmogenic nuclide exposure dating (Zehfuss et al., 2001; Dühnforth et al., 2007; Le et al., 2007), and weathering fractures in surface boulders whose dimensions can be precisely calibrated as age indicators (D'Arcy et al., 2015). Each dated surface contains deposits from many individual debris flow events of similar age.

4.4. Methods

4.4.1. Sampling

Debris flow deposits were sampled on 35 alluvial fan surfaces, distributed across 8 catchment-fan systems, in Owens Valley, California. These deposits have been mapped and dated in detail by previous workers using ^{10}Be cosmogenic radionuclides and correlation techniques (Zehfuss et al.,

2001; Dühnforth et al., 2007; Le et al., 2007; D'Arcy et al., 2015). We used the maps and stratigraphic model of D'Arcy et al. (2015), which assigns 4 main units (Q1 to Q4) to all 8 alluvial fan systems, with a combined depositional record spanning ~ 125 ka to present with a high density of age constraints in time and space. We also use the maps of D'Arcy et al. (2015) to identify range-bounding normal fault scarps, which were located in the field and using high resolution aerial imagery.

Grain size was measured in the field by Wolman point counting (Wolman, 1954) at 292 localities. At each locality, the long-axis diameters of a minimum of 100 randomly-selected clasts, above 1 mm in size, were recorded using a ruler (precise to 1 mm). At each location, separate counts were made for debris flow channels (15,737 clasts in total) and lateral levees (14,878 clasts). We did not sample finer particles as their mobility is likely to be high and fines have been documented in detail from cores through the Owens Lake sediments, which represent the end of the depositional system and are more suitable for characterising the < 1 mm fraction (Benson et al., 1996, 1997; Menking, 1997). Our grain size data therefore describe the gravel fraction that is well-preserved on the fans. On each dated fan surface, a minimum of 3 different localities (8 on average) were sampled. This ensures that repeat measurements were made on every dated surface, and that the overall grain size distributions are representative. Debris flows are spatially non-uniform (Iverson and Vallance, 2001), and repeat measurements also reduce the impact of local noise in our data. Such noise might arise from local fluctuations in slope, flow bends or obstructions, inheritance of pre-existing channels, or the chaotic mechanics of debris flows themselves. We characterised the fining rate from apex to toe on the Q4 (Holocene) surface of the Shepherd creek fan to constrain any effects arising from down-system grain size fining due to selective deposition. For all other fan surfaces we restricted our grain size sampling to the upper 3 km of the alluvial fans, to avoid fining effects and because many older deposits are only exposed near the fan apices (Fig. 4.1).

By sampling the grain sizes of ~ 125 ka to modern debris flow deposits in the field, our subsequent analysis relies on the assumption that the ≥ 1 mm grain size distribution measured is not significantly altered by post-depositional processes during this time-span. In our Wolman point counts, we avoided clasts that were obvious weathering products, e.g., thin sheets of granite or angular grains that had been exfoliated from boulders by thermal weathering. We selected localities on stable parts of older terraces, away from younger flow events. Clast varnishing was only observed on large boulders on the oldest Q1 surfaces, and assumed to not affect grain size distribution, and desert pavement formation is negligible on these fans. A diffusional loss of depositional (channel and levee) relief occurs with surface age on these fans, however it is still possible to discriminate flow levees on even the oldest surfaces from alignments of large boulders. While we document no correlation between deposit age

and systematic grain size fining, our data offer the opportunity to evaluate the importance of any post-deposition effects, which we discuss in section 4.6.

Debris flow widths were measured from the top of one lateral levee to the top of the parallel levee, perpendicular to the direction of flow. This was done both in the field using a laser range finder precise to < 1 m, and confirmed using high-resolution (< 1 m) aerial imagery. In total, 257 debris flow widths were recorded across all 8 fans. Vertical offsets were measured across range-bounding normal fault scarps where observed on dated surfaces, using a laser range finder precise to < 1 m in the field. Many scarps have already been measured by previous studies (Zehfuss et al., 2001; Le et al., 2007) and we add to these data by recording 10 additional vertical scarp offsets on alluvial surfaces subsequently dated by D'Arcy et al. (2015). These data help to refine the existing constraints on the vertical component of slip rate along the southern SNFFZ.

Sediment sources were also sampled in two of the parent catchments: Independence creek, which is relatively large (25.6 km^2) and was fully glaciated at the LGM, and Symmes creek, which represents the smaller catchments (11.8 km^2) and was not fully glaciated (Fig. 4.1). We used Wolman point counting to measure the grain size distributions of hillslope landslides, rockfall scree cones, and glacial moraine deposits in each catchment, using identical methods to the debris flow fan deposits described above. These represent the major sediment sources in these catchments. The locations of moraine deposits in Fig. 4.1 were mapped using field observations and high-resolution aerial imagery, and following the map of Moore and Mack (2008). All data are provided in full detail as supporting information.

4.4.2. Data analyses

For each dated fan surface, the Wolman point counts from every locality were compiled into a single cumulative grain size distribution curve. In order to convert the grain size data into quantitative time series, we measured the median (D_{50}) and 84th percentile (D_{84}) particle diameters from each distribution curve. By making repeat measurements across each surface, we were able to assign error bars to D_{50} and D_{84} values, equal to ± 1 standard deviation (σ) among all sampled localities per surface and illustrating spatial variability. To represent flow sizes, the median debris flow width was calculated for each dated surface, ± 1 σ.

We also repeated the same analyses of grain size and flow width on the data, but binned across all 8 alluvial fan systems, i.e., grain size data from all Q4 localities were assembled into a single cumulative distribution curve representing the Q4 unit across every fan, and likewise for each other stratigraphic unit, ± 1 σ. These data represent composite fan surfaces, and were assigned the average

ages for each unit, calculated by D'Arcy et al. (2015). This is effectively a smoothing technique that reduces the temporal resolution of the data set, but greatly increases the size of the data populations to produce D_{50} and D_{84} measurements that represent the landscape as a whole. In a similar way, the median flow widths were calculated for each stratigraphic unit (Q1, Q2, etc.) using all data from each underlying surface. These average data are discussed later, and plotted on all graphs using star symbols to distinguish them from individual fan surfaces.

These D_{50}, D_{84} and median flow width, W, data allow all 35 dated fan surfaces, plus stratigraphic composites, to be viewed as time series and compared with palaeoclimate records. For this purpose we selected the Devil's Hole $\delta^{10}O$ record (Winograd et al., 1997, 2006) and the sea surface temperature reconstruction from ODP site 1016 in the Santa Barbara basin (Yamamoto et al, 2007). These records are close to our study area and have high temporal resolutions, meaning the stratigraphic age control is the limiting factor in our analyses.

Data were analysed using OriginPro v.9.1 and ArcGIS v.10.0. No error weighting was used when calculating regressions or the standard errors on coefficients. Slope distributions for the parent catchments were derived from the National Elevation Dataset (NED) digital elevation model, which has horizontal and vertical spatial resolutions of 9 and 1.5 m, respectively (Gesch et al., 2002).

4.4.3. Exposure age adjustment

The alluvial fan surface ages reported by D'Arcy et al. (2015) are based on ^{10}Be chronologies from previous studies (Zehfuss et al., 2001; Le et al., 2007; Dühnforth et al., 2007). D'Arcy et al. (2015) standardised the assumptions in these age calculations using the linear ^{10}Be production rate and scaling scheme of Lal (1991) and Stone (2000), revised the clast surface lowering rate to 0.5 (+0.5/-0.3) mm ka^{-1}, and correlated the age model to previously-undated surfaces by calibrating the sizes of weathering fractures in surface boulders. As such, the error bars on the ages incorporate a number of factors: (i) erosion rate uncertainty; (ii) scaling scheme and calculation uncertainties; (iii) sampling and measurement uncertainties; (iv) the true range of individual flow ages on a given surface; and (v) uncertainties associated with the fracture-based correlation technique. Typically, the age uncertainties are less than ~ 10 ka for surfaces younger than 50 ka, and 10 to 20 ka for older deposits up to Q1 on Birch creek, which is the oldest surface. These error bars are relatively small in comparison to the actual ages, are largely systematic, and are typical for ^{10}Be exposure dating (e.g., Balco et al., 2008).

Nonetheless, the error bars matter when comparing dated surfaces with high resolution palaeoclimate records that may show significant variability within the estimated age range. For example, the Q1 exposure age on the Birch creek fan was estimated as 137 (± 14.5) ka by D'Arcy et al. (2015), after

Zehfuss et al. (2001), placing it in the middle of the penultimate deglaciation, but the uncertainties outlined above mean that it could date to the penultimate glacial maximum, or the last interglacial that followed. In actual fact, there is independent physical evidence that the Birch creek Q1 deposit dates to the last interglacial period. The Q1 surface is extensive and represents a large volume of sediment exported from this catchment, which was fully occupied by a valley glacier during both the LGM and the penultimate glaciation (Fig. 4.1) (Moore & Mack, 2008; Phillips et al., 2009). Moreover, there are no dated or mapped fan deposits throughout the last glacial period from approximately 120 to 16 ka, despite detailed investigation by Zehfuss et al. (2001) and D'Arcy et al. (2015). This shows that the catchment was relatively inactive during glacial periods with minor sediment export, and suggests that the extensive Q1 deposits were exported while the catchment was not glaciated. The penultimate glacial retreat has been tightly dated to ~ 135 ka by dated moraines (Phillips et al., 2009) and pollen records from Owens lake, which are potentially subject to a short lag time due to transport, show a drop in *Juniperus* pollen starting at 130-126 ka and lasting until ~ 115 ka (Woolfenden, 2003). This agrees very well with the global timing of the last interglacial period, which lasted from 129 to 116 ka (Masson-Delmotte et al., 2013).

Therefore, we interpret the mid-point of the 137 (± 14.5) ka age range reported by D'Arcy et al. (2015) to be a slight over-estimate, and we choose to pin the Birch creek Q1 surface to the mid-point age of 122.5 ka for the last interglacial period (Masson-Delmotte et al., 2013), in all our subsequent analyses. This adjustment is based on the physical observations outlined above, and is within the age uncertainty reported by D'Arcy et al. (2015), representing a reduction in the age estimate of 10 %. This disparity is likely to represent a systematic error that applies all of the fan surface age estimates, and offers a unique opportunity to check the ^{10}Be chronology. Therefore, for consistency we have chosen to apply the same correction factor of 0.9 to the age estimates for all the other fan surfaces in our analyses. This correction makes a negligible difference to the climatic conditions the fan surfaces are correlated to, in the case of deposits younger than 80 ka, and in every case the corrected exposure ages provided below are within the ^{10}Be and fracture width model uncertainties reported by D'Arcy et al. (2015). Consequently, we emphasize that we are simply using physical observations at Birch Creek (c.f., Zehfuss et al., 2001; Phillips et al., 2009; D'Arcy et al., 2015) to deduce that the true deposit age is likely to fall at the younger end of the ^{10}Be uncertainty range, which must be the case for at least the Birch creek fan Q1 surface. A slight over-estimation of the ages could be due to a number of factors. A linear ^{10}Be production rate and scaling scheme was applied by previous studies, but this may be non-linear, which may reduce the age estimates by approximately this amount (e.g., Balco et al., 2008). Additionally, the actual boulder surface lowering rate in Owens Valley may have been slightly lower than 0.5 mm yr^{-1} applied in the ^{10}Be age calculations for some periods of time; indeed, D'Arcy et al. (2015) presented evidence that this might have decreased in the glacial climate to as low as 0.3 mm yr^{-1}, which would also have reduced the age estimates by ~ 2 %.

4.5. Results

4.5.1. Fault scarp measurements

Figure 4.5 shows vertical offsets across measured fault scarps associated with the SNFFZ, against the exposure ages of the respective surfaces (see supplementary information for data). The scarps we measure supplement data from Zehfuss et al. (2001) and Le et al. (2007), agreeing well with these previous studies and giving a time-integrated vertical slip rate of 0.23 ± 0.01 m ka^{-1} (mm yr^{-1}). Measurements were made at various different fault strands (see respective studies and supplementary information) on the dated alluvial fan surfaces, and demonstrate that the strands are slipping at equal rates along the southern SNFFZ, which is to be expected for a simple en-echelon frontal system with no rotation. These data also agree very closely with other throw rate estimates made nearby as well (Gillespie, 1982; Greene et al., 2007; Rood et al., 2011).

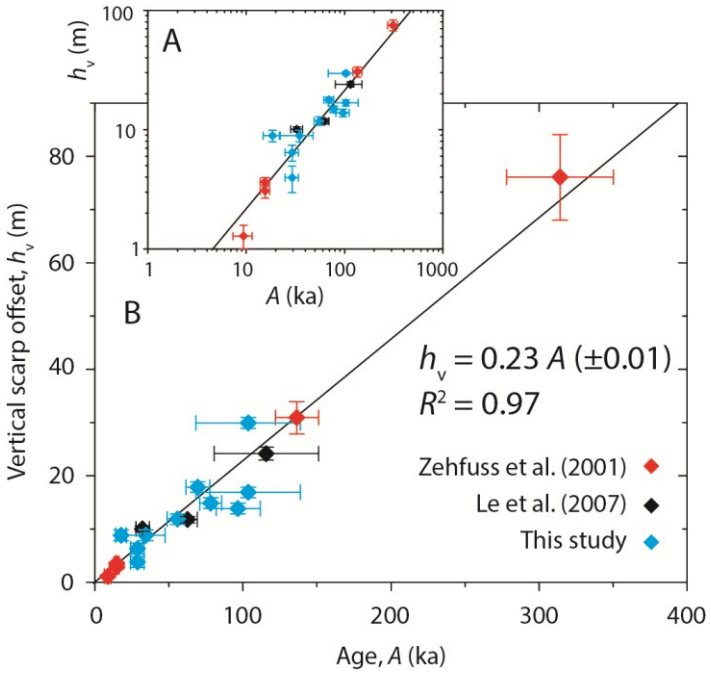

Fig. 4.5. Measured vertical offsets across normal fault scarps observed on surfaces of different age across all 8 alluvial fans, from this study and reported by Zehfuss et al. (2001) and Le et al. (2007). Details are provided in the supplementary information, and the data are plotted in log form (A) and linearly (B). Error bars shown the age uncertainty and measurement precision. All measured faults are slipping at an average rate of ~ 0.23 m ka^{-1} (mm yr^{-1}), for at least ~ 300 ka, and there are no significant changes in slip rate during the last glacial-interglacial cycle, meaning tectonic conditions have remained constant.

These rates derived from single fault strands must be less than the cumulative vertical displacement rate across the full SNFFZ, which has multiple strands (Fig. 4.1). In most areas, the fault zone has 3 to 5 active strands, giving a cumulative displacement rate of ~ 1 mm yr^{-1}, and this matches geodetic constraints from InSAR well (Hammond et al., 2012). This can be illustrated clearly on the Birch creek fan (Fig. 4.1b), where Zehfuss et al. (2001) estimate a vertical slip rate of ~ 0.2 mm yr^{-1} on a fault near the base of the fan, but where additional fault strands are slipping at 0.2 to 0.3 mm yr^{-1} at the catchment mouth/fan apex (Greene et al., 2007). As such, the relative uplift/subsidence rate between the catchments and fans is ~ 1 mm yr^{-1} in this study area, and importantly, has been steady for at least 300 ka. This includes throughout the last glacial-interglacial cycle and there are no effects attributable to post-glacial rebound.

4.5.2. Down-fan rates of grain size fining

We measured the rate of grain size fining from apex to toe on the Q4 (Holocene) surface of the Shepherd creek fan (Fig. 4.6; supplementary information). We sampled grain size every ~ 500 m, and then calculated 3-point moving averages of the data to assess the down-fan fining rate. Taking moving averages minimises local noise in the data (see Methods), ensures that each point represents 3 repeat sampling locations on the fan surface, and allows error bars to be assigned. Figure 4.6a shows the D_{50} grain size (circles) and Fig. 4.6b shows the D_{84} grain size (squares), along the full ~ 10 km length of the fan, for both debris flow channels (solid black) and their lateral levees (open red). In general, the grain size fining rates are very low, which we attribute to the high viscosity and long run-out lengths of the debris flows in this area. The D_{50} decreases by ~ 0.9 ± 0.2 mm km^{-1}, from an initial input grain size of 25 ± 1 mm in the channel (Fig. 4.6a), while D_{84} simultaneously decreases by 2.1 ± 0.4 mm km^{-1}, from an initial grain size of ~ 39 mm (Fig. 4.6b). These values represent 3.5 to 5.0 % of the initial grain size respectively. Similarly, D_{50} data from levee deposits show negligible downstream fining over the 10 km fan length (red circles, Fig. 4.6a); D_{84} decreases by 7.1 ± 1.1 mm km^{-1} from an input value of ~ 111 mm, a fining rate which is ~ 6 % of the initial grain size. The low down-system fining rates indicate that small differences in distance from fan apex to measurement site are unlikely to significantly affect grain size measurements for debris flow deposits in this study. Nevertheless, to minimise fining effects, we restricted all other grain size sampling to the upper 3 km of the fans near their apices (blue box), which is also where most raised terraces are exposed. The one exception to this is the Birch creek fan, where older and dated terraces are exposed at the base of the fan due to the presence of the Fish Springs fault (see Zehfuss et al., 2001; D'Arcy et al., 2015). As such, grain size data from the Birch creek surfaces may be slightly finer in comparison to the other systems, and we consider the importance of this later.

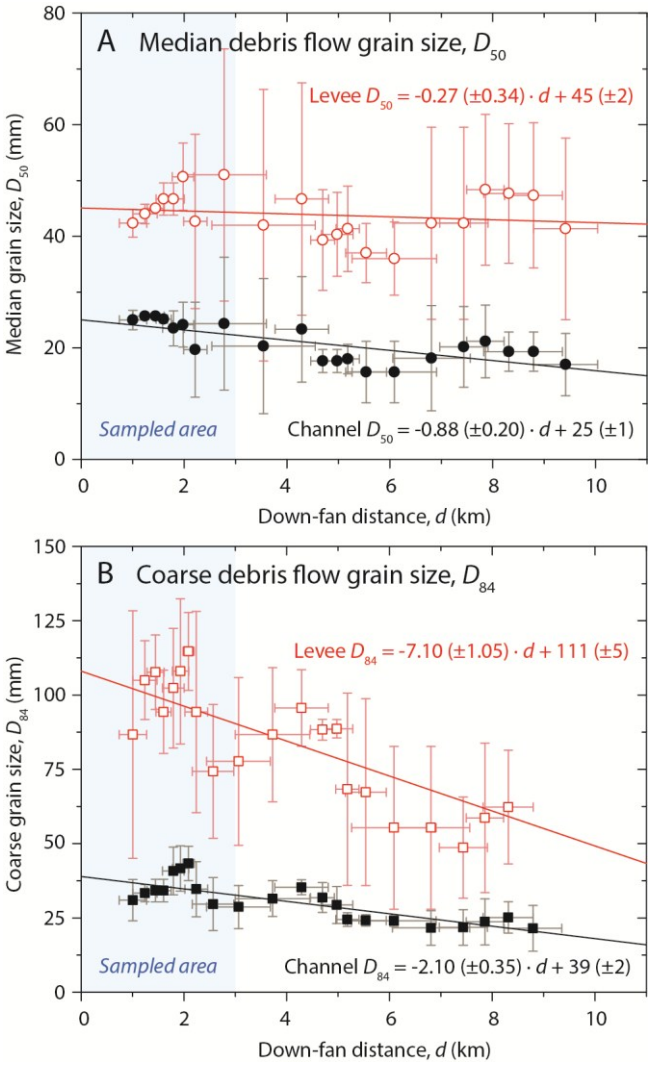

Fig. 4.6. Debris flow grain size data from the Q4 (Holocene) surface of the Shepherd creek fan, from apex to toe. Median, D_{50} (A), and coarse, D_{84} (B) grain sizes are shown. Each point is a spatial average of 3 Wolman point count measurements, each with 100 ≥ 1 mm clasts, and channels and levees were sampled separately. Error bars show the spatial spread of each 3 localities down-system and the variability in grain size between them. Repeat sampling is essential for a meaningful average, as the flow deposits are variable across space (see text for discussion). Down-system fining can be modelled with linear regressions, with average fining rates of ~ 0.3 to ~ 0.9 mm km^{-1} for D_{50} and ~ 2 to ~ 7 mm km^{-1} for D_{84}. To minimise these effects, all other grain size data were collected from the upper 3 km of the fans near their apices (blue box).

The down-fan fining effect is clearly smaller than the spatial variability in grain size between sampling sites on the same dated fan surface. On average, grain size varies by 20 to 25 % of the median value between sites on a fan surface, which is to be expected for debris flow deposits that are spatially variable. This underscores the importance of spatial averaging, and making repeat measurements at a minimum of 3 different localities per dated surface, to converge on a grain size distribution that is representative for that deposit overall (see Methods). In our subsequent analyses,

D_{50} and D_{84} values are calculated for cumulative grain size distributions including all localities measured on each surface, and for this reason we include ± 1 σ error bars that shows the standard deviation of D_{50} and D_{84} if they are calculated for each single sampling site. The data in Fig. 4.6 demonstrate that spatial averaging is a suitable approach for sampling debris flow grain size, and that the D_{50} and D_{84} measurements from multiple sampling sites (data points) are much less susceptible to noise than single sampling sites (error bars).

4.5.3. Grain size and flow width data

In Fig. 4.7 we show the cumulative grain size distribution curves for every dated fan surface on the 8 sampled alluvial fans (A to H), plus composite fan units containing grain size data measured on each stratigraphic unit across all 8 fan systems (I). These are coloured by stratigraphic unit, with warm colours corresponding to surfaces deposited under interglacial climatic conditions (Q1, Q4, Modern), and cool colours corresponding to surfaces deposited under glacial climatic conditions (Q2, Q3). In total, 35 individual surfaces were sampled. Debris flow channels and levees are presented separately, and the total number of clasts measured on each fan is given as '*n*'. Full data sets are available in the supplementary information. The *x*-axis is shown in log form to clearly display the grain size trends across 3 orders of magnitude in particle diameter from 1 mm to 1 m.

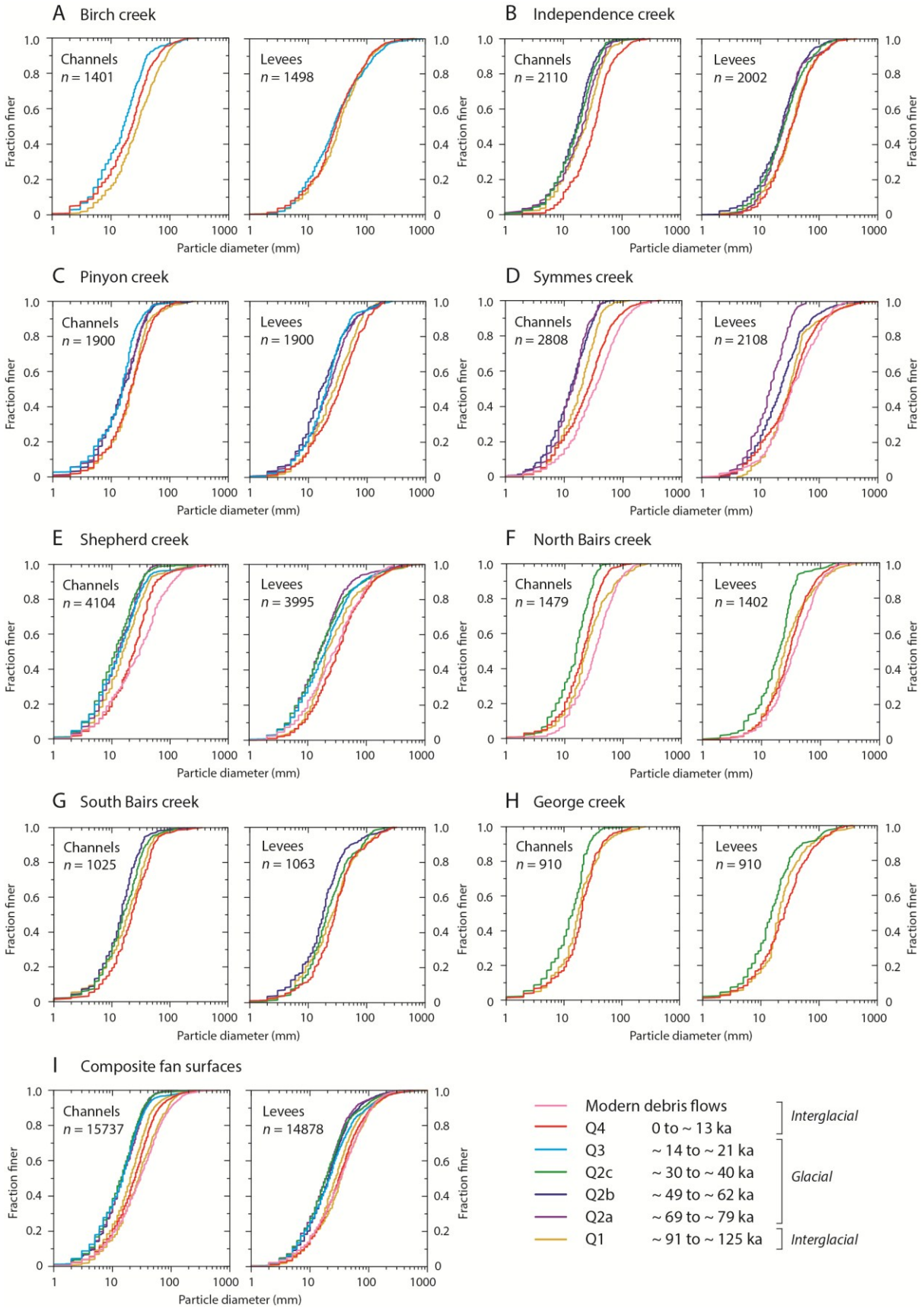
A Birch creek
Channels
n = 1401
Levees
n = 1498
B Independence creek
Channels
n = 2110
Levees
n = 2002
C Pinyon creek
Channels
n = 1900
Levees
n = 1900
D Symmes creek
Channels
n = 2808
Levees
n = 2108
E Shepherd creek
Channels
n = 4104
Levees
n = 3995
F North Bairs creek
Channels
n = 1479
Levees
n = 1402
G South Bairs creek
Channels
n = 1025
Levees
n = 1063
H George creek
Channels
n = 910
Levees
n = 910
I Composite fan surfaces
Channels
n = 15737
Levees
n = 14878
Fraction finer
Particle diameter (mm)
Modern debris flows
Q4 0 to ~ 13 ka
Q3 ~ 14 to ~ 21 ka
Q2c ~ 30 to ~ 40 ka
Q2b ~ 49 to ~ 62 ka
Q2a ~ 69 to ~ 79 ka
Q1 ~ 91 to ~ 125 ka
Interglacial
Glacial
Interglacial

Fig. 4.7. Cumulative grain size distribution curves for dated debris flow fan deposits (channels on the left, levees on the right), for the 8 alluvial fans sampled (A to H), and composite stratigraphic units combining data from all fans (I). The number of grains recorded per fan is given as '*n*'. Wolman point counting was performed in the field, with a minimum of 100 clasts per sampling locality, and a minimum of 3 localities (on average 8) per dated surface. Curves are coloured according to their stratigraphic units (see key); warm colours represent surfaces deposited under interglacial climate conditions, cool colours represent surfaces deposited under glacial climatic conditions. In all fan systems, the interglacial deposits are measurably coarser than glacial deposits. This effect is particularly clear in the composite grain size curves (I) containing the full data set.

Each cumulative grain size distribution has a sigmoid form with the majority of clasts between 10 and 100 mm in diameter. Levees are ~ 30 % coarser than channels deposits on average, which is due to grain size segregation within debris flows (e.g., Johnson et al., 2012). In all examples, the 'glacial' age surfaces (cool colours) are finer-grained than the 'interglacial' age surfaces (warm colours), by 10s of mm. The last interglacial (Q1, yellow) data are highly comparable to the current interglacial data (Q4, red, and Modern, pink), and always coarser than Q2 and Q3 surfaces. All 8 fans show similar grain size distributions, so it is meaningful to combine their grain size counts into composite curves for each stratigraphic unit (Fig. 4.7i), and these illustrate clearly how the Q1, Q4 and modern deposits are significantly coarser-grained than the Q2 and Q3 deposits across 3 orders of magnitude in grain size.

These curves can be converted into quantitative time series by extracting the D_{50} and D_{84} particle diameters (Table 4.1). We also recorded the widths of debris flow deposits in the field. All these data are plotted in Fig. 4.8a-e, for each individual catchment-fan system (coloured points), and also for composite alluvial fan surfaces (stars). In Fig. 4.8f, the Devil's Hole $\delta^{18}O$ record (Winograd et al., 1997, 2006) and sea surface temperatures from ODP site 1016 in the Santa Barbara basin (Yamamoto et al., 2007) are plotted as palaeoclimate indicators for comparison. All four grain size series show a sustained correlation with the palaeoclimate records for the entire last glacial-interglacial cycle. Grain size is coarser in warmer interglacial climates and finer in cooler glacial climates, typically doubling as the climate warmed and dried from the LGM to the present day. Grain size is coarser in lateral levees compared to the debris flow channels, as expected. The median particle diameter, D_{50}, reaches a minimum of ~ 15 mm (channels) and ~ 20 mm (levees) during the glacial period, and increases to ~ 25 to 30 mm during the current and last interglacials. Similarly, the D_{84}, increases from ~ 30 mm (channels) and ~ 50 mm (levees) in the glacial period to ~ 70 to 80 mm (channels) and ~ 90 mm (levees) in the interglacial periods. The rate of fining as the climate cooled is slower than the rate of coarsening after the LGM, mirroring the asymmetry of the glacial-interglacial cycle.

Alluvial fan	Surface	Surface exposure age		Channel grain size					Levee grain size					Debris flow width		
		Age (ka)	± (ka)	No. clasts	D_{50} (mm)	± (mm)	D_{84} (mm)	± (mm)	No. clasts	D_{50} (mm)	± (mm)	D_{84} (mm)	± (mm)	No. flows	Median width (m)	± (m)
Individual alluvial fan surfaces																
Symmes	Modern	-	-	497	34.0	6.3	86.0	19.7	210	34.0	1.4	108.2	18.6	12	26.0	4.1
Shepherd	Modern	-	-	699	30.0	11.2	80.3	20.6	500	28.5	11.2	90.0	33.2	23	28.0	15.1
North Bairs	Modern	-	-	302	33.5	6.5	72.8	3.7	300	36.0	9.8	82.0	8.9	5	36.0	6.1
Symmes	Q4	3.9	1.6	1,212	25.0	8.1	59.2	21.3	1,098	33.0	7.6	85.0	25.8	22	29.5	12.5
Shepherd	Q4	5.5	3.0	1,007	24.0	5.9	47.0	21.2	1,195	32.0	7.8	95.0	25.6	21	34.0	21.7
South Bairs	Q4	5.6	2.4	213	22.0	1.4	46.0	2.4	210	29.0	-	65.0	16.2	10	27.5	6.3
North Bairs	Q4	6.7	5.7	674	21.0	2.9	39.0	8.1	600	30.0	3.8	66.0	17.0	7	26.0	6.3
Pinyon	Q4	7.5	3.4	400	22.0	2.8	45.0	12.2	400	34.0	2.2	84.2	11.8	7	23.0	5.4
Birch	Q4	8.5	2.1	501	23.0	16.5	47.0	17.2	500	30.0	12.6	88.3	21.4	11	36.0	21.1
George	Q4	11.9	5.1	300	20.0	0.6	35.0	6.1	300	26.0	1.3	68.3	15.2	10	28.0	7.9
Independence	Q4	13.1	4.6	610	34.0	6.3	63.0	18.2	501	34.0	9.5	78.0	16.0	13	32.0	9.2
Birch	Q3	14.1	1.7	500	16.0	4.5	35.0	8.3	598	27.5	4.5	102.0	29.5	7	16.0	12.1
Shepherd	Q3	18.7	3.7	998	14.0	4.0	30.5	14.2	999	20.0	7.3	54.0	23.1	20	32.0	23.1
Pinyon	Q3	21.2	4.3	600	15.0	4.0	26.0	7.3	600	20.0	3.8	810.0	9.0	9	20.0	9.4
Shepherd	Q2c	29.6	4.5	900	12.0	3.3	26.2	6.3	801	16.0	8.1	190.0	20.1	12	21.5	3.8
George	Q2c	35.2	13.2	310	14.0	2.0	23.0	1.6	310	15.0	4.4	36.0	6.1	13	24.0	10.5
North Bairs	Q2c	36.4	9.4	200	16.0	1.1	28.0	1.4	200	20.0	4.9	183.0	3.8	9	24.0	13.2
South Bairs	Q2c	37.4	13.5	200	16.0	4.2	32.2	1.4	250	21.0	1.4	373.0	3.5	2	25.5	0.7
Independence	Q2c	40.2	10.4	400	18.0	1.7	34.0	2.3	401	25.0	1.6	61.0	14.4	6	20.5	3.2
Pinyon	Q2b	48.6	12.0	300	16.0	2.0	32.0	2.0	300	16.0	0.6	45.2	7.0	2	17.0	5.7
Symmes	Q2b	56.5	6.9	699	13.0	2.2	27.0	10.9	500	22.0	4.0	776.0	18.5	6	19.0	4.2
Independence	Q2b	58.6	13.9	500	17.0	2.4	32.0	6.1	500	23.0	3.2	156.0	6.5	4	22.0	2.6
South Bairs	Q2b	62.1	11.2	312	15.0	0.6	27.2	4.0	303	18.0	1.8	279.0	1.6	5	29.0	6.0
Shepherd	Q2a	68.2	7.5	300	13.0	3.0	30.0	7.4	400	15.5	3.8	40.0	3.2	7	25.0	6.8
Pinyon	Q2a	70.3	8.1	300	16.0	3.2	32.0	3.5	300	22.0	4.0	51.2	3.0			
Symmes	Q2a	72.5	14.6	100	14.0	-	24.2	-	100	15.0	-	29.0	-			
Independence	Q2a	79.0	7.4	100	21.0	-	41.0	-	100	24.5	-	48.5	-			
Independence	Q1	90.9	18.1	500	24.0	3.2	45.0	7.3	500	34.0	2.7	72.0	7.2	8	23.0	5.7
George	Q1	97.4	14.9	300	18.0	3.1	40.0	13.5	300	21.0	1.3	50.2	8.7	2	29.0	8.5
Symmes	Q1	104.1	35.1	300	19.0	2.6	36.0	5.9	200	31.0	1.1	61.1	25.5			
Shepherd	Q1	104.1	35.1	200	15.5	-	37.0	4.2	100	20.5	-	72.4	-			
South Bairs	Q1	104.1	35.1	300	19.0	1.5	40.2	9.2	300	25.0	2.8	69.2	8.2			
Pinyon	Q1	104.7	17.3	300	22.0	2.3	38.0	19.5	300	28.0	2.9	66.3	6.1	4	28.5	7.3
North Bairs	Q1	104.9	11.9	303	23.0	6.5	64.4	30.0	302	25.0	3.0	74.5	1.8			
Birch	Q1	122.5	14.5	400	28.0	7.7	68.2	22.7	400	34.0	5.5	91.0	19.3			

Alluvial fan	Surface	Surface exposure age		Channel grain size					Levee grain size					Debris flow width		
		Age (ka)	± (ka)	No. clasts	D_{50} (mm)	± (mm)	D_{84} (mm)	± (mm)	No. clasts	D_{50} (mm)	± (mm)	D_{84} (mm)	± (mm)	No. flows	Median width (m)	± (m)
Composite alluvial fan surfaces																
All fans	Modern	-	-	1,498	31.0	8.6	80.0	18.1	1,010	32.0	9.1	90.0	24.9	40	27.0	12.2
All fans	Q4	7.8	5.9	4,917	24.0	8.4	50.0	18.6	4,804	31.0	7.6	82.0	23.5	101	29.0	15.0
All fans	Q3	18.0	4.4	2,098	15.0	4.2	31.0	11.2	2,197	22.0	6.3	58.6	33.4	36	24.5	20.0
All fans	Q2c	35.8	6.9	2,010	14.0	3.5	29.0	5.7	1,962	19.0	6.3	48.2	17.3	42	22.0	8.7
All fans	Q2b	56.5	8.8	1,811	15.0	2.6	30.0	4.5	1,603	20.0	4.1	47.0	14.3	17	21.0	5.7
All fans	Q2a	72.5	7.3	800	15.0	3.3	31.0	6.7	900	19.0	4.6	42.0	7.2	7	25.0	6.8
All fans	Q1 *	101.4	11.8	2,203	20.0	4.0	41.0	14.5	2,002	27.0	5.2	69.0	11.1	14	24.5	6.8

Table 4.1. Exposure age estimates, grain size measurements, and debris flow width data for each individual alluvial fan surface, and composite surfaces calculated using data from all fans. Exposure ages are taken from D'Arcy et al. (2015), who re-interpret the data of Zehfuss et al. (2001), Duhnforth et al. (2007) and Le et al. (2007), adjusted by pinning Birch creek Q1 to the middle of the last interglacial period (see text for explanation). Error bars include all sources of uncertainty and the variation in ages observed across each surface. Grain size was measured by Wolman point counting in the field, and error bars on the median (D_{50}) and 84th percentile (D_{84}) show ± 1 standard deviation between values recorded at each individual sampling locality. This is also true for the flow width data, which were measured both in the field using a laser range finder, and using high resolution (< 1 m) aerial imagery.

***The composite Q1 surface excludes data from the Birch creek fan Q1 surface because this is substantially older and so is plotted separately.**

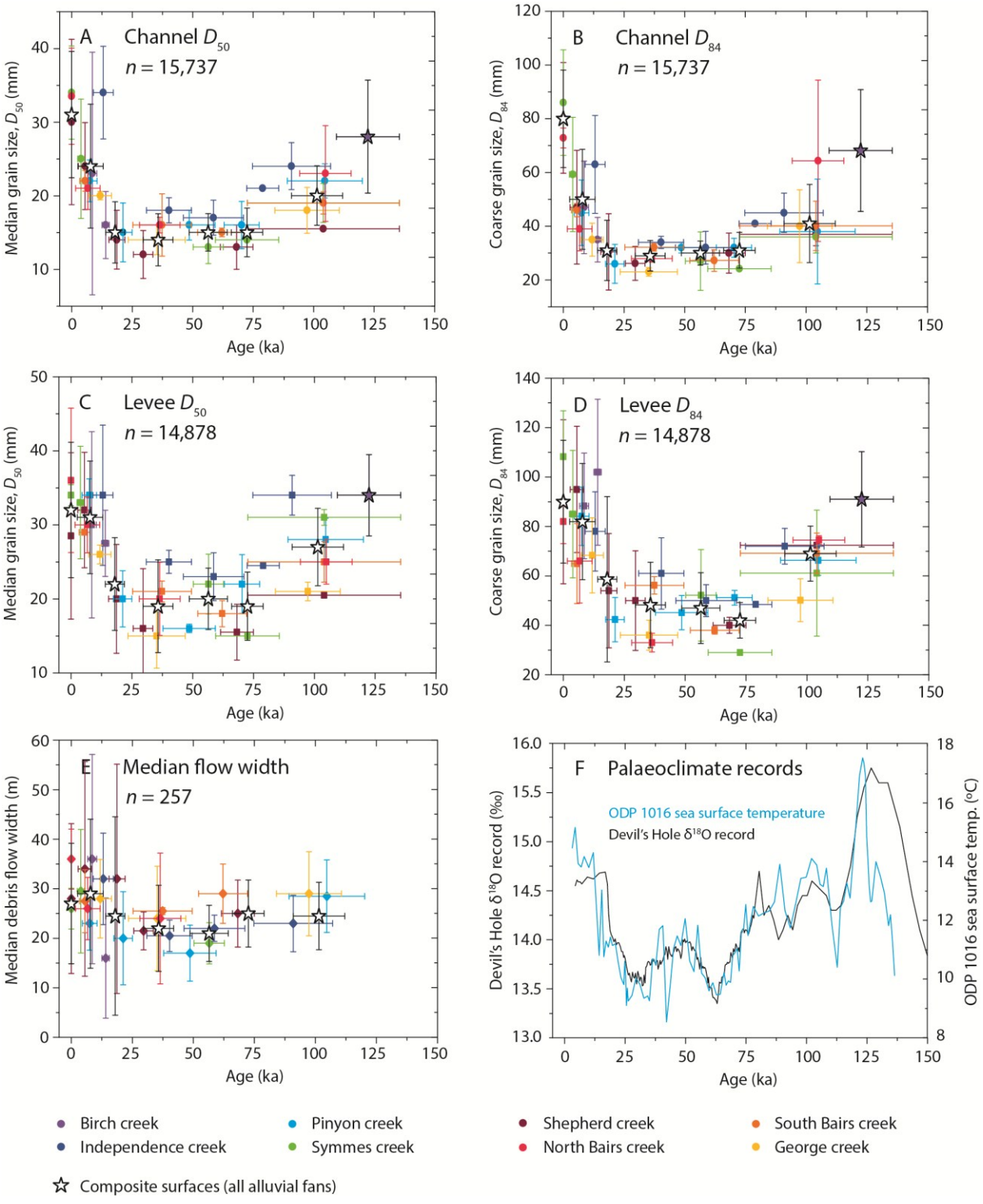

Fig. 4.8. Time series of debris flow grain size (A to D) and median flow width (E), compared with palaeoclimate records (F). ODP-1016 sea surface temperature is reported from Yamamoto et al. (2007) and the Devil's Hole $\delta^{18}O$ curve is reported from Winograd et al. (2006). Data are coloured according to the catchment-fan system, *n* is the number of clasts/flow widths measured, and error bars display age uncertainty (*x*) and ± 1 σ (*y*). Stars show composite surfaces for each stratigraphic unit, calculated using data from all 8 fans. The grain size data show sustained correlations with palaeoclimate, becoming finer

during the cooler glacial climate and approximately doubling in D_{50} and D_{84} as the climate warmed and dried to the present day. Similarly, flows are smaller on average (20 to 25 m) during the glacial period, and become larger (up to ~ 30 m wide) and more variable in size in the current interglacial. These alluvial fan deposits preserve a high-resolution record of the last glacial-interglacial cycle. Subtle differences exist between the systems, e.g., Independence creek deposits are relatively coarse and Shepherd creek deposits are fine, but these differences are much smaller than the amplitude of the overall climatic signal preserved, meaning all 8 fans can be combined into a single record.

All 8 catchment-fan systems show similar climate signals with only subtle differences, e.g., deposits on the Independence creek fan are slightly coarser, and deposits on the Shepherd creek fan are slightly finer. These differences are on the scale of several millimetres, an order of magnitude less than the differences observed with age. As such, the composite grain size data (stars), calculated across all fans, meaningfully average the grain size signal exported from the integrated eastern front of the southern Sierra Nevada. The spatial variability in grain size on a given surface, shown by the *y*-error bars, is also smaller than the total amplitude of the grain size variation observed during this ~ 125 ka record. As pointed out earlier, the Birch creek data were collected around the base of the fan, whereas all other surfaces were sampled in the top 3 km. Therefore the Birch creek points (coloured in purple) may slightly underestimate the D_{50} and D_{84} grain sizes. Figure 4.6 indicates that this will have a negligible effect on the D_{50} measurements, on the order of ~ 2 to 5 mm for levee and channel data, respectively. For the D_{84} measurements, the Birch creek data might be ~ 12 mm (channels) and ~ 40 mm (levees) finer as a result of being collected further down-fan (see Fig. 4.6). We do not apply a correction for this effect, but if we did it would only serve to amplify the overall trend, rather than diminish it.

The median flow width data (Fig. 4.8e) also show variations through time. In the early glacial period prior to ~ 70 ka, the flows are 20 to 30 m wide, decreasing to 15 to 25 m (~ 20 m on average) during the coolest part of the glacial period between 20 and 60 ka. The median width then increases to ~ 25 to 35 m during the current interglacial, i.e., Holocene flows are ~ 10 m larger than LGM flows on average, and some fans show an even greater difference. The spatial variability in flow width on a given surface (*y*-error bars) is ~ 10 m during the glacial period, but increases substantially after the LGM, to several tens of metres. This indicates that flow sizes became more variable, as well as larger on average, as the climate warmed.

4.5.4. Comparison with palaeoclimate records

Figure 4.8 shows that debris flow grain size in particular, and to some extent flow widths, are correlated with palaeoclimate records. This can be explored by plotting each data series against a

continuous palaeoclimate record directly. We have selected the ODP site 1016 sea surface temperature reconstruction reported by Yamamoto et al. (2007) for this purpose, because it is a high-resolution, low-noise, continuous record from offshore California, near to our study locations. It is highly correlated with the Devil's Hole $\delta^{18}O$ record reported by Winograd et al. (1997, 2006) (Fig. 4.4), but has the advantage that it allows the data to be compared with temperature, which is a primary climatic variable. In Fig. 4.9 we plot each grain size series against sea surface temperature (Table 4.2). The points for individual fan surfaces are coloured according to their exposure ages from blue (last interglacial), through green-yellow (glacial period) to red (modern), and data from all 8 systems are plotted together, given that they behave similarly (Figs 4.7 and 4.8). Stars again represent averages across all 8 systems. We have included exponential regressions (black lines), which best fit the data. Grain size shows a sustained correlation with temperature in each case, coarsening exponentially by 9 to 14 % per 1 °C of warming, over the full 5 to 6 °C temperature range during the last glacial-interglacial cycle. All 35 dated surfaces follow the same trends, with no obvious outliers. Two directions of temperature change are recorded; cooling from the last interglacial (blue) towards the LGM (green-yellow), and subsequent warming into the Holocene and present day (orange-red). The cooling and warming trends exhibit the same temperature dependence, with no evidence of hysteresis, meaning the grain size response is not sensitive to the trajectory of climate change, and the response timescale must be rapid. The majority of the data ($R^2 \sim 0.7$) are modelled effectively using an exponential relationship, and we return to the relevance of this in the discussion.

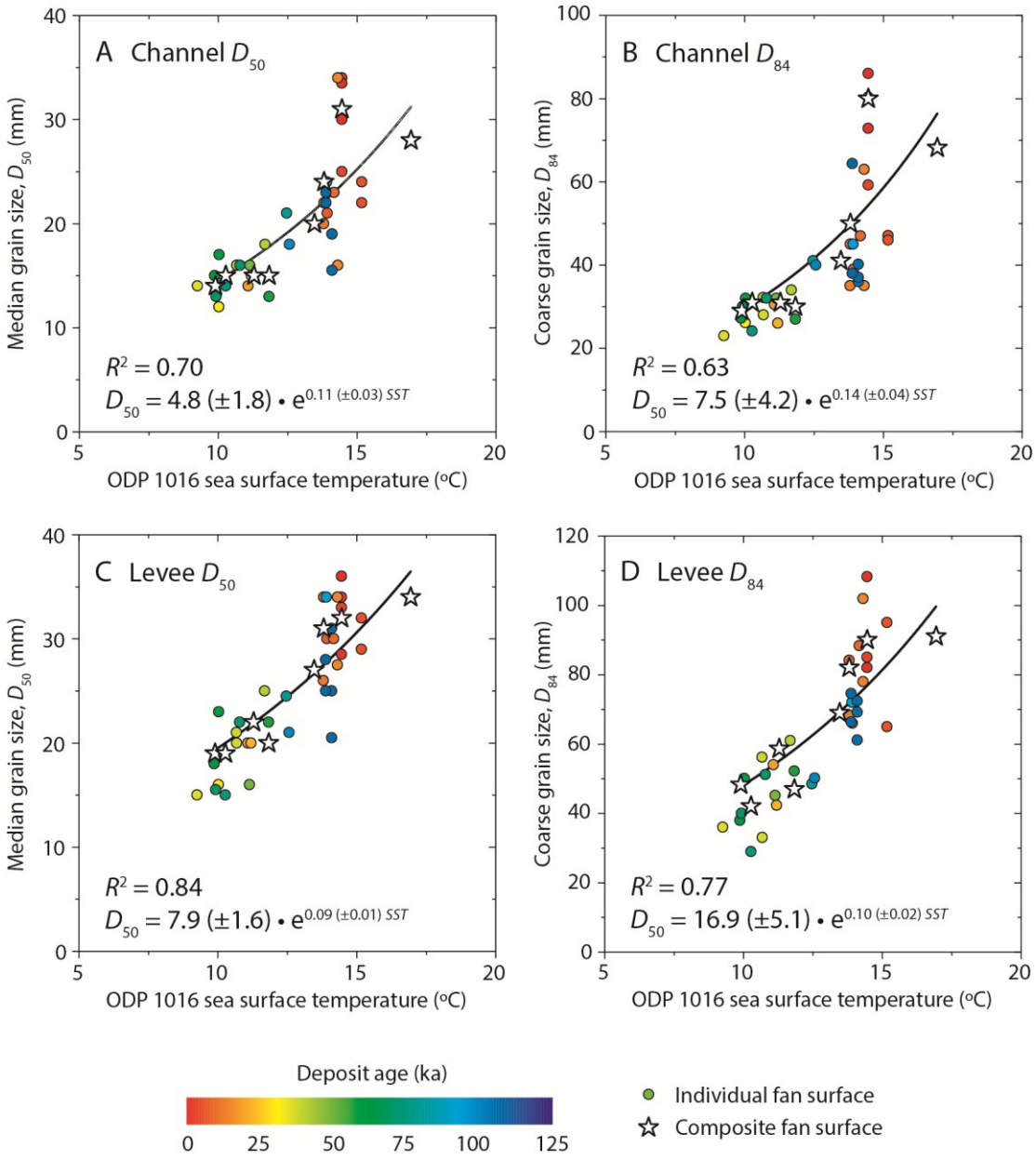

Fig. 4.9. Plots of grain size against ODP-1016 sea surface temperature (Yamamoto et al., 2007). All 35 fan surfaces are plotted together and each point is coloured according to exposure age from red (current interglacial) to blue (last interglacial). Stars represent composite fan units for which data has been combined across all 8 alluvial fans. The total amplitude of glacial-interglacial climate changes captured by this record is ~ 6 °C. Exponential trends fit the grain size data well (R^2 averages 0.74), increasing by an exponent of 9 to 14 % per 1 °C of warming. The cooling trend from the last interglacial (blue) to the glacial maximum (yellow) falls on the same trend as the subsequent warming, with no hysteresis.

Alluvial fan	Surface	Surface exposure age		ODP 1016 sea surface temperature		
		Age (ka)	± (ka)	Temperature (°C)	+ uncertainty (°C)	- uncertainty (°C)
Individual alluvial fan surfaces						
Symmes	Modern	-	-	14.5	-	-
Shepherd	Modern	-	-	14.5	-	-
North Bairs	Modern	-	-	14.5	-	-
Symmes	Q4	3.9	1.6	14.5	0.7	-
Shepherd	Q4	5.5	3.0	15.2	-	1.4
South Bairs	Q4	5.6	2.4	15.2	-	1.4
North Bairs	Q4	6.7	5.7	13.9	1.2	0.1
Pinyon	Q4	7.5	3.4	13.8	1.4	0.0
Birch	Q4	8.5	2.1	14.2	-	0.4
George	Q4	11.9	5.1	13.8	0.5	3.0
Independence	Q4	13.1	4.6	14.3	-	3.6
Birch	Q3	14.1	1.7	14.3	- 1.3	3.5
Shepherd	Q3	18.7	3.7	11.1	2.0	0.5
Pinyon	Q3	21.2	4.3	11.2	0.2	1.4
Shepherd	Q2c	29.6	4.5	10.0	0.1	0.9
George	Q2c	35.2	13.2	9.3	2.6	0.7
North Bairs	Q2c	36.4	9.4	10.7	1.1	2.2
South Bairs	Q2c	37.4	13.5	10.7	1.4	2.1
Independence	Q2c	40.2	10.4	11.7	0.4	3.2
Pinyon	Q2b	48.6	12.0	11.1	0.9	2.6
Symmes	Q2b	56.5	6.9	11.8	0.2	2.4
Independence	Q2b	58.6	13.9	10.0	2.0	0.6
South Bairs	Q2b	62.1	11.2	9.9	2.0	0.4
Shepherd	Q2a	68.2	7.5	9.9	2.6	0.5
Pinyon	Q2a	70.3	8.1	10.8	1.7	1.3
Symmes	Q2a	72.5	14.6	10.3	2.4	0.8
Independence	Q2a	79.0	7.4	12.5	0.1	2.2
Independence	Q1	90.9	18.1	13.9	0.2	2.4
George	Q1	97.4	14.9	12.6	1.5	0.8
Symmes	Q1	104.1	35.1	14.1	3.4	4.0
Shepherd	Q1	104.1	35.1	14.1	3.4	4.0
South Bairs	Q1	104.1	35.1	14.1	3.4	4.0
Pinyon	Q1	104.7	17.3	13.9	3.1	3.5
North Bairs	Q1	104.9	11.9	13.9	0.2	3.5
Birch	Q1	122.5	14.5	16.9	0.6	6.8
Composite alluvial fan surfaces						
All fans	Modern	-	-	14.5	-	-
All fans	Q4	7.8	5.9	13.8	1.4	0.0
All fans	Q3	18.0	4.4	11.3	1.7	0.7
All fans	Q2c	35.8	6.9	9.9	1.9	1.4
All fans	Q2b	56.5	8.8	11.8	0.2	2.4
All fans	Q2a	72.5	7.3	10.3	2.3	0.5
All fans	Q1 *	101.4	11.8	13.5	0.6	3.1

Table 4.2 (previous page). Sea surface temperature estimates from ODP site 1016 in the Santa Barbara basin offshore California (reported directly from Yamamoto et al., 2007). Temperature is reported for the estimated exposure age of each surface in Table 1, with + and – error bars showing the full range of possible temperatures that fall within the range of uncertainty on the exposure ages.

Debris flow widths are slightly less sensitive to past climate changes than the grain size measurements (Fig. 4.8e). This observation invites a direct comparison of grain size and flow width; a scaling that is not well documented. We plot the D_{50} and D_{84} data against median flow width for each dated surface (channels in black, levees in red), and composite surfaces, in Fig. 4.10. Larger debris flows do have coarser grain sizes in general terms, with the average D_{50} increasing by 1 to 2 mm per additional metre of flow width, and D_{84} increasing by 4 to 6 mm m^{-1} (c.f., McCoy et al., 2012; 2013). These regressions are fitted to the composite surface data, and the R^2 values are slightly higher for lateral levees (0.6 to 0.7) than for channels (0.4 to 0.5). In this sense, the regressions are statistical averages for an idealised flow, but single events in reality are much more stochastic. In section 6 we discuss what grain size therefore represents in debris flow deposits, but it is clear that (i) the grain size time series are particularly sensitive to past climate change, and (ii) flow widths partially correlate with palaeoclimate proxies and correlate with ~ 50 % of the observed grain size variations.

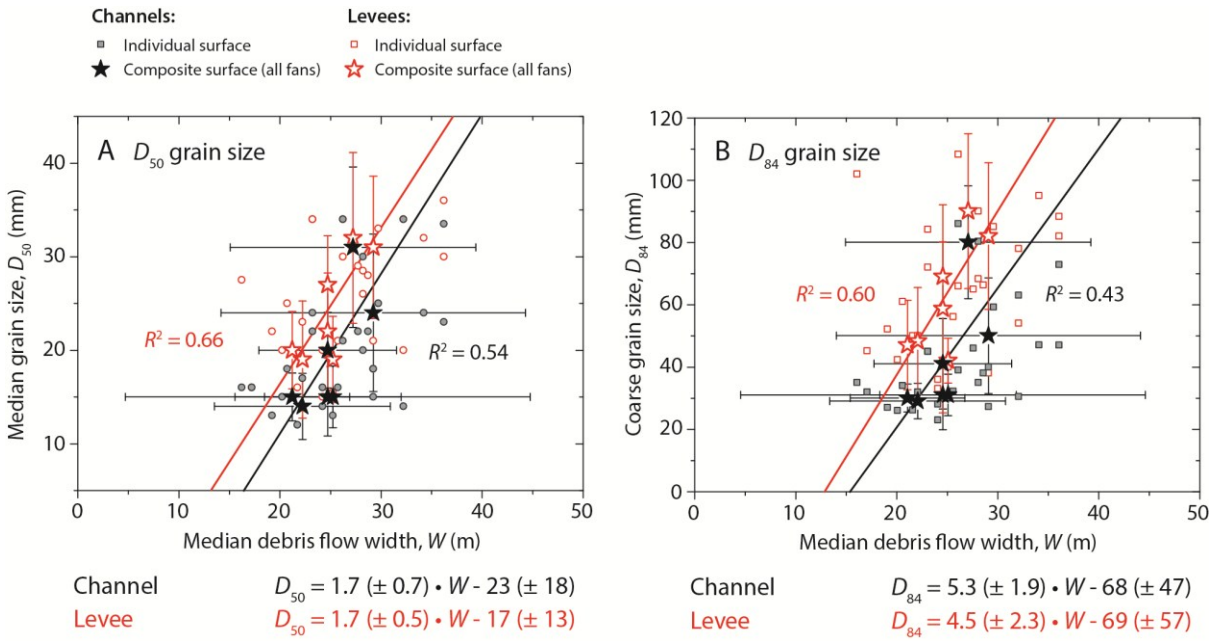

Fig. 4.10. Plots of D_{50} (A) and D_{84} (B) debris flow grain size (channels in black, levees in red) against median flow width on each dated fan surface. Points represent individual fan surfaces, and stars represent composite units averaged across all 8 systems. Error bars show ± 1 σ, and linear regressions are fitted to the composite data. Equations are given beneath each graph. In general, grain size is coarser in wider flows, and is therefore related to event size. However this correlation only explains 40 to 70 % of the data and requires sufficient spatial averaging, i.e., grain size and/or flow size are influenced by additional variables. The D_{50} and D_{84} grain sizes increase by an average of ~ 2 and ~ 5 mm m^{-1}, respectively.

4.5.5. Sediment sources

Sediment sources in Sierra Nevada catchments must exert a control on the grain size distribution delivered to the fans. Figure 4.11 shows slope distribution maps for the 8 systems, mapped using the National Elevation Dataset (NED) at a horizontal/vertical resolution of 9/1.5 m. All 8 catchments have similar slope distributions independent of total area or relief, with the steepest hillslopes distributed throughout the catchments, even at lower elevations. In fact, many of the highest elevations have lower slopes due to the presence of glacially-eroded troughs and cirques, and the former paths of glaciers can be clearly identified. Cumulative slope distributions (Fig. 4.11b) show few differences between the catchments. Those with the most extensive former glaciation (Birch creek and Independence creek) have slightly gentler slope distributions as a result, but slope is not correlated with total catchment area or relief. The median slope is 25 to 35°, i.e., the critical failure angle, resulting in widespread landsliding throughout the catchments (Fig. 4.3a).

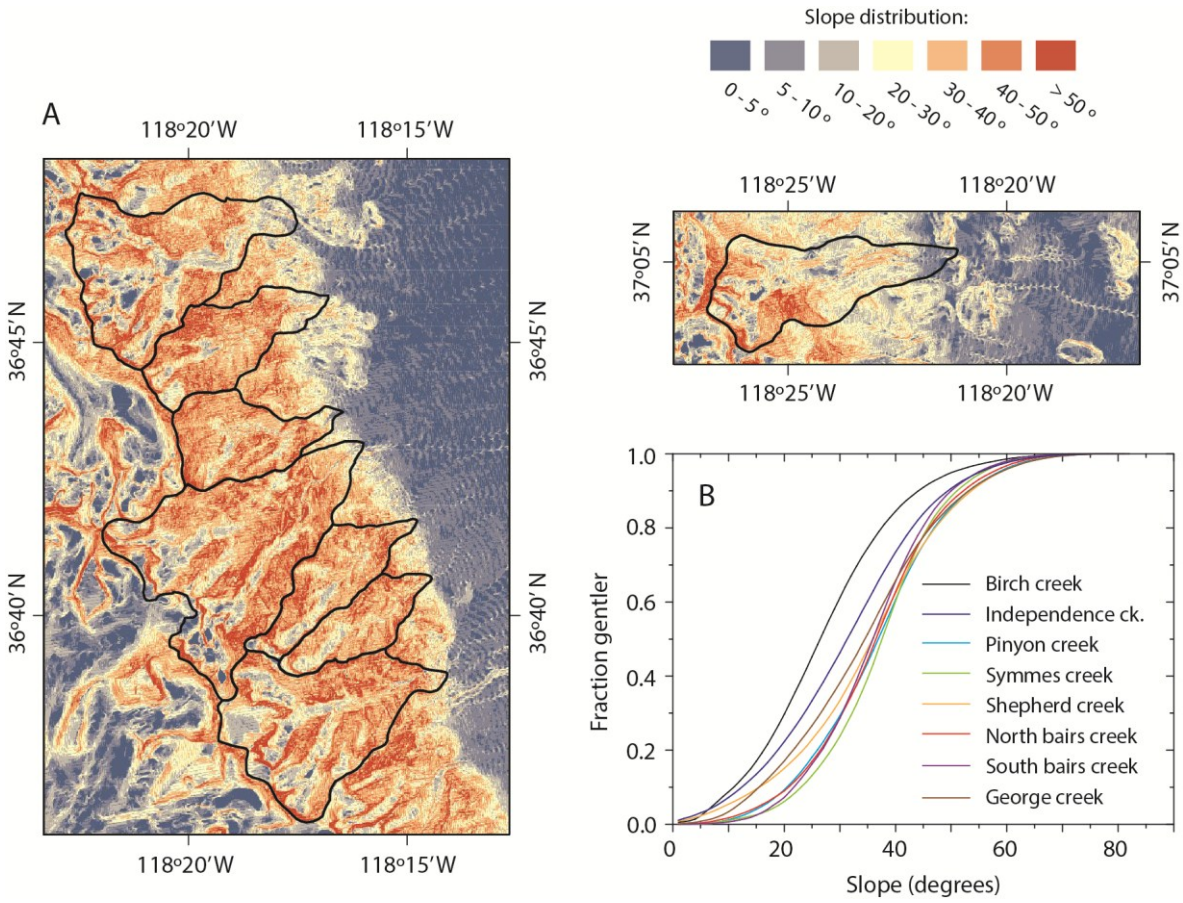

Fig. 4.11. Slope distributions in the study catchments. (A) Surface slope maps characterised using the National Elevation Dataset (NED) digital elevation model, with a horizontal/vertical resolution of 9/1.5 m. Catchments have similar slope distributions, and troughs formerly occupied by glaciers can be clearly identified. Slopes are often lower at the higher elevations, due to the presence of cirques. The steepest

slopes are distributed throughout the catchments, including below the full extents of past glaciers. The fans have low surface slopes < 10 °, and incision can be identified at the apices of fans constructed by the largest catchments, e.g., Independence, Shepherd and George creeks. (B) Cumulative slope distributions for all 8 catchment systems. Catchments that were fully glaciated at the LGM have lower slopes in general (Birch creek and Independence creek), due to the presence of glacial troughs and cirques. No other significant differences exist between the catchments; slope is not correlated with total area or relief. The median slope is ~ 25 to 35 °, i.e., the critical failure angle, resulting in widespread landsliding.

Landslides and rockfalls are the major sources of sediment in these systems, along with moraine sediments deposited by former glaciers (mapped in Fig. 4.1). Each of these sediment sources are sampled by debris flows, and their grain size distributions are characterised in Fig. 4.12 and Table 4.3, as measured in the Independence and Symmes creek catchments. Cumulative grain size distribution curves (Fig. 4.12a, coloured lines) are compared with the modern (black lines) and Q2c (grey lines) grain size distributions measured across all 8 alluvial fans for both channels (solid) and levees (dashed), taken from Fig. 4.7i and representing the coarsest and finest end members respectively. These curves show that landslides supply the finest grain size supply in both catchments (D_{50} ~ 30 mm). A representative example from Symmes creek (Fig. 4.12b) shows a landslide dissected by the modern debris flow channel (marked by trees). Rockfalls provide the coarsest grain size supply in both catchments, mostly comprising large granite blocks with dimensions of 10s of cm to several metres predetermined by bedrock joint spacing (Fig. 4.12c). The grain size distribution of rockfalls is an order of magnitude coarser than any of the fan deposits further down-system (Fig. 4.7). Moraine sediments represent an intermediate grain size source, with a D_{50} of ~ 40 mm and grain size distributions that are systematically coarser than landslide supply (Fig. 4.12a). A representative photograph through a road-cut section of the Independence creek moraine is shown in Fig. 4.12d, clearly illustrating a poorly-sorted mixture of large boulders embedded within a finer matrix. The grain size characteristics of landslides, rockfalls and moraine deposits are extremely similar in both the Independence creek and Symmes creek catchments, despite their differences in size and former extent of glaciation (Fig. 4.1). We attribute this to the uniform granitic lithology, which thus governs the input grain size distribution from each sediment supply process.

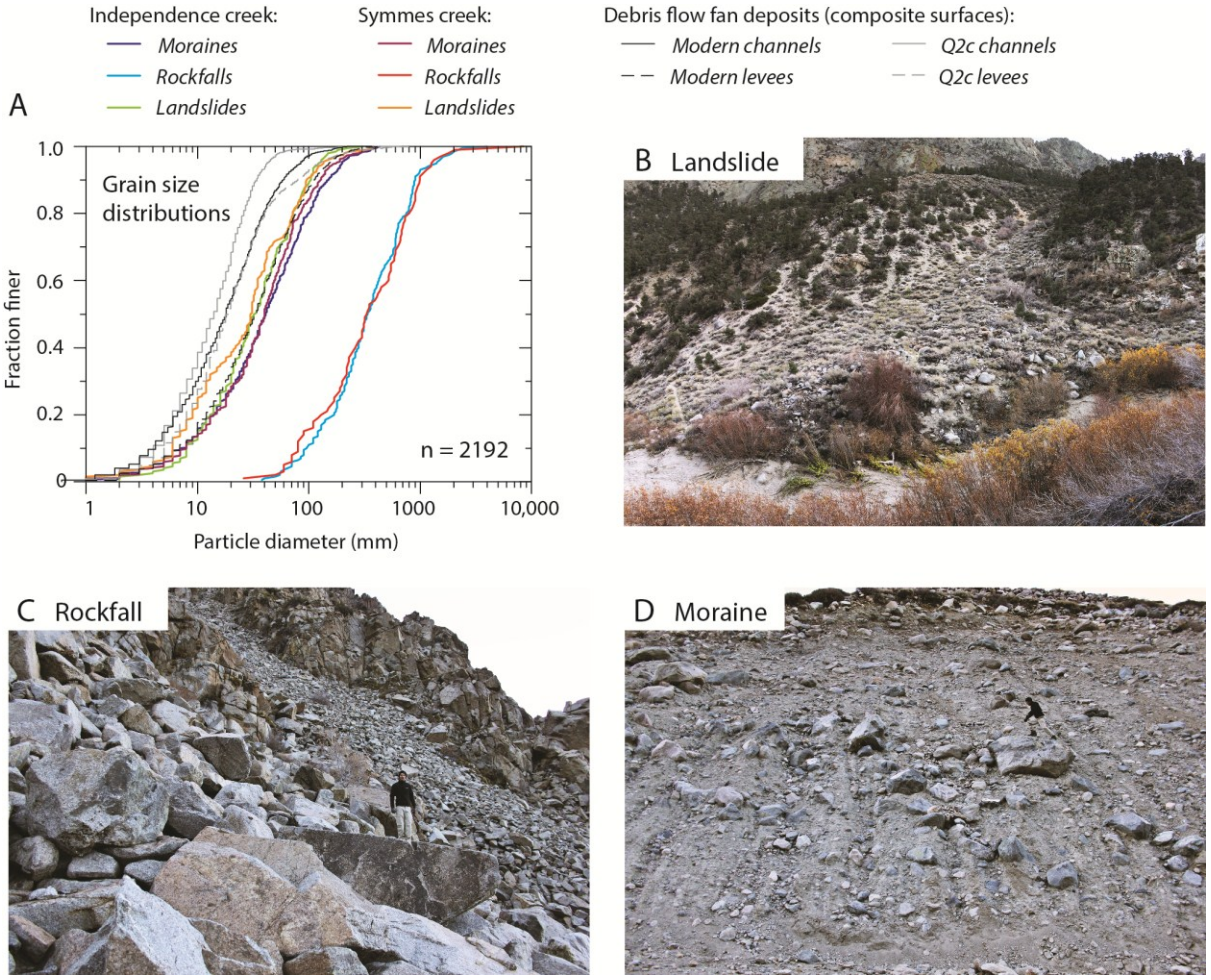

Fig. 4.12. Cumulative grain size distributions (A) for the major sediment sources, characterised in the Independence and Symmes creek catchments: landslides (B), rockfalls, (C), and moraine sediments (D). These are plotted as coloured lines, and compared with the Modern (black) and Q2c (grey) grain size distributions from the composite fan surfaces in Fig. 4.7i, representing the coarsest and finest fan deposits. Rockfalls have the coarsest grain size distributions, which are an order of magnitude coarser than any debris flow fan deposits. They supply sediment from steep hillslopes, with large granite blocks breaking along joints (C, Independence catchment, note man for scale). Moraines are coarser than landslides (D_{50} ~ 40 mm compared to ~ 30 mm) and occur throughout the catchments. Moraines form thick bodies of poorly sorted sediment, often directly sampled by debris flow channels and providing large granite blocks and a range of grain sizes down to clays (D, Independence catchment, note man for scale). (B) A typical landslide in the Symmes creek catchment, being sampled directly by a modern debris flow channel. The grain size distributions of sediment sources are very similar in both catchments, independent of total area, relief, or past extent of glaciation; this is attributed to the uniform granitic lithology.

Sediment source	No. clasts	Grain size measurements			
		D_{50} (mm)	± (mm)	D_{84} (mm)	± (mm)
Independence creek catchment					
Moraine	692	41.0	4.5	113.0	6.0
Rockfall	200	340.0	84.9	820.0	15.3
Landslide	200	33.0	-	82.0	18.3
Symmes creek catchment					
Moraine	400	40.0	5.1	100.0	26.4
Rockfall	200	335.0	-	900.0	-
Landslide	100	30.5	1.8	85.0	10.8

Table 4.3. Grain size measurements for sediment sources (moraines, rockfalls and landslides) sampled in the Independence and Symmes creek catchments. Both catchments show very similar sediment source grain size profiles, which is attributed to the uniform granitic lithology in this area.

4.6. Discussion

4.6.1. Nature of the climate cycle preserved

These debris flow fan systems along the eastern front of the Sierra Nevada, California, preserve a clear grain size signal of climate changes during the last glacial-interglacial cycle. The flow deposits are significantly coarser-grained during the warm and dry climates of the current and previous interglacials, compared to the cooler and wetter glacial climate. Comparing the LGM with the modern data, a warming of 5 to 6 °C and a halving of total rainfall has led to a doubling of grain size measured on the fan surfaces, e.g., with D_{50} increasing from ~ 15 to ~ 30 mm, and channel D_{84} from ~ 30 to > 60 mm (Fig. 4.8). At the same time, the median widths of debris flow deposits increased by ~ 10 m and the flows became significantly more variable in size (Fig. 4.8e). When the grain size time series are compared with sea surface temperatures from offshore California (Fig. 4.9), there is a positive and slightly non-linear correlation between D_{50} or D_{84} and sea surface temperature, with a coarsening rate of ~ 10 % per °C of warming (Fig. 4.9). This grain size signal partially scales with flow size, suggesting some dependence on debris flow transport capacity (Fig. 4.10).

Fundamentally, our results demonstrate that these alluvial fans preserve sustained records of high-amplitude climate changes. The grain size signals we observe are readily detectable in sedimentary deposits and the fans have reacted to past climate changes with a short response timescale of ≤ 10 ka, i.e., shorter than the temporal resolution of our data, and orders of magnitude shorter than the periodicity of a glacial-interglacial cycle. This reveals a high sensitivity to $10^{4\text{-}5}$ year climate changes, at least in this debris flow-dominated landscape. The similarity of the climate signal across 8 discrete

depositional systems is strong evidence for reproducibility in an area where tectonic and lithological boundary conditions are constant.

Before we explore the possible causes of the climate signal observed in fan stratigraphy, we note that it is unlikely to be explained by post-depositional alteration of fan surfaces during the last 125 ka. A number of in situ processes could conceivably change the grain size distributions of these sediments after deposition. Weathering of large clasts may produce finer material and reduce the average particle diameter. Selective mobilisation and removal of fines, or minor desert pavement formation, might do the opposite (e.g., Goudie, 2013). However, if post-depositional alteration processes were to explain the grain size changes observed in Fig. 4.8, they would need to adjust grain size at very different rates through time. Specifically, they would need to rapidly halve D_{50} within ~ 20 ka, then have little to no effect on grain size for a futher ~ 50 ka, before increasing it again thereafter. This is unlikely, and given the strong correlation between the grain size signals and past sea surface temperatures (Fig. 4.9), which themselves have fluctuated in an irregular pattern through time, the simplest explanation is that the data reveal a signal of climate changes. Weathering processes are undoubtedly occurring on these fan deposits, but we propose that the climatic signal is observed in spite of them, not because of them.

Promising explanations for the climate signal we observe in debris flow grain size should consider (i) sediment sources; and (ii) sediment transport, which we explore in the following sections.

4.6.2. Do changing sediment source characteristics explain the grain size signals observed?

Figure 4.12 characterises different sediment sources in two of the study catchments. Clearly, rockfalls provide very coarse blocks and little fine sediment and gravel, so if these were to represent the most common sediment source for debris flows, then the grain size distribution must be altered substantially from the source during flow, and would be primarily determined by transport mechanics. Landslides and moraine deposits provide input grain size distributions that are only slightly coarser than the debris flow deposits themselves, and represent more common sources throughout the catchments. Figure 4.13 is a summary diagram in which we plot the grain size trends from Fig. 4.8 (black points) alongside the range of D_{50} and D_{84} values of landslides and moraines measured in Fig. 4.12a (grey boxes). These plots first illustrate that the different catchment-fan systems can be viewed as one time series, demonstrating that the integrated sediment export from the eastern Sierra Nevada during the last ~ 125 ka preserves a common grain size climate signal that can be viewed at a high resolution in time by combining many different exposed terraces. The blue regressions are 4th-order

polynomials that summarise the overall trends in the data (the fit to the data stops improving at orders higher than 4th).

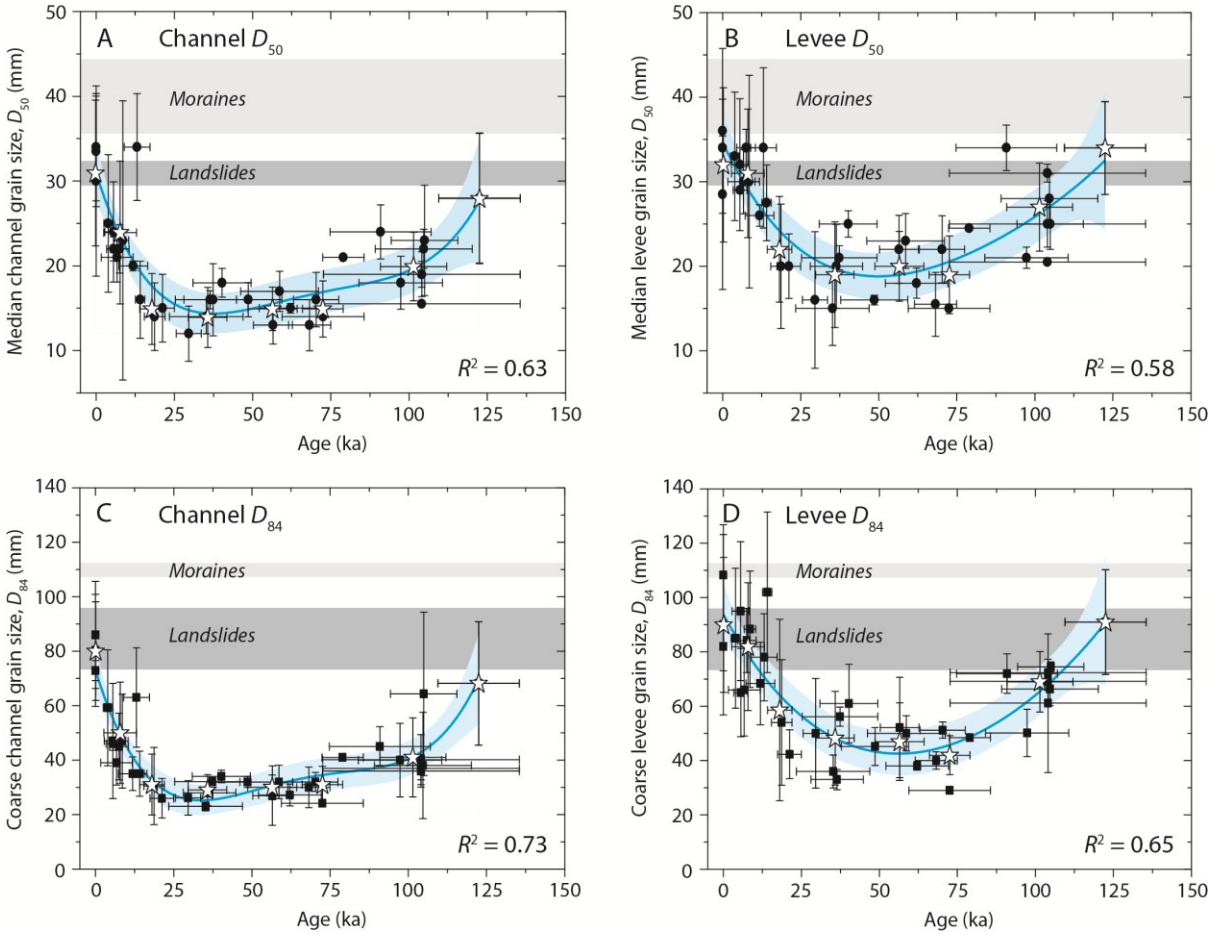

Fig. 4.13. Grain size data from all 8 fan systems; (A) channel D_{50}; (B) levee D_{50}; (C) channel D_{84}; and (D) levee D_{84}. Black points represent individual dated surfaces, white stars represent composite surfaces across all fans. Fourth order polynomial trends have been fitted, offering the best fit to the data (R^2 0.6 to 0.7) – see blue lines, with 95 % confidence intervals shown in pale blue. Grain size is coarse during the current and last interglacials, and fine during the glacial period. The D_{50} and D_{84} values of moraine and landslide sediment sources have been plotted in light and dark grey, respectively. Moraines are slightly coarser than landslides, by ~ 10 mm for D_{50} and ~ 25 mm for D_{84}. Although the transient export of coarser moraine material to the fans might amplify the relationship between warming and coarsening, the moraines are not coarse enough, or voluminous enough, to drive the signal observed; see text for discussion.

These graphs also illustrate that the grain size supplied by moraines is ~ 10 mm coarser than landslides for D_{50} and 20 – 30 mm coarser for D_{84}. While this is not equal to the total amplitude of the glacial-interglacial grain size signal (~ 15 mm for D_{50} and 40 – 50 mm for D_{84}) it might be argued that the temporary exposure and evacuation of moraine materials could explain part of the coarsening

trend during interglacials. We propose that this is not the main explanation for the signal for several reasons. First, the modern debris flow grain size measurements are almost as coarse as the moraines, which would mean moraines would need to contribute the majority of the fan sediments by volume. This is not the case because, as the maps in Fig. 4.1 show, the moraines have very small exposure areas compared to the alluvial fan deposits. Using our two test catchments of Independence and Symmes creek, we can place some first order constraints on the possible volumetric contribution of moraines. These catchments have moraine deposits with total plan-view areas of ~ 1.5 and ~ 0.8 Mm^2, respectively (Fig. 4.1). If we assume that the entire moraine surfaces have been lowered at a rate of 1 mm yr^{-1} (i.e., matching the uplift rate of the southern Sierra Nevada) for 18 ka, we can estimate the maximum volume of moraine sediment exported to the Independence and Symmes creek fans to be ~ 27 and ~ 14 Mm^3, respectively. In comparison, we can estimate the volumes of Q4 (post-glacial) sediments on both these fans, by assuming an average thickness of ~ 10 m and multiplying this by the plan-view areas of the Q4 units in Fig. 4.1, giving ~ 114 and ~ 208 Mm^3, respectively. In this scenario, the moraines would only have supplied 7 to 24 % of the total Q4 sediment volume, which is likely to be a maximum constraint. Even if around a quarter of the Q4 sediment was sourced from moraines, the ~ 10 mm difference in D_{50} would thereby be 'diluted' to an expected effect of only 2 to 3 mm in the fan deposits. It is clearly impossible for moraine evacuation to explain the amplitude of the climate signal recorded in Fig. 4.13. Additionally, exposing moraines as a coarse sediment source would be expected to generate a pulse of coarse sediment at the timing of deglaciation ~ 18 ka ago (Rood et al., 2011) that subsequently decays as the moraine material is exported to the fans. Instead, we observe a sustained coarsening with warming, which continues long after deglaciation throughout the Holocene and to the present day. Moraine exposure cannot explain this, so while they may act as secondary amplifiers, moraines are not coarse enough or voluminous enough to drive the climate signal observed.

Deglaciation also triggers paraglacial activity by releasing stresses created by the glacier loads themselves, including enhanced landsliding and failures on over-steepened hillslopes (e.g., Ballantyne et al., 2014). This enhanced sediment yield is exhausted exponentially through time, assuming transport conditions remain unchanged, i.e., there is no later increase in mobilisation (Ryder, 1971; Hinderer, 2001; Ballantyne, 2002; Savi et al., 2014). Different landscapes will have different paraglacial relaxation times, but the effects of stress release will generally occur over several thousand years (Ballantyne, 2002). For example, Savi et al. (2014) reconstruct erosion rates from a debris-flow dominated catchment in the Alps (33.5 km^2 in area, also underlain by crystalline bedrock), and show that debris flow erosion rates declined exponentially since the last deglaciation, giving a decay half-life of ~ 2.3 ka when fitted to the paraglacial response model of Ballantyne (2002). In other words, 50 % of the paraglacial supply will be exhausted within a timespan an order of magnitude shorter than the actual time since deglaciation. As we expect a similar exhaustion model to apply to the Sierra

Nevada, deglaciation at ~ 18 ka (Rood et al., 2011) would mean only ~ 0.5 % of paraglacial supply is expected to remain in the catchments today, available for export. However, the grain size signal continues to coarsen throughout the Holocene, and modern debris flow deposits are even coarser than Q4 (mid-Holocene) deposits (Fig. 4.13). The sustained correlation between debris flow grain size and temperature (Fig. 4.9) would not be expected if the signal were driven by deglaciation; instead a pulse of coarse sediment would be expected ~ 18 ka ago, decaying as temperatures continued to warm.

The differences in Fig. 4.8a-d between the Independence creek (dark blue; fully glaciated at the LGM) and the Shepherd creek (dark red; not fully glaciated and with smaller moraine deposits) catchments offer another opportunity to evaluate the combined glacial and paraglacial effect on the grain size signal. Independence creek deposits are generally coarser than Shepherd creek deposits by a difference of ~ 5 to 10 mm for D_{50} (channels and levees). So while this significant difference in past glaciation does create an effect, it is not large enough to explain the full climate signal recorded in grain size. Finally, we return to the lack of hysteresis in the temperature dependence of grain size shown in Fig. 4.9. This is important, because it demonstrates that the climate signal recorded is the same regardless of whether the climate is cooling (glaciers are advancing) or warming (glaciers are retreating), and therefore the effect of releasing moraines or stresses from glacial loads do not appear to be significant.

4.6.3. Explanations related to sediment mobilisation

As well as changes in the sediment sources supplying the fans, another explanation for the grain size signal is that the ability of debris flows to mobilise and deposit coarser particles has increased as the climate warmed. Indeed, whichever sediment sources are operating in the parent catchments, all sediment still needs to be transported to the alluvial fans in order to be transferred to stratigraphy. As such, the magnitude of transport events must be implicated in the grain size trends we observe.

Figure 4.9 clearly demonstrates that the grain sizes of these debris flow deposits increase with sea surface temperature from offshore California (Yamamoto et al., 2007), despite temperature varying irregularly through time (Fig. 4.4). This is important, because it is well documented that as temperature increases, the intensity of storm rainfall also increases because the capacity of the atmosphere to hold moisture rises exponentially with temperature (Trenberth et al., 2003; Wentz et al., 2007; Allan & Soden, 2008; Lenderink & Meijgaard, 2008, 2010; Berg et al., 2009, 2013; Liu et al., 2009). This effect is described by the Clausius-Clapeyron relationship, where moisture capacity increases by approximately 7 % per 1 °C of warming; an effect that has been documented in a range of locations and results in a similar rate of increase in maximum storm rainfall intensity with warming

(Trenberth et al., 2003; Berg et al., 2009; 2013). Even within modern records of climate variability, the intensity of rainfall sources affecting our study area correlates with warmer Pacific surface temperatures (Persson et al., 2005; Antinao & McDonald, 2013a). Given that debris flows are initiated by storms (Cannon et al., 2008; Coe et al., 2008; Kean et al., 2011, 2013), a simple explanation is that the grain size coarsening trend in Fig. 4.9 represents an increase in storm intensity with warming temperatures, and a corresponding increase in the surface runoff provided during the initiation of a debris flow event.

To explore this idea further, we have plotted the grain size data in log form against the sea surface temperature record of Yamamoto et al. (2007) from the Santa Barbara basin, in Fig. 4.14. Channel (a) and levee (b) grain size are compared, also with median flow width (c), and D_{50} data in black and D_{84} data in red. The grey lines behind the data show the Clausius-Clapeyron relation, i.e., an increase of 7 % per 1 °C. The lines are therefore a minimum constraint on the rate at which the maximum storm rainfall rate increases with temperature (Trenberth et al., 2003; Wentz et al., 2007; Allan & Soden, 2008; Lenderink & Meijgaard, 2008, 2010; Berg et al., 2009, 2013; Liu et al., 2009). We have fitted exponential regressions to the grain size data, with the form:

$$y = A \cdot e^{bx} \qquad [4.1]$$

Where A is a constant representing a grain size at 0 °C and b is an exponent that describes the rate of increase in y (grain size) per unit increase in x (sea surface temperature). Dashed lines are fitted to the individual fan surfaces, and solid lines to the composite surfaces (stars). These give the same trends within standard error. The R^2 values quoted for the composite surfaces average 0.74, and the exponent b ranges from 9 to ~ 14 % per 1 °C. If the true value of b is assumed to be the same for all 4 grain size series, i.e., the grain size series have the same sensitivity to climate change, then standard errors on each regression mean a value of b between 9.9 and 10.4 % per 1 °C satisfies all 4 data sets.

Clearly, grain size scales exponentially with sea surface temperature in a way that closely matches the relationship between storm intensity and temperature given by the Clausius-Clapeyron equation. Our data estimate a value of b around 10 % per 1 °C. This is slightly higher than 7 %, however recent observational studies have indicated that actual rainfall intensity during storms may be more sensitive to temperature than the Clausius-Clapeyron equation predicts and that b may have a higher value of ~ 10 to 14 % in some cases (Lenderink & Meijgaard, 2008; Liu et al., 2009; Berg et al., 2013; Singleton & Toumi, 2013). Therefore the grain size-temperature scaling we observe in these debris flow deposits has an exponential form that matches the effect of temperature change on storm intensity. Given the strong storm intensity control on debris flow activity in the Owens Valley area today (DeGraff et al., 2011), it therefore seems likely that these deposits record a history of changing storminess during the last glacial-interglacial cycle.

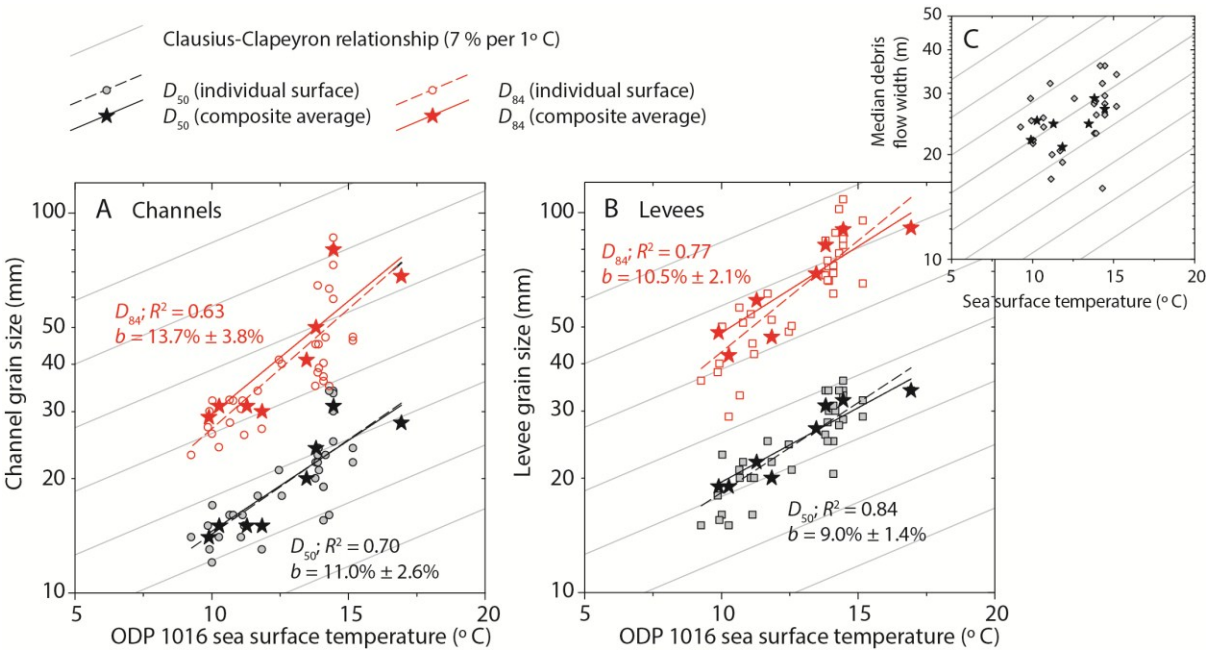

Fig. 4.14. Plots of log-scaled debris flow grain size for channels (A) and levees (B), and flow widths (C), against ODP 1016 sea surface temperature from the Santa Barbara basin (Yamamoto et al., 2007). The D_{50} data is shown in black and D_{84} is shown in red. Points represent individual fan surfaces, stars represent composite surfaces across all fans. Grey lines plotted behind the data show the Clausius-Clapeyron relation: a 7 % rate of increase per 1 °C of warming, which represents the rate at which moisture holding capacity increases in the atmosphere and is a minimum constraint on how storm rainfall intensity scales with temperature (e.g., Berg et al. 2013). Exponential trends are fitted to the grain size data, with dashed lines fitted to the individual surfaces and solid lines fitted to the composite surfaces. The R^2 is given for the composite surfaces, averaging 0.74 for the grain size data. The rate of increase in grain size, b, ranges from 9 to 14 % per 1 °C, i.e., slightly greater than Clausius-Clapeyron. This may indicate that the climate signal preserved in grain size records an increase in storm rainfall intensity with warming. Debris flow widths increase on average with temperature, but the correlation is not strong enough to extract a precise rate.

An important question is how the likely increase in the intensities of storms that have initiated debris flows physically translates into coarser grain size export on to the fan. To date, the transport mechanics of debris flows are not fully understood (e.g., Coe et al., 2008; Iverson et al., 2010; McCoy et al., 2012, 2013; Kean et al., 2013), so there is currently no general model for inverting grain size data for information about past water discharge or mechanical properties in debris flows. However, it has been demonstrated that (all other variables constant) larger debris flows carry coarser grain sizes (Coe et al., 2008; McCoy et al., 2012, 2013), indicating that the grain size distributions transported by debris flows are at least partially related to transport power. Our data also show a partial correlation between median flow width and the D_{50} and D_{84} grain sizes (Fig. 4.10), and that the average flow becomes larger as the climate warms (Fig. 4.8e). In the inset panel c of Fig. 4.14 we have also plotted the flow width data in log form against sea surface temperature. While the average flow widths (stars)

do follow the Clausius-Clapeyron equation, the data from individual surfaces show more scatter (points); as such we have not fitted a regression. So while the average flow has become larger as well as coarser with warmer temperatures, the climate signal is preserved with a much greater fidelity in the grain size of these deposits. Debris flows are complex sediment movements, and can have variable viscosities and internal buoyancy forces, which will affect their power to transport grains of different sizes in a non-trivial way. We are interested in their transport power, i.e., the energy available to transport particles of differing mobility, and in debris flow systems this may be less intimately linked with flow width than in fluvial channels. The variable viscosities and complex rheologies of debris flows mean that changes in power can be expressed as surges, changes in velocity, viscosity, flow height, or other complex responses to surface slope besides width.

Indeed, the debris flow deposits in Owens Valley contain metre-scale boulders that are much larger than the D_{50} and D_{84} variations that comprise the climate signal observed (Fig. 4.3), meaning the coarsening trend in the gravel fraction cannot be explicitly limited by the transport capacity of the flows, which can clearly mobilise larger particles. As debris flows are threshold-limited events triggered by surface runoff from high intensity storms (Griffiths et al., 2004; Cannon et al., 2008; DeGraff et al., 2011; Kean et al., 2013), the grain size mobilised during the early surface runoff phase will be controlled by transport power. This grain size signal will then be propagated down-system even once a high-viscosity debris flow has formed and is capable of rafting much larger boulders (Coe et al., 2008; McCoy et al., 2012, 2013; Kean et al., 2013). In this regard, the coarsening trend we observe with warming might be due to an increase in the entrainment potential during debris flow initiation in the catchments, i.e., more intense storms producing greater surface runoff rates (McCoy et al., 2012). The lack of significant grain size alteration with depositional length (Fig. 4.6) means the debris flows preserve this signal on the fans, even when they are able to raft larger boulders.

Supporting this ‘storm intensity’ interpretation, the modern debris flow channels on all 8 fan systems are now incising into older sediments (see Figs 4.3c and 4.4), and Q4 surfaces were incising into older deposits in two of the largest catchment-fan systems, Shepherd creek and George creek (Fig. 4.3c). Fan incision suggests increased discharge and transport capacity (Steffen et al., 2010). Given the continuing coarsening trend in grain size and the widespread supply of coarse sediment in the catchments today, this is more likely to result from an increase in water discharge per event rather than a depletion of sediment sources. In the nearby Mojave Desert, post-glacial aggradation of alluvial fans, including enhanced debris flow deposition, has been attributed to more intense and/or frequent storm events (McDonald et al., 2003; Miller et al., 2010; Antinao & McDonald, 2013a). Also, aggrading debris flow deposits have been interpreted to represent periods of greater precipitation intensity in similar arid/semi-arid areas such as western Peru (Keefer et al., 2003; Vargas et al., 2006; Steffen et al., 2010).

In reality, changes in sediment supply (section 6.2) and mobilisation (6.3) are likely to have occurred simultaneously, highlighting the complexity of the response to climate change, even in these relatively simple catchment-fan systems. However our analyses have shown that changes in sediment sources, including the effects of glaciation in the catchments and the erosion of moraines, cannot drive the climate signal observed in debris flow stratigraphy. Therefore, it is likely that the grain size of these flows is linked to transport capacity, and the non-linear Clausius-Clapeyron scaling with sea surface temperature indicates that, like today, debris flows in the past have been governed by the maximum intensity of storm rainfall. Our grain size time series highlight an important distinction between storminess and mean annual precipitation. Even though climate in the south-western USA was wetter overall during the LGM (see section 3.2), higher sea surface temperatures today suggest that the Holocene is likely stormier than the LGM; indeed it is well-known that magnitude-frequency distribution of precipitation can change independently of the total precipitation budget. This is very important, because many erosional processes influenced by climate are threshold-controlled. Therefore, while the climate has become about twice as dry since the LGM overall, it is likely that individual storms have intensified, leading to enhanced surface runoff during debris flow initiation and coarser grain size export to the fans in both the current and previous interglacials. As well as explaining the grain size changes, this mechanism also explains (i) the widespread modern incision of fan apices; (ii) the lack of hysteresis in Fig. 4.9; (iii) the lack of a lag time between climate changes and grain size response in Figs 4.8 and 4.9; (iv) the partial correlation between grain size and flow size in Fig. 4.10; and (v) the particular exponential form of the grain size-temperature relationship.

4.6.4. Implications

That a clear glacial-interglacial climate signal is preserved in the grain size distributions of debris flow fan deposits has a number of important implications. Most fundamentally, we have proposed that debris flows preserve a detailed record of past changes in storm intensity, and our data demonstrate the palaeoclimatic significance of debris flow stratigraphy. The response timescale of these systems is short, less than 10 ka and below the temporal resolution of our data. This indicates that rapid depositional processes like debris flows precondition sediment routing systems for climate sensitivity, by reducing sediment storage time in catchments and quickly transferring sediment to the basin.

Mechanical implications include a high degree of connectivity between threshold-controlled hillslopes supplying sediment by landslides and rockfalls, and the down-system alluvial fan deposits that make up the basin fill. The sediment is being transferred and deposited rapidly, and therefore landscape evolution models of simple catchment-fan systems may need to capture hillslope processes before they can accurately reproduce fan stratigraphy. Even streamflow-dominated systems may inherit a

grain size signal from processes like debris flows, e.g., if the axial Owens valley river were to toe-cut and erode these fan sediments in the future. Even though debris flows are somewhat different to the fluvial transport assumptions made in most landscape evolution models, a qualitative comparison can still be made with the simple catchment-fan models summarised in section 2.1 (e.g., Paola et al., 1992; Allen & Densmore, 2000; Morehead et al., 2001; Densmore et al., 2007; Armitage et al., 2011; Simpson & Castelltort, 2012; Allen et al., 2013). Our findings confirm that basin stratigraphy, at least in this setting, does record high-amplitude, high-frequency climate changes over $10^{4\text{-}5}$ year timescales in the sedimentology of basin fill, particularly clearly in grain size. One striking difference is that as the climate warmed and dried overall, the grain size export to alluvial fans became coarser, whereas theoretical models predict a fining due to decreased discharge. As our analyses show, this can be explained by the importance of high-intensity storm events, which are likely to have increased with climate warming in a way decoupled to the overall rainfall budget of the south-western USA. Therefore, our data reveal the importance of distinguishing between total precipitation and its magnitude-frequency distribution in future models, which can have opposing effects on basin stratigraphy. In this respect, our findings may suggest that the stratigraphic record of debris flows largely records high-magnitude events and not average climatic conditions. Figures 4.9 and 4.14 in particular illustrate the importance of climate thresholds in governing the sedimentology of these debris flow deposits. The sensitivity of the grain size response evidently increases with warmer temperatures, and if this trend continues with future warming scenarios then an even faster rate of grain size coarsening might be expected, with larger debris flow events as well. Existing ideas about debris flow erosion (e.g., Stock and Dietrich, 2006) indicate that flows with larger particles will themselves be more erosive, potentially leading to an erosive feedback in this landscape. We encourage further research into how debris flows transport sediment, in particular the controls on the grain size distributions of their deposits, but we propose that hillslope-dominated landscapes could become increasingly sensitive to future warming.

4.7. Conclusions

By measuring sedimentary grain size distributions in detail (> 30,000 clasts on 35 dated surfaces), we have shown that debris flow fans in Owens Valley, California are highly sensitive to glacial-interglacial climate variability over the last ~ 125 ka, recording known high-frequency climate shifts in alluvial fan stratigraphy. As the climate warmed by 5 – 6 °C from the LGM to the present day, total rainfall halved and storm intensity likely increased, measured D_{50} and D_{84} grain size approximately doubled, and average flows also became larger by ~ 10 m and more variable in size. The correlation between grain size and climate is sustained throughout the entire last glacial-interglacial cycle, with a

clear exponential scaling between grain size and Pacific sea surface temperatures from offshore California. The form of this scaling, with a rate of grain size increase of ~ 10 % per 1 °C, approximates the Clausius-Clapeyron relationship and closely matches observed records of how maximum storm rainfall intensity scales with temperature (Lenderink & Meijgaard, 2008; Liu et al., 2009; Berg et al., 2013; Singleton & Toumi, 2013). We therefore propose that debris flow stratigraphy in these systems is primarily a function of changing storm intensity throughout the pronounced glacial-interglacial climate changes that affected the south-western USA in the recent past. Our findings are reproducible in 8 different catchment-fan systems with precise age control and where tectonic and lithological boundary conditions are constant.

These systems have a rapid response timescale that is faster than the minimum temporal resolution of our data, i.e., < 10 ka, and is not damped, demonstrating that this debris-flow dominated landscape has a high sensitivity to orbital climate changes over 10^4 to 10^5 year periods. By characterising sediment sources in the parent catchments, we have demonstrated that the transient exposure of coarser-grained moraine sediments, compared to hillslope landslides, may serve to amplify the observed grain size signal along with paraglacial sediment supply. However, supply and glaciation effects cannot explain the full signal amplitude, the sustained correlation between grain size and temperature long after deglaciation, widespread recent incision of fan apices, changes in average debris flow sizes through time, or the lack of hysteresis in the temperature dependence shown in Fig. 4.9. Instead, we argue that changes in discharge/surface runoff during large storms has driven the majority of the grain size changes we document, and that the exponential scaling between debris flow grain size and sea surface temperature fits the expected rate of increase in storm intensity with warming. Our data therefore indicate that debris flow stratigraphy, at least in this study area, preserves a useful palaeoclimatic record of past storminess that matches modern observations of debris flows being threshold-limited events triggered by surface runoff (e.g., Cannon et al., 2008; DeGraff et al., 2011).

Our findings also provide useful constraints for future attempts to constrain a debris flow transport model that accounts for grain size and flow power explicilty. Additionally, our observations clearly demonstrate the importance of distinguishing between rainfall intensity and total rainfall amount in geomorphic studies and landscape evolution models. Finally, we highlight the potential risk of continued climate warming in the near future, which we predict will trigger larger and coarser-grained debris flows, thereby increasing the hazard presented by these important hillslope processes.

5. Measuring alluvial fan sensitivity to glacial-interglacial climate change using a self-similarity approach to grain size fining, Death Valley, California†

Chapter Abstract

The effects of climate change on eroding landscapes and the terrestrial sedimentary record are poorly understood. Using mountain catchment-alluvial fan systems as simple analogues for larger landscapes, a wide range of theoretical studies, numerical models and physical experiments have hypothesised that a change in precipitation rate could leave a characteristic signal in alluvial fan sediment flux, grain size, and down-system fining rate. However, this hypothesis remains largely untested in real landscapes. In this study, we measure grain size fining rates from apex to toe on two alluvial fan systems in northern Death Valley, California, which each have well-exposed modern and ~ 70 ka surfaces, and where the long-term tectonic boundary conditions can be constrained. Between them, these surfaces capture a well-constrained temporal gradient in climatic conditions. We adapt a grain size fining model, based on self-similarity and selective deposition, for application to these alluvial fans. We integrate this model with cosmogenic nuclide constraints on catchment erosion rates, and observed grain size fining data, to estimate the change in sediment flux from canyon to alluvial fan that occurred between early glacial and modern interglacial conditions. Our results show that a ~ 30 % decrease in average precipitation rate led to a ~ 20 % decrease in sediment flux and a clear increase in the down-fan rate of fining. This supports existing landscape evolution models that relate a decrease in precipitation rate to a decrease in sediment flux, and implies that the relationship between sediment flux and precipitation rate may be sub-linear. Consequently, this study shows that small mountain catchments and their alluvial fan stratigraphy can be highly sensitive to orbital climate changes over < 10^5 year timescales. However we also observe that this sensitivity is completely lost when sediment is remobilised and recycled over a time period longer than the duration of the climatic perturbation. Our analyses offer a new approach to quantitatively reconstructing the effects of past climate changes on sedimentation, using simple grain size data measured in the field.

---

†A version of this chapter is in review for *Sedimentology*, authored by **D'Arcy, M.**, Whittaker, A.C., and Roda Boluda, D.C.

M.D. conceived of the idea for the investigation, planned the data collection, conducted the analyses, prepared the figures, and wrote the manuscript. M.D. and D.C.R.B. collected data in the field. A.C.W. assisted with the modelling work. A.C.W. and D.C.R.B. commented on the manuscript.

5.1. Introduction

The terrestrial stratigraphic record is widely recognised as a valuable archive of information about past environmental change, including the history of major controls on sedimentation such as climate, tectonics and erosion (Molnar & England, 1990; Heller and Paola, 1992; Paola et al., 1992a; Blum & Törnqvist, 2000; Allen, 2008a). Changes in sediment volumes and characteristics delivered to basins, driven by temporal and spatial variations in these boundary conditions, are therefore translated into sedimentary deposits with varying degrees of preservation (Humphrey and Heller, 1995; Castelltort and Van Den Driessche, 2003; Jerolmack and Paola, 2010; Duller et al., 2010; Whittaker et al., 2010; Simpson and Castelltort, 2012; Foreman, 2014). While qualitative descriptions of sedimentary facies produced as result of these drivers are a mainstay of sedimentary research (Bull, 1991; Blair and McPherson, 1992; Blair 1999; Harvey et al., 1999; Castelltort et al., 2011; Huyghe et al., 2012; Nagel et al., 2013; Ballato and Strecker, 2014), in principle it should be possible to decode aspects of this physical record quantitatively for past environmental change (Robinson and Slingerland, 1998, Allen, 2008a). Alongside geomorphological analyses (DiBiase and Whipple, 2011; Whittaker, 2012; Champagnac et al., 2012; 2014; D'Arcy & Whittaker, 2014; Herman et al., 2014; Salcher et al., 2014), the ability to quantitatively invert terrestrial sediment characteristics as a function of past climate would, (i) enable us to constrain the magnitudes, timescales and impacts of past environmental change on the Earth's surface (Romans et al., 2009; Duller et al., 2012, Allen et al., 2013; Foreman, 2014); (ii) allow us to determine how sensitive eroding landscapes are to past climate, particularly when compared with tectonic drivers (Bull, 1991; Armitage et al., 2013; Allen et al., 2013; Michael et al., 2013; Ballato and Strecker, 2014); and (iii) give new insights into the erosional-depositional response of landscapes to future climate changes over a range of timescales and magnitudes (Pepin et al., 2010; Armitage et al., 2011; 2013; Simpson and Castelltort, 2012).

However, in practice it is difficult to extract past climatic information from the stratigraphy produced by real eroding landscapes. This is partly due to the potential for signal shredding and interference by self-organised criticality, autogenic processes, and chaotic behaviour within sediment routing systems themselves (Hallet, 1990; Humphrey and Heller, 1995; Clarke et al., 2010; Jerolmack and Paola, 2010). Such effects may mean that climate changes are not translated into a 'clean' sediment flux signal at a catchment outlet (Simpson and Castelltort, 2012; Armitage et al., 2013; Forzoni et al., 2014); indeed these signals may be highly damped and thus landscape response times to perturbation may be long (Castelltort and Van Den Driessche, 2003; Allen, 2008b; Jerolmack and Paola, 2010, Whittaker and Boulton, 2012). The sedimentary record is also fundamentally a selectively-sampled record of past surface fluxes over a depositional basin, with varying preservability (Fedele and Paola, 2007; Schumer and Jerolmack, 2009; Whittaker et al., 2010; Allen et al., 2013), so sediments may best record past environmental change only where accumulation rates are high. Finally, different

drivers of the surface process system, such as tectonics and climate, may produce similar stratigraphic responses. For instance the progradation of coarse wedges of gravel into a basin may be marker of a changing tectonic boundary conditions (e.g., Jones et al., 2004; Allen and Heller, 2011; Whittaker et al., 2010; Parsons et al., 2012), but may equally represent changes in rainfall or storminess (e.g., Duller et al., 2012; Armitage et al., 2013; Foreman, 2014). While diagnostic differences between these competing scenarios have been suggested from theoretical considerations (Allen and Heller, 2011; Armitage et al., 2011), applying these to real stratigraphic examples over long spatial scales where exposure is incomplete remains a significant challenge.

One solution to these issues is to collect field data that measure the sensitivities of sediment routing systems to climate changes in carefully-selected locations where boundary conditions are well-constrained and where some of the above problems can be eliminated or controlled. Coupled mountain catchments and alluvial fans are good systems to study for three main reasons (Bull, 1964; Hooke, 1968; Whipple and Traylor, 1996; Allen and Hovius, 1998); firstly, while their catchment processes include a range of sediment transfer functions (from hillslope sediment sources to the sediment flux at the fan apex), their geometry is both simple and tractable (Allen and Densmore, 2000; Armitage et al., 2011). Secondly, alluvial fans are often volumetrically-closed landforms with high sedimentation rates, comprising terraces of different ages that can be easily dated using exposure techniques (c.f., D'Arcy et al., 2015). Finally, small sediment-routing systems are likely to capture the effects of climatic or tectonic changes with greater sensitivity. They are likely to have shorter response times than large catchments (Castelltort and Van Den Driessche, 2003; McPhillips et al., 2013) and they may be less affected by the signal shredding and damping issues mentioned above (Allen, 2008b; Armitage et al., 2013).

Field studies have described a number of examples of alluvial fans aggrading during periods of enhanced precipitation and incising during subsequent drier conditions when sediment supply is depleted, for example in the south-western United States (Bull, 1991; McDonald et al., 2003; Spelz et al., 2008; Miller et al., 2010; Antinao & McDonald, 2013) and in Peru (Steffen et al., 2009, 2010; Bekaddour et al., 2014). In these cases, alluvial fans have responded to climate changes during the last glacial-interglacial cycle and hence the implied catchment response time is on the order of 10^3 - 10^4 years. Similarly, McPhillips et al. (2013) demonstrated that erosion rates and sediment fluxes in catchments along the western Peruvian Andes were greater during the wetter, stormier parts of the Pleistocene, compared to the Holocene. Recent studies have also pointed to the role of rapid climate changes in modulating the architecture and grain size of terrestrial sedimentary deposits. Waters et al. (2010) sampled grain size from late Pleistocene stream-flow dominated alluvial fan deposits in Cyprus, and found that coarser gravel was clearly deposited during periods of wetter climate. Further back in time, the deposition of coarse, prograding conglomerates in Colorado, Wyoming, and the

Pyrenees has been attributed to abrupt (~ 10^4 to 10^5 year) warming during the Palaeocene-Eocene Thermal Maximum (Foreman et al., 2012; Allen et al., 2013; Foreman, 2014). These studies generally agree that wetter climates promote greater sediment fluxes and coarser grain sizes, although uncertainties remain about the relative importance of storms compared to average precipitation (Miller et al., 2010; Antinao and McDonald, 2013), the role of vegetation in modulating sediment flux (Pelletier, 2014), and autogenic processes (Paola et al., 2009; Clarke et al., 2010). However, in terms of their three-dimensional architecture, it appears that alluvial fans are sensitive in at least some locations to high-amplitude climate changes over 10^3 to 10^5 year orbital timescales.

Numerical models and physical experiments also agree that alluvial fans might record climate changes in their stratal architecture and grain size distributions (e.g., Paola et al., 1992a; Allen and Densmore, 2000; Morehead et al., 2001; Densmore et al., 2007; Armitage et al., 2011; Rohais et al., 2012; Allen et al., 2013). In general, these models predict that doubling average precipitation rate would approximately double the sediment flux exported to an alluvial fan and trigger significant progradation of a coarse-grained deposit. A halving of precipitation rate causes the inverse response and is recorded by sediment fining, and in each case the climate change is preserved as a transient signal in fan stratigraphy. In these models, precipitation rate changes of 50 to 100 % typically generate measureable changes in the gravel fraction grain size exported to the fan. Consequently, climate changes of a similar magnitude to glacial-interglacial cycles may be expected to produce a macroscopic (> 10 mm amplitude) grain size signal locked into the sedimentary record and easily detected in the field (e.g., Allen and Densmore, 2000; Armitage et al., 2011; Allen et al., 2013). Likewise, physical analogue experiments also show that changing precipitation rate has a clear effect on landscape erosion and form (Bonnet and Crave, 2003), and that doubling precipitation rate causes increased sediment flux to an alluvial fan and a temporary spike of coarse sediment deposited (Rohais et al., 2012). These studies establish the clear hypothesis that climate changes should be recorded by both the sediment flux and grain size delivered to alluvial fan systems.

In this paper, we test this hypothesis explicitly using a combination of field measurements and numerical modelling of grain size fining (section 2). We examine two alluvial fan systems in northern Death Valley, California, which each have well-exposed and well-dated early glacial (~ 70 ka) and modern depositional units (Frankel et al., 2007a). Between the deposition of these fan surfaces, Death Valley experienced substantial climate changes associated with the last glacial-interglacial cycle (Phillips, 2008). We integrate a self-similarity approach to grain size analysis based on selective deposition with field observations and existing cosmogenic nuclide estimates of catchment-wide erosion rates, to quantitatively explore how past climate change and sediment recycling affected fan architecture and grain size in these simple sediment routing systems.

5.2. Grain size fining and the self-similarity model

Compared to a climatic signal being recorded by incision-aggradation sequences or catchment geomorphology, attempting to invert climate variables from sedimentary grain size brings several analytical advantages. Grain size can be measured easily in the field (even in very old deposits), and has an accessibility and preservation potential much greater than the three-dimensional architecture of an alluvial fan. It is known to record key information about sediment sources and transport (Whittaker et al., 2007; Duller et al., 2012; Attal et al., 2015) and boundary conditions such as tectonics and climate (e.g. Robinson and Slingerland,1998 Whittaker et al., 2007, 2010; Allen and Heller, 2011; Waters et al., 2010; Foreman et al., 2012; Allen et al., 2013; Foreman, 2014). Additionally, grain size data can easily be represented as a quantitative time series that can be compared to tectonic or climatic proxies (Whittaker et al., 2011; Parsons et al., 2012; Michael et al., 2013).

Recently, a number of studies have shown that careful measurements of grain size and fining rates along discrete stratigraphic time-lines can be used to quantitatively decode stratigraphy for driving variables such as tectonically-driven subsidence or sediment flux (c.f., Paola and Martin, 2012). Focusing on ~ 40 Ma old Eocene alluvial fans in the Pobla Basin of the Spanish Pyrenees, Duller et al. (2010) were able to demonstrate that an increasing grain size fining rate along two time-lines in the basin fill related to a period of enhanced subsidence, driven by increased displacement on the basin-bounding thrust. Similarly, Whittaker et al. (2011) quantitatively related changes in grain size fining rate in upper Eocene and Oligocene stratigraphy of the south-central unit of the Spanish Pyrenees to tectonically-mediated variations in sediment supply and accommodation. Similar insights have also been gained from changes to grain size fining rate within the Sis conglomerate (Parsons et al., 2012). Recently, down-system changes in sediment calibre within a mass-balance framework have been shown to reflect both the volume and grain size distribution supplied to the sediment routing system feeding the upper Cretaceous Castlegate sandstone in the western interior basin of the US (Hampson et al., 2014), and the mid-Eocene Escanilla Formation in north-eastern Spain (Michael et al., 2013; 2014).

Duller et al. (2010) and Whittaker et al. (2011) were able to invert stratigraphic grain size trends explicitly for tectonic subsidence and sediment supply variations using a self-similarity model for grain size fining, which was proposed in its current form by Fedele and Paola (2007). The modelling approach is described in detail by Fedele and Paola so only a brief account is given here. The existing model is a two-dimensional solution based on empirical observations that indicate the grain size distributions of stream flow-dominated deposits are self-similar. For gravel grain sizes, this means that the mean, $\overline{D}$, and standard deviation, σ, of surface and subsurface sediment both decrease at the

same rate downstream (c.f., Paola et al., 1992b; Paola and Seal, 1995; Toro-Escobar et al., 1996; Duller et al., 2010; Whittaker et al., 2011). A similarity variable, ξ, for gravels can thus be defined as:

$$\xi = \frac{D - \overline{D}}{\sigma} \quad [5.1]$$

where D is a given grain size, and $\overline{D}$ and σ are the local mean and standard deviation of the gravel sediments at any down-system distance, x. If self-similar, the shape of the gravel grain size distribution at any position along the length of the depositional system is the same when scaled by the similarity variable, ξ. Exploiting this self-similarity, the modelling approach of Fedele and Paola (2007) uses a version of a fractional Exner sediment mass balance (c.f., Toro-Escobar et al., 1996) to account for particle transfer between the transporting system and deposited stratigraphy, and to describe the extraction of sediment along the length of the depositional system. The rate of change of a grain size fraction in the deposit, f, as a function of dimensionless distance down-system, $x*$, can therefore be expressed as:

$$\frac{df}{dx*} = f\left[R* \left(1 - \frac{1}{J}\right)\right] - \frac{1}{J}\frac{dJ}{dx*} \quad [5.2]$$

where J is a relative mobility function ($J = p/f$, where p is the fraction of a given sediment size in the transport system), and $R*$ represents the spatial distribution of deposition downstream, which can be expressed in two-dimensional form as:

$$R*(x*) = (1 - \lambda_p) L \frac{r*(x*)}{Q_S(x*)} \quad [5.3]$$

where λ_p is sediment porosity; L is the total length of the sediment routing system in downstream direction x ; $r*(x*)$ is the spatial distribution of tectonic subsidence; and $Q_S(x*)$ is the sediment flux at any down-system distance. Numerical modelling suggests that the form of J is also approximately self-similar (Fedele and Paola, 2007; Duller et al., 2010), so this means that down-system sediment extraction can be collapsed via J. Moreover, both f and J can therefore be expressed as functions of ξ. It is important to stress that the spatial distribution of deposition, $R*$, represents the relative distribution of sediment mass down-system, due to selective extraction into stratigraphy. It can therefore be determined directly from stratigraphic data (c.f., Whittaker et al., 2011). To find deposit grain size for any value of $R*(x*)$, a dimensionless distance transformation $y*(x*)$ is used, which integrates the downstream distribution of sediment mass $R*$ as a function of dimensionless down-system distance:

$$y*(x*) = \int_0^{x*} R^*(x*)dx* \quad [5.4]$$

The mean grain size of gravel, $\overline{D}$, at any down-system distance can be expressed as an exponential function of $y*$ and it is therefore explicitly linked to R^* (Fedele and Paola, 2007):

$$\overline{D}(x*) = \overline{D}_0 + \sigma_0 \frac{C_2}{C_1}(e^{-C_1 y*} - 1) \quad [5.5]$$

In this case, $\overline{D}_0$ and σ_0 represent the mean and standard deviation of the size distribution of the sediment supply at the initial point of deposition, and C_1 and C_2 are constants that express the relative partitioning of the variability in gravel supply arising from systematic down-system change in mean grain size (C_2) compared to the at-site variation (C_1) (Fedele and Paola, 2007; Whittaker et al., 2011). This ratio can be approximated by measuring the coefficient of variation of the grain size distribution in the supply:

$$C_v = \frac{\sigma(x*)}{\overline{D}(x*)} = \frac{C_1}{C_2} \quad [5.6]$$

Values of constant C_1 used in previous studies lie between 0.5 and 0.8 (e.g. Duller et al., 2010), and numerical models suggest that $0.5 < C_1 < 0.9$ (c.f. Fedle and Paola, 2007). The coefficient of variation, C_V, for gravels is easy to measure from field data, and has been observed to lie between 0.7 and 1.0 (e.g. Fedele and Paola, 2007; Duller et al., 2010, Whittaker et al., 2010, Michael et al., 2013). Consequently, C_2 can also be calculated.

The sensitivity of this model to changing sediment flux and subsidence rate has been explored in previous studies (Duller et al., 2010; Parsons et al., 2012), and a key implication of equations 5.3, 5.4 and 5.5 is that a larger sediment flux, relative to an unchanged rate of accommodation generation, would generate a slow grain size fining rate down-system, resulting in progradation and a coarsening of grain size at a particular down-system point in cross-section. For a system of fixed depositional length, this would result in increased sediment bypass, e.g., to an axial river system. A decrease in sediment flux would generate a fast rate of grain size fining, relative retrogradation, a decrease in cross-sectional grain size at a particular point down-system, and reduced sediment bypass at the end of a system of fixed length.

This approach provides a clear opportunity to derive quantitative information about sediment fluxes and tectonic subsidence rate directly from gain size data. Advantageously, the model requires knowledge of only a small number of parameters (c.f., Whittaker et al., 2011): (i) the length of the depositional system, L; (ii) the rate and spatial distribution of subsidence, $r*(x*)$; (iii) an estimate of sediment flux to the fan, Q_{S0}; and (iv) knowledge of the input grain size distribution ($\overline{D}_0$ and σ_0). Limitations of the model include that assumption that grain size distributions are indeed self-similar and that fining is driven by selective extraction. Additionally, it is assumed that there are no down-system point sources of sediment with very different grain size. Here, we apply the self-similar grain

size fining model to two alluvial fans in northern Death Valley that are well-suited to this type of analysis. They have well-exposed surfaces on which grain size fining can be measured all the way from fan apex to toe, and existing cosmogenic nuclide constraints on catchment-wide erosion rates allow us to break the coupled ratio between sediment flux and extraction in Eq. 5.3.

5.3. Study area

We examine two neighbouring catchment-fan systems along the eastern margin of northern Death Valley, eastern California (Fig. 5.1), which drain the Grapevine Mountains directly below Grapevine peak. These are the Backthrust canyon and Moonlight canyon systems, which have similar geomorphology and total drainage areas of 46.2 km^2 and 36.7 km^2, respectively. The canyons drain south-westwards into the northern Death Valley extensional basin (the Mesquite flat), constructing ~ 6 km long coalesced alluvial fans mantling the western range front. These fans are shown in Fig. 5.1a, which is a contrast-enhanced LandSat 8 false colour composite (bands 642-RGB) in which modern deposits appear bright blue and older incised terraces appear red-brown. Both fans are toe-cut by the axial Death Valley wash.

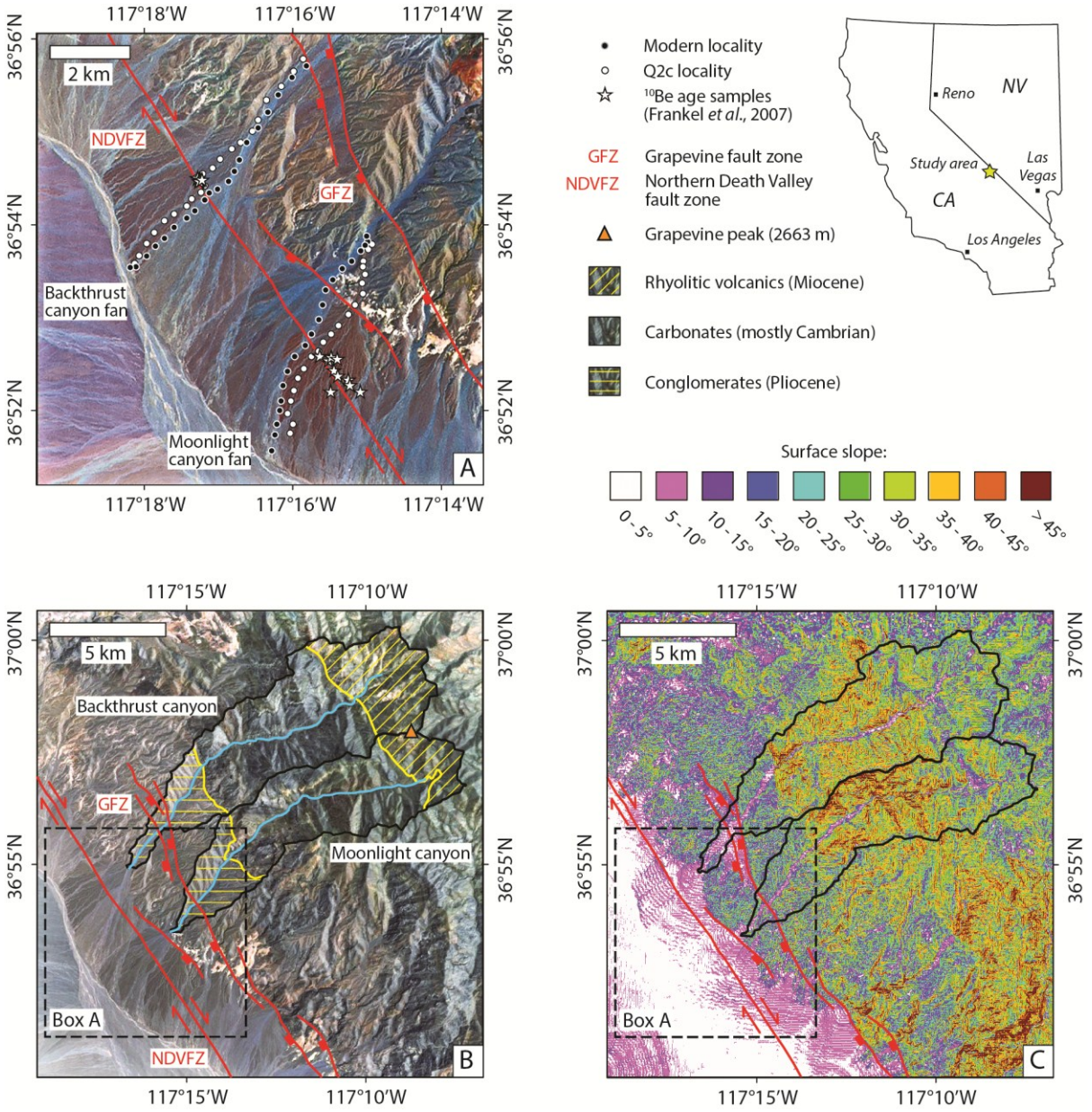

Fig. 5.1. Maps locating the two targeted catchment-fan systems in northern Death Valley, California. (A) Landsat 8 contrast-enhanced (bands 642-RGB) false colour image of the alluvial fans. Modern deposits appear bright blue, Q2c deposits reflect brown-red and were dated to ~ 70 ka using ^{10}Be cosmogenic nuclides by Frankel et al. (2007); stars show their sampling localities. Dots show the down-fan grain size sampling localities in this study (black on modern surfaces, white on Q2c surfaces). Two fault systems are shown: the Northern Death Valley Fault Zone (NDVFZ), a dextral strike-slip fault with a horizontal displacement rate of ~ 4.5 mm yr^{-1} (Frankel et al., 2007a); and the Grapevine Fault Zone (GFZ), a range-bounding normal fault system across which the vertical displacement rate is poorly constrained (we provide new data in this study). The two fans are toe-cut by the axial Death Valley wash, flowing towards the south-east. (B) Aerial imagery of both catchments (outlined in black). They have similar forms and geomorphology, and drainage areas of 46.2 km^2 (Backthrust canyon) and 36.7 km^2 (Moonlight canyon). The catchments are mostly eroding early Palaeozoic carbonates, with smaller outcrops of Miocene volcanics at the headwaters and Pliocene conglomerates near the canyon mouths (Niemi, 2012; see text for details). (C) Slope map of the catchments calculated from the National Elevation Dataset, with a horizontal/vertical elevation of 9/1.5 m at this location.

Faulting in this area is dominated by extension, but this is distributed into two fault systems. The Northern Death Valley Fault Zone (NDVFZ) dissects the alluvial fan terraces (Fig. 5.1a) and has a small scarp visible in the field. This is a dextral strike-slip fault with a horizontal geologic slip rate of ~ 4.5 mm yr^{-1} measured at this location (Frankel et al., 2007a). The Grapevine Fault Zone (GFZ) is a south-west-dipping normal fault system (Mabey, 1963; Reynolds, 1969; Niemi, 2012) located about 3 km north-east of the NDVFZ (Fig. 5.1a). The GFZ is the range-bounding fault system responsible for some of the relative subsidence/uplift between the alluvial fans and the catchments, however its age, throw, and throw rate are not fully constrained (Niemi, 2002). Nonetheless, the northern Death Valley basin contains deposits several kilometres thick, estimated using gravity data (Blakely et al., 1999), and as such the GFZ was evidently a major frontal fault system with substantial throw from the Pliocene onwards (Niemi, 2002). The GFZ is likely to be active, and Machette et al. (2002) estimate that it has a low slip rate of ~ 0.2 mm yr^{-1}. Additional subsidence is due to regional extension along a NNW-SSE axis (Reynolds, 1969; Klinger, 2001; Hammond et al., 2012), which is responsible for the complex placement of a strike slip fault near the frontal normal fault. Hammond et al. (2012) present detailed vertical motion constraints from interferometric synthetic aperture radar (InSAR) that reveal the average subsidence rate in central and northern Death Valley is ~ 0.5 mm yr^{-1}. We exploit these constraints as a starting point in our analyses, but our approach offers a new opportunity to refine estimates of both the rate and spatial variation of subsidence beneath our target alluvial fans, and we explore this as a topic of interest later.

The Backthrust and Moonlight canyon catchments have equivalent outcrop patterns of bedrock lithologies (Fig. 5.1b), which we have broadly classified into three groups: volcanics, carbonates, and conglomerates. Niemi (2012) provides a detailed geological map and full lithological descriptions. The majority of the catchments are eroding carbonates from the Bonanza King and Carrara formations, composed of Cambrian (and minor Ordovician-Devonian) limestones and dolostones with some siltstones and shales (Niemi, 2012). These carbonate hillslopes also have the steepest slopes (Fig. 5.1c) and provide the majority of sediment to the channels. The headwaters of the catchments have gentler slope distributions and are underlain by Miocene volcanics, comprising rhyolitic lavas, tuffs, and ash flows (Niemi, 2012; Fig. 5.1c). The lowermost parts of the catchments have extended basin-wards through partially consolidated conglomerates, likely of Pliocene age, that form local topographic relief (Niemi, 2012). Although sediment supply to the alluvial fans integrates these different sources, more than 80 % of the fan gravels are derived from carbonates, owing to the large extent and steep hillslopes of the carbonate bedrock.

The Backthrust and Moonlight canyon alluvial fans are dominated by channelized gravel deposits on two distinct depositional surfaces: modern deposits, and older raised surfaces mapped as Q2c in previous stratigraphic frameworks (Bull, 1991; Klinger, 2001; 2002; Frankel et al., 2007a; Niemi,

2012). Representative photographs of the alluvial fan surfaces are shown in Fig. 5.2. Photographs 2a and 2b are taken near the apices of both fans, looking upstream towards the catchments. The modern gravel surfaces (foreground) and raised Q2c terraces (marked by yellow triangles) are clearly visible. The modern surface is incising on both fans, but the magnitude of this incision is significantly greater on the Moonlight canyon fan. At the apex of the Backthrust canyon fan, the modern surface has only incised a few metres into Q2c, whereas on the Moonlight canyon fan this incision averages 40 m, with the Q2c surface forming a paved terrace at the top of a heavily dissected cliff, which provides a cross-section exposure of older alluvial fan conglomerates onto which Q2c aggraded. In this fan, the Q2c terrace is landsliding into the modern depositional surface, which is therefore recycling material via steep scree cones and large blocks visible on the right of Fig. 5.2b.

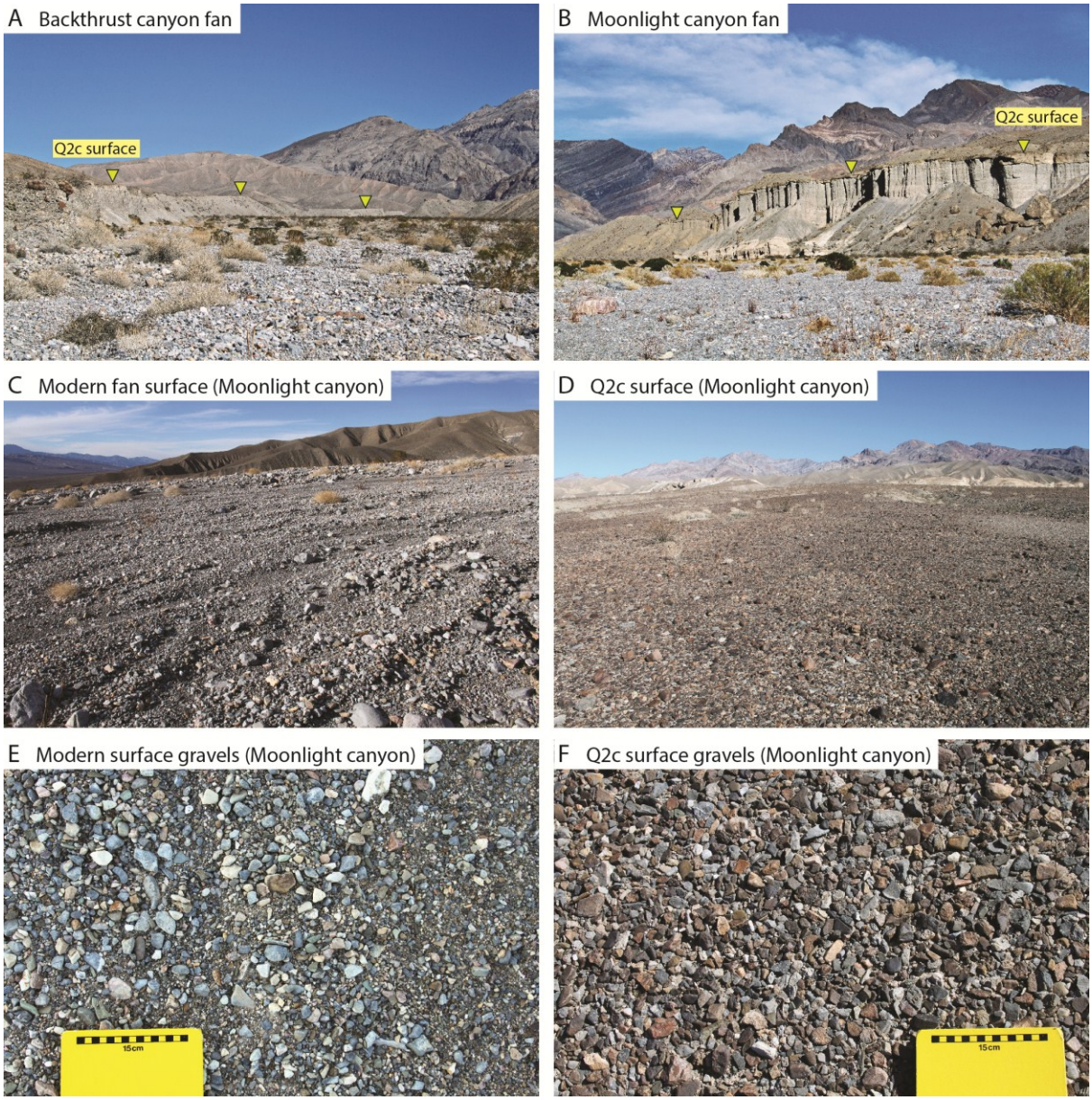

Fig. 5.2. Field photographs of the alluvial fan systems sampled. (A) Photograph taken on the modern surface of the Backthrust canyon fan near the apex, looking upstream towards the catchment. The Q2c terrace is highlighted by yellow arrows, and has been incised by 2-3 m by the modern surface. This incision quickly diminishes down-fan and it is possible to step from one to the other for most of the length of the fan. A ridge of Pliocene conglomerates is visible in the background, with carbonate bedrock in the mountain range beyond. (B) Photograph taken on the modern surface of the Moonlight canyon fan near the apex, looking upstream. On this fan, the Q2c surface has been heavily incised by the modern surface, exposing a ~ 40 m tall cliff that is recycling material into the modern channels via large blocks, landslides, and steep scree cones. The carbonate bedrock strata are visible in the Grapevine Mountains (background), and the lack of significant vegetation cover is clear. (C) Representative photo of the modern fan surfaces, which comprise gravels, pebbles and cobbles distributed by low-relief channels. The channels are active during storms, owing to the arid climate of Death Valley. This photo is near the fan apex, and a ridge of Pliocene conglomerates is visible in the background. (D) An equivalent photograph of the Q2c surface exposed near the apex of Moonlight canyon fan. The surface has a mature desert pavement, the clasts are heavily varnished and oxidised and the depositional relief has been lost. (E) Representative photograph of the modern surface grain size distribution. The notebook scale bar is 15 cm long with 1 cm intervals. Clasts are mostly derived from carbonates. (F) Representative photograph of

the Q2c surface grain size distribution. The clasts have been varnished and arranged into an interlocking pattern characteristic of desert pavements.

Figure 5.3 shows the longitudinal profiles of the fan surfaces studied. The solid lines represent the modern surfaces and the dashed lines represent the Q2c terraces. From apex to toe, the Q2c surfaces have greater slopes than the modern surfaces, reflecting this recent incision. This difference is larger on the Moonlight canyon fan (4.3 ° on the Q2c surface, 3.8 ° on the modern surface), compared to the Backthrust canyon fan (with a difference in slope of only 0.1 °), reflecting the enhanced down-cutting observed on the Moonlight canyon fan. We therefore select these two fan systems as comparable examples where one (Moonlight canyon fan) has experienced substantial incision and recycling, and the other (Backthrust canyon fan) has not. We return to this comparison later.

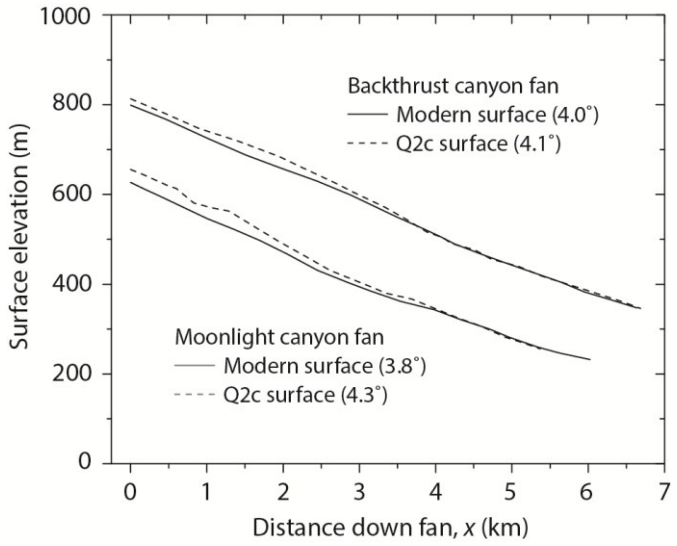

Fig. 5.3. Longitudinal profiles of the modern (solid lines) and Q2c (dashed lines) fan surfaces along the sampling routes shown in Fig. 5.1a. Elevation is given above sea level and was measured from the National Elevation Dataset model with a vertical precision of 1.5 m. The Backthrust canyon fan lies at a higher overall elevation as it is further north in Death Valley. It has similar modern (4.0 °) and Q2c (4.1 °) surface slopes, reflecting the negligible degree of modern incision. The Moonlight canyon fan has a slightly steeper Q2c surface (4.3 °), which has been heavily incised by a gentler (3.8 °) modern surface.

Figures 5.2c and 5.2d show representative outcrop-scale photographs of the modern and Q2c surfaces as exposed on the Moonlight canyon fan near its apex. The modern surface is predominantly composed of carbonate gravels, pebbles and cobbles distributed by small channels with subtle topographic relief < 1 m. These channels are active during flash floods triggered by infrequent storms, reflecting the arid modern climate of Death Valley. Frankel et al. (2007) documented debris flow deposits on the alluvial fans; we observed primarily channel deposition resulting from flash floods,

and did not sample any boulder-rich levees that could be attributed to debris flows. Figure 5.2e shows a typical image of the modern deposits used for characterising the grain size distribution (see Methods). The majority of the clasts are partially-rounded white/grey limestone and dolostone gravels and pebbles. The Q2c surface (Fig. 5.2d) has lost its original depositional relief due to desert pavement formation, and is composed of equivalent sediment to the modern deposits (Fig. 5.2f), only heavily oxidised and varnished, giving the terraces a rust-red colour and making them easy to distinguish. As is typical of desert pavements, the clasts are arranged in an interlocking pattern (Goudie, 2013).

Frankel et al. (2007) dated the Q2c surface on both fans to 70 (+22 / -20) ka using ^{10}Be cosmogenic nuclide measurements. They analysed 16 samples in total, and we have reproduced their exposure age probability distributions here in Fig. 5.4. We note that Frankel et al. (2007) used different names for the alluvial fans that do not correspond to the names of the parent canyons (Niemi, 2002; 2012). We have updated the fan names in this study, according to the map of Niemi (2012). As such, the Backthrust canyon fan is the 'Big Dip' fan of Frankel et al. (2007) and the Moonlight canyon fan is the 'Red Wall' fan of Frankel et al. (2007). This clarification is necessary because Red Wall canyon is actually the next canyon ~ 7 km south-east of Moonlight canyon. Figures 5.4a and b show the probability distributions for age estimates on each fan separately, with clear peaks centred at ~ 70 ka. The Moonlight canyon fan data include two inherited clasts, dating to ~ 120 ka and ~ 220 ka, presumably recycled from older aggraded units that were later remobilised. The presence of an inherited signal on this fan may be significant given that it also shows more evidence for incisional recycling of earlier deposits today, compared to the Backthrust canyon fan (Fig. 5.4a and b). Frankel et al. (2007) also combined the samples from each fan deposit, reproduced here as Fig. 5.4c, to calculate their final Q2c age estimate. It is reasonable to assume that the two Q2c surfaces were deposited co-synchronously, given the widespread occurrence of fan terraces dating to ~ 70 ka in Death Valley, e.g., the Indian creek fan (Frankel et al., 2007b), the Perry Aiken creek fan (Ganev et al., 2010), and the Hanaupah canyon fan (Machette et al., 2008). The uncertainty on the exposure ages spans from 50 ka to 92 ka, and we have highlighted this period of activity on the benthic Pacific δ^{18}O stack of Lisiecki and Raymo (2009) for comparison in Fig. 5.4d. As well as providing ^{10}Be exposure dates for the Q2c surface, Frankel et al. (2007) also used two ^{36}Cl depth profiles to estimate the Q2c source area erosion rate for the Moonlight canyon system. They obtained values of 46 ± 9 mm ka^{-1} and 83 ± 10 mm ka^{-1}, giving an overall average erosion rate of ~ 65 ± 20 mm ka^{-1} for this catchment at ~ 70 ka.

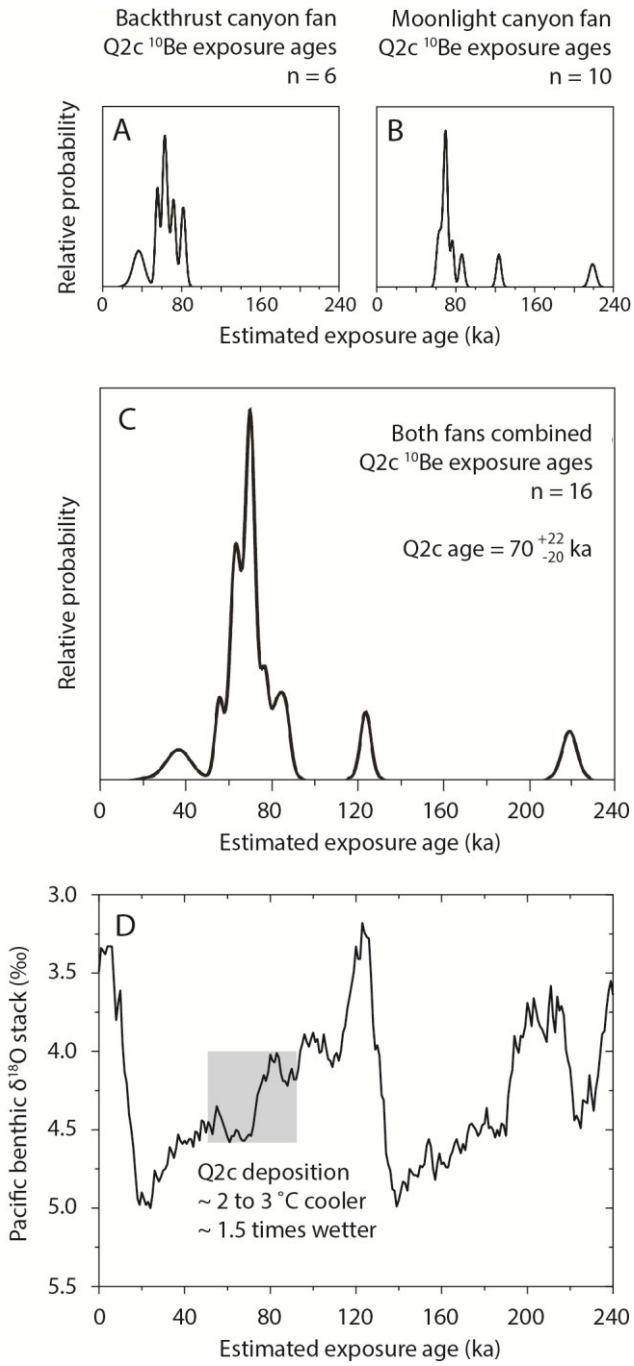

Fig. 5.4. Exposure dating of the Q2c surface, reproduced from from Frankel et al. (2007). Probability distributions of the 6 ^{10}Be samples measured on the Backthrust canyon fan (A) and the 10 samples measured on the Moonlight canyon fan (B) both give peaks at ~ 70 ka. Frankel et al. (2007) combined these Q2c age estimates to obtain an overall exposure age of 70 (+ 22, - 20) ka (C). See the original study for further details. In (D), we plot this period of activity as a grey box on the benthic δ^{18}O stack for the Pacific Ocean reported by Lisiecki and Raymo (2009). The Q2c surface was deposited in early glacial conditions during the middle of the cooling phase of the previous glacial-interglacial cycle, and we estimate a temperature depression of 2-3 °C and a 1.5 factor increase in mean annual precipitation relative to modern conditions (see text for details).

Today, Death Valley has an arid desert climate, and records between 1911 and 2015 give a mean annual precipitation rate of 57 mm yr^{-1} and a mean temperature of 25 °C (Western Regional Climate Center, 2015). The valley occupies a powerful rain shadow created by the Sierra Nevada and White-Inyo mountain ranges to the west, and the entire catchment-fan systems are virtually un-vegetated apart from sparse desert scrub (Fig. 5.2). However, the south-western United States was cooler and wetter during the last glacial period, and Death Valley contained a large pluvial lake called Lake Manly (Blackwelder, 1933; Ku et al., 1998; Lowenstein et al., 1999). A variety of terrestrial palaeoclimate proxies from this area have constrained the Last Glacial Maximum (LGM) as between 5 and 6 °C colder, and 2 times wetter overall, than the present day. These include pollen records (Thompson et al., 1999), hydrological restorations of pluvial lakes (Menking et al., 2004), oxygen isotope data (Quade et al., 2003), and mass-balance models of former Sierra Nevada glaciers (Kessler et al., 2006). Given that Q2c deposition occurred during a benthic Pacific $\delta^{18}O$ value of ~ 4.0 to 4.5 ‰, halfway between the modern and LGM values of ~ 3.5 and 5.0 ‰, respectively (Fig. 5.3d; Lisiecki and Raymo, 2009), it is reasonable to assume that the Q2c climate excursion was half the LGM excursion, i.e., a temperature depression of 2 to 3 °C and an overall increase in precipitation of ~ 1.5 times, relative to present conditions.

5.4. Methods

5.4.1. Grain size sampling

The alluvial fan surfaces were sampled from the fan apices (at the Grapevine fault zone) to their toes (intersecting the axial Death Valley wash) at intervals of approximately 300 m (Fig. 5.1a). We used scaled, high-resolution photographs of channel deposits (e.g., Fig. 5.2e and f) to reconstruct the grain size distributions of the > 1 mm size fraction by Wolman point counting (Wolman, 1954). A range of studies have demonstrated that the grain size distribution of the gravel fraction can be characterised effectively using Wolman point counting of high-resolution photographs, and that this approach is equivalent to Wolman point counting in the field (Cowie et al., 2008; Duller et al., 2010; Whittaker et al., 2010; Michael et al., 2013; Litwin Miller et al., 2014). At each locality, a minimum of 6 photographs were taken of channel gravel deposits, to ensure representative coverage of the channel surface. We note that the channels on the fan surfaces braid and interact, forming a wide distribution surface (Fig. 5.2a to c), so it is not possible to follow one single channel from apex to toe. As such, our grain size measurements sample a variety of discrete sediment paths down the alluvial fans, making them representative of many individual flow events. Using all photographs taken at each site, the maximum diameters of 100 randomly-selected clasts were measured and compiled into a

cumulative grain size distribution curve, from which the mean diameter, $\overline{D}$, and the standard deviation, σ, were calculated. These were then used to characterise the grain size fining rate from apex to toe. In Appendix 5.1, we evaluate the uncertainty associated with this method of characterising grain size distribution, and demonstrate that averaging 100 clasts is sufficient to obtain a mean grain size value within a precision uncertainty of ~ 2 % in the majority of cases.

5.4.2. Self-similarity analysis and model design

We apply the self-similarity equations of Fedele and Paola (2007) (see section 2) to the Backthrust and Moonlight canyon alluvial fan surfaces in a multi-step analysis, and we adapt them to predict sediment extraction and grain size fining in 3D across the fans.

The starting point is the ^{36}Cl cosmogenic nuclide estimate of catchment-wide erosion rate, ε, during the Q2c time period, provided by Frankel et al. (2007). We use this erosion rate (~ 65 mm ka^{-1}) and the catchment areas, A, to estimate the sediment flux, Q_{S0}, exported to the alluvial fans during Q2c deposition. We combine this sediment flux, the observed Q2c grain size fining rates, the surface geometry of the alluvial fans, and the self-similarity equations of Fedele and Paola (2007), to derive the subsidence profile beneath the alluvial fans at this location. With this information, we then estimate the adjustment in sediment flux that is needed to explain the different grain size fining rate observed on the modern alluvial fan surface.

To accomplish this, we first adapt the equation for sediment extraction, $R*(x*)$ (Eq. 5.3) for application to three-dimensional alluvial fans. The volumetric extraction of sediment into stratigraphy is the multiple of the vertical subsidence profile creating accommodation and the horizontal distribution of sediment across the fan surface (Fig. 5.5). Therefore, we add an expression for how the fan width changes down-system into Eq. 5.3 such that:

$$R^*(x*) = \left(1-\lambda_p\right)L\frac{r*(x*)W^*(x*)}{Q_s(x*)} \qquad [5.7]$$

where $W^*(x*)$ represents the plan-view width of the depositional fan surface at each point $x*$ down the length of the fan. It is essential to make this modification when applying the equations to alluvial fan systems that distribute the input sediment flux at the fan apex, Q_{S0}, across a wide surface and many channels. This means it is impossible to know $Q_s(x*)$ at any individual grain size sampling location without knowing the spatial distribution of sediment flux and integrated extraction upstream of that point. Furthermore, multiplying the cosmogenically-derived catchment-wide erosion rate by catchment area gives an estimate of Q_{S0} that is clearly averaged over many depositional events and a long integration time period. Over this long term, the locus of deposition will avulse across the fan

surface, so it is entirely unrealistic to model the input sediment flux, Q_{S0}, as being deposited in one single two-dimensional path along the alluvial fan. Instead, the flux exported from the catchment must be distributed across the active fan surface, and incorporating $W^*(x*)$ into Eq. 5.7 acts to normalise $Q_s(x*)$ in this way.

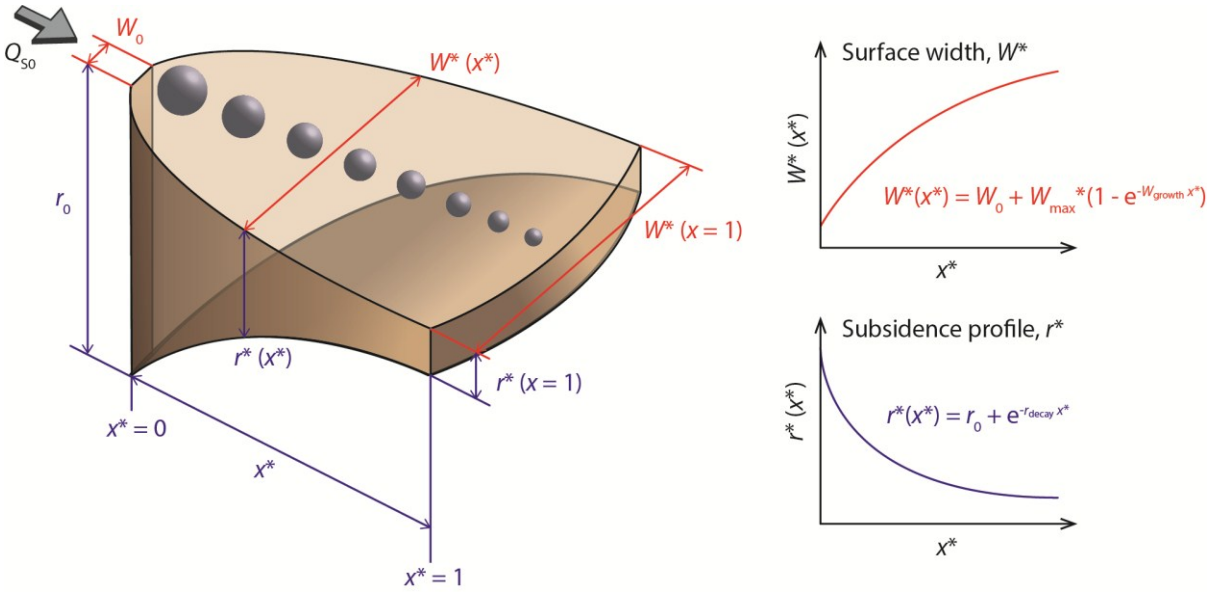

Fig. 5.5. Schematic diagram of the model approach taken in this study. The input sediment flux at the fan apex, Q_{S0}, is the total sediment export from the canyon, via a channel of initial width W_0. Grain size fines down-fan from x = 0 to x = 1 by selective deposition of larger clasts, and the sediment extraction depends on (i) how sediment is distributed across the fan surface according to its changing width, $W*(x*)$, and (ii) the accommodation generated by the changing subsidence rate beneath the fan, $r*(x*)$. We use exponential equations to describe both of these relationships (see inset graphs), which can be easily parameterised and represent our target alluvial fans well. Due to the lateral extraction of sediment on alluvial fans, the application of the self-similarity equations requires this 3D solution.

We calculate $Q_s(x*)$ as the input sediment flux, Q_{S0}, minus the integrated volume of sediment deposited on the fan upstream of location $x*$, which we equate to the accommodation created by the subsidence profile (i.e., we assume topographic steady-state):

$$Q_s(x*) = Q_{S0} - \int_0^{x*} \frac{dr*(x*)W*(x*)}{dx*}(1-\lambda_p) \qquad [5.8]$$

We assume a typical subsidence profile that decays exponentially down-system away from the range-bounding normal fault zone (Fig. 5.5):

$$r*(x*) = r_0 + e^{-r_{decay}x*} \quad [5.9]$$

where r_0 is the subsidence rate at the fan apex; and r_{decay} is a decay constant that describes the rate at which $r*$ decreases with $x*$. We also use an exponential equation to describe how the alluvial fan surfaces become wider down-system, which reproduces reality well:

$$W*(x*) = W_0 + W_{max} \cdot \left(1 - e^{-W_{growth}x*}\right) \quad [5.10]$$

Here, W_0 is the alluvial fan surface width at the fan apex; W_{max} is the maximum surface width; and W_{growth} describes the rate at which $W*$ increases with $x*$. Note that W_{max} is not the same as the width of the alluvial fan surface at the fan toe, especially if it is dissected by an axial river system, as the shape may have continued to widen according to W_{growth} if the fan were able to prograde further.

We are able to parameterise Eq. 5.6 for these alluvial fans, to describe how sediment is distributed across the fan surfaces. The total widths of the modern incised fan surfaces were measured at 500 m intervals down-fan using high-resolution aerial imagery (Fig. 5.6a,b), and were then plotted these against the normalised down-system distance (Fig. 5.6c). We then simulate equation 5.6 using different values of the exponent W_{growth} (dashed lines), which is varied at intervals of 0.1. A low value of W_{growth} produces a narrow fan, and a high value produces a wide fan. We find that a value of 0.5 best reproduces the observed fan surface geometry in both cases (solid line), meaning that the fan widths grow with length following an inverse square law. These lines are plotted using a W_0 of 100 m, as this is the width of both modern channel surfaces where they emerge from the canyons at the fan apices. The parameter W_{max} cannot be measured directly because the fans are toe-cut by Death Valley wash. However, it trades off with the exponent W_{growth} to determine the width of the fan at the toe, which can be measured also. We find values of W_{max} that produce the correct toe width of the modern surfaces are 7500 m for Moonlight canyon fan and 9500 m for Backthrust canyon fan. The curves in Fig. 5.6c are therefore plotted with a middle value of 8500 m for illustrative purposes; we emphasise that this difference has an immaterial effect on the estimated value of W_{growth} (see supplementary information), and is simply required to generate the correct plan-view form of the alluvial fan surfaces. It is not possible to repeat this analysis for the Q2c terraces, which are partially buried by modern deposits (Figs 5.1 and 5.7a), so we assume that the aspect ratios of the fans can be taken to be constant over 70 ka, and this is qualitatively supported by the aerial imagery.

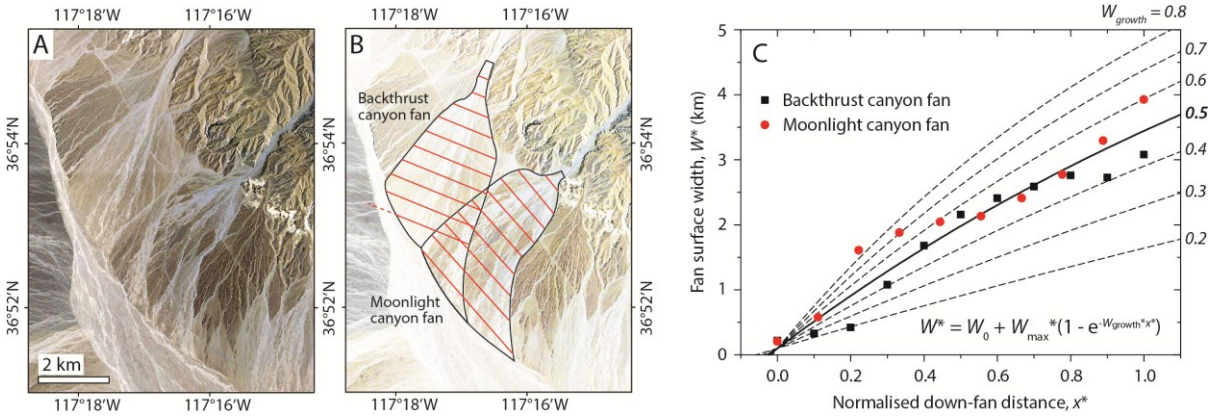

Fig. 5.6. Observed widening of modern alluvial fan surfaces on the Backthrust and Moonlight canyon alluvial fans. High-resolution aerial imagery (A) was used to measure the width of the sediment distribution surfaces, $W*$, at 500 m intervals down-fan (B). These widths are plotted against the normalised down-fan distance, $x*$, in (C), and simulated using the modelling scheme given in Fig. 5.5 (dashed curves). The starting width, W_0, can be measured directly as the width of the modern surfaces where they emerge from the canyons; this is 100 m in both cases. The theoretical maximum width of the fans if they were not toe-cut by the axial system, W_{max}, is approximated at 8500 m, giving the simulated curves the correct convexity. We allow the growth exponent, W_{growth}, to vary at intervals of 0.1, and the data are best-fitted by an exponent of ~ 0.5 (solid curve). The exponent is dimensionless in this plot because the length scale has been normalised to $x*$.

Together, the subsidence profile and the fan surface geometry determine the sediment extraction (Fig. 5.5). As such, our approach is a three-dimensional model of how sediment flux, and therefore grain size fining, varies down-fan. With the known growth in fan surface width parameterised (Eq. 5.10, above), we are in a position to derive the subsidence profile in our results, using equations 5.7 and 5.9, because $R*(x*)$ can be calculated from measured grain size fining rates via equations 5.4 and 5.5. Note that we obtain values of C_1 and C_2 from Eq. 5.6, and also an analysis of the similarity variable, ξ, described in Eq. 5.1. We explain this sub-section of the analysis in Appendix 5.2.

5.4.3. Data processing

We analyse our data using Microsoft Excel and OriginPro v.9.1. Locality elevations (above sea level) and the surface slope map in Fig. 5.1c were determined using the National Elevation Dataset (NED) digital elevation model (Gesch et al., 2002), which has a horizontal spatial resolution of 9 m and a vertical resolution of 1.5 m in this area. Geospatial data were processed using ArcGIS v.10. All our data and calculations are provided as supplementary information.

5.5. Results

5.5.1. Grain size measurements

In total, we measured 9000 grains across 80 individual sampling localities, distributed from apex to toe across 4 different alluvial fan surfaces (modern and Q2c on both the Backthrust canyon and Moonlight canyon fans). In Fig. 5.7, we plot these data as cumulative grain size distribution curves for each fan surface, including all localities. As such, these curves characterise the total body of sediment delivered to the fans, and do not capture any down-system changes in grain size. In general, the curves are similar, with the majority of particles between ~ 10 and 40 mm in diameter. The Q2c surface is marginally finer-grained than the modern surface by 2 to 3 mm on the Backthrust canyon fan. There is no significant difference between modern and Q2c sediments on the Moonlight canyon fan.

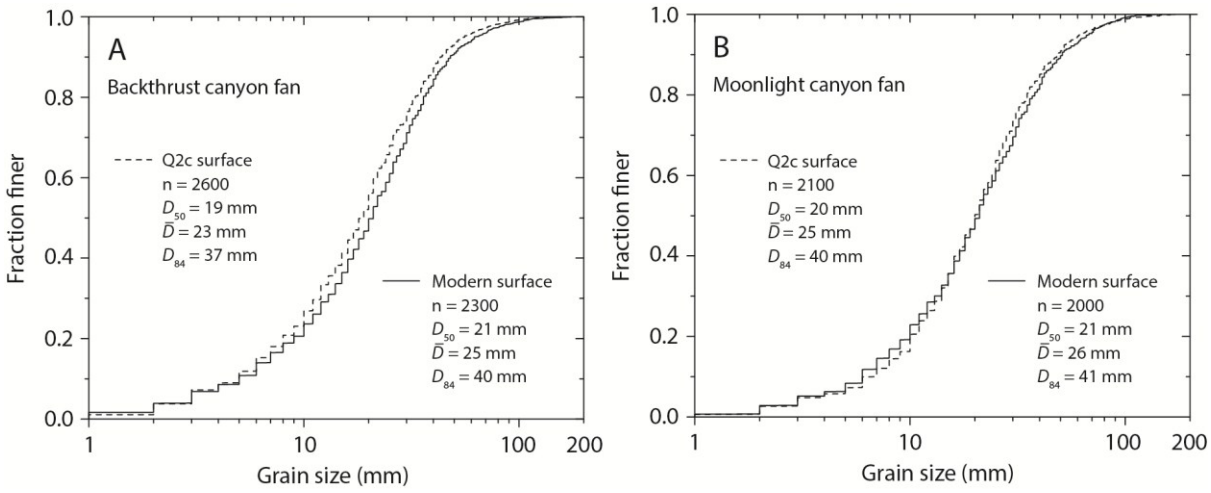

Fig. 5.7. Cumulative grain size distribution curves for all localities measured on modern (solid lines) and Q2c surfaces (dashed lines) on the Backthrust canyon fan (A) and the Moonlight canyon fan (B). The number of clasts (n), the mean grain size, $\overline{D}$, and the 50th and 84th percentile grain sizes, D_{50} and D_{84}, are quoted for each surface. Around 80 % of clasts are between 5 and 50 mm in diameter, with a smaller fraction of smaller and larger grains. Our sampling strategy does not include sediment finer than 1 mm (see Methods). In general, the surfaces all have comparable grain size distributions. The modern surface on the Backthrust canyon fan is slightly coarser-grained by 2-3 mm.

In Fig. 5.8, we plot the mean grain size, $\overline{D}$, at each locality, showing the trends from apex to toe on each fan surface. The Q2c localities are shown as open symbols and the modern localities as solid symbols. Exponential regressions fit the data well following Sternberg's law (Sternberg, 1875), with R^2 averaging 0.75. The input grain size, $\overline{D}_0$ at x = 0 km (the fan apices) is ~ 29 (± < 1) mm, the

exception being the modern surface on the Backthrust canyon fan where $\overline{D}_0$ is slightly coarser at ~ 33 (± 1.2) mm. The rate at which grain size decreases down-fan is very similar on the two Moonlight canyon surfaces (5.6 and 5.9 % per km), and higher on the Backthrust canyon fan (6.7 % per km on the Q2c surface, rising to 8.9 % per km on the modern surface. Significantly, these fining rates do not overlap, even accounting for standard error. We have not included error bars reflecting the uncertainty on $\overline{D}$ at each locality, as Appendix 5.1 and the standard errors on $\overline{D}_0$ show, this is ~ 1 mm or less in terms of precision. Importantly, an increase in the fining rate from the Q2c surface to the modern surface on the Backthrust canyon fan indicates a relative decrease in sediment flux (see section 5.2), and we quantify this later on.

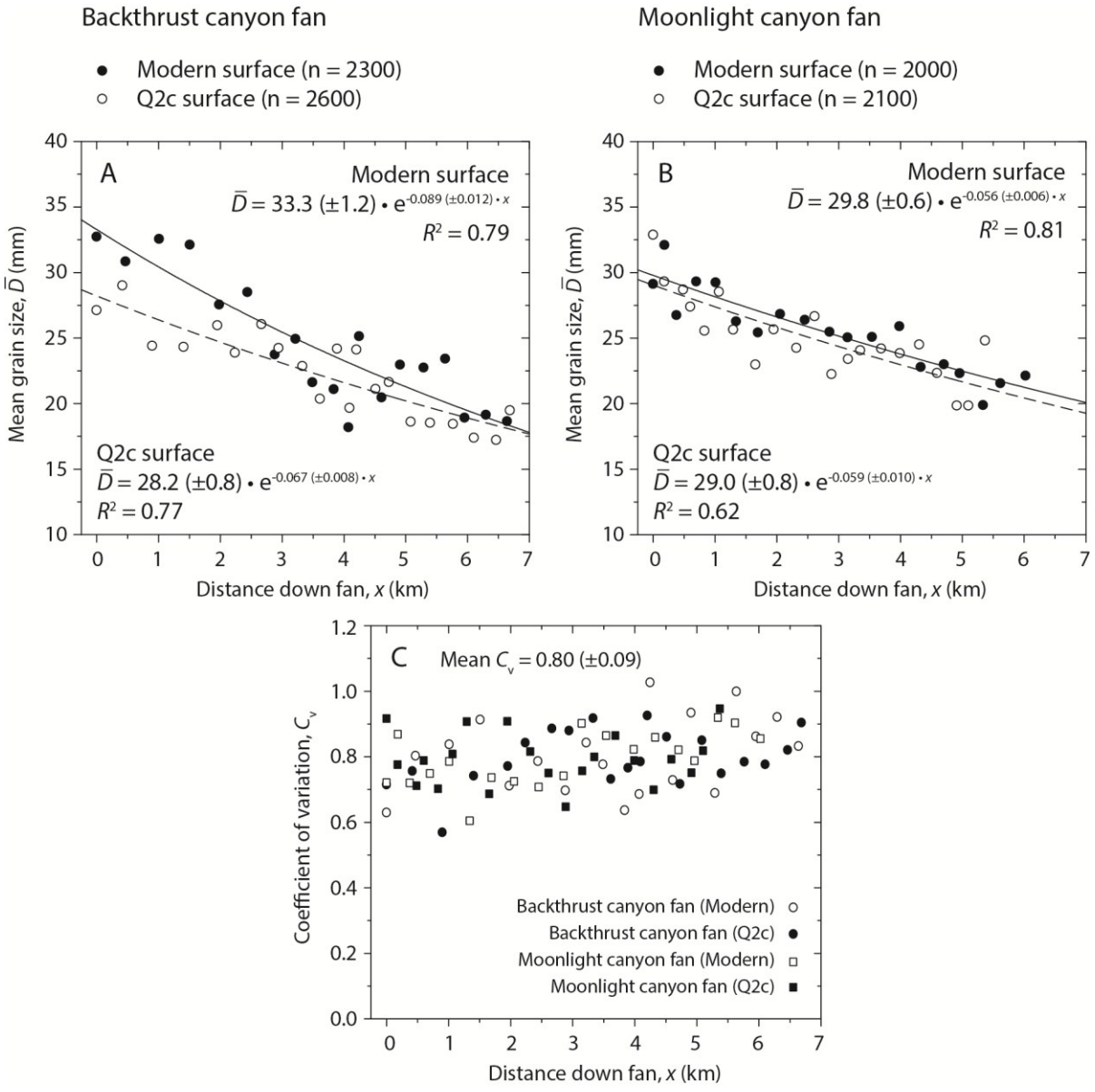

Fig. 5.8 (previous page). Mean grain size, $\overline{D}$, for each locality plotted against distance down fan (where the apex = 0 km), for modern (solid symbols) and Q2c (open symbols) surfaces on the Backthrust canyon fan (A) and the Moonlight canyon fan (B). Exponential regressions fit the data well, with R^2 averaging 0.75, and provide an estimate of $\overline{D}_0$ at the fan apex that has a typical uncertainty of ~ 1 mm. The $\overline{D}_0$ is ~ 28 to 30 mm on the Moonlight canyon fan and both Q2c surfaces, and slightly coarser (~ 33 mm) on the modern surface of the Backthrust canyon fan. On the Backthrust canyon fan, the down-system grain size fining rates are ~ 6.7 % km^{-1} (Q2c) and ~8.9 % km^{-1} (modern), and do not overlap within standard error. On the Moonlight canyon fan, where significant sediment recycling is observed (Fig. 5.2b), the fining rates are indistinguishable (5.6 and 5.9 % km^{-1} on the modern and Q2c surfaces, respectively), matching the Q2c regression in (A). In (C) we plot the coefficient of variation, C_v (equation 5.6) for every locality. There is no significant variation in C_v down-fan or between the surfaces, which averages 0.80 (± 0.09) and demonstrates that the standard deviation and mean grain sizes decay similarly along the length of each fan surface.

The coefficient of variation, C_v, (Eq. 5.6) for each locality down-fan is shown in Fig. 5.8c. There are no significant differences between the Backthrust canyon fan (circles) and Moonlight canyon fan (squares), or between the modern (open symbols) and Q2c (solid symbols) surfaces. The C_v averages 0.80 (± 1σ = 0.09) for the entire data set, in close agreement with other examples of gravel channel deposits, which generally have values of C_v between 0.7 and 0.9 (White et al., 1978; Ferguson et al., 1996; Fedele and Paola, 2007; Duller et al., 2010). A constant C_v requires that, for these fans, the standard deviation in grain size declines down-system at a similar rate to the mean grain size $\overline{D}$ (Fedele and Paola, 2007; Whittaker et al., 2011). This indicates that the grain size distributions are self-similar.

5.5.2. Similarity variable, ξ

To test this idea explicitly, we calculated the probability distributions of the similarity variable, ξ, as described in Eq. 5.1 and Appendix 5.2. These are shown in Fig. 5.9. This was done for each individual locality (coloured lines), and each fan surface on average by combining all localities (black lines). The calculated values of the similarity variable are distributed around a value of 0, and as expected for self-similar deposits there is no change in the shape or position of these curves from apex to toe on any surface, between the two alluvial fans, or between the Q2c and modern deposits (Fig. 5.9e). The distribution of ξ can therefore be modelled as one representative curve for all the data (red dashed line, Fig. 5.9e), and this is further evidence for self-similar selective deposition. The ξ probability distributions have a long upper tail, reflecting the decreasing frequency of larger particles. The short lower tail reflects the truncation of the grain size distributions at 1 mm, as Wolman point counting cannot sample smaller particles.

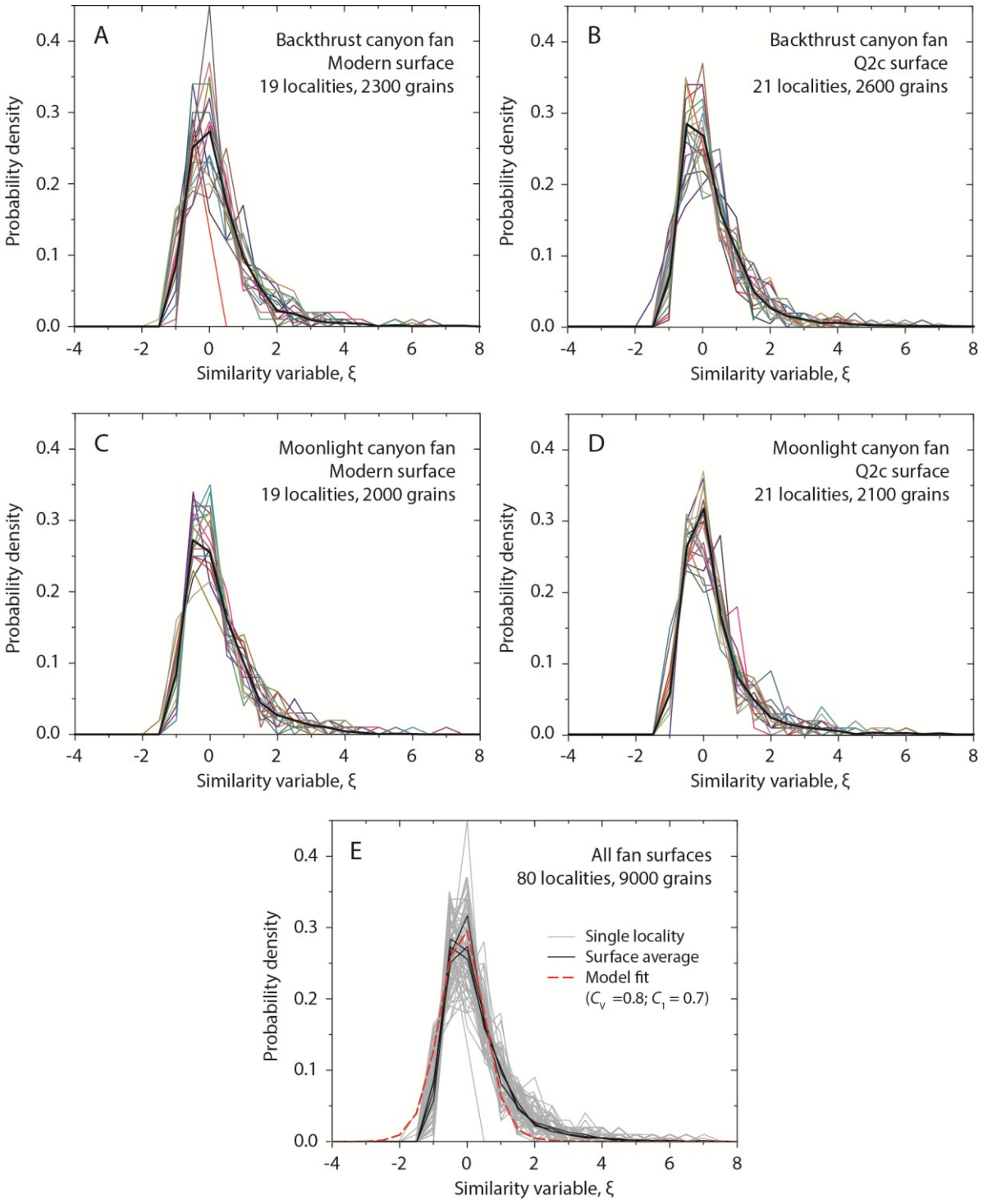

Fig. 5.9. Observed probability distributions of the similarity variable, ξ, on the Backthrust canyon fan (modern surface in A, Q2c surface in B) and the Moonlight canyon fan (modern surface in C, Q2c surface in D). Coloured lines show the distributions for individual sampling localities, bold black lines show the average distribution of ξ for the entire surface. There is no systematic variation in ξ down-system on each surface, between modern and Q2c deposits, or between the two fans. This indicates that grain size fining along the fan lengths obeys self-similarity as defined by Fedele and Paola (2007). See section 5.2 and Appendix 5.2 for equations. (E) All observed probability distributions of ξ from panels A to D collapsed onto a single plot, for all localities on all 4 fan surfaces (grey curves), and the 4 surface average distributions (bold black curves). A self-similar model of selective deposition can be used to model these probability distributions (red dashed line) given a number of empirical constants. We use C_V = 0.8 (Fig. 5.8), and find a value of C_1 = 0.7 provides the best fit to the data; see Appendix 5.2 for full details.

We explore the best-fit modelling of the ξ probability distribution in detail in Appendix 5.2, and consider the implied relative mobility of clasts on these alluvial fans. Importantly, modelling of the similarity variable can be used to derive a value of constant C_1, and as the best-fit model curve in Fig. 5.9e shows, this gives a value of $C_1 = 0.7$. Other workers have found C_1 to vary between 0.5 and 1.0 in different locations, typically averaging 0.7 to 0.8, and so our findings agree precisely with existing constraints (Fedele and Paola, 2007; Duller et al., 2010; Whittaker et al., 2011). With a preferred value of C_1 of 0.7 and an average value of C_v of 0.8, C_2 must be equal to 0.9 (see Eq. 5.6), and the governing equations (5.4, 5.5, and 5.7) are thereby calibrated for application to these systems. We test the effects of uncertainty on the value of C_1 explicitly later on.

5.5.3. Fan comparison

The analyses above suggest the grain size fining on these fans is suitable to be modelled using the self-similarity approach. The Q2c fining rate profiles closely match on both fans, within standard error, indicating that these systems were behaving in the same way ~ 70 ka ago (Fig. 5.8a, b). On the Backthrust canyon fan, the modern fining rate is significantly greater (by > 0.02 km^{-1}) than the Q2c fining rate, and the difference in the overall grain size distributions is also reflected in Fig. 5.7a. On this fan, modern incision into Q2c is negligible, only reaching 2-3 m at the fan apex (Fig. 5.2a) and quickly diminishing to almost no vertical separation for most of the fan (Fig. 5.1a); i.e., it is possible to step from the modern channel onto the Q2c surface in the field. Therefore, the modern deposits on the Backthrust canyon fan have not been significantly affected by recycling driven by fan-head incision. What does this statistically significant increase in modern grain size fining represent? In general terms, an increase in grain size fining rate could be due to an increase in the amplitude and distribution of subsidence, and/or a decrease in the sediment supply from catchment to the fan (c.f., Whittaker et al., 2011; Parsons et al., 2012). A change in the subsidence profile is unlikely over such a short period of time, and because the vertical rates of movement in Death Valley are so low and there is no evidence for significant changes in fault slip rates during this period (see section 2). Given the pronounced climate changes that have occurred between 70 ka and the present day, it is much more likely that a change in grain size fining rate on the fan represents a change in sediment flux (equation 5.7). We proceed under this assumption (section 5.4 below) and our ultimate goal is to estimate the change in Q_S needed to explain this change in the grain size fining rate on the Backthrust canyon fan.

However, on the Moonlight canyon fan, the modern and Q2c surfaces show no difference in their grain size fining rates (Fig. 5.8b). We suspect that this similarity is due to the heavy recycling of the Q2c terrace by the modern channels (Fig. 5.2b), via landsliding, scree cones, and the direct input of large blocks that we have observed in the field. Consequently, we estimate the order of magnitude of

this recycled volume of sediment, compared to the flux of sediment exported from Moonlight canyon. Frankel et al. (2007) reported ^{36}Cl cosmogenic nuclide estimates of catchment-wide erosion rates for Moonlight canyon, averaging 65 mm ka^{-1}. This is for the period of Q2c deposition, not the modern state, but gives an order of magnitude constraint on erosion rate. Converted to standard units and multiplied by the catchment area of 36.7 km^2 gives an estimate of sediment flux of ~2360 m^3 yr^{-1}. In comparison, the incised length of the Q2c cliff is ~ 3 km, has an average depth of 40 m, and the modern channel surface has a width of 100 m in the canyon (Figs 5.1a, 5.2b). A cuboid of these dimensions has a volume of 12,000,000 m^3, making this an order-of-magnitude estimate of the volume of terrace sediment cannibalized by the modern surface. This volume is much greater than the annual sediment flux, but of course the down-cutting and recycling was not instantaneous. It is impossible to know when the incision started, however many alluvial fans in the south-western USA have been incising since the Holocene (Bull, 1991; Pelletier, 2014), so the last 10 ka might be a reasonable assumption. Recycling this 12 Mm^3 of material over 10 ka still gives a flux of 1200 m^3 yr^{-1}, i.e., an equivalent order of magnitude to the sediment flux exported from the canyon. Consequently, the modern surface on the Moonlight canyon fan appears to have received a substantial fraction of sediment from the recycling of older terraces (Figs 5.8 and 5.9).

5.5.4. Recovery of the subsidence profile

The first step in modelling grain size fining as a function of sediment flux is to recover the subsidence profile beneath the alluvial fans, $r*(x*)$ (equation 5.5). We are able to do this by fitting equations 5.4, 5.5, and 5.7 to the observed grain size fining data for the Moonlight canyon fan Q2c surface, because we know Q_S for this particular case: the catchment-average erosion rate of 65 mm ka^{-1} obtained by Frankel et al. (2007) can be multiplied by the catchment area of 36.7 km^2 to estimate sediment flux as 2366 m^3 yr^{-1}. This gives Q_{S0}, the sediment flux exported from the canyon mouth to the apex of the fan.

With Q_{S0} known (2366 m^3 yr^{-1}) and equation 5.10 calibrated for the Moonlight canyon fan Q2c surface (W_0 = 100 m; W_{growth} = 0.5; W_{max} = 7500 m; see Methods), equation 5.7 can be fitted to the observed Q2c grain size data in order to recover the subsidence profile $r*(x)$ (Eq. 5.9), which is the only remaining unknown. We use a measured fan length, L, of 6 km and a porosity of 0.3, and take C_1 equal to 0.7 as determined by the similarity variable analysis in section 5.2, although we also explore the uncertainty on C_1 later. We model the subsidence profile using two constants, the input subsidence rate, r_0, and the rate at which this decays away from the Grapevine fault zone, r_{decay} (Fig. 5.5). Constraints from InSAR suggest that the subsidence rate should be around 0.5 mm yr^{-1} (Hammond et

al., 2012), while geologic estimates are around 0.2 mm yr^{-1} (Machette et al., 2002) (see study area). As r_0 is the largest rate in our formulation, we start by setting this as 0.5 mm yr^{1} and investigate how r_{decay} affects the shape of the grain size fining profile (Fig. 5.10a). The blue line in the background shows the regression fitted to the data in Fig. 5.8 (R^2 = 0.62), with pale blue shading illustrating the standard error of this regression. Dashed black lines show the fining profile generated using different values of r_{decay}. Higher values (e.g., 3 or 4 km^{-1}) mean that subsidence rate decreases quickly down-fan, reducing the accommodation available for sediment extraction, which in turn reduces the rate of fining by selective deposition. Lower values of the exponent (e.g., 1 or 1.5 km^{-1}) mean the subsidence rate remains greater along the length of the fan, and the fining rate is faster due to enhanced sediment extraction. The shape of the curve changes from convex to concave with increasing r_{decay} as a result of the way equations 5.9 and 5.10 trade off in the model. The Q2c data are best represented using a value of r_{decay} between 2 and 3 km^{-1}; the greatest goodness of fit is obtained for r_{decay} = 2.2 km^{-1} and this value agrees well with normal fault geometry in other extensional settings (e.g., Anders et al., 1993; Schlische and Anders, 1996). In Fig. 5.10b, we show the effect of varying r_0 when r_{decay} is fixed at 2.2 km^{-1}. The fining rate becomes too slow when r_0 has low values of 0.2 or 0.3 mm yr^{-1}, and too fast when r_0 has high values of 0.7 or 0.8 mm yr^{-1}.

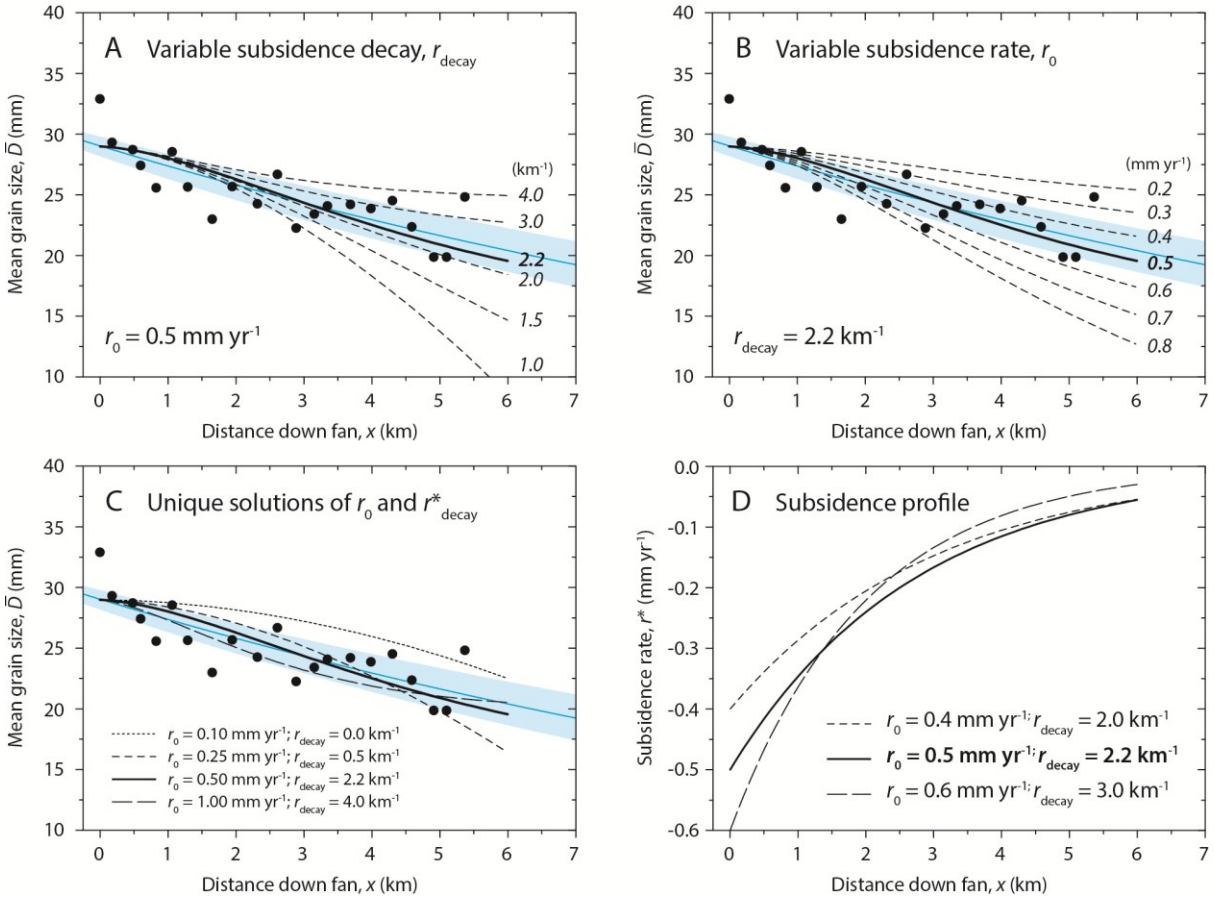

Fig. 5.10. Recovery of the subsidence profile beneath the fans, derived using the Moonlight canyon Q2c surface for which Q_{S0} = 2366 m^3 yr^{-1}, and using the expression for the subsidence profile given in equation 5.9. (A) The input subsidence rate, r_0 is set to 0.5 mm yr^{-1} in agreement with InSAR measurements (Hammond et al., 2012), and r_{decay} is allowed to vary (black dashed lines). The grain size data are fitted with the best fit regression (blue curve) from Fig. 5.8 and the pale blue shading shows the standard error on this regression. The best-fit solution of r_{decay} is 2.2 km^{-1}. (B) We fix r_{decay} as 2.2 km^{-1} and test the effect of varying r_0. Only a small range of rates (~ 0.4 to 0.6 mm yr^{-1}) can be tolerated by the grain size data. (C) There are multiple unique solutions of r_0 and r_{decay} that give the correct overall fining gradient. The subsidence rate must be > 0.1 mm yr^{-1}, as even with no decay (maximum sediment extraction), the fining rate is too slow. For r_0 = 0.25 mm yr^{-1} and r_{decay} = 0.5 km^{-1}, the overall gradient of the fining profile is correct but the form is too convex for the observed data. For a fast r_0 = 1 mm yr^{-1}, r_{decay} must be unreasonably large (4 km^{-1}), and the fining profile becomes concave. While this is within the scatter of the data, geodetic and geologic constraints rule out such a fast subsidence rate (Machette et al., 2002; Hammond et al., 2012). A predicted calibration of r_0 = 0.5 mm yr^{-1} and r_{decay} = 2.2 km^{-1} offers the best fit to the Q2c grain size data. (D) The best-estimate subsidence profile beneath the fans (solid line). Tolerating the uncertainty on r_0 of ± 0.1 mm yr^{-1} (A) and r_{decay} between 2 to 3 km^{-1} (B) makes little difference to the subsidence pattern observed.

Of course, there are multiple solutions of equation 5.9 that could produce a fining rate with the correct overall gradient to fit the grain size measurements, but we can find a plausible fit for the subsidence profile by considering the geologic data and our grain size fining rates together. We compare four such scenarios in Fig. 5.10c. The first is a low subsidence scenario: If r_0 = 0.1 mm yr^{-1} then the

sediment extraction can never be great enough to produce the observed fining rate, even if r_{decay} is set to 0 and the maximum subsidence rate (and accommodation) is maintained for the full length of the fan (dotted line). Consequently, the subsidence rate beneath the fans must be greater than 0.1 mm yr^{-1}. In the second model, a slightly faster r_0 of 0.25 mm yr^{-1} requires a r_{decay} of 0.5 km^{-1} to achieve a fining profile with the correct overall gradient, however the shape of the curve does not match the data well, becoming very convex along the fan (short dashed line). As r_0 is increased to 0.5 mm yr^{-1}, r_{decay} must also increase to 2.2 km^{-1} as seen above (Fig. 5.10a) to maintain the correct fining gradient, and the grain size profile is approximately linear down-fan, reproducing the measurements and the regression well (solid line). Finally, a high initial subsidence rate of r_0 = 1 mm yr^{-1} requires an extremely high r_{decay} of 4.0 km^{-1} to generate a plausible concave fining profile (long dashed line). This is a poorer fit to the regression than the r_0 = 0.5 mm yr^{-1} case, although it still lies within the scatter of the data. However, such high subsidence rates can be ruled out by (i) geodetic observations (Hammond et al., 2012); (ii) geologic constraints (Machette et al., 2002); and (iii) the unreasonable changes in subsidence rate magnitude required over small horizontal distances if r_{decay} is 4.0 km^{-1}.

Our grain size fining measurements therefore support a subsidence profile that has a maximum rate of 0.4 to 0.6 mm yr^{-1}, and which decays away from the GFZ to 0.1 to 0.2 mm yr^{-1} at the fan toes. These profiles are shown in Fig. 5.10d, all of which agree well with existing constraints (Machette et al., 2002; Hammond et al., 2012). Our best fit profile (solid line) is used for the subsequent sediment flux modelling.

5.5.5. Consideration of uncertainty effects

Other sources of uncertainty on the best-fit model grain size fining profile include our parameterisation of fan width, the catchment-averaged erosion rate and our estimate of input sediment grain size. Using the best-fit subsidence profile of r_0 = 0.5 mm yr^{-1}; r_{decay} = 2.2 km^{-1} as a boundary condition for the Moonlight canyon Q2c surface, we explore how these additional sources of uncertainty affect our results. In Fig. 5.11a, we allow W_{growth} to vary from 0.3 to 0.7 km^{-1}. Figure 5.6 shows that this exponent does not occupy a wide range of values, and can be well-constrained to within 0.4 and 0.6 km^{-1}. The effect of this range on the modelled grain size fining profile is indistinguishable from the scatter in the observed measurements.

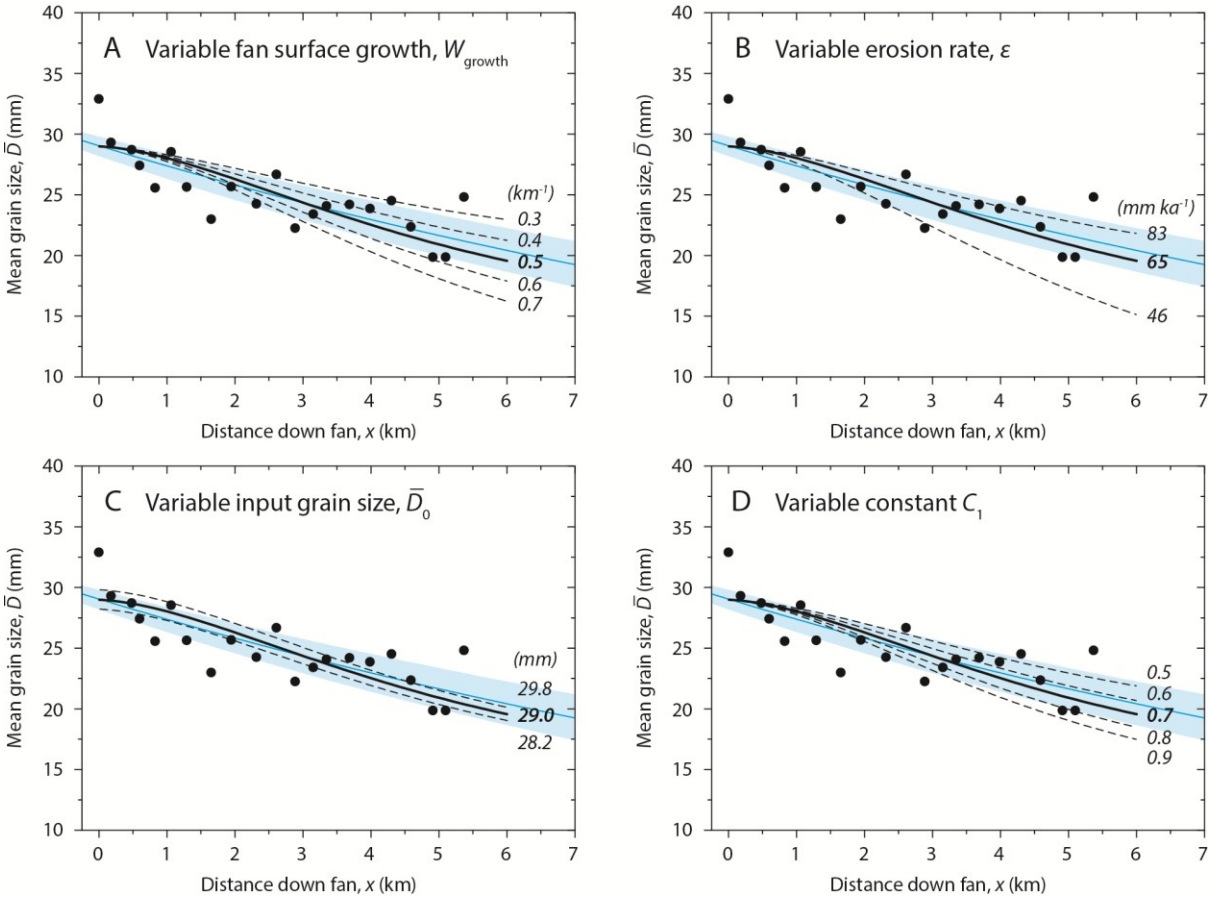

Fig. 5.11. The effect of parameter uncertainties on the fining rate predicted for the Moonlight canyon fan Q2c surface. In each panel, we use the subsidence profile recovered in Fig. 5.10, and known sediment flux details (see text) to explore how each parameter affects the grain size fining rate in our model. The blue line is the regression from Fig. 5.8, and the pale blue shading shows ± 1 standard error on this regression. Apart from each parameter being varied, we keep all other parameters at their best-estimate values (W_{growth}= 0.5; W_0 = 100 m; W_{max} = 7500 m; ε = 65 mm ka^{-1}; $\bar{D}_0$ = 29.0 mm; C_1 = 0.7; C_v = 0.8; r_0 = 0.5 mm yr^{-1}; r_{decay} = 2.2 km^{-1}). (A) The uncertainty on exponent W_{growth}, which is measured as ~ 0.5 km^{-1} (solid line) in Fig. 5.6 lies within the scatter of the data and the error on the regression. Higher and lower values (dashed lines) produce slower and faster fining rates, respectively. (B) The maximum and minimum catchment-wide erosion rates, ε, estimated by Frankel et al. (2007) produce slower and faster fining rates, respectively. The average value of 65 mm ka^{-1} fits the data well (solid line) and the grain size profile is more sensitive to slower erosion rates (and lower sediment fluxes). (C) The standard error on the input grain size distribution, $\bar{D}_0$, (dashed lines) cannot be discriminated from the scatter in the data. (D) The value of C_1 of 0.7 derived in Fig. 5.9 fits the fining profile well, but the scatter in the data can tolerate a range of values of C_1 between 0.6 and 0.8. These analyses show that reasonable uncertainties on each of these parameters do not cause the fining rate to deviate significantly more than the standard error on the regression to which it is being fitted. Therefore, our model setup can tolerate these uncertainties well.

In Fig. 5.11b we show the effect of varying the catchment-averaged erosion rate between the maximum and minimum values reported by Frankel et al. (2007) using ^{36}Cl cosmogenic nuclides. Arguably this is the largest source of uncertainty, because this changes the fining rate by directly

modulating our estimate of sediment flux, for which we assumed the best-fit rate of 65 mm yr^{-1} in the modelling above. The maximum rate derived by Frankel et al. (2007) fits within the upper bounds of our data, but we find the model grain size curve is more sensitive to a decrease in erosion rate (sediment flux). We return to this important finding later, but we note that if these minimum erosion rates were indeed 'correct', a plausible r_0 ~ 0.4 mm yr^{-1} would fit the data well with the same value of r_{decay}. This effect is therefore small, and as we assume subsidence is constant between 70 ka and today, it is also systematic in terms of calculating a change in sediment flux through time. In Fig. 5.11c we show the effect of the standard error on $\overline{D}_0$ obtained from the regression fitted in Fig. 5.8b; this uncertainty cannot be resolved within the scatter of the data and clearly does not influence our modelling. Finally, in Fig. 5.11d we show how sensitive the fining profile is to the constant C_1. Our analyses use an estimated value of 0.7 obtained by evaluating the co-efficient of variation, C_v, directly from field data, and from our similarity variable, ξ, and which agrees well with previous workers (Fedele and Paola, 2007; Duller et al., 2010; Whittaker et al., 2011). In fact, values of C_1 between 0.5 and 0.8 cannot be discriminated from the standard error on the grain size regression.

These graphs show that reasonable uncertainties assigned to each of the parameters do not cause the grain size trend to deviate more than the standard error on the regression to which the model curve is being fitted. Our self-similarity model for alluvial fans can therefore tolerate the uncertainties present. Importantly, our next step is to explore what change in Q_{S0} is required to explain the enhanced modern grain size fining rate, compared to Q2c, on the Backthrust canyon fan. As we keep all other parameters constant, their uncertainties are systematic and have no substantial effect on the relative change in sediment flux reconstructed.

5.5.6. Comparison of Q2c and modern fining rates

With the self-similarity model calibrated and the subsidence profile recovered using the Moonlight canyon Q2c case, a comparison can be made between the modern and Q2c deposits, which represent a climatic gradient through time (see section 2). As explained earlier, we cannot compare the Q2c and modern deposits on the Moonlight canyon fan because of the substantial recycling of grain size resulting from incision. Instead, a comparison is made on the Backthrust canyon fan, for which incision is minimal and documented changes in grain size fining rates are well-constrained. (Fig. 5.8a). We therefore explore the change in Q_{S0} needed to change the gradient of the Q2c fining profile to match the modern surface.

The calibrated grain size fining model is applied to the Backthrust canyon Q2c surface (Fig. 5.12a). We assume the same catchment-wide erosion rate as the Moonlight Canyon, but as the catchment is

slightly larger (46.2 km^2), this produces a slightly greater Q_{S0} of 2981 m^3 yr^{-1}. We also used a value of W_{max} of 9500 m (see section 4.2) from our fan width estimates (see also the supplementary information). The Backthrust canyon fan is slightly longer, at 7 km, so we updated L accordingly in Eq. 5.7, and we used the input mean grain size $\overline{D}_0$ obtained from the regression in Fig. 5.8a. Otherwise, the same parameters are used for $r*(x*)$, $W*(x*)$, C_1, C_2, C_v and porosity. Significantly, these same parameters and sediment flux estimates reproduce the observed Q2c grain size data very well (Fig 5.12a, white circles). Therefore, our reasonable interpretation is that the two fan systems are experiencing the same subsidence profile and can be modelled realistically using the simplifications in Fig. 5.5. We have also calculated the excess sediment fraction delivered to the alluvial fan, F_{excess}. We define this as the flux of sediment exported from the catchment, divided by the volume required to fill the accommodation space generated by the subsidence profile used (Fig. 5.10d), which in this scenario is 1494 m^3 yr^{-1}. As such, a Q_{S0} of 2981 m^3 yr^{-1} represents a F_{excess} of 1.99, i.e., half of the sediment flux is transferred to fan stratigraphy and half is bypassed to the axial Death Valley wash. This is a reasonable figure, given that the size and amount of sediment carried by the axial system increase significantly as it toe-cuts the two alluvial fans (see Fig. 5.1).

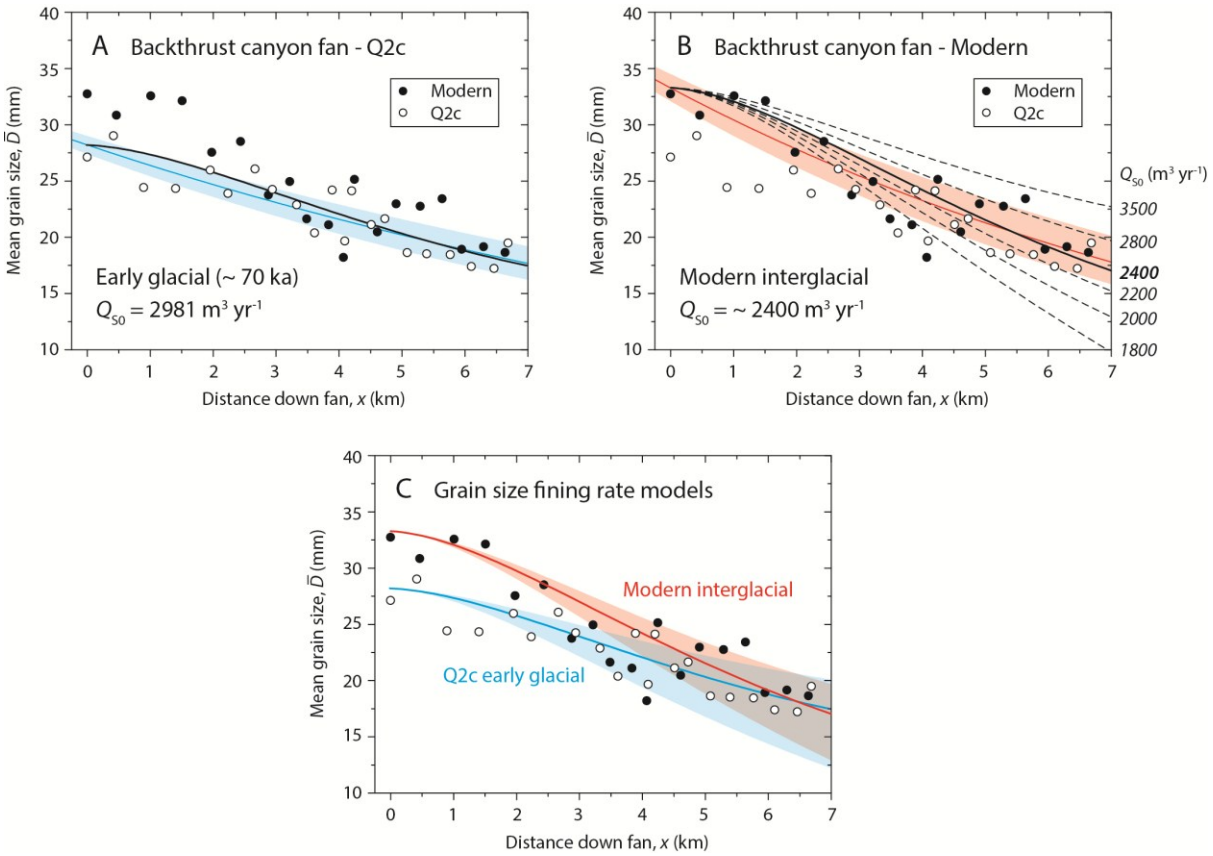

Fig. 5.12. A comparison of modern (solid symbols) and Q2c (open symbols) Q_{S0} scenarios on the Backthrust canyon fan. The best-estimate values of all parameters are used (W_{growth} = 0.5; W_0 = 100 m; W_{max} = 9500 m; C_1 = 0.7; C_v = 0.8; r_0 = 0.5 mm yr^{-1}; r_{decay} = 2.2 km^{-1}). The grain size regressions from Fig. 5.8 are shown as blue (Q2c) and red (modern) lines, with associated pale shading showing ± 1 standard error on the regressions. The input grain size, $\bar{D}_0$, has been taken from Fig. 5.8 in both cases. (A) Q_{S0} is calculated by multiplying the Q2c erosion rate of 65 mm ka^{-1} (Frankel et al., 2007a) by the catchment area of 46.2 km^2, giving 2981 m^3 yr^{-1}. The parameterisation of the model fits the observed fining rate very well. (B) For the modern case, where $\bar{D}_0$ = 33.3 mm, the observed fining rate is faster. We have allowed Q_{S0} to vary between 1800 and 3500 m^3 yr^{-1} (black dashed lines), of which the 2400 m^3 yr^{-1} scenario fits the observed data best, representing a 20 % decrease in Q_{S0} compared to Q2c. We propose a maximum uncertainty of ± 400 m^3 yr^{-1}, tolerating the 2000 to 2800 m^3 yr^{-1} scenarios. (C) The best-fit fining models are shown for the Q2c surface (blue, with uncertainty displayed as the full uncertainty on Q_{S0} deriving from ε in Fig. 5.11b) and the modern surface (red, with Q_{S0} = 2400 ± 400 m^3 yr^{-1}). The modelling approach taken here reproduces the observed grain size data well.

We assume that the subsidence profile, rate, and fan geometry has not changed between the deposition of the Q2c surface ~ 70 ka ago and today. Therefore, we only allow $\bar{D}_0$ and the input sediment flux, Q_{S0}, to change when we fit the model to the modern surface of the Backthrust canyon fan (Fig. 5.12b). The $\bar{D}_0$ is taken from the regression in Fig. 5.8a, so this is already known, and in Fig. 5.12b we show how the fining profile changes with different values of Q_{S0} between 1800 and 3500 m^3 yr^{-1}

(black dashed lines). This is compared to the best-fit regression through the measured data ± 1 standard error (red). As the modern fining rate is faster than the Q2c fining rate, the sediment flux must be reduced in order to enhance the selective deposition of larger particles down-system, and so increase the overall slope of the model fining curve. A high Q_{S0} above ~ 2800 m^3 yr^{-1} cannot model the observed data, as the fining rate is too low. Reducing Q_{S0} to ~ 2400 m^3 yr^{-1} provides the best fit to the data; this is equivalent to a reduction in sediment flux from the catchment of ~ 20 % under modern conditions, compared to the early glacial climate of the Q2c period. Even lower values of Q_{S0} over-estimate the rate of fining and produce grain size profiles that are too fine-grained at the fan toe. A value of Q_{S0} of 2400 m^3 yr^{-1} is equal to a F_{excess} of 1.61, i.e., the accommodation space generated by the subsidence profile is still over-filled, but the percentage of the sediment flux that is eventually transferred to the axial system has decreased from 50 % to 38 %.

Figure 5.12c shows both model curves from Figs 5.14a and b against the grain size data. For the Q2c case, the fining model matches Fig. 5.12a as described above (blue); an uncertainty envelope (pale blue shading) shows the full uncertainty on Q_{S0} that arises from the uncertainty on the erosion rate ε (shown in Fig. 5.11b, this is the largest source of uncertainty). For the modern case, the model curve is for the best-fit reduction in Q_{S0} to 2400 m^3 yr^{-1} shown in Fig. 5.12b, but we have also included an uncertainty envelope of Q_{S0} ± 400 m^3 yr^{-1}, i.e., equivalent to the 2000 and 2800 m^3 yr^{-1} curves in Fig. 5.12b. This is a large tolerance on the possible range of Q_{S0} that could satisfy the data, as it is greater than the standard error on the regression (R^2 = 0.79), however it accommodates the magnitude of the erosion rate uncertainty shown in Fig. 5.11b. Our approach shows that the modern and Q2c curves can be clearly discriminated, not just in terms of their respective grain size fining rates, but also in terms of the 20% reduction in sediment flux that generated the fan deposits over this time period.

5.6. Discussion

5.6.1. Sediment flux and past climate change

The analysis presented above suggests that down-system variations in grain size fining, in these alluvial fans over a 70 ka interval, can be linked to changes in sediment flux. A key question to address is what is driving these changes, given that there is no evidence for a change in tectonic subsidence rate during this time period. Climate change is an obvious cause for this mid-glacial to Holocene variation, and we return to the benthic Pacific $\delta^{18}O$ stack of Lisiecki and Raymo (2009) in Fig. 5.13a, onto which we have marked the Q2c (blue) and modern (red) surfaces, annotated with the estimated sediment fluxes and climatic conditions (see section 3) for the Backthrust canyon system as

a summary. The implied decrease in sediment flux in the Holocene is associated with both warmer mean annual temperatures and a decrease in mean annual rainfall. It should also be noted that a decrease in sediment flux is expected to promote fan incision (Van Den Berg Van Saparoea and Postma, 2008; Simpson and Castelltort, 2012), which reconciles with the incision of the modern surfaces into the Q2c surfaces on these fans. In other words, this sedimentological signal of climate change agrees well with the expression of fan morphology observed in the field.

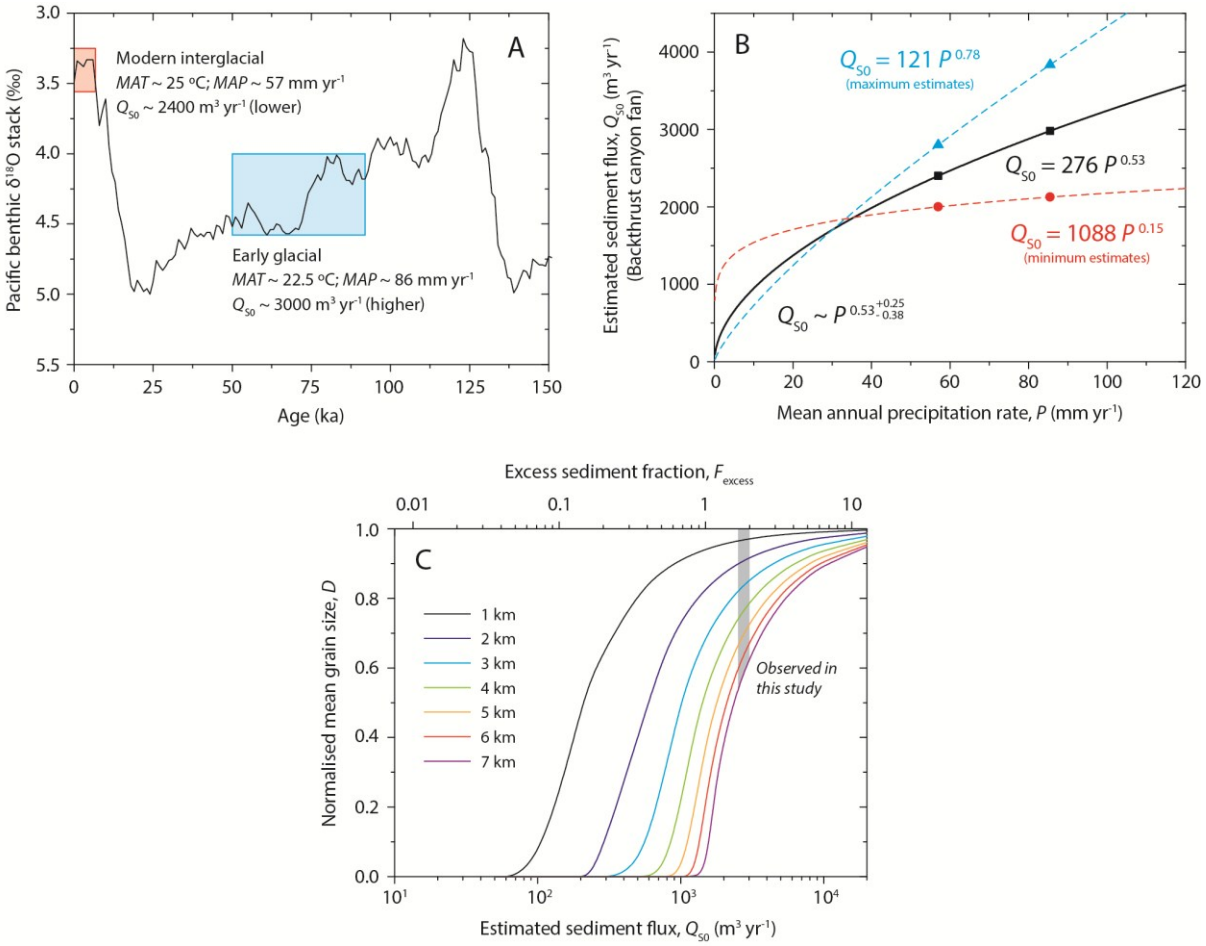

Fig. 5.13. Summary diagram of the Backthrust canyon fan sensitivity to past climate change. (A) The modern (red) and Q2c (blue) surfaces marked on the benthic $\delta^{18}O$ Pacific stack of Lisiecki and Raymo (2009) and annotated with the estimated climatic conditions (see text) and reconstructed sediment fluxes. The change in Q_{S0} we estimate here corresponds to a mid-glacial to interglacial climatic gradient. (B) Best estimates of sediment flux (black squares) plotted against modern and estimated Q2c climate (see text for details). A power law regression that intersects the origin has an exponent of ~ 0.5. Using maximum (blue triangles) and minimum (red circles) sediment flux estimates (see Fig. 5.12c) gives exponents of ~ 0.8 and ~ 0.2, respectively. Thus, the relationship between sediment flux to the fan and precipitation rate is likely to be sub-linear. (C) Predicted mean grain size, $\overline{D}$, at length intervals of 1 km (coloured curves) down-system on the Backthrust canyon fan, modelled using the calibration in Fig. 5.12 for a wide range of hypothetical sediment fluxes between 50 and 20,000 m^3 yr^{-1}. Grain size is normalised to an input value of 1 to generalise the results. The excess sediment fraction, F_{excess}, is given on the top *x*-axis (see text for

explanation), and the range of Q_{S0} predicted for the modern and Q2c scenarios is highlighted as a grey box. Much larger perturbations are explored here. As Q_{S0} increases above Q2c values, the fining rate (the difference between $\overline{D}$ at 1 and 7 km) becomes increasingly small and sensitivity to Q_{S0} decreases. The difference between $\overline{D}$ at 1 and 7 km is greatest (~ 95 %) at F_{excess} = 1 (Q_{S0} = 1494 m^3 yr^{-1}). As Q_{S0} decreases further, the basin is under-filled and the grain size decays to zero at progressively shorter distances from the apex. The sensitivity of the fining rate is much higher to a drying perturbation (reduced Q_{S0}) than a wetting perturbation (increased Q_{S0}), implying directionality in the grain size response to climate change.

The estimated reduction in sediment flux of ~ 600 m^3 yr^{-1}, between Q2c deposition and today, represents a decline of ~ 20 %. This coincided with a ~ 30 % decline in the average annual precipitation rate (see section 2). Broadly, this agrees with numerical models, which predict a decrease in sediment flux resulting from a decrease in average precipitation rate (e.g., Paola et al., 1992a; Allen and Densmore, 2000; Morehead et al., 2001; Densmore et al., 2007; Armitage et al., 2011; Rohais et al., 2012; Allen et al., 2013). Therefore, these data from Death Valley reveal that, in some cases, the grain size fining rate of alluvial fan sediments is highly sensitive to climate changes over glacial-interglacial timescales. This suggests a short stratigraphic response timescale < 10^5 years, and implies that terrestrial sediments can provide high-resolution palaeoclimate information.

The estimated decline in sediment flux is slightly smaller in magnitude than the ~ 30 % decline in mean annual precipitation indicated by palaeoclimate proxies. If the maximum decrease in Q_{S0} to 2000 m^3 yr^{-1} is considered, this equates to a 33 % decline in sediment flux, so while this is likely to be a slight over-estimate (Fig. 5.12b), the magnitude of the sediment flux response would then match the magnitude of the change in precipitation rate. The minimum decrease in Q_{S0} to 2800 m^3 yr^{-1} represents a 6 % decline. This range of possible responses means the sediment flux response to a change in precipitation rate is potentially sub-linear, given that we expect no sediment flux from the catchment to the fan in the theoretical end-member case where precipitation rate is zero. In Fig. 5.13b, we plot the Q2c and modern sediment flux estimates for the Backthrust canyon fan against the estimated mean annual precipitation (black line). For the Q2c case, we have simply multiplied the modern average rainfall rate by a factor of 1.5; this is compatible with a range of palaeoclimate proxies including pollen records, pluvial lake reconstructions, glacier extents in the Sierra Nevada, and δ^{18}O records (see section 3 for details). Assuming our regression intersects the origin, the data are fitted by a power law with an exponent of ~ 0.5. Using the maximum estimates of Q_{S0} in both cases (blue triangles), and the minimum estimates (red circles), changes this exponent to ~ 0.8 and ~ 0.2, respectively. Therefore while there is a range of uncertainty on this exponent (and we have not attempted to quantify the uncertainty on the palaeoclimate constraints, as this is debatable), these data suggest that sediment flux to alluvial fans may in fact be less sensitive to precipitation than some models suggest (e.g., Armitage et al., 2011; Simpson and Castelltort, 2012; Armitage et al., 2013).

Additionally, this result is important, because it suggests that the sediment flux response to climate change may be more sensitive to a drying event than a wetting event.

It is worth considering what this change in sediment input to the alluvial fans represents. Our analyses only give an estimate of how the input sediment flux received at the apex of the fan has changed between mid-glacial and current interglacial conditions. Perhaps it equates to a change in the catchment-wide erosion rate, in which case the modern Q_{S0} of 2400 (± 400) m^3 yr^{-1} would be equivalent to an erosion rate of 52 (± 9) mm ka^{-1} (adjusted from the average Q2c erosion rate of 65 mm ka^{-1}). However we caution against making this interpretation, because it could also be the case that hillslope erosion rates have remained the same or even accelerated as the climate warmed and vegetation cover declined (e.g., Pelletier, 2014), but the sediment is not being exported out of the catchments as efficiently under a drier climate. This would not be surprising, and there is a degree of sediment storage in the main channel of both canyons today, clearly visible in the field and in aerial imagery, so this possibility cannot be ruled out.

5.6.2. Sediment flux sensitivity

In Fig. 5.13c, we take this sensitivity analysis a step further and investigate how this kind of system would respond to a wide range of sediment flux variations. We have used the Backthrust canyon-fan system as a model case, and simulated a much greater range of sediment flux scenarios from 50 to 20,000 m^3 yr^{-1} (see supplementary material for each model run). We have calculated the grain size at 1 km intervals from the fan apex to the toe, which we have normalised by a dimensionless input grain size of 1 in order to generalise the results. We have also equated the sediment flux with the excess sediment fraction, F_{excess}, given the particular subsidence profile derived in Fig. 5.10d. Note that when Q_{S0} is equal to the volume of sediment needed to fill accommodation (1494 m^3 yr^{-1}), F_{excess} = 1 and the basin is filled, and the grain size decays to exactly 0 at the 7 km point, i.e., the toe of the fan. There is no sediment bypassed to the axial system in this case, or with lower values of Q_{S0}. At higher values of Q_{S0}, the excess fraction increases. The range of sediment flux represented by the modern and Q2c cases is highlighted as a thin grey box; evidently much larger perturbations are explored here.

The system is less sensitive to an increase in sediment flux, which might correlate with even wetter conditions. The 7 km curve (the fan toe) is < 20 % finer than the input grain size above a Q_{S0} of ~ 5000 m^3 yr^{-1} (F_{excess} ~ 3.4), and < 10 % finer above a Q_{S0} of ~ 8000 m^3 yr^{-1} (F_{excess} ~ 5.4). Thus, in an extremely wet (high Q_{S0}) scenario, fan stratigraphy might be expected to record the progradation of a coarse-grained sheet conglomerate that supplies a large volume of sediment to the axial system,

making the fining rate difficult to measure (although the significant progradation of a thick conglomerate layer would be easy to identify in itself). However, we find the fining rate is much more sensitive to a decrease in sediment flux, which would correlate with a drying event. The grain size difference between the 1 km and 7 km curves becomes rapidly larger as Q_{S0} decreases, to a maximum of ~ 95 % at F_{excess} = 1. At sediment fluxes lower than 1494 m^3 yr^{-1}, F_{excess} drops below 1 and the basin becomes under-filled. No sediment reaches the fan toe at 7 km, or at progressively shorter distances from the fan apex as Q_{S0} declines further. In the range of scenarios from Q_{S0} between 10^2 and 10^3 m^3 yr^{-1} and F_{excess} between ~ 0.1 and 1, the fining rate in the upper portion of fan stratigraphy is extremely sensitive to sediment flux. These hypotheses are based on an empirical calibration for a small glacial-interglacial range of Q_{S0} scenarios, but might offer useful insights into the effects of more dramatic climate changes on alluvial fan stratigraphy, and the sensitivity of the grain size response.

A final important comment on sensitivity is that these scenarios only apply if the alluvial fan sediments are not reworked. As shown by the Moonlight canyon fan, ~ 40 m of incision into older terraces is sufficient to destroy any climate signal recorded in stratigraphy, because the timescale between sediment production and permanent storage in the basin exceeds the periodicity of orbital climate cycles, i.e., the signal is damped. Indeed, we are only able to recover the change in sediment flux since ~ 70 ka on the Backthrust canyon fan because there is negligible incision of the older deposits. Our findings support the idea that a high sensitivity to climate change is promoted by rapid sediment transfer and minimal post-depositional recycling (e.g., McPhillips et al., 2013), but there is no single 'response timescale' for alluvial fans reacting to a climate change. Of course, we must also ask why the Moonlight canyon fan heavily incised itself during the Holocene while the Backthrust canyon fan did not. This difference in behaviour clearly cannot be attributed to climatic or tectonic differences on such a local spatial scale, nor to lithological or sediment supply processes in the parent catchments, which are the same (Fig. 5.1). Therefore, it is likely to emerge from autogenic processes operating in the alluvial fan systems. For example, Fig. 5.3 shows that the Moonlight canyon fan Q2c surface achieved the greatest slope (4.3 °) of all 4 surfaces sampled, and that after incision the fan slope has readjusted to 3.8 °. Consistent with equilibrium slope models (e.g., Van Den Berg Van Saparoea and Postma, 2008; Simpson and Castelltort, 2012) and physical experiments (Clarke et al., 2010), it may be that the Moonlight canyon fan simply reached a critical slope that triggered a period of incisional re-adjustment, independent of allogenic forcings like tectonics and climate. We encourage more work to demonstrate how the effects of autogenic and allogenic processes can be decoupled in well-studied alluvial fan deposits such as these.

5.6.3. Input grain size

Our analysis has explored the rate of grain size fining from fan apex to toe. However another topic of interest is the input grain size delivered to the alluvial fans from the catchments, and we consider this briefly here.

The $\overline{D}_0$ measured for the Q2c surfaces on both fans overlap within standard error (Fig. 5.8). This reflects how both surfaces were deposited synchronously under the same climate, and that the parent catchments are eroding the same bedrock lithologies with similar slope distributions and sediment supply (Fig 5.1). On the Moonlight canyon fan, where Q2c recycling contributes a large volume of sediment to the modern deposits, the modern $\overline{D}_0$ is also indistinguishable from the Q2c $\overline{D}_0$. In all three cases, the input grain size is 28 to 30 mm and fines to ~ 20 mm at the fan toes. In contrast, the modern $\overline{D}_0$ on the Backthrust canyon fan is coarser at ~ 33 mm, and does not overlap with the other input grain sizes within standard error. This may be slightly surprising, as the coarsest $\overline{D}_0$ is found on the surface for which the sediment flux is estimated to be lower. One issue we have not discussed so far is the formation of desert pavement on the Q2c fan surfaces (Fig. 5.2d and f). A range of processes during desert pavement formation might conceivably alter the surface grain size distribution, including clast sorting, clast fragmentation, deflation, and upwards clast migration (Goudie, 2013). However very few data sets are available that quantify the integrated effect of all these processes on the surface grain size distribution..

Al-Farraj and Harvey (2000) measured grain size on alluvial fan surfaces in Wadi Al-Bih, Oman, which are also dominated by limestone clasts and have mature desert pavements similar to our study sites. They found that the paved surfaces have a slightly finer grain size distribution than the unexposed subsurface, an effect that becomes more pronounced with age. On ~ 100 ka surfaces, they find the average clast diameter on the paved surface to be ~ 25 mm, compared to ~ 30 mm clasts in the subsurface. These data indicate that in a comparable location, desert pavement formation (albeit over a ~ 30 % longer timescale than considered here) reduces the mean in the overall grain size distribution by ~ 16%. This effect is not expected to change the rate of grain size fining down-system, but it could alter the intercept ($\overline{D}_0$) of the fining curve. The magnitude of this effect is sufficient to explain the input grain size difference between modern and Q2c values on the Backthrust canyon fan. Therefore, we cannot rule out the possibility that the catchments supply a lithologically-mediated constant $\overline{D}_0$ of > 30 mm through time, but desert pavement formation on the Q2c terraces (or subsequent recycling of them) reduces the overall grain size distribution by a few millimetres in a systematic way.

Nevertheless, we stress that our sediment flux analysis actually depends on the rate of grain size fining from apex to toe, and the relative change in the gradient of the fining profile through time. We

do not expect any grain size changes resulting from desert pavement formation to vary spatially across the fan surfaces, and indeed in the field we observed uniform pavement formation on the Q2c terraces. Therefore, we consider our estimates of relative grain size fining rates, sediment flux and subsidence to be reasonable.

5.7. Conclusions

In this study, we have examined two mountain canyon-alluvial fan systems draining the Grapevine Mountains in northern Death Valley, California. We have demonstrated that the grain size fining rate is self-similar from apex to toe on four alluvial fan surfaces: a modern surface and a ~ 70 ka surface on each fan, dated by Frankel et al. (2007). By adapting the self-similarity equations of Fedele and Paola (2007) for alluvial fans, we are able to first derive the subsidence profile in this part of the basin, and secondly estimate that a ~ 20 % decrease in sediment flux has occurred between the mid-glacial climate state and modern conditions. This coincides with a decrease in mean annual precipitation of approximately one third (Thompson et al., 1999; Quade et al., 2003; Menking et al., 2004; Kessler et al., 2006; Phillips, 2008; Lisiecki and Raymo, 2009), supporting the majority of numerical catchment-fan models that predict such a sediment flux response to climate change (e.g., Paola et al., 1992a; Allen and Densmore, 2000; Morehead et al., 2001; Densmore et al., 2007; Armitage et al., 2011; Rohais et al., 2012; Allen et al., 2013). This may be due to a proportionate decrease in catchment-wide erosion rates, but could equally be due to a decrease in the efficiency at which sediment is evacuated from the canyon.

Our approach offers one method of reconstructing sediment fluxes in the past from sedimentological data collected in the field, and demonstrates that grain size data can be used to quantify the primary controls (tectonics, climate, erodibility) on landscape evolution and the stratigraphic record. Our findings are supported by additional observations. (i) The maximum subsidence rate we recover for this part of northern Death Valley is ~ 0.5 mm yr^{-1}, and not only fits the observed grain size fining rate well, but also agrees with geodetic data (Hammond et al., 2012) and geologic constraints (Machette et al., 2002), offering new information about the subsidence rate in this valley. (ii) We observe that the alluvial fans have incised at a time when sediment flux has declined, and this also reconciles with numerical models such as Van Den Berg Van Saparoea and Postma (2008) and Simpson and Castelltort (2012), indicating that sedimentological signals of climate change in alluvial fans complement incision-aggradation architecture. (iii) The grain size data from the Death Valley fans also require a low-mobility calibration of the self-similarity model, in agreement with the real environment.

The Moonlight canyon and Backthrust canyon systems demonstrate when the stratigraphic record is sensitive and insensitive to high-frequency (e.g., orbital, $< 10^5$ year timescale) climate perturbations. When sediment recycling is high, e.g., due to 40 m down-cutting on the Moonlight canyon fan, the grain size signal of orbital climate change is damped because the sediment is reworked over a time period longer than the climate cyclicity. The signal is preserved on the Backthrust canyon fan, because incision and recycling of older terraces is minimal. This implies that landscapes, and the terrestrial sedimentary record, can have a range of response timescales that depend on the time taken for sediment to be permanently locked into stratigraphy, but without further recycling taking place. Our sensitivity analysis also indicates that alluvial fan grain size might be more sensitive to drying than wetting. This has implications for future climate change scenarios, and suggests that at least the arid and semi-arid landscapes of the south-western United States may be increasingly sensitive to further drying as the climate continues to warm.

Appendix 5.1. Uncertainty analysis of photo Wolman point counting

We take this opportunity to evaluate the Wolman point counting technique, using scaled field photographs, as a method for characterising the grain size distribution of the gravel fraction. Using all the grain size counts we make in this study, in Fig. 5.A1a, we plot how $\overline{D}$ changes as additional clasts are measured, up to a total of 100 particles, for every individual Wolman point count locality. The grain size has been normalised by the final mean grain size (at 100 counts), so that all 80 curves converge on a value of 1. Therefore, this plot shows how $\overline{D}$ converges on a stable value as more clasts are sampled. With only 20 clasts, for example, $\overline{D}$ might be 40 % larger or smaller than the final value. This error declines to within ~ 10 % by approximately 70 clasts, and to within ~ 5 % by 80-90 clasts (see inset). The envelope containing all these curves represents the maximum limits of the variation in $\overline{D}$ with increasing counts, and declines exponentially as more particles are measured. Many curves converge on a normalised value of 1 after 50 or 60 clasts.

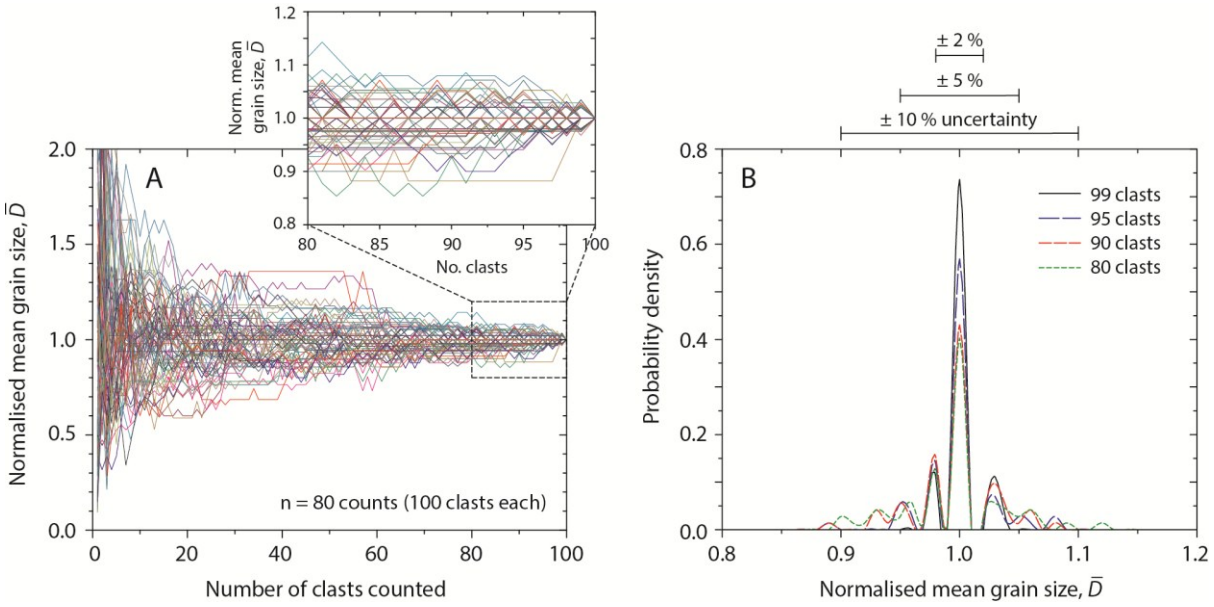

Fig. 5.A1. (A) This plot shows, for each photographic Wolman point count sampled (n = 80 localities), how the estimated mean grain size, $\overline{D}$, changes as additional clasts are sampled from 1 to 100 particles. The $\overline{D}$ is normalised by the $\overline{D}$ obtained using 100 clasts so all curves converge on a value of 1, and the inset shows an expanded view between 80 and 100 grain size counts. The spread of the curves around a normalised $\overline{D}$ of 1 shows the uncertainty on the measurement precision, which decreases exponentially as more clasts are counted. Averaging only ~ 20 clasts means the uncertainty on the precision of $\overline{D}$ will be approximately ± 40 %, and this decreases to within ± 10 % after approximately 70 particles, although some curves reach this precision after fewer counts. In (B), we show probability distributions of the normalised $\overline{D}$ at slices across the inset of (A) at 80, 90, 95 and 99 counts. For the majority of localities, the precision on $\overline{D}$ estimated using these sample sizes is within ~ 2 %. The probability of obtaining a precision within 2 % or less (the integrated area under the probability distributions within this range) improves

from 0.57 with 80 clasts to 0.74 with 95 clasts. The probability of obtaining a precision within 5 % or less improves from 0.79 with 80 clasts to 0.92 with 95 clasts. For a true $\overline{D}$ of 25 mm, for example, precision within 5 % gives a measurement uncertainty of ± 1.25 mm, and within 2 % gives ± 0.5 mm. We therefore argue that this grain size sampling technique is acceptable for our investigation, and uncertainty on measurement precision is smaller than other sources of uncertainty.

To visualize how these curves are distributed around a value of 1, in Fig. 5.A1b we have plotted probability densities using all curves, across slices of the inset Fig. 5.A1a. At sample sizes of 80, 90, 95, and 99 clasts, these show the relative deviation of the mean particle size from that estimated using 100 clasts. The majority of mean values are within 2 % of the final estimate, even after 80 counts. There is little improvement in the uncertainty of the mean diameter between 80 and 99 counts. Figure 5.A1 therefore shows that sampling 100 clasts is sufficient to converge on a stable mean grain size within ~ 2 % in the clear majority of cases, i.e., for a $\overline{D}$ of 20 mm, increasing the sample size by more than 100 particles will only refine the value of $\overline{D}$ within a typical uncertainty of < 0.5 mm. In fact, the exponential decline in the outer envelope of Fig. 5.A1a means that to significantly improve upon the uncertainty obtained by averaging 100 clasts, one would need to average an order of magnitude more grains. Wolman point counting cannot sample anything below the resolution of the images being used (or what can be measured in the field, if performed in situ), which is 1 mm in this study. Therefore it only characterises the > 1 mm gravel fraction of sediment. On these alluvial fans, this represents the majority of sediment (see Figs 5.2e and 5.2f), and we use the self-similarity equations of Fedele and Paola (2007) that are specifically formulated for the gravel fraction only. Therefore, we consider this Wolman point counting method to be suitable for the purposes of our investigation.

Appendix 5.2. Analysis of the similarity variable, ξ

Values of C_1 and C_2 can be obtained by analysis of the similarity variable, ξ, defined by Fedele and Paola (2007). We calculate values of this variable for each particle measured in each Wolman point count, according to:

$$\xi = \frac{D - \overline{D}(x_*)}{\sigma(x_*)} \qquad [5.A1]$$

where D is the diameter of each individual clast, and ξ is dimensionless. We calculated frequency distributions for values of ξ at intervals of 0.5, which also reveal that these alluvial fan deposits obey self-similarity (Fig. 5.9). Frequency distributions of ξ can be modelled using equations from Fedele and Paola (2007):

$$f(\xi) = Ce^{-\phi(\xi)} \quad [5.A2]$$

Consequently, $f(\xi)$ depends on the exponent $\Phi(\xi)$, which is the integral of a parameter $\varphi(\xi)$ (Eq. 5.A3, below) and thus relates to the grain size variance parameters C_1, C_2 (Eq. 5.5) and the relative mobility function, J.

$$\phi(\xi) = -\int \varphi(\xi) d\xi \quad [5.A3]$$

$$\varphi(\xi) = \frac{1}{C_1\left(1+\frac{C_2}{C_1}\xi\right)}\left(1-\frac{1}{J}\right) - \frac{J'}{J} \quad [5.A4]$$

J ,the self-similar relative mobility function, is defined as:

$$J = a_g e^{-b_g \xi} + c_g \quad [5.A5]$$

where a_g, b_g and c_g are constants, and J is also equal to the ratio of the fraction of a given grain size in transport to the fraction transferred to the deposit (i.e., it increases with greater particle mobility).

The probability distribution of ξ can be used to derive the values of the constant C_1, providing that the relative mobility function J can be estimated (Eq. 5.A5). Once C_1 is derived, then C_2 is implied from Eq. 5.6, given that we know the average value of C_v equal to 0.80 (Fig. 5.8c). Previous studies have found c_g to have a constant value of 0.15 (Fedele and Paola, 2007; Duller et al., 2010), and we maintain this value here, as it fits our data well. Documented values of a_g vary between 0.5 (Duller et al., 2010) and 0.9 (Fedele and Paola, 2007), while values of b_g vary between 0.2 (Fedele and Paola, 2007) and 0.8 (Duller et al., 2010). Equation 5.A5 shows that a_g scales with the mobility of all particles, while b_g describes the rate at which particles of increasing size become less mobile than smaller particles; therefore, these constants embody information about the relative mobility of clasts and are expected to vary between study areas. Existing work has calibrated these constants for rivers in which clasts are presumably more mobile than on the arid alluvial fan surfaces of Death Valley. The constant C_1 may be as low as 0.5 (Duller et al., 2010) or have a higher value of 0.7 to 0.8 (Fedele and Paola, 2007), but in general lies between 0.5 and 1.0.

In Fig. 5.A2a, we have collapsed all of the single-locality ξ distributions from Fig. 5.9a-d into a single plot (grey lines), along with the four surface average ξ distributions (black lines). We have then graphically derived the best-fit values of C_1, a_g and b_g that reproduce the shape of these distributions. We find the greatest goodness of fit using values of C_1 = 0.7, a_g = 0.15, and b_g = 2.2; and all our analyses are available as interactive spreadsheets in the supporting information. In Fig. 5.A2b to d, we vary each of these three constants in turn, keeping the other two at their optimum values, to demonstrate the sensitivity of the similarity distributions to their values (coloured lines). Clearly, C_1 may take a range of values between 0.6 and 0.9, with a preferred value of 0.7 (Fig. 5.A2b), and we

therefore evaluate the uncertainty associated with varying C_1 within this range in our modelling. With a preferred value of C_1 of 0.7 and an average value of C_v of 0.8, C_2 must be equal to 0.9 (Eq. 5.6), and the governing equations (5.4, 5.5, and 5.7) are thereby calibrated for application to these systems. These values of the constants are in very close agreement with previous work and other locations (Fedele and Paola, 2007; Duller et al., 2010; Whittaker et al., 2011).

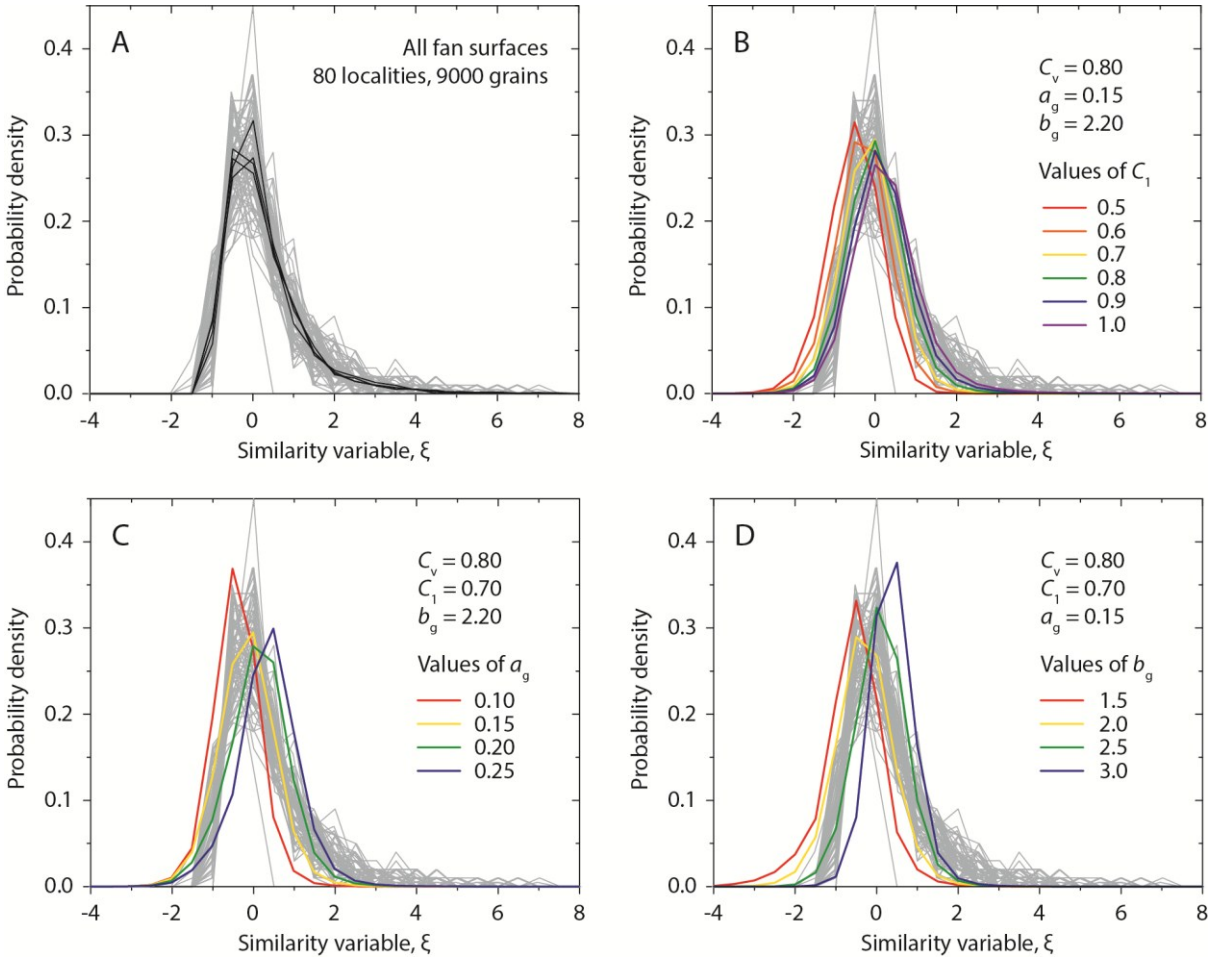

Fig. 5.A2. (A) Observed probability distributions of the similarity variable, ξ, for all localities on all 4 fan surfaces (grey curves), and the 4 surface average distributions (bold black curves). This graph collapses the 4 panels from Fig. 5.9 into one plot. A self-similar model of selective deposition can be used to model these probability distributions given a number of empirical constants. We use a value of C_v of 0.8 obtained from Fig. 5.8c, and a value of c_g of 0.15 (Fedele and Paola, 2007; Duller et al., 2010) to graphically derive the values of C_1 (0.7), a_g (0.15) and b_g (2.2) that best fit the observed data. In panels B to D we demonstrate how the probability distribution changes as each constant is varied in turn, with the other 2 constants kept at their optimum values. An interactive model is available in the supporting information. Values of C_1 between 0.6 and 0.8 fit the observed distributions well, and agree with previous findings (Fedele and Paola, 2007; Duller et al., 2010; Whittaker et al., 2011). The short negative tail of the distribution is due to the truncation of the grain size distribution at 1 mm by our sampling technique, and we therefore do not try to reproduce it. Values of a_g must be between ~ 0.1 and 0.2, and values of b_g must be between ~ 2 and 2.5. These ranges are smaller and larger, respectively, than previous constraints obtained for channels (Fedele and Paola, 2007), however these constants are expected to vary

geographically and indicate low-mobility transport conditions proportionate to alluvial fan surfaces in Death Valley.

Although the values of the constants a_g and b_g are not important for the governing equations, and are therefore tangential to our analyses, they contain useful information about particle mobility on these alluvial fans. As Fig. 5.A2 shows, the ξ distributions can only be effectively modelled with values of a_g less than ~ 0.2 and values of b_g greater than ~ 1.5 to 2.0. This low value of a_g and high value of b_g (compared to other studies, e.g., Fedele and Paola, 2007, and Duller et al., 2010) clearly reflect a low mobility transport environment. This is encouraging, as it arises from the data without any prior knowledge of the study area, but matches well the arid and low-mobility conditions on these Death Valley alluvial fans. This observation suggests that the self-similar fining model can accurately describe sediment transport in these systems.

6. Discussion

6.1. Summary of main findings

The Earth's landscapes are sensitive to climate in different ways, and over different spatial and temporal scales. In Chapters 2 to 5, I have demonstrated this with some new examples. Here, I summarise the main research findings of this thesis, and refer back to the aims and objectives from section 1.2 where applicable.

In Chapter 2, I address Aim 1 and establish that the longitudinal geometry of river channels, quantified by the channel steepness index, k_{sn}, is sensitive to climate in a general way that conforms to predictions made using a simple stream power erosion law. Over a range of mean annual precipitation rates from 100 to 1000 mm yr^{-1}, tectonically active areas with catchment uplift rates of ~ 1 mm yr^{-1} show increasing k_{sn} with precipitation rate where rainfall is orographic, i.e., precipitation rate scales with uplift rate (objective 1.1). This is because precipitation rate acts as an uplift proxy, but it also modulates the uplift-k_{sn} relationship simultaneously by making it non-linear. Assuming that channel steepness scales linearly with uplift rate (i.e., the slope exponent 'n' in the stream power erosion law has a value of 1), I found that increasing precipitation rate acts to limit the rate at which channels can steepen in response to tectonics, producing a sub-linear increase in k_{sn} with rainfall that has an exponent equal to $1 - m$ (the discharge exponent in the stream power erosion law). In the 2 areas where there are a wide spread of precipitation rates across small geographic areas (California, with fast maximum uplift rates ~ 1 mm yr^{-1}, and Idaho with slower maximum uplift rates of < 0.3 mm yr^{-1}), I found a consistent value of m around 0.4 ± 0.1, independent of tectonics. This is in good agreement with expectations from theoretical work and empirical data elsewhere (Sklar and Dietrich, 1998; Stock and Montgomery, 1999; Snyder et al., 2000; Wobus et al., 2006; Ferrier et al., 2013), and indicates that the climatic signal can be separated from tectonics (objective 1.2).

I then examined just the steepest channels, averaged in areas of different climate but similar uplift rates. I found that k_{sn} decreases with precipitation rate following a power law with an exponent of ~ 0.5 (where tectonics can be controlled), which is another approach to estimating the value of the discharge exponent m. In Chapter 2, I discuss how these complementary methods of measuring m agree with each other; one analysis performed within individual study areas, the other comparing results between different mountain ranges. However, the foremost implication of the results is that the channel steepness index, k_{sn}, is inversely proportional to approximately the square root of average precipitation rate, and that this can be demonstrated empirically even when channel steepness is also coupled with tectonics (objective 1.3). Steep landscapes are therefore not only promoted by fast uplift

rates, but also by dry climates with low rainfall rates (e.g., the Western Cordillera of the Peruvian Andes), in a predictable way. Glacial-interglacial climate variability is likely to have only a secondary effect on my findings, the magnitude of which I also estimate in Chapter 2, and even if the long-term average climate is considered, the channel steepness index still declines as the climate becomes wetter. This effect is large, with k_{sn} halving in value from 300–400 $m^{0.9}$ to 100–200 $m^{0.9}$ as precipitation rate increases from 100 to 1000 mm yr^{1}, for an uplift rate of ~ 1 mm yr^{-1}. That is a significant depression of channel steepness for a relatively modest range of rainfall rates, and is likely to explain some of the geographic variation in k_{sn} that cannot be explained by tectonics alone (e.g., Snyder et al., 2000; Boulton and Whittaker, 2009); see section 2.1. Importantly, at slow uplift rates of < 0.3 mm yr^{-1}, no sensitivity is observed to climate; this implies that the effects of tectonics and climate are truly coupled in the landscape and that significant uplift (and therefore active, dynamic sediment routing systems) promotes climatic sensitivity.

Of course, these findings also indicate that dry, steep, actively uplifting sediment routing systems are likely to be highly sensitive to external forcings, whether these are tectonic or climatic. This important observation pre-empts Chapters 3 to 5, in which I explore the effects of climate changes during the last glacial-interglacial cycle on small sediment routing systems in the drylands of California. This work addresses Aim 2 of my thesis and focuses on small catchment-alluvial fan systems. It is divided between the debris flow-dominated systems of the southern Sierra Nevada in Owens Valley, and the more channelized fan systems in Death Valley further east.

There is much that we still do not understand about debris flows, especially about their transport mechanics and how to quantitatively interpret the sedimentology of their deposits. This leaves many opportunities for making new discoveries about how debris flow stratigraphy records climate changes. I chose to sample a number of debris flow fans in southern Owens Valley for many reasons outlined in Chapters 3 and 4, but primarily because detailed exposure age constraints have been published by Zehfuss et al. (2001), Dühnforth et al. (2007), and Le et al. (2007). Between these studies, 89 different ^{10}Be exposure dates are reported for granitic debris flow fan sediments, spanning the full glacial cycle back to the previous interglacial period ~ 125 ka ago, and where tectonics and lithology are broadly constant in time and space (objective 2.1). These unique and detailed boundary conditions offer an unprecedented opportunity to extract a high resolution glacial-interglacial time series from alluvial fan deposits. I chose to focus on the grain size distribution of debris flow channels and levees, and make use of the high density of age constraints by analysing grain size as a time series. This is discussed at length in Chapter 4, but in principle grain size records the mixing of different sediment sources and the transport conditions during sediment mobilisation (e.g., Fedele and Paola, 2007; Whittaker et al., 2007a, 2010; Duller et al., 2010; Waters et al., 2010; Foreman et al., 2012; Allen et al., 2013; Foreman, 2014; Michael et al., 2014; Attal et al., 2015; among others), which are the two major

mechanisms by which environmental (climatic) changes are communicated to landscapes and sedimentary deposits.

The most striking finding from the Owens Valley data is that grain size time series from debris flows produce such sensitive time series of the last glacial-interglacial cycle (e.g., Fig. 4.8); these records could almost be used as terrestrial palaeoclimate records themselves. The response timescale of the catchment-fan systems in Owens Valley is rapid—below the temporal resolution of our data set, certainly < 10 ka—and at the same time, the amplitude of the climate signal preserved by the sediments is large, i.e., the D_{50} doubles from 15-20 mm in the glacial period to 30-40 mm today. These kinds of signals are therefore easy to detect, if a sufficiently detailed chronostratigraphy is available, and indicate a strong sensitivity to relatively rapid (10^4 to 10^5 year) climate changes. It is extraordinary that the climatic signal is so consistent across 8 separate sediment routing systems, perhaps most prominently shown by the channel D_{84} time series in Fig. 4.8 where grain size increases from 30 mm at the glacial maximum 25 ka ago, to 50 mm by the mid-Holocene, and then so rapidly to ~ 80 mm today (objective 2.3).

A key finding in the Owens Valley work is that the climatic signal recorded in grain size cannot be driven by changes in sediment supply, such as the transient evacuation of glacial moraines or paraglacial supply, and is therefore likely to be due to sustained variations in transport and mobilisation. I found that grain size scales exponentially with temperature in a way that broadly matches the Clausius-Clapeyron relation, which itself provides a measure of how maximum storm rainfall intensity increases with warming climate. On this basis, and given that today debris flows are triggered by high-magnitude storm events (e.g., DeGraff et al., 2011, give a detailed account of modern debris flow events in Owens Valley), I hypothesise that the grain size time series in these fan deposits primarily reflect changing storm intensity during the last glacial-interglacial cycle. This is a hypothesis that needs to be tested further, including in other study areas, and I outline some next steps in the following section. However it offers a new way to test the effects of 'storminess' on sedimentary records that are clearly sensitive to climate, and represents one step in making sense of complex, poorly-understood debris flow stratigraphy. On that note, the analyses I make in Chapter 4 underscore the importance of discriminating between average conditions and high-magnitude climate events. The glacial period was wetter overall in the south-western United States (this is known from a range of palaeoclimate indicators that are reviewed in detail in section 4.3.2), so a simplistic approach would predict coarser grain sizes reflecting enhanced discharge in the wettest parts of the last glacial period. This is clearly incorrect. In fact, I observe the coarsest material being exported in the arid interglacial periods, and this can only really be explained by the decoupling of the total rainfall budget and the intensity of high-magnitude storms, which are ultimately the events that trigger debris flows. However, this has important implications for landscape evolution models, particularly of small

sediment routing systems that generally do not deal with the magnitude-frequency distribution of rainfall, or threshold-controlled hillslope processes like debris flows and landslides.

Broadly, the Owens Valley work demonstrates that (i) some small sediment routing systems with rapid sediment transfer can be highly sensitive to climate; (ii) debris flow deposits contain useful information about past climate changes, and can be quantified with respect to fundamental drivers like temperature; (iii) high-magnitude storm events are important, and can be decoupled from the total or average rainfall budget in a way that complicates how sedimentary records capture past climate change; and (iv) high resolution, empirical field data sets are essential for advancing our understanding of landscape sensitivity to climate. My findings also have clear implications for how we understand debris flows as hazards, because larger, coarser-grained and more erosive debris flows may accelerate their responses and become even more sensitive to a warmer, stormier future world.

Obtaining such a detailed data set as that in Chapter 4 requires a detailed age model for alluvial fan deposits. It is therefore worth summarising the main findings of Chapter 3, largely a methodological chapter, where much of this age model is established. Ultimately, the Owens Valley chronostratigraphy is based on ^{10}Be exposure dating work reported by others (Zehfuss et al., 2001; Dühnforth et al., 2007; Le et al., 2007): a technique that continues to revolutionise geomorphology by providing accurate exposure ages. However, despite this total of 89 individual exposure ages, measured by 3 separate teams of researchers studying these alluvial fans over several years (and at an expense of surely tens of thousands of pounds), the timing of deposition was only constrained for 9 of the fan surfaces in Owens Valley. Clearly, techniques for correlating and extending absolute age models are still necessary. Chapter 3 develops one new technique in the Owens Valley study area, based on my observation that vertical weathering fractures in surface boulders widen at a steady rate of ~ 1 mm ka^{-1} through time on these fan surfaces. These features can therefore be used as absolute age indicators, having been calibrated with the cosmogenic nuclide data, and I use this discovery to estimate the ages of an additional 27 alluvial fan surfaces in my study area (objective 2.2).

The observation that the time-averaged rate of surface lowering on a boulder fracture plane is ~ 0.5 mm ka^{-1}, which precisely agrees with the erosion rate on the surfaces of fresh granitic boulders in Owens Valley (Phillips et al., 2009; Rood et al., 2011), indicates that they are created by weathering. In detail, even this weathering rate may be sensitive to past glacial-interglacial climate cycles (Fig. 3.6), and I am able to show how reconciling the ^{10}Be age calculations with the surface lowering rate can reduce the exposure age uncertainties significantly, thus improving the accuracy of the technique and the reliability of the overall age model (see the discussion around Fig. 3.5). As such, these weathering fractures are fascinating features in their own right and merit further research. However within the overall scope of this thesis, the most important contribution of Chapter 3 is adding a further 27 dated fan surfaces to the 9 surfaces already dated using cosmogenic nuclides. The grain size

analyses performed in Chapter 4 would be much poorer without the temporal density of age control established in Chapter 3. All of the data points would have been pinned to the 9 ^{10}Be calibration ages, meaning none of the temporal details would have been detected, e.g., the asymmetry of the glacial-interglacial signal in Fig. 4.8, the lack of grain size hysteresis with temperature in Fig. 4.9, or the exponential form of the grain size-temperature dependency. These important observations would have been missed, and this highlights the importance of developing new and innovative methods of estimating deposit ages and correlating these constraints across time and space. I elaborate on another potential opportunity in the next section.

The time series in Chapter 4 are informative, but it would also have been useful to know past sediment fluxes and volumes, as well as deposit sedimentology. Unfortunately it is not possible to reconstruct sediment volumes on the Owens Valley fans, because older fan surfaces have been buried quite significantly by Holocene deposits on the lower half of the bajada. Therefore, other approaches are needed to test whether sediment flux—like deposit sedimentology and grain size—is sensitive to past climate change. One approach is using a self-similar model of down-system grain size fining based on selective extraction of larger clasts into stratigraphy, to reconstruct sediment flux for a given depositional surface. Based on a mathematical model developed by Fedele and Paola (2007), this approach has been used effectively to study the climatic and tectonic controls on sediment flux in various locations in recent years (Duller et al., 2010; Whittaker et al., 2011; Paola and Martin, 2012; Parsons et al., 2012; Michael et al., 2013; 2014; Hampson et al., 2014). However it cannot be applied to debris flow systems, requiring channelized stream flow-dominated deposits where the mobility of a clast is proportional to its size. Therefore, in Chapter 5 I move to Death Valley and measure the down-system rates of grain size fining on 2 carefully-selected alluvial fans with glacial age (~ 70 ka) and modern (interglacial) surfaces that are exposed from apex to toe, and use these data to reconstruct sediment flux changes through this temporal climate gradient (objective 2.4).

The Death Valley fans lie adjacent to each other on the eastern side of the northern Death Valley basin, and therefore have experienced identical climatic and tectonic histories, and also have equivalent catchment sizes, shapes, geomorphology and bedrock outcrop patterns. On one of the fans (Backthrust canyon fan), the 70 ka and modern fan surfaces have simply avulsed, with little modern incision into older deposits and therefore minimal sediment recycling. Here, a relative decrease in total precipitation rate of ~ 30 % led to an increase in the grain size fining rate of ~ 25 %, and I adapt the grain size fining model of Fedele and Paola (2007) to estimate a corresponding decrease in sediment flux of ~ 20 %. This implies that a decrease in rainfall leads to a decrease in sediment flux, which supports the majority of numerical catchment-fan models and physical experiments (e.g., Paola et al., 1992a; Allen and Densmore, 2000; Morehead et al., 2001; Densmore et al., 2007; Armitage et al., 2011; Rohais et al., 2012; Allen et al., 2013). These data serve as an important empirical test of

such landscape evolution models. They imply that the relationship between sediment flux and precipitation rate may be sub-linear, although this now needs to be evaluated with a much larger range of examples, and I conduct a sensitivity analysis that predicts the effects of a broad range of drier/wetter scenarios. This indicates that the grain size fining rate on an alluvial fan is much more sensitive to a drying event, but that a wetting event would result in the progradation of a coarse-grained gravel deposit with reduced down-system fining, that itself would be equally diagnostic.

Interestingly, coarse prograding units have been identified in Colorado, Wyoming, and the Pyrenees at the precise timing of the rapid warming event at the Palaeocene-Eocene Thermal Maximum, PETM (Foreman et al., 2012; Allen et al., 2013; Foreman, 2014). The work in Chapter 5 demonstrates that, at least in these Death Valley sediment routing systems, a wetter climate results in progradation and slower grain size fining. Therefore, extrapolation would indicate that the warmer PETM world was also wetter, and this is supported by the basic principle that a warmer atmosphere holds more moisture (linking again to Chapter 4). However, a very important distinction between the Death Valley and Owens Valley results are that while the Death Valley fans experienced greater sediment flux during the wetter glacial period, the Owens Valley fans show coarser grain sizes and larger debris flow events during the stormier interglacial period. Both of these study areas lie at precisely 36.5 °N, in the rain shadow of the Sierra Nevada, a mere 90 km apart in neighbouring valleys. So how can it be that they show completely opposite reactions to the last glacial-interglacial cycle? The important distinction is that the Owens Valley fans have been built by debris flows, while the Death Valley fans have been built by channelized stream flows. Debris flows are threshold-limited events that only occur, and therefore mobilise sediment, at high rainfall intensities during storms. This threshold control acts to filter out any sensitivity to lower-magnitude rainfall events, and so debris flow sediments record changes in the history of high-intensity storms. The stream-flow channel deposits of the Death Valley fans can transport sediment under any rainfall conditions so long as the stream power is sufficient to mobilise clasts of a given size, meaning they are sensitive to all intensities of rainfall. As the glacial period was wetter overall (e.g., Phillips, 2008, and references within), even if less stormy, the Death Valley data show enhanced glacial sediment flux. This comparison of the findings in Chapters 4 and 5 is testament to the importance of understanding sediment transport processes, and supports the claim made by Allen (2008b) that sediment routing systems have a range of response timescales and sensitivities to external perturbations that reflect the range of transport processes operating within them.

6.2. Landscape response times

It is important to know how quickly landscapes can respond, not only to climate changes, but to any kind of external perturbation. As one example, the climate changes associated with glacial-interglacial cycles are most clearly expressed over periods of 10^4 years, with a full cycle taking place over 10^5 years. It has been pointed out that, like any signal propagated through a system, if a sediment routing system cannot respond as quickly as the periodicity of the climate signal, then the signal will be damped and that landscape (and its sedimentary products) will be buffered against it, lacking sensitivity and failing to record the climate perturbation (e.g., Castelltort and Van Den Driessche, 2003; Armitage et al., 2013). If sediment routing systems can respond with a 10^4 to 10^5 year timescale, then they will be sensitive to a glacial-interglacial climatic signal in terms of their sediment fluxes and sedimentology (e.g., Paola et al, 1992a; Densmore et al., 2007; Armitage et al., 2011), and may even amplify it (Simpson and Castelltort, 2012). This is why we need empirical observations from real sedimentary records in order to determine the temporal sensitivities of simple landscapes.

The first part of this thesis (Chapter 2) is concerned with longitudinal channel geometry, and the channel steepness index, k_{sn}, is measured from a plot of upstream drainage area and channel slope along the fluvially-dominated section of a river profile. As such, the response timescale of these data are limited by the time it takes for the longitudinal profile to adjust to any change in tectonic or climatic boundary conditions. The most common way for this to happen is by the upstream migration of a knick point (Howard, 1994; Crosby and Whipple, 2006; Whittaker et al., 2007a,b; 2008; Kirby and Whipple, 2012), which generally occurs over timescales of 10^6 years (Whittaker and Boulton, 2012; Whittaker and Walker, 2015). Therefore, while indices like k_{sn} would be suitable metrics for examining the effects of longer wavelength climate changes over 1 Ma or longer, we would not expect these kinds of geomorphological measurements to capture glacial-interglacial cycles. This is why accounting for glacial-interglacial climate variability does not fundamentally alter my findings in Chapter 2 (i.e., Fig. 2.8) or the fact that k_{sn} declines with increasing precipitation rate. Although important questions exist about how landscapes react to climate changes over these longer time periods, we do already have much higher-resolution records of the effects of more rapid climate changes on the Earth's surface. So, a more interesting question with regard to landscape response timescales is what temporal resolution can be obtained from sedimentary records that capture known climate perturbations?

In the alluvial fan case studies from Chapters 3 to 5, I find that the stratigraphic response time to climate changes depends on the sediment transport process. Allen (2008b) pointed out that a range of response timescales exist within simple sediment routing systems, reflecting the range of processes operating within them and the variable residence times of sedimentary particles as they follow

individual trajectories through the landscape before being permanently deposited. The case studies I present in this thesis provide examples of high sensitivity to climate change (the Owens Valley fans), moderate sensitivity (Backthrust canyon fan in northern Death Valley), and low sensitivity (Moonlight canyon fan in northern Death Valley). These are some of the reasons for these differences:

Owens Valley fans: High sensitivity to climate change (<< 10^4 years)

These systems are dominated by debris flows, and so experience rapid sediment transfer from source to sink; most particles will have a short residence time in the catchments. There is a high preservation potential, with lots of abandoned alluvial fan terraces that avulse or incise within 10-20 ka, and the rapid subsidence rate of Owens Valley relative to the Sierra Nevada (~ 1 mm yr^{-1}) means that incised terraces quickly become inactive and experience little/no reworking or post-depositional alteration. There is also abundant sediment supply (that is therefore non-limiting), and the climate is relatively arid, meaning soil development and vegetation effects on the fan surfaces are negligible. These fans have also not been toe-cut or reworked by the Owens River axial system. Finally, there are many simple, small catchment-fan systems (I sampled 8, but there are many more along the eastern front of the Sierra Nevada) that share the same bedrock lithology and erodibility, underwent similar past glaciation, and experience the same uplift rates and tectonic boundary conditions. This means that a detailed time series of deposition can be obtained by combining many discrete sedimentary records.

Backthrust canyon fan, Death Valley: Medium sensitivity (~ 10^4 years)

This catchment-fan system also experiences relatively rapid sediment transfer, as the system is short (~ 20 km long), and the change in down-fan fining rate can be detected because the modern and ~ 70 ka fan surfaces have simply avulsed, with minimal modern down-cutting and incisional recycling of material. There is also a high preservation potential, as the fan surfaces remain relatively untouched post-deposition, the climate is extremely arid, and desert pavement formation does not substantially alter the grain size distribution. However, the slower subsidence rate of Death Valley relative to the catchments (< 0.5 mm yr^{-1} compared to ~ 1 mm yr^{-1} in Owens Valley) reduces the accommodation available for sediment storage and increases the likelihood of reworking alluvial fan terraces. As a result, the Death Valley fans only have 2 clear terraces (Q2c and modern), whereas the Owens Valley fans have multiple terraces of differing ages, increasing the temporal resolution of the sedimentary record. This limits the temporal resolution of the Backthrust canyon record to several 10s of ka. The Death Valley fans are also toe-cut by the axial Death Valley Wash, meaning approximately half the sediment flux from Backthrust canyon is bypassed to the Mesquite Flat and is lost.

Moonlight canyon fan, Death Valley: Low sensitivity (~ 10^5 years)

This fan may receive relatively rapid sediment transfer as well, but its terraces have experienced significant reworking over a time period of > 70 ka (the Q2c terrace is being recycled today, but additionally the down-cutting of the modern surface is remobilising even older stratigraphy deposited beneath the Q2c surface). This means that the residence time of many particles within the sediment routing system is on the order of 10^5 years, before they are permanently transferred to stratigraphy. As this is equivalent to the periodicity of a glacial-interglacial cycle, this system is buffered against associated climate signals, and I observed no glacial to interglacial change in the down-fan rate of grain size fining. Incisional recycling of sediment is promoted by the slow subsidence rate in northern Death Valley, providing minimal accommodation for sediment storage. The Moonlight canyon fan is also toe-cut by the axial system, meaning around half of the sediment export from the canyon is lost.

Clearly, it is unreasonable to attempt to measure a single "landscape response time" or a single "catchment-fan response time" to climate change. Simple, small sediment routing systems can have a range of response times between < 10 ka and ~ 100 ka or longer, as demonstrated by the examples in this thesis. These differences depend not only on transport process, but tectonics as well, because a faster basin subsidence rate promotes sediment preservation by providing more accommodation for storage. Therefore, a high sensitivity to climate change in these systems is promoted by greater tectonic activity as well as arid climates. This echoes the findings of Chapter 2 over much longer timescales of ~ 10^6 years, where I found that the steepening of channels was most sensitive where tectonic uplift rates are rapid and the climate is dry, and that the effects of climate and tectonics are closely coupled. Future research should continue to determine the various sensitivities and response timescales of the range of erosional, transport, and depositional processes that operate within sediment routing systems of different scales (Allen, 2008b). It is important that we improve our understanding of the connections between these processes, e.g., how sensitive are landslides to a change in storm intensity, and what happens to these signals when sediment is transferred from a landslide to a trunk channel? Numerical models are unlikely to make realistic predictions about sedimentary deposits if they model sediment transport as a single diffusional process, rather than capturing the range of inter-connected and very different transport processes that occur even in simple, small systems. Overall, the comparison I make above between the different case studies in this thesis highlights the importance of sediment recycling in buffering against signal preservation, supporting the predictions made by theoretical work in recent years (e.g., Castelltort and Van Den Driessche, 2003; Armitage et al., 2013).

6.3. Debris flow behaviour

The Owens Valley fans display the greatest temporal sensitivity to climate change, because debris flows are capable of evacuating large volumes of sediment from the catchments and moving material to alluvial fans so rapidly. However, we lack a clear set of debris flow transport equations that would (i) help to further interpret sedimentological data such as grain size, and thereby extract more quantitative information from debris flow deposits; (ii) quantify the relative controls on debris flow processes, e.g., storm intensity and surface runoff rates; and (iii) enable us to integrate debris flows (and other hillslope processes) properly into landscape evolution models. There is a clear need to improve our understanding of debris flow mechanics and obtain useful transport laws.

In Chapter 4, I demonstrate that debris flow grain size is unmistakably sensitive to past climate changes. Although there is promising evidence that the grain size signal is a product of changing storm intensity, without debris flow transport laws it is impossible to formally relate grain size back to hydrological conditions, water discharge, or surface runoff rates, for example. In Fig. 4.8 I show that debris flow width is partly related to climate, however this signal only becomes particularly clear when the data are combined into average widths for each stratigraphic unit; i.e., there is an underlying trend that cannot be detected using single flow deposits, which are more stochastic, but it does emerge with a more detailed data set. Yet even when these average flow widths are plotted against average grain size (for Q4 surfaces, Q3 surfaces, etc.), width only explains ~ 50 % of the variation in grain size (Fig. 4.10). In actual fact this is not surprising, given that debris flows are complex mass movements whose power to transport grains of different size does not only depend on their flow widths. Future research should aim to quantify which factors determine the transport power of a debris flow, and whether/how a measure of transport power can be inverted from grain size.

One possible starting point might be to examine how high-viscosity debris flow segregate coarse and fine particles into lateral levees and central channels, respectively. Recent work has shown that the magnitude of grain size segregation by a debris flow may be inversely related to its water content; in other words a 'watery' debris flow would be less viscous and exhibit reduced grain size segregation because the particles are freer to move around (Johnson et al., 2012). In Fig. 6.1 I have plotted the ratio of levee D_{50} to channel D_{50} against age, using the total grain size data set for each of the Owens Valley stratigraphic units (averaged across all fans to obtain the largest sample sizes, e.g., Q4, Q3, etc). This is compared with the benthic Pacific $\delta^{10}O$ stack reported by Lisiecki and Raymo (2009), and both series are plotted on inverted *y*-axes so that the coolest periods plot at the bottom of the graph and the warmest periods at the top.

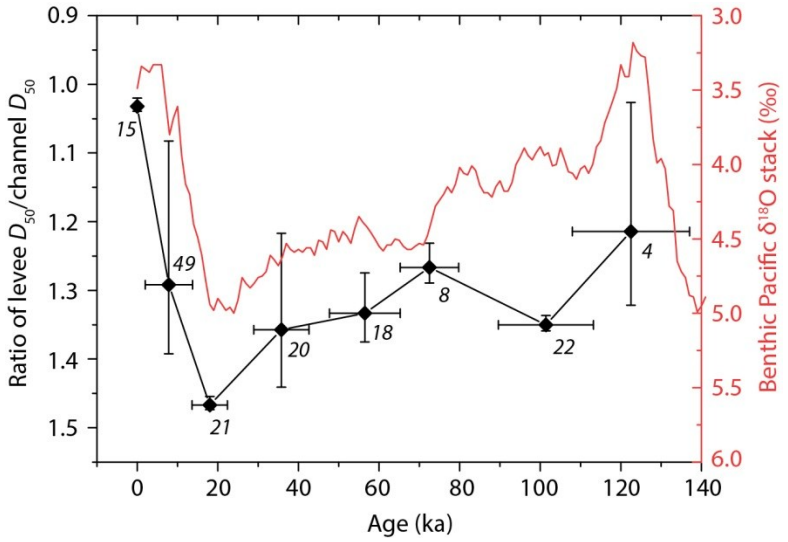

Fig. 6.1. The ratio of levee D_{50} to channel D_{50} grain size, for the debris flow deposits sampled on the Owens Valley fans in Chapter 4 (black). The grain size data represent the segregation of particles into coarse lateral levees and fine channels (larger ratio represents greater segregation), and is averaged for each stratigraphic unit with error bars showing ± 1 σ and age uncertainties. This is compared with the benthic Pacific δ^{18}O stack of Lisiecki and Raymo (2009), shown in red. Both *y*-axes have been inverted to display the coldest glacial periods at the bottom of the graph. Italic numbers give the number of sampling sites included in each point.

Clearly, there is a relationship between the average segregation of particles into levees and channels, and climate changes during the last glacial-interglacial cycle. In the glacial period, the lateral levee deposits are ~ 1.3 times coarser than their corresponding channel deposits (for D_{50}), increasing to almost 1.5 times at the LGM. In contrast, the deposits from the warmer interglacial periods show reduced grain size segregation, and the levee/channel D_{50} ratio is little above 1.0 today. These data may support my interpretations in Chapter 4. In the glacial period, reduced surface runoff from less intense storms might have generated debris flows with lower water contents, which were thereby able to segregate grain size into levees and channels more effectively as a result of their higher viscosities. As the climate warmed and storms became more intense, the surface runoff and therefore the water content of a typical debris flow increased, making them less viscous and allowing particles of all sizes to move more freely throughout a flow, leading to reduced grain size segregation. Interestingly, the grain size data in Chapter 4 coarsen at a rate of ~ 10 % per 1 °C of warming, and if this is indeed a proxy for past changes in storm intensity, we would therefore expect a cumulative ~ 50 % relative decrease in storm intensity at the LGM (if it is assumed to have been ~ 5 °C cooler), relative to today. This would potentially match the ~ 50 % enhancement in grain size segregation shown in Fig. 6.1, if grain size segregation is a linear function of water content.

Unfortunately, these analyses remain completely speculative, because we do not fully understand debris flow mechanics, how they segregate larger grains into lateral levees, and in particular how this

process is related to water discharge (Iverson et al., 2010; Johnson et al., 2012; McCoy et al., 2012; Kean et al., 2013). However the potential usefulness of this information is clear from the Owens Valley data, and future work should attempt to build a set of debris flow transport equations that explicitly relate grain size to a measure of flow power and, if possible, water discharge. This may not be a trivial relation between power and grain size, and may require more complex information such as grain size segregation as a proxy for viscosity, but the data I present in this thesis offer a promising starting point.

One of the key hypotheses resulting from this work is my suggestion that the grain size of debris flow deposits is related to changes in storm intensity driven by temperature (Chapter 4). This also needs to be tested further. In the Californian data set, this idea is tested by examining a climatic gradient through time (i.e., the 5 – 6 °C temperature variation associated with a glacial-interglacial cycle). Another way this idea could be tested is by examining modern (and past) climatic gradients across space. For example, comparable catchment-fan systems (similar sizes, granitic bedrock lithology, etc) could be identified in the tropics (e.g., south-eastern Brazil, where debris flows are common natural hazards) where modern temperatures are much warmer and storms are more intense. My findings in Chapter 4 would predict coarser-grained, larger debris flow deposits in such locations, and it would be useful to test whether the observed coarsening trend (Fig. 4.14) can be extrapolated to a much larger temperature range (e.g., > 10 °C) across space today. This is one opportunity for future research on this theme, and of course the reproducibility of my findings in Owens Valley should be directly tested in similar areas where the last glacial-interglacial cycle is well-constrained also.

6.4. Chronostratigraphy

Absolute exposure age models, whether based on ^{10}Be or other cosmogenic nuclides, optically-stimulated luminescence dating (OSL), ^{14}C dating, or other techniques, are clearly essential for the study of how sedimentary systems have responded to climate changes throughout the last several 100 ka. Cosmogenic nuclide techniques also offer the important opportunity to measure average erosion rates, as I make use of in Chapter 5. However, these techniques are not the only way that depositional age models can be created, extended, or improved. In Chapter 3, I demonstrate that the sizes of weathering fractures in surface boulders can be calibrated using ^{10}Be exposure ages on the Owens Valley fan surfaces, and can be used as absolute age indicators themselves. This concept greatly improved the density of age constraints available for these alluvial fans, in time and across space, which in turn enabled a much more detailed analysis of their sedimentological properties in Chapter 4. These kinds of dating techniques based on quantitative correlation should be explored further by

future work, as they have the potential to dramatically increase the information gained from a set of exposure age constraints.

Concerning the weathering fractures examined in Chapter 3 specifically, the relationship between their sizes and ages should now be measured in other locations. Important questions include: (i) Do these fractures also widen with time in other locations? (ii) If so, does the surface lowering rate on a fracture plane similarly reconcile with independent measurements of boulder surface lowering rates? (iii) Can similar age models be developed elsewhere? (iv) What effects do climate and lithology have on the application of this technique? (v) Do these fractures occur in clasts outside of arid landscapes, e.g., in temperate or tropical settings as well? (vi) Can more be learned about the precise physical mechanisms by which these fractures are initiated and subsequently widened?

Ultimately, the effects of weathering on clasts (e.g., meridional fractures) are just one example of how time-dependent, post-depositional processes can be calibrated with an age model. Other exposure-controlled processes could potentially be quantified as well, given the increasing number of absolute exposure age chronologies being reported from many different study areas. Examples might include the precipitation of carbonate content in soils, the formation of varnish on clasts in deserts, or the rate at which depositional relief is lost by particle diffusion on a surface. I have already started exploring another opportunity presented by the age model I established for the Owens Valley fans, which is based on changes in the visible and infrared reflectance of the alluvial fan surfaces as recorded by LandSat 8 multispectral imagery.

In Fig. 6.2a, I show a band 642 (RGB) multispectral image of some of the Owens Valley target fans, created using LandSat 8 data. This image has been contrast enhanced to make the colour differences clearer, and the satellite imagery is compared with the mapped fan surfaces from Chapter 4. These are coloured according to the exposure ages from the chronostratigraphy in this thesis, and close inspection reveals that the apparent colour of the surface in this false colour composite correlates with exposure age, with Holocene fan surfaces reflecting bright blue, and older surfaces reflecting more orange-yellow. This effect can be quantified, by plotting brightness ratios of different wavelengths of light reflected from dated surfaces, against their known exposure ages. Whether plotted linearly or on log-log axes (Fig. 6.2b,c), this reveals a clear redshift signal in the spectral data with age, following a power law relationship. Given that the fan surfaces are exclusively granitic in composition, this redshift cannot be attributed to changes in lithology. It may be caused by weathering reactions on the fan surfaces, clast varnishing, clay production, or perhaps crystallographic damage caused by solar radiation. I will explore these possibilities further in future work and evaluate the potential for using this effect as a technique for estimating exposure ages of alluvial fan surfaces in this environment. However, this example illustrates the wide variety of new exposure dating opportunities that have

become possible with the existence of absolute chronologies, e.g., from cosmogenic nuclides. Future work should identify and develop additional opportunities.

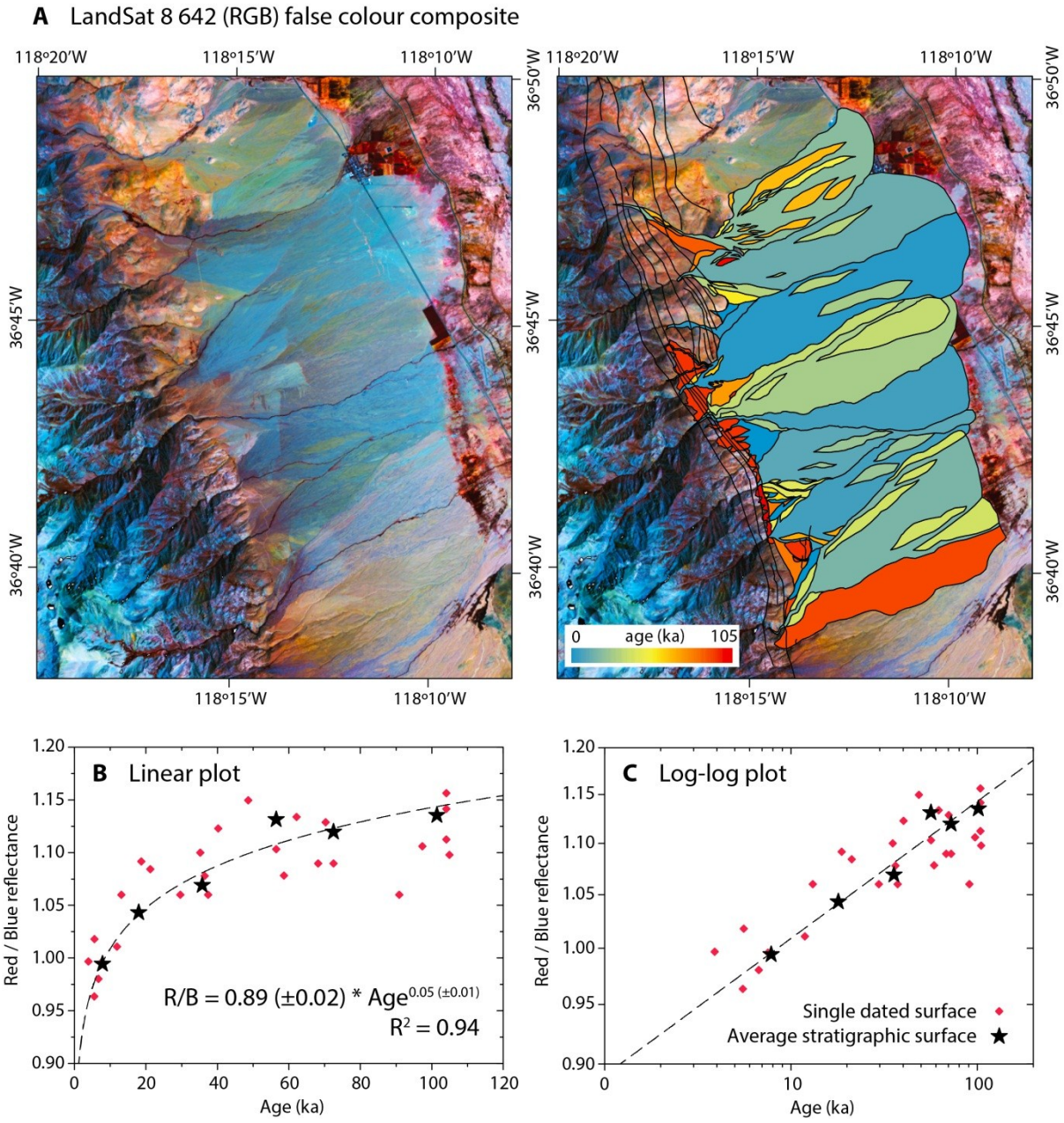

Fig. 6.2. (A) False colour composite image of LandSat 8 bands 642 (RGB) for some of the Owens Valley fans studied in Chapter 4. The image has been contrast enhanced, and is displayed on the left and with the mapped stratigraphic surfaces overlain on the right. Surfaces are coloured according to the age model from Chapter 4, from blue (modern) to red (~ 105 ka). The oldest surface from Birch Creek is not included on this map as it lies further north. Despite all the fan deposits having uniform granitic compositions, there are clear differences in their visible and infrared spectral reflectance that correlate with surface exposure age. Below, the ratio of red/blue light reflected from each surface (red diamonds) and averaged for each stratigraphic unit (Q4, Q3, etc) (black stars), plotted against age linearly (B) and as a log-log plot (C). A power law relationship is fitted to the average data (dashed line), which represents the data well ($R^2 > 0.9$) and shows a characteristic red-shift in the spectral signature with age.

Returning to the chronostratighraphy applied in this thesis, in Chapter 4 I note that the grain size correlation with palaeoclimate can be used as a sense-check on the exposure ages. I apply an adjustment of ~ 10 % on the exposure age model in light of evidence that the Birch creek Q1 deposit must date to the last interglacial period (see section 4.4.3), and that the ages derived from ^{10}Be dating (and extrapolated using weathering fractures) are most likely slight over-estimates. This is not a surprising finding, as it is also likely that non-linear ^{10}Be scaling schemes and production rates may be more accurate than linear schemes, yet we lack strong calibration data sets for all scaling schemes to demonstrate this (c.f., Balco et al., 2008). In fact, in a recent review of the state of cosmogenic nuclide research, Fred Phillips and co-authors emphasise the pressing need for data sets with which exposure age estimates can be sense-checked and calibrated (Phillips et al., 2015). Strong climate correlations like the time series in Chapter 4, which have many individual exposure age points, are ideal data sets with which to explore the accuracy of exposure age calculations.

Additionally, this age adjustment has no material effect on the results of Chapter 3. In section 3.4.2, I found that the best-estimate fracture surface lowering rate is 0.52 ± 0.02 mm ka^{-1}. The age adjustment made in Chapter 4 would only increase this fracture surface lowering rate to ~ 0.59 mm ka^{-1}, which is well within the range of uncertainty placed on this rate during all my analyses and age calculations (which tolerate a range from 0.2 to 1.0 mm ka^{-1} and arguably smaller error bars could have been used). Most satisfyingly, it also agrees slightly more precisely with the erosion rates measured by Phillips et al. (2009) (0.7 mm ka^{-1}) and Rood et al. (2011) (0.6 mm ka^{-1}), using ^{10}Be measurements from granitic boulders in Owens Valley in both cases. In other words, when the ages are 'pinned' to an independent record of climate change, the ^{10}Be erosion rates measured in this location then reconcile perfectly, which is very encouraging. Future work could make use of time series like those in Chapter 4 to improve our understanding of ^{10}Be scalings and calibrations.

6.5. Landscape sensitivity to future warming

The current state of rapid global warming (see the IPCC report, 2014, for an up-to-date summary) presents obvious risks to the environment and society. Many of the likely risks of continued climate change are associated with changes in rainfall patterns, including aridification and increased storm intensity (IPCC, 2014); alongside other effects due to rising temperatures, ocean acidification, changes in global circulation, the collapse of ecosystems, etc. Examining past landscape responses to known climate changes is one approach to predicting the effects of global warming in the future. In this sense, the results in this thesis may be informative for models that deal with future landscape responses to climate change.

For example, my findings in Chapter 4 imply that with continued warming, debris flows in at least the eastern Sierra Nevada (and potentially elsewhere) will become larger, coarser-grained, and more erosive. There is already compelling evidence that storms are becoming more intense as global temperatures warm, and will continue to intensify in the near future (Trenberth et al., 2003; Knutson et al., 2010; Berg et al., 2013). The risks associated with intensifying storms and hillslope processes are clearly illustrated by a case study from south-eastern Brazil, with densely-populated regions like Rio de Janeiro built in high-relief areas where landslides and debris flows are common hazards. Tropical storms affecting this area are intensifying, and the first hurricane recorded in the South Atlantic made landfall slightly further south in Brazil in 2004 (Pezza and Simmonds, 2005; Pezza et al., 2009). Seven years later, the worst landslide disaster in Brazil's history occurred, when intense storms on January 11th 2011 triggered 3,562 individual debris flows and landslides and killed more than 1500 people overnight (Avelar et al., 2011). Clearly, it is important that we understand how landscape processes will respond to future climate changes, as well as how they have responded to past climate changes, but these questions are two sides of the same coin. For example, a debate is currently taking place about how to incorporate precipitation extremes into general climate models, including how rapidly effective storm intensities will increase with temperature rises in the future (e.g., Singleton and Toumi, 2013). The sedimentary record allows us to examine how various processes, e.g., debris flows, stream flow, floods, etc., have changed in response to known climate changes in the past. Therefore these data, such as those in Chapters 4 and 5, must be useful as a benchmark for future climate models as well.

7. Conclusions

The following key points outline the conclusions of this thesis:

1. **Longitudinal channel profiles are sensitive to average precipitation rate in landscapes that are tectonically-active.**
    - Channel steepness is reduced by enhanced rainfall rates, following an inverse power law relationship proportional to a value of the stream power discharge exponent, m, of ~ 0.5, which agrees with independent theory and observations (e.g., Sklar and Dietrich, 1998; Stock and Montgomery, 1999; Snyder et al., 2000; Wobus et al., 2006; Ferrier et al., 2013). The sensitivity of channel longitudinal geometry to climatic gradients is additionally supported by independent observations (e.g., Schlunegger et al., 2011; Bookhagen and Strecker, 2012), and may offer an explanation for some geographic variations in channel steepness that cannot be explained by tectonics.
    - The effect of precipitation on the channel steepness index, k_{sn}, is coupled with the tectonic effect (increased uplift rate acts to increase k_{sn}), and where precipitation is orographic it therefore acts as an uplift proxy and these signals superpose. The result is a sub-linear increase in k_{sn} with rainfall rate (where there is an orographic pattern), and the degree of sub-linearity can be used to estimate an expected value of m ~ 0.4 to 0.5 also.
    - In general, steeper channels are promoted by drier climates as well as faster uplift rates. Steep, dry, and actively uplifting landscapes may therefore be more sensitive to climate and climate changes.

2. **Exposure age constraints from ^{10}Be cosmogenic nuclide data can be quantitatively correlated across time and space using age-dependent weathering fractures in surface boulders.**
    - The Owens Valley fans offer a proof of this concept, which also serves to increase the density of age constraints available. Here, meridional fractures are common in granitic boulders, and widen on average at a rate of ~ 1 mm ka^{-1} for > 100 ka. In detail this rate may have a small climatic sensitivity, but a linear age calibration can be applied effectively for dating equivalent surfaces (R^2 = 0.99).
    - The lowering rate on a single fracture surface is ~ 0.5 mm ka^{-1}, which agrees precisely with the granitic boulder surface erosion rate estimated by Phillips et al. (2009) and Rood et al. (2011) using cosmogenic nuclides. This supports a weathering explanation for fracture enlargement. Furthermore, this surface lowering rate is relatively insensitive to the assumed surface lowering rate adopted in the ^{10}Be calibration age calculations. This

means the uncertainty on the exposure ages can be reduced significantly, if it is assumed that the weathering rate on a fracture plane is similar to elsewhere on the clast surface (within limits, e.g. ± a factor of 2).

- This technique can be applied to adjacent alluvial fan surfaces within the calibrated age range and with the same compositional, climatic, and exposure properties. The calculated ages based on average fracture dimensions agree with the predicted stratigraphic ages estimated in the field using traditional correlation techniques.

3. **Debris flow fan deposits from the south-eastern Sierra Nevada (Owens Valley), California, are sensitive to glacial-interglacial climate changes, particularly in terms of their grain size distribution.**
    - Debris flow deposit sedimentology contains signals of past climate and climate change, which can be quantified by grain size measurements. This means that, in principle, it should be possible to describe sediment transport by debris flows as a function of climate using mechanical equations (which remain unknown). Debris flow deposits have the advantage of rapid deposition, which minimises the buffering of primary signals (e.g., climate).
    - As the climate warmed (by 5 to 6 °C) and dried (by a factor of ~ 2) from the Last Glacial Maximum to the present day, the D_{50} and D_{84} grain sizes of debris flow channel and levee deposits approximately doubled. Debris flow deposits are also observed to become wider (by ~ 10 m on average), and more variable in size as the climate warmed and dried.
    - Grain size shows a sustained and rapid response to climate change, meaning grain size data can be plotted as time series that correlate clearly with the last glacial-interglacial cycle for > 100 ka.
    - There is an exponential increase in debris flow grain size with sea surface temperature measured from offshore California, which approximately follows the Clausius-Clapeyron relationship (grain size increases by ~ 10 % per 1 °C of warming, R^2 ranges from 0.63 to 0.84). This indicates a storm intensity control, which is supported by the observation that modern debris flows are initiated by storms (e.g., DeGraff et al., 2011; Kean et al., 2011, 2013; McCoy et al., 2012, 2013), that there is a lack of hysteresis in the grain size-temperature relationship, and the rapid response (and lack of lag time) between climate changes and sedimentology.
    - The observed climate signal recorded in grain size cannot be explained by changes in sediment supply associated with glaciation/deglaciation, although the evacuation of moraine material and paraglacial sediment supply may act as secondary signal amplifiers

with an effect an order of magnitude smaller (~ 1 – 2 mm) than the effect attributable to storm intensity and sediment mobilisation (10s of mm).

- The sensitivity of these fans to climate change, and the rate of change of grain size with temperature, has accelerated with warming. This indicates that drier landscapes may be more sensitive to climate change (supporting the findings of Chapter 2), and has implications for future responses to anthropogenic warming.

4. **Grain size fining rates, sediment flux estimates from cosmogenic nuclide data, and a fining model based on selective deposition, can be integrated to model alluvial fan responses to climate change in Death Valley, California.**
    - As the climate dried and average precipitation rate decreased by ~ 30 % in association with the last glacial-interglacial cycle, the sediment flux delivered to a typical alluvial fan declined by ~ 20 %. This supports—and serves as a direct empirical test of—existing theoretical models of how alluvial fan systems might react to a change in rainfall rate (e.g., Paola et al., 1992a; Densmore et al., 2007; Armitage et al., 2011; Allen et al., 2013).
    - Incision and recycling of alluvial fan deposits has the potential to destroy climatic signals that occur at a higher frequency than the time taken to permanently store fan sediments as basin fill. These field data demonstrate when this buffering effect occurs, and its magnitude, and offer a direct test of associated theoretical models also (e.g., Castelltort and Van Den Driessche, 2003; Simpson and Castelltort, 2012; Armitage et al., 2013).
    - The self-similar grain size fining model of Fedele and Paola (2007) can be adapted for alluvial fan systems, and calibrated with field observations. It can then be used to model the sensitivity of simple sediment routing systems in a general way. I find that the grain size fining rate is likely to be more sensitive to a drying event than a wetting event (supporting the findings of Chapters 2 and 4), but that a wetting event would produce a prograding, coarse-grained deposit that may be equally diagnostic (and would support the observations of 'PETM conglomerates', for example, e.g., Foreman, 2014).

In general terms, I conclude that landscapes can be highly sensitive to climate and climate change, which are recorded both in geomorphology and sedimentology. This sensitivity is promoted by active tectonics, which generates sediment supply and accommodation, accelerates erosion, and produces dynamic, evolving, responsive sediment routing systems. In some ways, drier landscapes appear to be more sensitive to climate than wetter landscapes. Specific examples of this from my thesis are the steepening of channel longitudinal profiles (Chapter 2), debris flow grain size (Chapter 4) and alluvial fan fining rate from apex to toe (Chapter 5). However, one of the most important conclusions of this

thesis is that the climatic controls on different parts of sediment routing systems are complex, and that this complexity must be appreciated in order to understand the full range of landscapes and sedimentary deposits that we observe. For example, there is no one 'landscape response time', either in general terms or in response to climate change in particular. Another example is how storm intensity can exert an important control on the sedimentary record, but may be completely decoupled from the overall rainfall budget that is reflected in archives such as pollen and lake shorelines. A further example is how different alluvial fan deposits in the same region/latitude/semi-arid setting can give completely different responses to identical climate changes, depending on whether they are governed by different processes (e.g., debris flows versus stream flow) or have experienced different amounts of recycling/incision. Therefore, the *complexity* of the climatic control on the landscape is critically important: the *details* about sediment transport processes, the *magnitude-frequency distribution* of rainfall, and the *combined* effects of different (but simultaneous) processes (e.g., moraine exposure and storm intensification) must all be understood if we are to recover how past climate changes have shaped the Earth's surface, and predict the effects of future climate changes as well.

8. References

Abbühl, L.M., Norton, K.P., Jansen, J.D., Schlunegger, F., Aldahan, A. and Possnert, G. (2011) Erosion rates and mechanisms of knickzone retreat inferred from ^{10}Be measured across strong climate gradients on the northern and central Andes Western Escarpment. *Earth Surface Processes and Landforms*, **36**, 1464-1473.

Adelsberger, K.A., Smith, J.R. (2009) Desert pavement development and landscape stability on the Eastern Libyan Plateau, Egypt. *Geomorphology*, **107**, 178–194.

Aguilar, G., Riquelme, R., Martinod, J., Darrozes, J. and Maire, E. (2011) Variability in erosion rates related to the state of landscape transience in the semi-arid Chilean Andes. *Earth Surface Processes and Landforms*, **36**, 1736-1748.

Ahnert, F. (1970) Functional relationships between denudation, relief, and uplift in large mid-latitude drainage basins. *American Journal of Science*, **268**, 243-263.

Al Farraj, A. and Harvey, AM. (2000) Desert pavement characteristics on wadi terrace and alluvial fan surfaces: Wadi Al-Bih, U.A.E. and Oman. *Geomorphology* **35**, 279-297.

Allan, R.P. and Soden, B.J. (2008) Atmospheric warming and the amplification of precipitation extremes. *Science*, **321**, 1481-1484.

Allen, P.A. (1997) Earth Surface Processes (1st Ed). John Wiley and Sons, Hoboken, NJ, pp. 416.

Allen, P.A. (2008a) From landscapes into geological history. *Nature*, **451**, 274-276.

Allen, P.A. (2008b) Time scales of tectonic landscapes and their sediment routing systems. *Geological Society, London, Special Publications*, **296**, 7-28.

Allen, P.A., and Hovius, N. (1998) Sediment supply from landslide-dominated catchments: Implications for basin-margin fans. *Basin Research,* **10**, 19-35.

Allen, P.A. and Densmore, A.L. (2000) Sediment flux from an uplifting fault block. *Basin Research*, **12**, 367-380.

Allen, P.A. and Heller, P.L. (2011) Dispersal and preservation of tectonically generated alluvial gravels in sedimentary basins. In: Busby, C. and Azor, A. (Eds) *Tectonics of Sedimentary Basins: Recent Advances*, John Wiley and Sons, Ltd., Chichester, UK, pp. 111-130.

Allen, P.A., Armitage, J.J., Carter, A., Duller, R.A., Michael, N.A., Sinclair, H.D., Whitchurch, A.L. and Whittaker, A.C. (2013) The Qs problem: Sediment volumetric balance of proximal foreland basin systems. *Sedimentology,* **60**, 102-130.

Anders, A.M., Roe, G.H., Montgomery, D.R. & Hallet, B., (2008) Influence of precipitation phase on the form of mountain ranges.*Geology*, **36**, 479-482.

Anders, M.H., Spiegelman, M., Rodgers, D.W. and Hagstrum, J.T. (1993) The growth of fault-bounded tilt blocks. *Tectonics,* **12**, 1451-1459.

Anderson, D.E. and Wells, S.G. (2003) Latest Pleistocene lake highstands in Death Valley, California. In: Enzel, Y., Wells, S.G. and Lancaster, N. (Eds), In: Enzel, Y., Wells, S.G. and Lancaster, N. (Eds) *Paleoenvironments and paleohydrology of the Mojave and southern Great Basin Deserts*, Special Paper 368. Geological Society of America: Boulder, CO; pp. 115-128.

Anderson, R.S. and Anderson, S.P. (2010) *Geomorphology: The mechanics and chemistry of landscapes*. Cambridge University Press, Cambridge, United Kingdom, pp. 651.

Antinao, J.L. and McDonald, E. (2013a) An enhanced role for the tropical Pacific on the humid Pleistocene-Holocene transition in southwestern North America. *Quaternary Science Reviews*, **78**, 319-341.

Antinao, J.L. and McDonald, E. (2013b) A reduced relevance of vegetation change for alluvial aggradation in arid zones. *Geology*, **41**, 11-14.

Antonioli, F., Ferranti, L., Lambeck, K., Kershaw, S., Verrubbi, V. & Dai Pra, G. (2006) Late Pleistocene to Holocene record of changing uplift rates in southern Calabria and northeastern Sicily (southern Italy, central Mediterranean Sea). *Tectonophysics*, **422**, 23-40.

Antonioli, F., Ferranti, L., Fontana, A., Amorosi, A., Bondesan, A., Braitenberg, C., Dutton, A., Fontolan, G., Furlani, S., Lambeck, K., Mastronuzzi, G., Monaco, C., Spada, G. & Stocchi, P. (2009) Holocene relative sea-level changes and vertical movements along the Italian and Istrian coastlines. *Quaternary International*, **206**, 102-133.

Armitage, J.J., Duller, R.A., Whittaker, A.C. and Allen, P.A. (2011) Transformation of tectonic and climatic signals from source to sedimentary archive. *Nature Geoscience,* **4**, 231-235.

Armitage, J.J., Dunkley Jones, T., Duller, R.A., Whittaker, A.C. and Allen, P.A. (2013) Temporal buffering of climate-driven sediment flux cycles by transient catchment response. *Earth and Planetary Science Letters,* **369-370**, 200-210.

Arzani, N. (2012) Catchment lithology as a major control on alluvial megafan development, Kohrud Mountain range, central Iran. *Earth Surface Processes and Landforms*, **37**, 726-740.

Attal, M., Tucker, G.E., Whittaker, A.C., Cowie, P.A. and Roberts, G.P. (2008) Modeling fluvial incision and transient landscape evolution: influence of dynamic channel adjustment. *Journal of Geophysical Research*, **113**, F03013.

Attal, M., Mudd, S.M., Hurst, M.D., Weinman, B., Yoo K. and Naylor, M. (2015) Impact of change in erosion rate and landscape steepness on hillslope and fluvial sediments grain size in the Feather River basin (Sierra Nevada, California). *Earth Surface Dynamics,* **3**, 201-222.

Atzori, P., Ghisetti, F., Pezzino, A. and Vezzani, L. (1983) Carta geologica del bordo occidentale dell'Aspromonte, scale 1:50,000. SELCA, Firenze, Italia.

Avelar, A.S., Coelho Netto, A.L., Lacerda, W.A., Becker, L.B. and Mendonça, M.B. (2011) Mechanisms of the recent catastrophic landslides in the mountainous range of Rio de Janeiro, Brazil. *Proceedings of the Second World Landslide Forum, 3-7 October 2011, Rome*, pp. 5.

Balco, G., Stone, J.O., Lifton, N.A. and Dunai, T.J. (2008) A complete and easily accessible means of calculating surface exposure ages or erosion rates from ^{10}Be and ^{26}Al measurements. *Quaternary Geochronology,* **3**, 174–195.

Ballantyne, C.K. (2002) Paraglacial geomorphology. *Quaternary Science Reviews*, **21**, 1935-2017.

Ballantyne, C.K., Wilson, P., Gheorghiu, D. and Rodés, À. (2014) Enhanced rock-slope failure following ice-sheet deglaciation: timing and causes. *Earth Surface Processes and Landforms*, **39**, 900-913.

Ballato, P. and Strecker, M.R. (2014) Assessing tectonic and climatic causal mechanisms in foreland-basin stratal architecture: insights from the Alborz Mountains, northern Iran. *Earth Surface Processes and Landforms,* **39**, 110-125.

Bartov, Y., Stein, M., Enzel, Y., Agnon, A. and Reches, Z. (2002) Lake levels and sequence stratigraphy of Lake Lisan, the Late Pleistocene precursor of the Dead Sea. *Quaternary Research*, **57**, 9-21.

Beaty, C.B. (1963) Origin of alluvial fans, White Mountains, California and Nevada. *Annals of the Association of American Geographers*, **53**, 516-535.

Beaumont, C., Jamieson, R.A., Nguyen, M.H. and Lee, B. (2001) Himalayan tectonics explained by extrusion of a low-viscosity crustal channel coupled to focused surface denudation. *Nature*, **414**, 738-742.

Bekaddour, T., Schlunegger, F., Vogel, H., Delunel, R., Norton, K.P., Akçar, N. and Kubik P. (2014) Paleo erosion rates and climate shifts recorded by Quaternary cut-and-fill sequences in the Pisco valley, central Peru. *Earth and Planetary Science Letters,* **390**, 103-115.

Benedict, J.B. (1993) Influence of snow upon rates of granodiorite weathering, Colorado Front Range, USA. *Boreas*, **22**, 87-92.

Benson L.V., Burdett J.W., Kashgarian M., Lund S.P., Phillips F.M., and Rye R.O. (1996) Climatic and hydrologic oscillations in the Owens Lake basin and adjacent Sierra Nevada, California. *Science,* **274**, 746-749.

Benson, L., Burdett, J., Lund, S., Kashgarian, M. and Mensing, S. (1997) Nearly synchronous climate change in the Northern Hemisphere during the last glacial termination. *Nature*, **388**, 263-265.

Berg, P., Haerter, J.O., Thejll, P., Piani, C., Hagemann, S. and Christensen, J.H. (2009) Seasonal characteristics of the relationship between daily precipitation intensity and surface temperature. *Journal of Geophysical Research*, **114**, D18102.

Berg, P., Moseley, C. and Haerter, J.O. (2013) Strong increase in convective precipitation in response to higher temperatures. *Nature Geoscience*, **6**, 181-185.

Bierman, P. and Gillespie, A. (1991) Range fires: A significant factor in exposure-age determination and geomorphic surface evolution. *Geology*, **19**, 641-644.

Bischoff, J.L., Menking, K.M., Fitts, J.P. and Fitzpatrick, J.A. (1997) Climatic oscillations 10,000-155,000 yr B.P. at Owens Lake, California reflected in glacial rock flour abundance and lake salinity in Core OL-92. *Quaternary Research*, **48**, 313-325.

Blackwelder, E. (1933) Lake Manly: An extinct lake of Death Valley. *Geographical Review,* **23**, 464-471.

Blair, T.C. and McPherson, J.G. (1992) The Trollheim alluvial fan and facies model revisited. *Geological Society of America Bulletin,* **104**, 762-769.

Blair, T.C. (1999) Cause of dominance by sheetflood vs debris-flow processes on two adjoining fans, Death Valley, California. *Sedimentology,* **46**, 1015-1028.

Blakely, R.J., Jachens, R.C., Calzia, J.P. and Langenheim, V.E. (1999) Cenozoic basins of the Death Valley extended terrane as reflected in regional-scale gravity anomalies. In: Wright, LA. and Troxel, BW. (Eds) *Cenozoic basins of the Death Valley region*. Geological Society of America Special Paper 333, Boulder, CO, USA, pp. 1-16.

Blum, M.D. and Törnqvist, T.E. (2000) Fluvial responses to climate and sea-level change: a review and look forward. *Sedimentology,* **47**, 2-48.

Bonnet, S. and Crave, A. (2003) Landscape responses to climate change: Insights from experimental modeling and implications for tectonic versus climatic uplift of topography. *Geology,* **31**, 123-126.

Bookhagen, B. and Strecker, M.R. (2012) Spatiotemporal trends in erosion rates across a pronounced rainfall gradient: Examples from the southern Central Andes. *Earth and Planetary Science Letters*, **327-328**, 97-110.

Borradaile, G.J. (2003) *Statistics of Earth Science Data*. Springer-Verlag: Berlin Heidelberg New York, pp. 280.

Boulton, S.J. and Whittaker, A.C. (2009) Quantifying the slip rates, spatial distribution and evolution of active normal faults from geomorphic analysis: field examples from an oblique-extensional graben, southern Turkey. *Geomorphology*, **104**, 299-316.

Braconnot, P., Otto-Bliesner, B., Harrison, S., Joussaume, S., Peterchmitt, J-Y., Abe-Ouchi, A., Crucifix, M., Driesschaert, E., Fichefet, Th., Hewitt, C.D., Kageyama, M., Kitoh, A., Laîné, A., Loutre, M-F., Marti, O., Merkel, U., Ramstein, G., Valdes, P., Weber, S.L., Yu, Y. and Zhao, Y. (2007) Results of PMIP2 coupled simulations of the mid-Holocene and Last Glacial Maximum – Part 1: experiments and large-scale features. *Climates of the Past*, **3**, 261-277.

Bull, W.B. (1964) *Geomorphology of segmented alluvial fans in western Fresno County, California*. U.S. Geological Survey Professional Paper 352-E, Washington D.C., USA, pp. 129.

Bull, W.B. (1991) *Geomorphic responses to climate change*. Oxford University Press, New York, USA, pp. 326.

Burbank, D.W. and Pinter, N. (1999) Landscape evolution: the interactions of tectonics and surface processes. *Basin Research*, **11**, 1-6.

Burbank, D.W. and Anderson, R.S. (2011) *Tectonic Geomorphology* (2nd edition). Wiley-Blackwell: Oxford; pp. 472.

Burke, K., Francis, P. and Wells, G. (1990) Importance of the geological record in understanding global change. *Palaeogeography, Palaeoclimatology, Palaeoecology*, **89**, 193-204.

Cannon, S.H., Gartner, J.E., Wilson, R.C., Bowers, J.C. and Laber, J.L. (2008) Storm rainfall conditions for floods and debris flows from recently burned areas in southwestern Colorado and southern California. *Geomorphology*, **96**, 250-269.

Castelltort, S. and Van Den Driessche, J. (2003) How plausible are high-frequency sediment supply-driven cycles in the stratigraphic record? *Sedimentary Geology,* **157**, 3-13.

Carretier, S. and Lucazeau, F. (2005) How does alluvial sedimentation at range fronts modify the erosional dynamics of mountain catchments? *Basin Research*, **17**, 361-381.

Castelltort, S., Nagel, S., Mouthereau, F., Tien-Shun Lin, A., Wetzel, A., Kaus, B., Willett, S., Chiang, S-P. and Chiu, W-Y. (2011) Sedimentology of early Pliocene sandstones in the south-western Taiwan foreland: Implications for basin physiography in the early stages of collision. *Journal of Asian Earth Sciences,* **40**, 52-71.

Castelltort, S., Goren, L., Willett, S., Champagnac, J-D., Herman, F. and Braun, J. (2012) River drainage patterns in the New Zealand Alps primarily controlled by plate tectonic strain. *Nature Geoscience,* **5**, 744-748.

Champagnac, J-D., Molnar, P., Sue, C. and Herman, F. (2012) Tectonics, climate, and mountain topography. *Journal of Geophysical Research,* **117**, B02403.

Champagnac, J-D., Valla, P.G. and Herman, F. (2014) Late-Cenozoic relief evolution under evolving climate: A review. *Tectonophysics,* **614**, 44-65.

Clark, M.K., Maheo, G., Saleeby, J. and Farley, K.A. (2005) The non-equilibrium landscape of the southern Sierra Nevada, California. *Geological Society of America Today*, **15**, 4-10.

Clarke, L., Quine, T.A. and Nicholas, A. (2010) An experimental investigation of autogenic behaviour during alluvial fan evolution. *Geomorphology,* **115**, 278-285.

Coe, J.A., Kinner, D.A. and Godt, J.W. (2008) Initiation conditions for debris flows generated by runoff at Chalk Cliffs, central Colorado. *Geomorphology*, **96**, 270-297.

Coelho-Netto, A.L. (1999) Catastrophic landscape evolution in a humid region (SE Brasil): Inheritances from tectonic, climatic and land use induced changes. *Geografia Fisica e Dinamica Quaternaria Supplement*, **111**, 21-48.

Covault, J.A., Romans, B.W., Fildani, A., McGann, M. and Graham, S.A. (2010) Rapid climatic signal propagation from source to sink in a southern California sediment-routing system. *The Journal of Geology*, **118**, 247-259.

Cowie, P.A., Whittaker, A.C., Attal, M., Roberts, G., Tucker, G.E. and Ganas, A. (2008) New constraints on sediment-flux-dependent river incision: Implications for extracting tectonic signals from river profiles. *Geology,* **36**, 535-538.

Crosby, B.T. and Whipple, K.X. (2006) Knickpoint initiation and distribution within fluvial networks: 236 waterfalls in the Waipaoa River, North Island, New Zealand. *Geomorphology*, **82**, 16-38.

Cyr, A.J., Granger, D.E., Olivetti, V. and Molin, P. (2010) Quantifying rock uplift rates using channel steepness and cosmogenic nuclide-determined erosion rates: examples from northern and southern Italy. *Lithosphere*, **2**, 188-198.

D'Arcy, M. and Whittaker, A.C. (2014) Geomorphic constraints on landscape sensitivity to climate in tectonically active areas. *Geomorphology,* **204**, 366-381.

D'Arcy, M., Roda Boluda, D.C., Whittaker, A.C. and Carpineti, A. (2015) Dating alluvial fan surfaces in Owens Valley, California, using weathering fractures in boulders. *Earth Surface Processes and Landforms,* **40**, 487-501.

Dadson, S.J., Hovius, N., Chen, H., Dade, W.B., Hsieh, M-L., Willett, S.D., Hu, J-C., Horng, M-J., Chen, M-C., Stark, C.P., Lague, D. and Lin, J-C. (2003) Links between erosion, runoff variability and seismicity in the Taiwan orogen. *Nature*, 426, 648-651.

Daly, C., Halblieb, M., Smith, J.I., Gibson, W.P., Doggett, M.K., Taylor, G.H., Curtis, J. and Pasteris, P.P. (2008) Physiographically sensitive mapping of climatological temperature and precipitation across the conterminous United States. *International Journal of Climatology*, **28**, 2031-2064.

Danskin, W.R. (1988) Preliminary Evaluation of the Hydrogeologic System in Owens Valley, California. U.S. Geological Survey Water Resources Investigations Report 88-4003, Sacramento, CA, USA, pp. 76.

David-Novak, H.B., Morin, E. and Enzel, Y. (2004) Modern extreme storms and the rainfall thresholds for initiating debris flows on the hyperarid western escarpment of the Dead Sea, Israel. *Geological Society of America Bulletin*, **116**, 718-728.

DeGraff, J., Wagner, D., Gallegos, A., DeRose, M., Shannon, C. and Ellsworth, T. (2011) The remarkable occurrence of large rainfall-induced debris flows at two different locations on July 12, 2008, Southern Sierra Nevada, CA, USA. *Landslides*, **8**, 343-353.

Densmore, A.L., Allen, P.A. and Simpson, G. (2007a) Development and response of a coupled catchment fan system under changing tectonic and climatic forcing. *Journal of Geophysical Research,* **112**, F01002.

Densmore, A.L., Gupta, S., Allen, P.A. and Dawers, N.H. (2007b) Transient landscapes at fault tips. *Journal of Geophysical Research,* **112**, F03S08.

DiBiase, R.A., Whipple, K.X., Heimsath, A.M. and Ouimet, W.B. (2010) Landscape form and millennial erosion rates in the San Gabriel Mountains, CA. *Earth and Planetary Science Letters*, **289**, 134-144.

DiBiase, R.A. and Whipple, K.X. (2011) The influence of erosion thresholds and runoff variability on the relationships among topography, climate, and erosion rate. *Journal of Geophysical Research,* **116**, F04036.

DiBiase, R.A., Heimsath, A.M. and Whipple, K.X. (2012) Hillslope response to tectonic forcing in threshold landscapes. *Earth Surface Processes and Landforms*, **37**, 855-865.

Dixon J.L, Heimsath A.M, Amundson R. (2009a) The critical role of climate and saprolite weathering in landscape evolution. *Earth Surface Processes and Landforms,* **34**, 1507-1521.

Dixon, J.L., Heimsath, A.M., Kaste, J. and Amundson, R. (2009b) Climate-driven processes of hillslope weathering. *Geology*, **37**, 975-978.

Dixon, T., Decaix, J., Farina, F., Furlong, K., Malservisi, R., Bennett, R., Suarez-Vidal, F., Fletcher, J. and Lee, J., (2002) Seismic cycle and rheological effects on estimation of present-day slip rates for the Agua Blanca and San Miguel-Vallecitos faults, northern Baja California, Mexico. *Journal of Geophysical Research*, **107**, B102226.

Dühnforth M., Densmore A.L., Ivy–Ochs S., Allen P.A., Kubik P.W. (2007) Timing and patterns of debris flow deposition on Shepherd and Symmes creek fans, Owens Valley, California, deduced from cosmogenic ^{10}Be. *Journal of Geophysical Research: Earth Surface* **112**, F03S15.

Dühnforth M., Densmore A.L., Ivy–Ochs S., Allen P.A. (2008) Controls on sediment evacuation from glacially modified and unmodified catchments in the eastern Sierra Nevada, California. *Earth Surface Processes and Landforms,* **33**, 1602-1613.

Duller, R.A., Whittaker, A.C., Fedele, J.J., Whitchurch, A.L., Springett, J., Smithells, R., Fordyce, S. and Allen, P.A. (2010) From grain size to tectonics. *Journal of Geophysical Research,* **115**, F03022.

Duller, R.A., Whittaker, A.C., Swinehart, J.B., Armitage, J.J., Sinclair, H.D., Bair, A. and Allen, P.A. (2012) Abrupt landscape change post-6 Ma on the central Great Plains, USA. *Geology,* **40**, 871-874.

Egholm, D.L., Pedersen, V.K., Knudsen, M.F., and Larsen, N.K. (2012) On the importance of higher order ice dynamics for glacial landscape evolution. *Geomorphology*, **141-142**, 67-80.

Enzel, Y., Amit, R., Grodek, T., Ayalon, A., Lekach, J., Porat, N., Bierman, P., Blum, J.D. and Erel, Y. (2012) Late Quaternary weathering, erosion, and deposition in Nahal Yael, Israel: An impact of climatic change on an arid watershed? *Geological Society of America Bulletin*, **124**, 705-722.

Eppes, M.C., McFadden, L.D., Wegmann, K.W. and Scuderi, L.A. (2010) Cracks in desert pavement rocks: Further insights into mechanical weathering by direction insolation. *Geomorphology*, **123**, 97–108.

Eyal, M., Bartov, Y., Shimron, A.E. and Bentor, Y.K., (1980) Sinai – Geological Map, 1:500,000 scale. Survey of Israel.

Fedele, J.J. and Paola, C. (2007) Similarity solutions for fluvial sediment fining by selective deposition. *Journal of Geophysical Research,* **112**, F02038.

Ferguson, R., Hoey, T., Wathen, S. and Werritty, A. (1996) Field evidence for rapid downstream fining of river gravels through selective transport. *Geology* **24**, 179-182.

Fernandes, N.F. and Dietrich, W.E. (1997) Hillslope evolution by diffusive processes: The timescale for equilibrium adjustments. *Water Resources Research*, **33**, 1307-1318.

Fernandes, N.F., Guimarães, R.F., Gomes, R.A.T., Vieira, B.C., Montgomery, D.R. and Greenberg, H. (2004) Topographic controls of landslides in Rio de Janeiro: field evidence and modeling. *Catena*, **55**, 163-181.

Ferranti, L., Antonioli, F., Mauz, B., Amorosi, A., Dai Pra, G., Mastronuzzi, G., Monaco, C., Orrù, P., Pappalardo, M., Radtke, U., Renda, P., Romano, P., Sansò, P. and Verrubbi, V., (2006) Markers of the last interglacial sea level highstand along the coast of Italy: tectonic implications. *Quaternary International*, **145-146**, 30-54.

Ferrier, K.L., Huppert, K.L. and Perron, J.T., (2013) Climatic control of bedrock river incision. *Nature*, **496**, 206-209.

Finnegan, N.J., Roe, G., Montgomery, D.R. and Hallet, B. (2005) Controls on the channel width of rivers: implications for modeling fluvial incision of bedrock. *Geology*, **33**, 229-232.

Foreman, B.Z. (2014) Climate-driven generation of a fluvial sheet sand body at the Paleocene-Eocene boundary in north-west Wyoming (USA). *Basin Research,* **26**, 225-241.

Foreman, B.Z., Heller, P.L. and Clementz, M.T. (2012) Fluvial response to abrupt global warming at the Palaeocene/Eocene boundary. *Nature,* **491**, 92-95.

Forzoni, A., Storms, J.E.A., Whittaker, A.C. and de Jager, G. (2014) Delayed delivery from the sediment factory: modelling the impact of catchment response time to tectonics on sediment flux and fluvio-deltaic stratigraphy. *Earth Surface Processes and Landforms,* **39**, 689-704.

Foster, D., Brocklehurst, S.H. and Gawthorpe, R.L., (2008) Small valley glaciers and the effectiveness of the glacial buzzsaw in the northern Basin and Range, USA. *Geomorphology*, **102**, 624-639.

Frankel, K.L., Brantley, K.S., Dolan, J.F., Finkel, R.C., Klinger, R.E., Knott, J.R., Machette, M.N., Owen, L.A., Phillips, F.M., Slate, J.L. and Wernicke, B.P. (2007a) Cosmogenic ^{10}Be and ^{36}Cl geochronology of offset alluvial fans along the northern Death Valley fault zone: Implications for transient strain in the eastern California shear zone. *Journal of Geophysical Research,* **112**, B06407.

Frankel, K.L., Dolan, J.F., Finkel, R.C., Owen, L.A. and Hoeft, J.S. (2007b) Spatial variations in slip rate along the Death Valley-Fish Lake Valley fault system determined from LiDAR topographic data and cosmogenic ^{10}Be geochronology. *Geophysical Research Letters,* **34**, L18303.

Frankel, K.L., Dolan, J.F., Owen, L.A., Ganev, P. and Finkel, R.C (2011) Spatial and temporal constancy of seismic strain release along an evolving segment of the Pacific-North America plate boundary. *Earth and Planetary Science Letters*, **304**, 565-576.

Ganev, P.N., Dolan, J.F., Frankel, K.L. and Finkel, R.C. (2010) Rates of extension along the Fish Lake Valley fault and transtensional deformation in the Eastern California shear zone-Walker Lane belt. *Lithosphere,* **2**, 33-49.

Gesch, D.B., Oimoen, M., Greenlee, S.K., Nelson, C., Steuck, M. and Tyler, D. (2002) The National Elevation Dataset. *Photogrammetric Engineering and Remote Sensing,* **68**, 5-11.

Gillespie, A.R. (1982) *Quaternary glaciation and tectonism in the Southeastern Sierra Nevada*. Ph.D. thesis, California Institute of Technology, Pasadena, CA, USA, pp. 720.

Giraudi, C. (1989) Lake levels and climate for the last 30,000 years in the Fucino area (Abruzzo – central Italy) – a review. *Palaeogeography, Palaeoclimatology, Palaeoecology*, **70**, 249-260.

Gonzalez, L. and Pfiffner, O.A. (2012) Morphologic evolution of the central Andes of Peru. *International Journal of Earth Sciences*, **101**, 307-321.

Goudie, A.S. (2013) *Arid and Semi-Arid Geomorphology*. Cambridge University Press, New York, USA, pp. 461.

Greene, D., Kirby, E., Dawers, N., Phillips, F., McGee, S. and Burbank, D. (2007) Quantifying accommodation of active strain along distributed fault arrays in Owens Valley, California. *Geological Society of America Abstracts with Programs*, **39**, 441.

Gregory-Wodzicki, K.M. (2000) Uplift history of the central and northern Andes: a review. *Geological Society of America Bulletin*, **112**, 1091-1105.

Griffiths, J.S., Fookes, P.G., Goudie, A.S. and Stokes, M. (2012) Processes and landforms in deserts. In: Walker M.J. (Ed) *Hot deserts: Engineering, geology and geomorphology – Engineering group working party report,* Special Publication **25**. Geological Society of London, London, pp. 33-95.

Griffiths, P.G., Webb, R.H. and Melis, T.S. (2004) Frequency and initiation of debris flows in Grand Canyon, Arizona. *Journal of Geophysical Research*, **109**, F04002.

Grohmann, C.H., Campanha, G.A.C. and Soares Jr, A.V. (2011) OpenStereo: um programa livre e multiplataforma para análise de dados estruturais. *XIII Simpósio Nacional de Estudos Tectônicos*, Campinas, SP. Anais, Brazil.

Hack, J.T. (1957) Studies of Longitudinal Stream Profiles in Virginia and Maryland. U.S. Geological Survey Professional Paper 294-B, Washington, DC, pp. 45-97.

Hall, K. (1999) The role of termal stress fatigue in the breakdown of rock in cold regions. *Geomorphology*, **31**, 47-63.

Hall, K., Guglielmin, M. and Strini, A. (2008) Weathering of granite in Antarctica: I. Light penetration into rock and implications for rock weathering and endolithic communities. *Earth Surface Processes and Landforms,* **33**, 295-307.

Hallet, B. (1990) Spatial self-organization in geomorphology: from periodic bedforms and patterned ground to scale-invariant topography. *Earth-Science Reviews,* **29**, 57-75.

Hammond, W.C., Blewitt, G., Li, Z., Plag, H-P. and Kreemer, C. (2012) Contemporary uplift of the Sierra Nevada, western United States, from GPS and InSAR measurements. *Geology,* **40**, 667-670.

Hampson, G.J., Duller, R.A., Petter, A.L., Robinson, R.A.J. and Allen, P.A. (2014) Mass-balance constraints on stratigraphic interpretation of linked alluvial-coastal-shelf deposits from source to sink: Example from Cretaceous Western Interior Basin, Utah and Colorado, U.S.A. *Journal of Sedimentary Research,* **84**, 935-960.

Harkins, N., Kirby, E., Heimsath, A., Robinson, R. and Reiser, U. (2007) Transient fluvial incision in the headwaters of the Yellow River, northeastern Tibet, China. *Journal of Geophysical Research,* **112**, F03S04.

Harvey, A.M., Silva, P.G., Mather, A.M., Goy, J.L., Stokes, M. and Zazo, C. (1999) The impact of Quaternary sea-level and climatic change on coastal alluvial fans in the Cabo de Gata ranges, southeast Spain. *Geomorphology,* **28**, 1-22.

Hay, W.W., Sloan II, J. L. and Wold, C.N. (1988) The mass/age distribution of sediments on the ocean floor and the global rate of loss of sediment. *Journal of Geophysical Research*, **93**, 14,933-14,940.

Hays, J.D., Imbie, J. and Shackleton, N.J. (1976) Variations in the Earth's orbit: Pacemaker of the ice ages. *Science*, **194**, 1121-1132.

Heller, P.L. and Paola, C. (1992) The large-scale dynamics of grain-size variation in alluvial basins, 2: Application to syntectonic conglomerate. *Basin Research,* **4**, 91-102.

Herbert, T.D., Yasuda, M. and Burnett, C. (1995) Glacial-interglacial sea-surface temperature record inferred from alkenone unsaturation indices, site 893, Santa Barbara basin. In: Kennett, J.P., Baldauf, J.G. and Lyle, M. (Eds) *Proceedings of the Ocean Drilling Program, Scientific Results*, **146** (Part 2), 257-264.

Herman, F., Seward, D., Valla, P.G., Carter, A., Kohn, B., Willett, S.D. and Ehlers T.A. (2014) Worldwide acceleration of mountain erosion under a cooling climate. *Nature,* **504**, 423-426.

Hijmans, R.J., Cameron, S.E., Parra, J.L., Jones, P.G. and Jarvis, A., (2005) Very high resolution interpolated climate surfaces for global land areas. *International Journal of Climatology*, **25**, 1965-1978.

Hillyer, R., Valencia, B.G., Bush, M.B., Silman, M.R. and Steinitz-Kannan, M. (2009) A 24,700-yr paleolimnological history from the Peruvian Andes. *Quaternary Research*, **71**, 71-82.

Hinderer, M. (2001) Late Quaternary denudation of the Alps, valley and lake fillings and modern river loads. *Geodinamica Acta*, **14**, 231-263.

Holmgren, C.A., Betancourt, J.L. and Rylander, K.A. (2011) Vegetation history along the eastern, desert escarpment of the Sierra San Pedro Mártir, Baja California, Mexico. *Quaternary Research*, **75**, 647-657.

Hooke, R.L. (1968) Steady-state relationships on arid-region alluvial fans in closed basins. *American Journal of Science,* **266**, 609-629.

Hostetler, S.W. and Clark, P.U. (1997) Climatic controls of western U.S. glaciers at the last glacial maximum. *Quaternary Science Reviews*, **16**, 505-511.

Howard, A.D. (1994) A detachment-limited model of drainage basin evolution. *Water Resources Research,* **30**, 2261-2285.

Humphrey, N.F. and Heller, P.L. (1995) Natural oscillations in coupled geomorphic systems: An alternative origin for cyclic sedimentation. *Geology,* **23**, 499-502.

Hurst, M.D., Mudd, S.M., Walcott, R., Attal, M. and Yoo, K. (2012) Using hilltop curvature to derive the spatial distribution of erosion rates. *Journal of Geophysical Research,* **117**, F02017.

Huyghe, D., Castelltort, S., Mouthereau, F., Serra-Kiel, J., Filleaudeau, P-Y., Emmanuel, L., Berthier, B. and Renard, M. (2012) Large scale facies change in the middle Eocene South-Pyrenean foreland basin: The role of tectonics and prelude to Cenozoic ice-ages. *Sedimentary Geology,* **253-254**, 25-46.

Incarbona, A., Zarcone, G., Agate, M., Bonomo, S., Di Stefano, E., Masini, F., Russo, F. and Sineo, L. (2010) A multidisciplinary approach to reveal the Sicily Climate and Environment over the last 20,000 years. *Central European Journal of Geosciences*, **2**, 71-82.

IPCC (2013) Climate Change 2013: The Physical Science Basis. Contribution of Working Group I to the Fifth Assessment Report of the Intergovernmental Panel on Climate Change. Stocker, T.F., Qin, D., Plattner, G-K., Tignor, M., Allen, S.K., Boschung, J., Nauels, A., Xia, Y., Bex, V. and Midgley, P.M. (Eds). Cambridge University Press, Cambridge, United Kingdom and New York, NY, USA, pp. 1535.

IPCC (2014) Climate Change 2014: Synthesis Report. Contribution of Working Groups I, II and III to the Fifth Assessment Report of the Intergovernmental Panel on Climate Change. Pachauri, R.K. and Meyer, L.A. (Eds). IPCC, Geneva, Switzerland, pp. 151.

Issar, A.S. and Bruins, H.J. (1983) Special climatological conditions in the deserts of Sinai and the Negev during the latest Pleistocene. *Palaeogeography, Palaeoclimatology, Palaeoecology*, **43**, 63-72.

Issar, A.S., Ginat, H. and Zohar, M., (2012) Shifts from deserted to inhabited terrain in the arid part of the Middle East, a function of climate changes. *Journal of Arid Environments,* **86**, 5-11.

Istanbulluoglu, E. and Bras, R.L. (2005) Vegetation-modulated landscape evolution: effects of vegetation on landscape processes, drainage density, and topography. *Journal of Geophysical Research,* **110**, F02012.

Istanbulluoglu, E. and Bras, R.L. (2006) On the dynamics of soil moisture, vegetation, and erosion: Implications of climate variability and change. *Water Resources Research*, **42**, W06418.

Iverson, R.M. and Vallance, J.W. (2001) New views of granular mass flows. *Geology*, **29**, 115-118.

Iverson, R.M., Logan, M., LaHusen, R.G. and Berti, M. (2010) The perfect debris flow? Aggregated results from 28 large-scale experiments. *Journal of Geophysical Research*, **115**, F03005.

Ivy-Ochs, S., Dühnforth, M., Densmore, A.L. and Alfimov, V. (2013) Dating fan deposits with cosmogenic nuclides. In *Dating torrential processes on fans and cones: Methods and their application for hazard and risk assessment,* Schneuwly-Bollschweiler, M., Stoffel, M., Rudolf-Miklau, F. (Eds), Advances in Global Change Research, **47**. Springer Science and Business Media, Dordrecht, pp. 243-263.

Jayko, A.S. (2009) Deformation of the late Miocene to Pliocene Inyo Surface, eastern Sierra Region, California. In: Oldow, J.S. and Cashman, P.H. (Eds) *Late Cenozoic structure and evolution of the Great Basin-Sierra Nevada transition*, Special Paper **447**. Geological Society of America, Boulder, CO, pp. 313-350.

Jerolmack, D.J. and Paola, C. (2010) Shredding of environmental signals by sediment transport. *Geophysical Research Letters*, **37**, L19401.

Johnson, B.G., Thackray, G.D. and Van Kirk, R. (2007) The effect of topography, latitude, and lithology on rock glacier distribution in the Lemhi Range, central Idaho, USA. *Geomorphology*, **91**, 38-50.

Johnson, C.G., Kokelaar, B.P., Iverson, R.M., Logan, M., LaHusen, R.G. and Gray, J.M.N.T. (2012) Grain-size segregation and levee formation in geophysical mass flows. *Journal of Geophysical Research*, **117**, F01032.

Jones, C.H., Farmer, G.L. and Unruh, J. (2004) Tectonics of Pliocene removal of lithosphere of the Sierra Nevada, California. *Geological Society of America Bulletin*, **116**, 1408-1422.

Jones, M.A., Heller, P.L., Roca, E., Garcés, M. and Cabrera, L. (2004) Time lag of syntectonic sedimentation across an alluvial basin: theory and example from the Ebro Basin, Spain. *Basin Research,* **16**, 467-488.

Kanner, L.C., Burns, S.J., Cheng, H. and Edwards, R.L. (2012) High-latitude forcing of the South American summer monsoon during the Last Glacial. *Science*, **335**, 570-573.

Kean, J.W., Staley, D.M. and Cannon, S.H. (2011) In situ measurements of post-fire debris flows in southern California: Comparisons of the timing and magnitude of 24 debris-flow events with rainfall and soil moisture conditions. *Journal of Geophysical Research*, **116**, F04019.

Kean, J.W., McCoy, S.W., Tucker, G.E., Staley, D.M. and Coe, J.A. (2013) Runoff-generated debris flows: Observations and modeling of surge initiation, magnitude and frequency. *Journal of Geophysical Research: Earth Surface*, **118**, 2190-2207.3

Keefer, D.K., Moseley, M.E. and deFrance, S.D. (2003) A 38,000-year record of floods and debris flows in the Ilo region of southern Peru and its relation to El Niño events and great earthquakes. *Palaeogeography, Palaeoclimatology, Palaeoecology*, **194**, 41-77.

Kessler, M.A., Anderson, R.S. and Stock, G.M. (2006) Modeling topographic and climatic control of east-west asymmetry in Sierra Nevada glacier length during the Last Glacial Maximum. *Journal of Geophysical Research,* **111**, F02002.

Kirby, E. and Whipple, K.X. (2001) Quantifying differential rock-uplift rates via stream profile analysis. *Geology*, **29**, 415-418.

Kirby, E., Whipple, K.X., Tang, W. and Chen, Z. (2003) Distribution of active rock uplift along the eastern margin of the Tibetan Plateau: inferences from bedrock channel longitudinal profiles. *Journal of Geophysical Research,* **108**, B42217.

Kirby, E., Burbank, D.W., Reheis, M. and Phillips, F. (2006) Temporal variations in slip rate of the White Mountains Fault Zone, eastern California. *Earth and Planetary Science Letters,* **248**, 168-185.

Kirby, E. and Whipple, K.X. (2012) Expression of active tectonics in erosional landscapes. *Journal of Structural Geology*, **44**, 54-75.

Klinger, R.E. (2001) Evidence for large dextral offset near Red Wall Canyon. In: Machette, MN., Johnson, M.L. and Slate, J.L. (Eds) *Quaternary and Late Pliocene geology of the Death Valley region: Recent observations on tectonics, stratigraphy, and lake cycles (Guidebook for the 2001*

Pacific Cell – Friends of the Pleistocene fieldtrip). U.S. Geological Survey Open-File Report 01-51, pp. A32-A37.

Klinger, R.E. (2002) Quaternary stratigraphy and geomorphology of northern Death Valley – Implications for tectonic activity along the northern Death Valley fault. *Ph.D. thesis*, University of Colorado, Boulder, CO, USA, pp. 312.

Knutson, T.R., McBride, J.L., Chan, J., Emanuel, K., Holland, G., Landsea, C., Held, I., Kossin, J.P., Srivastava, A.K. and Sugi, M. (2010) Tropical cyclones and climate change. *Nature Geoscience*, **3**, 157-163.

Kohn, B.P. and Eyal, M. (1981) History of uplift of the crystalline basement of Sinai and its relation to opening of the Red Sea as revealed by fission track dating of apatites. *Earth and Planetary Science Letters*, **52**, 129-141.

Ku, T-L., Luo, S., Lowenstein, T.K., Li, J. and Spencer, R.J. (1998) U-series chronology of lacustrine deposits in Death Valley, California. *Quaternary Research,* **50**, 261-275.

Kuhlemann, J., Frisch, W., Székely, B., Dunkl, I. and Kázmér, M. (2002) Post-collisional sediment budget history of the Alps: tectonic versus climatic control. *International Journal of Earth Science*, **91**, 818-837.

Kummerow, C., Barnes, W., Kozu, T., Shiue, J. and Simpson, J. (1998) The Tropical Rainfall Measuring Mission (TRMM) Sensor Package. *Journal of Atmospheric and Oceanic Technology*, **15**, 809-817.

Kutzbach, J.E., Guetter, P.J., Ruddiman, W.F. and Prell, W.L. (1989) Sensitivity of climate to late Cenozoic uplift in southern Asia and the American west: Numerical experiments. *Journal of Geophysical Research*, **94** (D15), 18393-18407.

Lague, D. and Davy, P. (2003) Constraints on the long-term colluvial erosion law by analyzing slope-area relationships at various tectonic uplift rates in the Siwaliks Hills (Nepal). *Journal of Geophysical Research,* **108**, B22129.

Lal, D. (1991) Cosmic ray labeling of erosion surfaces: In situ nuclide production rates and erosion models. *Earth and Planetary Science Letters,* **104**, 424-439.

Langbein, W.B. and Schumm, S.A. (1958) Yield of sediment in relation to mean annual precipitation. *Transactions, American Geophysical Union*, **39**, 1076-1084.

Le Pera, E. and Sorriso-Valvo, M. (2000) Weathering and morphogenesis in a mediterranean climate, Calabria, Italy. *Geomorphology*, **34**, 251-270.

Le, K., Lee, J., Owen, L.A., Finkel, R. (2007) Late Quaternary slip rates along the Sierra Nevada frontal fault zone, California: Slip partitioning across the western margin of the Eastern California Shear Zone – Basin and Range Province. *GSA Bulletin*, **119**, 240-256.

Lee, J., Miller, M.M., Crippen, R., Hacker, B. and Ledesma Vazquez, J., (1996) Middle Miocene extension in the Gulf Extensional Province, Baja California: evidence from the southern Sierra Juarez. *Geological Society of America Bulletin*, **108**, 505-525.

Lee, J., Stockli, D.F., Owen, L.A., Finkel, R.C. and Kislitsyn, R. (2009) Exhumation of the Inyo Mountains, alifornia: Implications for the timing of extension along the western boundary of the Basin and Range Province and distribution of dextral fault slip rates across the eastern California shear zone. *Tectonics*, **28**, TC1001.

Lenderink, G. and Van Meijgaard, E. (2008) Increase in hourly precipitation extremes beyond expectations from temperature changes. *Nature Geoscience*, **1**, 511-514.

Lenderink, G. and Van Meijgaard, E. (2010) Linking increases in hourly precipitation extremes to atmospheric temperature and moisture changes. *Environmental Research Letters*, **5**, 025208.

Leopold, L.B., Wolman, M.G. and Miller, J.P. (1964) *Fluvial processes in geomorphology*. W.H. Freeman and Co., San Francisco, pp. 544.

Lisiecki, L.E. and Raymo, M.E. (2009) Diachronous benthic $\delta^{18}O$ responses during late Pleistocene terminations. *Paleoceanography,* **24**, PA3210.

Litwin Miller, K., Reitz, M.D. and Jerolmack, D.J. (2014) Generalized sorting profile of alluvial fans. *Geophysical Research Letters,* **41**, 1-9.

Liu, S.C., Fu, C., Shiu, C-J., Chen, J.P. and Wu, F. (2009) Temperature dependence of global precipitation extremes. *Geophysical Research Letters*, **36**, L17702.

Lowenstein, T.K., Li, J., Brown, C., Roberts, S.M., Ku, T.L., Luo, S., Yang, W. (1999) 200 k.y. palaeoclimate record from Death Valley salt core. *Geology,* **27**, 3-6.

Lyle, M., Heusser, L., Ravelo, C., Andreasen, D., Lyle, A.O. and Diffenbaugh, N. (2010) Pleistocene water cycle and eastern boundary current processes along the California continental margin. *Paleoceanography*, **25**, PA4211.

Mabey, D.R. (1963) Complete Bouguer anomaly map of the Death Valley region, California. *U.S. Geological Survey Geophysical Investigation Map GP-305.*

Machette, M.N., Klinger, R.E. and Piety, L.A. (2002) Fault number 184, Grapevine fault. *Quaternary fault and fold database of the United States.* U.S. Geological Survey website: http://earthquakes.usgs.gov/hazards/qfaults (accessed 05/12/2014).

Machette, M.N., Slate, J.L. and Phillips, F.M. (2008) Terrestrial cosmogenic-nuclide dating of alluvial fans in Death Valley, California. *U.S. Geological Survey Professional Paper 1755*, pp. 54.

Martel, S.J., Harrison, T.M. and Gillespie, A.R. (1987) Late Quaternary vertical displacement rate across the Fish Springs fault, Owens Valley fault zone, California. *Quaternary Research*, **27**, 113-129.

Martinson, D.G., Pisias, N.G., Hays, J.D., Imbrie, J., Moore, T.C., Shackleton, N.J. (1987) Age dating and the orbital theory of the ice ages: development of a high-resolution 0 to 300,000-year chronostratigraphy. *Quaternary Research*, **27**, 1-29.

Massari, F., Capraro, L. and Rio, D. (2007) Climatic modulation of timing of systems-tract development with respect to sea-level changes (middle Pleistocene of Crotone, Calabria, southern Italy). *Journal of Sedimentary Research*, **77**, 461-468.

Masson-Delmotte, V., Schultz, M., Abe-Ouchi, A., Beer, J., Ganopolski, A., González Rouco, J.F., Jansen, E., Lambeck, K., Luterbacher, J., Naish, T., Osborn, T., Otto-Bliesner, B., Quinn, T., Ramesh, R., Rojas, M., Shao, X. and Timmermann, A. (2013) Information from palaeoclimate archives. In: Stocker, T.F., Qin, D., Plattner, G-K., Tignor, M., Allen, S.K., Boschung, J., Nauels, A., Xia, Y., Bex, V. and Midgley, P.M. (Eds) *Climate change 2013: The physical science basins. Contribution of working group I to the Fifth Assessment Report of the Intergovernmental Panel on Climate Change*. Cambridge University Press, Cambridge, United Kingdom and New York, NY, USA, pp. 383-464.

McCoy, S.W., Kean, J.W., Coe, J.A., Tucker, G.E., Staley, G.M. and Wasklewicz, T.A. (2012) Sediment entrainment by debris flows: In situ measurements from the headwaters of a steep catchment. *Journal of Geophysical Research*, **117**, F03016.

McCoy, S.W., Tucker, G.E., Kean, J.W. and Coe, J.A. (2013) Field measurement of basal forces generated by erosive debris flows. *Journal of Geophysical Research: Earth Surface*, **118**, 589-602.

McDonald, E., McFadden, L.D. and Wells, S.G. (2003) Regional response of alluvial fans to the Pleistocene-Holocene climatic transition, Mojave Desert, California. In: Enzel, Y., Wells, S.G. and Lancaster, N. (Eds) *Paleoenvironments and paleohydrology of the Mojave and southern Great Basin Deserts*, Special Paper 368. Geological Society of America: Boulder, CO; pp. 189-205.

McFadden, L.D., Eppes, M.C., Gillespie, A.R. and Hallet, B. (2005) Physical weathering in arid landscapes due to diurnal variation in the direction of solar heating. *Geological Society of America Bulletin*, **117**, 161-173.

McPhillips, D., Bierman, PR., Crocker, T. and Rood, DH. (2013) Landscape response to Pleistocene-Holocene precipitation change in the Western Cordillera, Peru: ^{10}Be concentrations in modern sediments and terrace fills. *Journal of Geophysical Research: Earth Surface*, **118**, 2488-2499.

Menking, K.M. (1997) Climatic signals in clay mineralogy and grain-size variations in Owens Lake core OL-92. southeast California. In: Smith, G.I. and Bischoff, J.L. (Eds) *An 800,000-year paleoclimatic record from core OL-92, Owens Lake, southeast California*, Special Paper 317. Geological Society of America: Boulder, CO; pp. 25-36.

Menking, K.M., Anderson, R.Y., Shafike, N.G., Syed, K.H. and Allen, B.D. (2004) Wetter or colder at the Last Glacial Maximum? Revisiting the pluvial lake question in southwestern North America. *Quaternary Research*, **62**, 280-288.

Meyer, G.A., Fawcett, P.J., and Locke, W.W. (2004) Late-Pleistocene equilibrium line altitudes, atmospheric circulation, and timing of mountain glacier advances in the interior northwestern United States. In: Haller, K.M. and Wood, S.H. (Eds), Geological Field Trips in Southern Idaho, Eastern Oregon, and Northern Nevada. U.S. Geological Survey Open File Report **1222**, Reston, VA, pp. 61-66.

Miall, A.D. (1991) Stratigraphic sequences and their chronostratigraphic correlation. *Journal of Sedimentary Research*, **61**, 497-505.

Miall, A.D. (1996) The geology of fluvial deposits: Sedimentary facies, basin analysis, and petroleum geology. Springer Verlag, Berlin, pp. 582.

Michael, N.A., Whittaker, A.C. and Allen, P.A. (2013) The functioning of sediment routing systems using a mass balance approach: Example from the Eocene of the southern Pyrenees. *The Journal of Geology,* **121**, 581-606.

Michael, N.A., Whittaker, A.C., Carter, A. and Allen, P.A. (2014) Volumetric budget and grain-size fractionation of a geological sediment routing system: Eocene Escanilla Formation, south-central Pyrenees. *Geological Society of America Bulletin,* **126**, 585-599.

Miller, D.M., Schmidt, K.M., Mahan, S.A., McGeehin, J.P., Owen, L.A., Barron, J.A., Lehmkuhl, F. and Löhrer, R. (2010) Holocene landscape response to seasonality of storms in the Mojave Desert. *Quaternary International*, **215**, 45-61.

Miller, K.G., Fairbanks, R.G. and Mountain, G.S. (1987) Tertiary oxygen isotope synthesis, sea level history, and continental margin erosion. *Paleoceanography*, **2**, 1-19.

Miller, S.R., Baldwin, S.L. and Fitzgerald, P.G. (2012) Transient fluvial incision and active surface uplift in the Woodlark Rift of eastern Papua New Guinea. *Lithosphere*, **4**, 131-149.

Molaro J and Byrne S. (2012) Rates of temperature change of airless landscapes and implications for thermal stress weathering. *Journal of Geophysical Research: Planets*, **117**, E10011.

Molnar, P. (2001) Climate change, flooding in arid environments, and erosion rates. *Geology,* **29**, 1071-1074.

Molnar, P (2004) Late Cenozoic increase in accumulation rates of terrestrial sediment: How might climate change have affected erosion rates? *Annual Review of Earth and Planetary Sciences*, **32**, 67-89.

Molnar, P. and England, P. (1990) Late Cenozoic uplift of mountain ranges and global climate change: chicken or egg? *Nature*, **346**, 29-34.

Molnar, P., England, P. and Martinod, J. (1993) Mantle dynamics, uplift of the Tibetan plateau, and the Indian Monsoon. *Reviews of Geophysics*, **31**, 357-396.

Montgomery, D.R., Balco, G. and Willett, S.D. (2001) Climate, tectonics, and the morphology of the Andes. *Geology*, **29**, 579-582.

Moore, J.G. (1981) *Geologic map of the Mount Whitney quadrangle, Inyo and Tulare Counties, California*. Geologic Quadrangle Map GQ-1545, U.S. Geological Survey (1:62,500).

Moore, J.G. and Sisson, T.W. (1987) *Preliminary geologic map of Sequoia and Kings Canyon National Parks*. Open File Report 87-651, U.S. Geological Survey (1:125,000).

Moore, J.G. and Mack, G.S. (2008) *Map Showing Limits of Tahoe Glaciation in Sequoia and Kings Canyon National Parks, California*. Scientific Investigations Map 2945, U.S. Geological Survey (1:125,000).

Moores, J.E., Pelletier, J.D. and Smith, P.H. (2008) Crack propagation by differential insolation on desert clasts. *Geomorphology,* **102**, 472–481.

Morehead, M.D., Syvitski, J.P. and Hutton, E.W.H. (2001) The link between abrupt climate change and basin stratigraphy: a numerical approach. *Global and Planetary Change*, **28**, 107-127.

Mudd, S.M., Attal, M., Milodowski, D.T., Grieve, S.W.D. and Valters, D.A. (2014) A statistical framework to quantify spatial variation in channel gradients using the integral method of channel profile analysis. *Journal of Geophysical Research: Earth Surface*, **119**, 138-152.

Nagel, S., Castelltort, S., Wetzel, A., Willett, S.D., Mouthereau, F. and Lin, A.T. (2013) Sedimentology and foreland basin paleogeography during Taiwan arc continent collision. *Journal of Asian Earth Sciences,* **62**, 180-204.

Nichols, K.K., Bierman, P.R., Ross Foniri, W., Gillespie, A.R., Caffee, M. and Finkel, R. (2006) Dates and rates of arid region geomorphic processes. *Geological Society of America Today*, **16**, 4-11.

Niemi, N.A. (2002) Extensional tectonics in the Basin and Range province and the geology of the Grapevine Mountains, California and Nevada. *Ph.D. thesis*, California Institute of Technology, Pasadena, CA, USA, pp. 356.

Niemi, N.A. (2012) Geologic map of the central Grapevine Mountains, Inyo County, California, and Esmeralda and Nye Counties, Nevada. *The Geological Society of America Digitial Map and Chart Series* **12**.

NOAA National Climatic Data Center (2014), 2004–2013 climate records from Independence station. Climate Data Online: www.ncdc.noaa.gov/cdo-web/datasets (accessed 07/10/2014).

O'Connor, J.E. and Chase, C.G. (1989) Uplift of the Sierra San Pedro Mártir, Baja California, Mexico. *Tectonics*, **8**, 833-844.

Olivetti, V., Cyr, A.J., Molin, P., Faccenna, C. and Granger, D.E. (2012) Uplift history of the Sila Massif, southern Italy, deciphered from cosmogenic ^{10}Be erosion rates and river longitudinal profile analysis. *Tectonics*, **31**, TC3007.

Orme, A.R. and Orme, A.J. (2008) Late Pleistocene shorelines of Owens Lake, California, and their hydroclimatic and tectonic implications. In: In: Reheis, M.C., Hershler, R. and Miller, D.M (Eds) *Late Cenozoic drainage history of the southwestern Great Basin and lower Colorado River region: Geologic and biologic perspectives*. Geological Society of America Special Paper 439, Boulder, CO, USA, pp. 207-225.

Ouimet, W.B., Whipple, K.X. and Granger, D.E. (2009) Beyond threshold hill-slopes: channel adjustment to base-level fall in tectonically active mountain ranges. *Geology,* **37**, 579-582.

Owen, L.A., Clemmens, S.J., Finkel, R.C. and Gray, H. (2014) Late Quaternary alluvial fans at the eastern end of the San Bernardino Mountains, Southern California. *Quaternary Science Reviews*, **87**, 114-134.

Pakiser, L.C., Kane, M.F. and Jackson, W.H. (1964) Structural geology and volcanism of Owens Valley region, California - a geophysical study. Professional Paper 438, U.S. Geological Survey, pp. 68.

Paola, C. (2000) Quantitative models of sedimentary basin filling. *Sedimentology*, **47**, 121-178.

Paola, C., Heller, P.L. and Angevine, C.L. (1992a) The large-scale dynamics of grain-size variation in alluvial basins, 1: Theory. *Basin Research*, **4**, 73-90.

Paola, C., Parker, G., Seal, R., Sinha, S.K., Southard, J.B. and Wilcock, P.R. (1992b) Downstream fining by selective deposition in a laboratory flume. *Science,* **11**, 1757-1760.

Paola, C. and Seal, R. (1995) Grain size patchiness as a cause of selective deposition and grain size fining. *Water Resources Research,* **31**, 1395-1407.

Paola, C. and Foufoula-Georgiou (2001) *Statistical geometry and dynamics of braided rivers*. In: Mosley, M. P. (Ed) Gravel-Bed Rivers. New Zealand Hydrological Society, Wellington, pp. 47-71.

Paola, C., Straub, K., Mohrig, D. and Reinhardt, L. (2009) The "unreasonable effectiveness" of stratigraphic and geomorphic experiments. *Earth-Science Reviews*, **97**, 1-43.

Paola, C. and Martin, J.M. (2012) Mass-balance effects in depositional systems. *Journal of Sedimentary Research,* **82**, 435-450.

Parsons, A.J., Michael, N.A., Whittaker, A.C., Duller, R.A. and Allen, P.A. (2012) Grain-size trends reveal the late orogenic tectonic and erosional history of the south-central Pyrenees, Spain. *Journal of the Geological Society,* **169**, 111-114.

Pedoja, K., Ortlieb, L., Dumont, J.F., Lamothe, M., Ghaleb, B., Auclair, M. and Labrousse, B. (2006) Quaternary coastal uplift along the Talara Arc (Ecuador, northern Peru) from new marine terrace data. *Marine Geology,* **228**, 73-91.

Pelletier, J.D. (2014) The linkages among hillslope-vegetation changes, elevation, and the timing of late-Quaternary fluvial-system aggradation in the Mojave Desert revisited. *Earth Surface Dynamics*, **2**, 455-468.

Pepin, E., Carretier, S. and Herail, G. (2010) Erosion dynamics modelling in a coupled catchment-fan system with constant external forcing. *Geomorphology,* **122**, 78-90.

Persson, P.O.G., Neiman, P.J., Walter, B., Bao, J-W. and Ralph, F.M. (2005) Contributions from California coastal-zone surface fluxes to heavy coastal precipitation: A CALJET case study during the strong El Niño of 1998. *Monthly Weather Review*, **133**, 1175-1198.

Pezza, A.B. and Simmonds, I. (2005) The first South Atlantic hurricane: Unprecedented blocking, low shear and climate change. *Geophysical Research Letters*, **32**, L15712.

Pezza, A.B., Simmonds, I. and Pereira Filho, A.J. (2009) Climate perspective on the large-scale circulation associated with the transition of the first South Atlantic hurricane. *International Journal of Climatology*, **29**, 1116-1130.

Phillips, F.M. (2008) Geological and hydrological history of the paleo-Owens River drainage since the late Miocene. In: Reheis, M.C., Hershler, R. and Miller, D.M (Eds) *Late Cenozoic drainage history of the southwestern Great Basin and lower Colorado River region: Geologic and biologic perspectives*. Geological Society of America Special Paper 439, Boulder, CO, USA, pp. 115-150.

Phillips, F.M., Zreda, M., Plummer, M.A., Elmore, D. and Clark, D.H. (2009) Glacial geology and chronology of Bishop Creek and vicinity, eastern Sierra Nevada, California. *Geological Society of America Bulletin*, **121**, 1013-1033.

Phillips, F.M., Argento, D.C., Bourlès, D.L., Caffee, M.W., Dunai, T.J., Goehring, B., Gosse, J.C., Hudson, A.M., Jull, A.J.T., Kelly, M., Lifton, N., Marrero, S.M., Nishiizumi, K., Reedy, R.C. and Stone, J.O.H. (2015) Where now? Reflections on future directions for cosmogenic nuclide research from the CRONUS Projects. *Quaternary Geochronology*, in press, doi:10.1016/j.quageo.2015.04.010.

Pinet, P. and Souriau, M. (1988) Continental erosion and large-scale relief. *Tectonics,* **7**, 563-582.

PRISM Climate Group (2004), Oregon State University: http://prism.oregonstate.edu/ (created 04/02/2004).

Quade, J., Forester, R.M. and Whelan, J.F. (2003) Late Quaternary paleohydrologic and paleotemperature change in southern Nevada. In: Enzel, Y., Wells, S.G. and Lancaster, N. (Eds) *Paleoenvironments and paleohydrology of the Mojave and southern Great Basin deserts*. Geological Society of America Special Paper 368, Boulder, CO, USA, pp. 165-188.

Raymo, M.E. and Ruddiman, W.F. (1992) Tectonic forcing of late Cenozoic climate. *Nature*, **359**, 117-122.

Reheis, M.C. and Sawyer, T.L. (1997) Late Cenozoic history and slip rates of the Fish Lake Valley, Emigrant Peak and Deep Springs fault zones, Nevada and California. *Geological Society of America Bulletin,* **109**, 280-299.

Reynolds, M.W. (1969) Stratigraphy and structural geology of the Titus and Titanothere Canyons area, Death Valley, California. *Ph.D. thesis*, University of California, Berkeley, CA, USA, pp. 310.

Rhode, D. (2002) Early Holocene Juniper woodland and chaparral taxa in the central Baja California peninsula, Mexico. *Quaternary Research,* **57**, 102-108.

Ritter, J.B., Miller, J.R. and Husek-Wulforst, J. (2000) Environmental controls on the evolution of alluvial fans in Buena Vista Valley, North Central Nevada, during late Quaternary time. *Geomorphology*, **36**, 63-87.

Robinson, R.A.J. and Slingerland, R.L. (1998) Origin of fluvial grain-size trends in a foreland basin: The Pocono Formation on the Central Appalachian Basin. *Journal of Sedimentary Research A,* **68**, 473-486.

Roe, G.H., Montgomery, D.R. and Hallet, B. (2002) Effects of orographic precipitation variations on the concavity of steady-state river profiles. *Geology*, **30**, 143-146.

Rohais, S., Bonnet, S. and Eschard, R. (2012) Sedimentary record of tectonic and climatic erosional perturbations in an experimental coupled catchment-fan system. *Basin Research,* **24**, 198-212.

Romans, B.W., Normark, W.R., McGann, M.M., Covault, J.A. and Graham, S.A. (2009) Coarse-grained sediment delivery and distribution in the Holocene Santa Monica Basin, California: Implications for evaluating source-to-sink flux at millennial time scales. *Geological Society of America Bulletin,* **121**, 1394-1408.

Rood, D.H., Burbank, D.W. and Finkel, R.C. (2011) Chronology of glaciations in the Sierra Nevada, California, from ^{10}Be surface exposure dating. *Quaternary Science Reviews*, **30**, 646-661.

Royden, L. and Perron, J.T. (2013) Solutions of the stream power equation and application to the evolution of river longitudinal profiles. *Journal of Geophysical Research: Earth Surface*, **118**, 497-518.

Ruddiman, W.F. and Kutzbach, J.E. (1989) Forcing of late Cenozoic northern hemisphere climate by plateau uplift in southern Asia and the American west. *Journal of Geophysical Research*, **94** (D15), 18409-18427.

Ruddiman, W.F., Prell, W.L. and Raymo, M.E. (1989) Lake Cenozoic uplift in southern Asia and the American west: Rationale for general circulation modeling experiments. *Journal of Geophysical Research*, **94**, 18379-18391.

Ryder, J.M. (1971) The stratigraphy and morphology of paraglacial alluvial fans in south-central British Columbia. *Canadian Journal of Earth Sciences*, **8**, 279-298.

Saillard, M., Hall, S.R., Audin, L., Farber, D.L., Regard, V. and Hérail, G. (2011) Andean coastal uplift and active tectonics in southern Peru: ^{10}Be surface exposure dating of differentially uplifted marine terrace sequences (San Juan de Marcona, ~15.4°S). *Geomorphology*, **128**, 178-190.

Salcher, B.C., Kober, F., Kissling, E. and Willett, S.D. (2014) Glacial impact on short-wavelength topography and long-lasting effects on the denudation of a deglaciated mountain range. *Global and Planetary Change,* **115**, 59-70.

Savi, S., Norton, K.P., Picotti, V., Akçar, N., Delunel, R., Brardinoni, F., Kubik, P. and Schlunegger, F. (2014) Quantifying sediment supply at the end of the last glaciation: Dynamic reconstruction of an alpine debris-flow fan. *Geological Society of America Bulletin*, **126**, 773-790.

Schlische, R.W. and Anders, M.H. (1996) Stratigraphic effects and tectonic implications of the growth of normal faults and extensional basins. In: Beratan, K.K (Ed.) Reconstructing the history of Basin and Range extension using sedimentology and stratigraphy. Geological Society of America Special Paper 303, Boulder, CO, USA, pp. 183-203.

Schlunegger, F., Norton, K.P. and Zeilinger, G. (2011) Climatic forcing on channel profiles in the Eastern Cordillera of the Coroico region, Bolivia. *The Journal of Geology*, **119**, 97-107.

Schumer, R. and Jerolmack, D.J. (2009) Real and apparent changes in sediment deposition rates through time. *Journal of Geophysical Research: Earth Surface,* **114**, F00A06.

Schumm, S.A. (1968) Speculations concerning paleohydrologic controls of terrestrial sedimentation. *Bulletin of the Geological Society of America*, **79**, 1573-1588.

Seidl, M.A. and Dietrich, W. (1992) The problem of channel erosion into bedrock. *Catena Supplement*, **23**, 101-124.

Sepúlveda, S.A., Rebolledo, S. and Vargas, G. (2006) Recent catastrophic debris flows in Chile: Geological hazard, climatic relationships and human response. *Quaternary International*, **158**, 83-95.

Sharp, I.R., Gawthorpe, R.L., Armstrong, B. and Underhill, J.R. (2000) Propagation history and passive rotation of mesoscale normal faults: implications for synrift stratigraphic development. *Basin Research*, **12**, 285-305.

Simpson, G. and Castelltort, S. (2012) Model shows that rivers transmit high-frequency climate cycles to the sedimentary record. *Geology,* **40**, 1131-1134.

Singleton, A. and Toumi, R. (2013) Super-Clausius-Clapeyron scaling of rainfall in a model squall line. *Quarterly Journal of the Royal Meteorological Society*, **139**, 334-339.

Sklar, L.S. and Dietrich, W.E. (1998) River longitudinal profiles and bedrock incision models: stream power and the influence of sediment supply. In: Tinkler, K.J. and Wohl, E.E. (Eds), Rivers Over Rock: Fluvial Processes in Bedrock Channels. American Geophysical Union, Washington, DC, pp. 237-260.

Small, E., Anderson, R.A., Repka, J.L. and Finkel, R. (1997) Erosion rates of alpine bedrock summit surfaces deduced from in situ ^{10}Be and ^{26}Al. *Earth and Planetary Science Letters*, **150**, 413-425.

Snyder, N.P., Whipple, K.X., Tucker, G.E. and Merritts, D.J. (2000) Landscape response to tectonic forcing: digital elevation model analysis of stream profiles in the Mendocino triple junction region, northern California. *Geological Society of America Bulletin,* **112**, 1250-1263.

Sólyom, P.B. and Tucker, G.E. (2004) Effect of limited storm duration on landscape evolution, drainage basin geometry, and hydrograph shapes. *Journal of Geophysical Research*, **109**, F03012.

Spelz, R.M., Fletcher, J.M., Owen, L.A. and Caffee, M.W. (2008) Quaternary alluvial-fan development, climate and morphologic dating of fault scarps in Laguna Salada, Baja California, Mexico. *Geomorphology*, **102**, 578-594.

Steffen, D., Schlunegger, F. and Preusser, F. (2009) Drainage basin response to climate change in the Pisco valley, Peru. *Geology,* **37**, 491-494.

Steffen, D., Schlunegger, F. and Preusser, F. (2010) Late Pleistocene fans and terraces in the Majes valley, southern Peru, and their relation to climatic variations. *International Journal of Earth Sciences,* **99**, 1975-1989.

Sternberg, H. (1875) Untersuchungen über Längen und Querprofil geschiebeführnde Flüsse. *Z Bauwesen,* **25**, 483-506.

Stock, J.D. and Montgomery, D.R. (1999) Geologic constraints on bedrock river incision using the stream power law. *Journal of Geophysical Research*, **104**, 4983-4993.

Stock, G.M., Anderson, R.S. and Finkel, R.C. (2004) Pace of landscape evolution in the Sierra Nevada, California, revealed by cosmogenic dating of cave sediments. *Geology*, **32**, 193-196.

Stock, J.D., Montgomery, D.R., Collins, B.D., Dietrich, W.E. and Sklar, L. (2005) Field measurements of incision rates following bedrock exposure: Implications for process controls on the long profiles of valleys cut by rivers and debris flows. *Geological Society of America Bulletin*, **117**, 174-194.

Stock, J.D. and Dietrich, W.E. (2006) Erosion of steepland valleys by debris flows. *Geological Society of America Bulletin*, **118**, 1125-1148.

Stolar, D.B., Willett, S.D. and Roe, G.H. (2006) Climatic and tectonic forcing of a critical orogen. In: Willett, S.D., Hovius, N., Brandon, M.T. and Fisher, D.M. (Eds) Tectonics, Climate, and Landscape Evolution. *Geological Society of America Special Paper 398*, Penrose Conference Series, 241-250.

Stone, J.O. (2000) Air pressure and cosmogenic isotope production. *Journal of Geophysical Research: Solid Earth*, **105** (B10), 23753-23759.

Taylor, J.R. (1997) *An introduction to error analysis: The study of uncertainty in physical measurements* (2nd edition). University Science Books, Sausalito, CA, pp. 327.

Thompson, R.S., Anderson, K.H. and Bartlein, P.J. (1999) *Quantitative paleoclimatic reconstructions from late Pleistocene plant macrofossils of the Yucca Mountain region*. U.S. Geological Survey Open-File Report 99-338, pp. 39.

Tippett, J.M. and Kamp, P.J.J. (1995) Quantitative relationships between uplift and relief parameters for the Southern Alps, New Zealand, as determined by fission track analysis. *Earth Surface Processes and Landforms*, **20**, 153-175.

Toro-Escobar, C., Parker, G. and Paola, C. (1996) Transfer function for deposition of poorly sorted gravel in response to streambed aggradation. *Journal of Hydraulic Research,* **34**, 35-53.

Trauth, M.H., Bookhagen, B., Marwan, N. and Strecker, M.R. (2003) Multiple landslide clusters record Quaternary climate changes in the northwestern Argentine Andes. *Palaeogeography, Palaeoclimatology, Palaeoecology*, **194**, 109-121.

Trenberth, K.E., Dai, A., Rasmussen, R.M. and Parsons, D.B. (2003) The changing character of precipitation. *Bulletin of the American Meteorological Society*, **84**, 1205-1217.

Tucker, G.E. (2004) Drainage basin sensitivity to tectonic and climatic forcing: Implications of a stochastic model for the role of entrainment and erosion thresholds. *Earth Surface Processes and Landforms,* **29**, 185-205.

Tucker, G.E. (2009) Natural experiments in landscape evolution. *Earth Surface Processes and Landforms,* **34**, 1450-1460.

Tucker, G.E. and Slingerland, R. (1997) Drainage basin responses to climate change. *Water Resources Research*, **33**, 2031-2047.

Tucker, G.E. and Whipple, K.X. (2002) Topographic outcomes predicted by stream erosion models: Sensitivity analysis and intermodal comparison. *Journal of Geophysical Research*, **107**, B92179.

U.S. Geological Survey (USGS), California Geological Survey, and Nevada Bureau of Mines and Geology (2006). Quaternary fault and fold database for the United States. Accessed Nov. 2011. Available online: http//earthquakes.usgs.gov/regional/qfaults/.

Van Den Berg Van Saparoea, A-P.H. and Postma, G. (2008) Control of climate change on the yield of river systems. In: Hampson, G.J., Steel, R.J., Burgess, P.M. and Dalrymple, R.W. (Eds) *Recent advances in models of siliciclastic shallow-marine stratigraphy*. SEPM (Society for Sedimentary Geology) Special Publication, **90**, 15-33.

Vargas, G., Rutllant, J. and Ortlieb, L. (2006) ENSO tropical-extratropical climate teleconnections and mechanisms for Holocene debris flows along the hyperarid coast of western South America (17°-24°S). *Earth and Planetary Science Letters*, **249**, 467-483.

Vermeesch, P. (2012) On the visualisation of detrital age distributions. *Chemical Geology*, **312-313**, 190-194.

Vogel, M., Jayko, A.S., Wooden, J. and Smith, R.S.U. (2002) Quaternary exhumation rate, central Panamint Range, California, from U-Pb zircon ages. *Geological Society of America Abstracts with Programs*, **34**, 249.

Wakabayashi, J. and Sawyer, T.L. (2001) Stream incision, tectonics, uplift, and evolution of topography of the Sierra Nevada, California. *The Journal of Geology*, **109**, 539-562.

Waters, J.V., Jones, S.J. and Armstrong, H.A. (2010) Climatic controls on late Pleistocene alluvial fans, Cyprus. *Geomorphology,* **115**, 228-251.

Wentz, F.J., Ricciardulli, L., Hilburn, K. and Mears, C. (2007) How much more rain will global warming bring? *Science*, **317**, 233-235.

Western Regional Climate Center (2015) Climate summary for Death Valley, California (station 042319). *Cooperative climatological data summaries*. Western Regional Climate Center website: http://www.wrcc.dri.edu/climatedata/climsum/ (accessed 10/10/2014).

Whipple, K.X. (2004) Bedrock rivers and the geomorphology of active orogens. *Annual Review of Earth and Planetary Sciences*, **32**, 151-185.

Whipple, K.X. and Dunne, T. (1992) The influence of debris-flow rheology on fan morphology, Owens Valley, California. *GSA Bulletin*, **104**, 887-900.

Whipple, K.X. and Traylor, C.R. (1996) Tectonic control of fan size: the importance of spatially variable subsidence rates. *Basin Research,* **8**, 351-366.

Whipple, K.X. and Tucker, G.E. (1999) Dynamics of the stream-power river incision model: implications for height limits of mountain ranges, landscape response timescales, and research needs. *Journal of Geophysical Research,* **104** (B8), 17,661-17,674.

Whipple, K.X. and Tucker, G.E. (2002) Topographic outcomes predicted by stream erosion models: sensitivity analysis and intermodal comparison. *Journal of Geophysical Research,* **107** (B2), ETG3.

Whipple, K.X., Wobus, C., Crosby, B., Kirby, E. and Sheehan, D. (2007) New Tools for Quantitative Geomorphology: Extraction and Interpretation of Stream Profiles from Digital Topographic Data. *Geological Society of America Annual Meeting*, 28/10/2007, Boulder, CO, USA.

White, W.R., Milli, H. and Crabbe, A.D. (1978) Sediment transport: An appraisal of existing methods. *Hydraulic Research Station,* **119**, Wallingford, England.

Whittaker, A.C. (2012) How do landscapes record tectonics and climate? *Lithosphere,* **4**, 160-164.

Whittaker, A.C., Cowie, P.A., Attal, M., Tucker, G.E. and Roberts, G.P. (2007a) Contrasting transient and steady-state rivers crossing active normal faults: new field observations from the Central Apennines, Italy. *Basin Research*, **19**, 529-556.

Whittaker, A.C., Cowie, P.A., Attal, M., Tucker, G.E., Roberts, G.P. (2007b) Bedrock channel adjustment to tectonic forcing: Implications for predicting river incision rates. *Geology*, **35**, 103-106.

Whittaker, A.C., Attal, M., Cowie, P.A., Tucker, G.E., Roberts, G. (2008) Decoding temporal and spatial patterns of fault uplift using transient river long profiles. *Geomorphology*, **100**, 506-526.

Whittaker, A.C., Attal, M. and Allen, P.A. (2010) Characterising the origin, nature and fate of sediment exported from catchments perturbed by active tectonics. *Basin Research*, **22**, 809-828.

Whittaker, A.C. and Boulton, S.J. (2012) Tectonic and climatic controls on knickpoint retreat rates and landscape response times. *Journal of Geophysical Research*, **117**, F02024.

Whittaker, A.C. and Walker, A.S. (2015) Geomorphic constraints on fault throw rates and linkage times: Examples from the Northern Gulf of Evia, Greece. *Journal of Geophysical Research: Earth Surface*, **120**, 137-158.

Willett, S.D. (1999) Orogeny and orography: The effects of erosion on the structure of mountain belts. *Journal of Geophysical Research*, **104** (B12), 28957–28981.

Willett, S.D., Slingerland, R. and Hovius, N. (2001) Uplift, shortening, and steady state topography in active mountain belts. *American Journal of Science*, **301**, 455-485.

Willett, S.D., McCoy, S.W., Perron, J.T., Goren, L. and Chen, C.Y. (2014) Dynamic reorganization of river basins. *Science*, **343**, 1117-1126.

Wilson, L. (1976) Variations in mean annual sediment yield as a function of mean annual precipitation. *American Journal of Science*, **273**, 335-349.

Winograd, I.J., Landwehr, J.M., Ludwig, K.R., Coplen, T.B. and Riggs, A.C. (1997) Duration and structure of the past four interglaciations. *Quaternary Research*, **48**, 141-154.

Winograd, I.J., Landwehr, J.M., Coplen, T.B., Sharp, W.D., Riggs, A.C., Ludwig, K.R. and Kolesar, P.T. (2006) Devils Hole, Nevada, $\delta^{18}O$ record extended to the mid-Holocene. *Quaternary Research*, **66**, 202-212.

Wobus, C., Whipple, K.X., Kirby, E., Snyder, N., Johnson, J., Spyropolou, K., Crosby, B. and Sheehan, D. (2006) Tectonics from topography: Procedures, promise, and pitfalls. In: Willet, S.D., Hovius, N., Brandon, M.T. and Fisher, D.M. (Eds), Tectonics, Climate and Landscape Evolution. *Geological Society of America Special Paper*, **398**, Boulder, CO, pp. 55-74.

Wobus, C.W., Tucker, G.E. and Anderson, R.S. (2010) Does climate change create distinctive patterns of landscape incision? *Journal of Geophysical Research*, **115**, F04008.

Wolman, M.G. (1954) A method of sampling coarse river bed material. *Transactions, American Geophysical Union,* **35**, 951-956.

Woolfenden, W.B. (2003) A 180,000-year pollen record from Owens Lake, CA: Terrestrial vegetation change on orbital scales. *Quaternary Research*, **59**, 430-444.

Wulf, H., Bookhagen, B. and Scherler, D. (2010) Seasonal precipitation gradients and their impact on fluvial sediment flux in the northwest Himalaya. *Geomorphology*, **118**, 13-21.

Yamamoto, M., Yamamuro, M. and Tanaka, Y. (2007) The California current system during the last 136,000 years: Response of the North Pacific High to precessional forcing. *Quaternary Science Reviews*, **26**, 405-414.

Zachos, J.C., Dickens, J.R. and Zeebe, R.E. (2008) An early Cenozoic perspective on greenhouse warming and carbon-cycle dynamics. *Nature*, **451**, 279-283.

Zehfuss, P.H., Bierman, P.R., Gillespie, A.R., Burke, R.M. and Caffee, M.W. (2001) Slip rates on the Fish Springs fault, Owens Valley, California, deduced from cosmogenic ^{10}Be and ^{26}Al and soil development on fan surfaces. *Geological Society of America Bulletin*, **113**, 241–255.

Zic, M., Negrini, R.M. and Wigand, P.E. (2002) Evidence of synchronous climate change across the Northern Hemisphere between the North Atlantic and the northwestern Great Basin, United States. *Geology*, **30**, 635-638.